

THÈSE DE DOCTORAT  
DE SORBONNE UNIVERSITÉ

Spécialité : Physique

École doctorale n°564: Physique en Île-de-France

réalisée

au Laboratoire Kastler Brossel

sous la direction de Pierre-François Cohadon

présentée par

**Pierre-Edouard Jacquet**

pour obtenir le grade de :

**DOCTEUR DE SORBONNE UNIVERSITÉ**

Sujet de la thèse :

**Squeezed light optomechanics: Theory and Experiments**

soutenue le 26 Février 2026

devant le jury composé de :

M <sup>me</sup>	Agnès MAITRE	PU	INSP (SU)	Présidente
M	Pierre VERLOT	MC	LuMIn (UPSaclay)	Rapporteur
M	Jean-Pierre ZENDRI	DR	INFN (UPadova)	Rapporteur
M <sup>me</sup>	Sara DUCCI	PU	MPQ (UPCité)	Examinaterice
M	Jack HARRIS	PU	Yale University	Examinateur
M	Pierre-François COHADON	MC	LKB (ENS)	Directeur









# **Remerciements**

Merci bien



# Contents

<b>Introduction</b>	<b>3</b>
Historical background . . . . .	3
State of the art . . . . .	3
Relevance of this work . . . . .	3
<b>I Theory: Background</b>	<b>5</b>
I.1 Optics . . . . .	7
I.1.1 Spatial Modes . . . . .	7
I.1.2 Quantum Description . . . . .	7
I.1.3 Coherent and Squeezed States . . . . .	15
I.1.4 Classical Modulations . . . . .	20
I.1.5 Quantum Sideband Diagram . . . . .	22
I.2 Cavities . . . . .	22
I.2.1 Cavity Geometries and Stability Conditions . . . . .	23
I.2.2 Cavity Resonances . . . . .	24
I.2.3 Mode-Matching . . . . .	25
I.2.4 Simple Cavities . . . . .	26
I.2.5 Non Linear Cavities . . . . .	36
I.2.6 Optomechanical Cavities . . . . .	42

I.3 Detection . . . . .	49
I.3.1 Direct detection . . . . .	49
I.3.2 Balanced Homodyne Detection . . . . .	52
<b>II Theory: Squeezed Light &amp; Optomechanics</b>	<b>55</b>
II.1 Squeezed Light and Optomechanics . . . . .	57
II.1.1 Standard Quantum Limit . . . . .	57
II.1.2 Frequency Independent Squeezing in Optomechanical Cavities . . . . .	60
II.1.3 Frequency Dependent Squeezing in Optomechanical Cavities . . . . .	63
II.1.4 Filter Cavities for Frequency Dependent Squeezing . . . . .	64
II.2 Cavity Optomechanics with Membrane based systems . . . . .	65
II.2.1 Classical Description . . . . .	65
II.2.2 Quantum Description . . . . .	69
<b>III Experimental Methods</b>	<b>75</b>
III.1 Feedback control . . . . .	76
III.1.1 Overview . . . . .	76
III.1.2 Proportion-Integral (PI) Controllers . . . . .	77
III.1.3 PyRPL overview . . . . .	79
III.1.4 IQ modules . . . . .	81
III.2 Locking techniques . . . . .	83
III.2.1 Temperature Lock . . . . .	84
III.2.2 Optical phase Lock . . . . .	84
III.2.3 Cavity Locks . . . . .	85
III.2.4 Offset Frequency Locks and Phase Lock Loop . . . . .	88
<b>IV Experiments: Optomechanics</b>	<b>91</b>

IV.1 System Description and Setup . . . . .	92
IV.1.1 Previous LKB work and Motivation . . . . .	92
IV.1.2 Specifications and Design . . . . .	93
IV.1.3 Flexure Actuation . . . . .	97
IV.1.4 Experimental Setup . . . . .	99
IV.1.5 Alignment Procedures . . . . .	101
IV.2 Experimental Characterization . . . . .	102
IV.2.1 Cavity Scans . . . . .	102
IV.2.2 Cavity Locking and Mechanical Characterization . . . . .	111
IV.2.3 Bistability . . . . .	115
IV.3 Optomechanical Fibered Cavity . . . . .	116
IV.3.1 Design considerations . . . . .	117
IV.3.2 Fiber mirror fabrication . . . . .	121
IV.3.3 Designs and optical layout . . . . .	123
IV.4 Conclusion & perspectives . . . . .	127
<b>V Experiments: Squeezed Light</b>	<b>129</b>
V.1 Optical Setup Overview . . . . .	130
V.2 Cavity Resonances and Locks . . . . .	133
V.2.1 IRMC Cavity . . . . .	133
V.2.2 SHG Cavity . . . . .	135
V.2.3 OPO Cavity . . . . .	141
V.3 Squeezed State Detection . . . . .	145
V.3.1 Configuration I . . . . .	145
V.3.2 Configuration II . . . . .	147
V.4 Filter Cavity Concept . . . . .	148

V.4.1 Virgo Filter Cavity . . . . .	149
V.4.2 Lock and thermal effects . . . . .	151
V.4.3 Filter cavity for tabletop experiments . . . . .	153
V.5 Conclusion & perspectives . . . . .	153
<b>Conclusion</b>	<b>155</b>
Summary of Work . . . . .	155
Outlooks . . . . .	155
Final Remarks . . . . .	155
<b>Appendix A: Two-photon derivations</b>	<b>157</b>
Field Quantization . . . . .	157
Two photon formalism . . . . .	159
Derivation of the optimal angle . . . . .	165
<b>Appendix B: Error Signals</b>	<b>167</b>
Direct detection error signals . . . . .	167
PDH error signal . . . . .	169
<b>Appendix C: Three Mirror cavities</b>	<b>173</b>
<b>Bibliography</b>	<b>179</b>





# **Introduction**

**Historical background**

**State of the art**

**Relevance of this work**



# Chapter I

## Theory: Background

This chapter covers the elementary concepts required to describe a membrane based optomechanical system in a quantum regime. We will first recall basics on optical field quantization as well as describe a coherent and squeezed light field, to then turn to the more specific frequency-dependent squeezed light fields. Secondly, we will cover the mathematical description of a mechanical resonator interacting with a generic coherent optical field, highlighting the differences with the seminal optomechanical system of a mirror on a spring. Finally, we will derive the equations of motions of a membrane based optomechanical system with a frequency-dependent squeezed optical field.

**Contents**

---

<b>I.1</b>	<b>Optics</b>	<b>7</b>
I.1.1	Spatial Modes	7
I.1.2	Quantum Description	7
I.1.3	Coherent and Squeezed States	15
I.1.4	Classical Modulations	20
I.1.5	Quantum Sideband Diagram	22
<b>I.2</b>	<b>Cavities</b>	<b>22</b>
I.2.1	Cavity Geometries and Stability Conditions	23
I.2.2	Cavity Resonances	24
I.2.3	Mode-Matching	25
I.2.4	Simple Cavities	26
I.2.5	Non Linear Cavities	36
I.2.6	Optomechanical Cavities	42
<b>I.3</b>	<b>Detection</b>	<b>49</b>
I.3.1	Direct detection	49
I.3.2	Balanced Homodyne Detection	52

---

## I.1 Optics

### I.1.1 Spatial Modes

The spatial structure of an electromagnetic wave propagating along the  $z$ -axis can be described by a set of well-defined transverse modes, which are solutions of the paraxial Helmholtz equation. The most fundamental solution is the Gaussian mode, whose electric field amplitude reads

$$E(\mathbf{r}) = E_0 \frac{w_0}{w(z)} \exp\left(-\frac{x^2 + y^2}{w^2(z)}\right) \exp\left[-i\left(kz + \frac{k(x^2 + y^2)}{2R(z)} - \psi(z)\right)\right], \quad (\text{I.1})$$

where  $\mathbf{r} = (x, y, z)$ ,  $E_0$  is the field amplitude at the beam waist,  $k = 2\pi/\lambda$  the wavenumber, and  $\lambda$  the optical wavelength. The various quantities introduced above are defined as

$$\begin{aligned} w(z) &\equiv w_0 \sqrt{1 + (z/z_R)^2}, & z_R &\equiv \pi w_0^2 / \lambda, \\ R(z) &\equiv z \left[1 + (z_R/z)^2\right], & \psi(z) &\equiv \arctan(z/z_R), \end{aligned}$$

with  $w_0$  the waist,  $z_R$  the Rayleigh range,  $R(z)$  the wavefront curvature, and  $\psi(z)$  the Gouy phase. A compact expression of the Gaussian envelope is written as

$$E(\mathbf{r}) = E_0 \frac{iz_R}{q(z)} \exp\left(-\frac{ik(x^2 + y^2)}{2q(z)}\right) e^{-ikz} \quad \text{with} \quad q(z) \equiv z + iz_R, \quad (\text{I.2})$$

where we defined the complex beam parameter  $q(z)$ . Beyond the fundamental Gaussian mode, more general solutions of the paraxial equation can be constructed. In Cartesian coordinates, these are the Hermite–Gaussian modes  $\text{TEM}_{mn}$ , given by

$$\begin{aligned} E_{mn}(\mathbf{r}) &= E_0 \frac{w_0}{w(z)} H_m\left(\frac{\sqrt{2}x}{w(z)}\right) H_n\left(\frac{\sqrt{2}y}{w(z)}\right) \exp\left(-\frac{x^2 + y^2}{w^2(z)}\right) \\ &\quad \times \exp\left[-i\left(kz + \frac{k(x^2 + y^2)}{2R(z)} - (m + n + 1)\psi(z)\right)\right], \quad (\text{I.3}) \end{aligned}$$

where  $H_m, H_n$  are Hermite polynomials.

### I.1.2 Quantum Description

#### Quantised Electromagnetic Field

We will consider both cases of a finite quantisation volume  $V$  and an infinite volume: when dealing with cavity modes, we will use the finite volume description, while for propagating modes carrying sideband correlations we will use the infinite volume description, under the

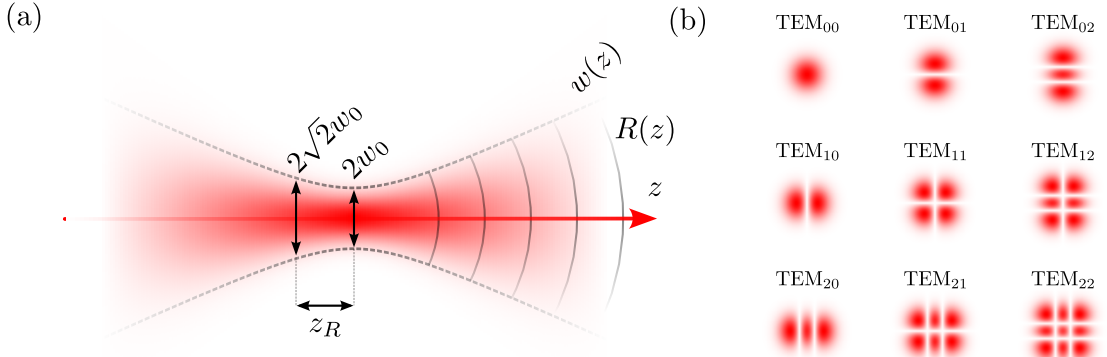


Fig. I.1 Gaussian beam characteristics: (a) Intensity profile of the fundamental Gaussian mode at different positions along the propagation axis  $z$ . The various quantities introduced in the text are indicated. (b) Transverse intensity profiles of the first few Hermite–Gaussian modes  $\text{TEM}_{mn}$ . These modes form an orthonormal basis to describe the spatial structure of paraxial beams: any realistic beam can be decomposed as a superposition of these modes.

two-photon formalism prescription. Both descriptions are linked through the input-output formalism introduced later on.

We first consider the quantised electromagnetic field in a volume  $V$ . The electric field operator can be written as

$$\hat{\mathbf{E}}(\mathbf{r}, t) = i \sum_{\ell} \mathcal{E}_{\ell} \left[ \hat{a}_{\ell} \mathbf{f}_{\ell}(\mathbf{r}) e^{-i\omega_{\ell}t} - \hat{a}_{\ell}^{\dagger} \mathbf{f}_{\ell}^*(\mathbf{r}) e^{+i\omega_{\ell}t} \right], \quad (\text{I.4})$$

where  $\mathcal{E}_{\ell} = \sqrt{\hbar\omega_{\ell}/2\varepsilon_0V}$  is the field amplitude per photon in mode  $\ell$ ,  $\hbar$  is the reduced Planck constant,  $\omega_{\ell}$  is the angular frequency of mode  $\ell$ , and  $\varepsilon_0$  is the vacuum permittivity. The spatial mode functions  $\mathbf{f}_{\ell}(\mathbf{r})$  form an orthonormal basis in  $V$  according to

$$\int_V d^3r \mathbf{f}_{\ell}^*(\mathbf{r}) \cdot \mathbf{f}_{\ell'}(\mathbf{r}) = \delta_{\ell\ell'}, \quad \mathbf{f}_{\ell}(\mathbf{r}) \propto E_{mn}(\mathbf{r}) \boldsymbol{\epsilon}_x$$

where we assumed a linearly-polarized field along the  $x$ -axis, with  $\boldsymbol{\epsilon}_x$  the corresponding unit vector. The index  $\ell = (m, n)$  then labels the different spatial modes, the Hermite–Gaussian modes in our case.

In the limit of an infinite quantisation volume  $V \rightarrow \infty$ , the discrete mode index  $\ell$  becomes a continuous variable i.e. the mode spacing becomes infinitesimal. As detailed in the Appendix A, we now need to consider a continuum of modes with annihilation operator  $\hat{a}[\omega]$  labeled by their angular frequency  $\omega$ . To come down to the two-photon formalism, we make

the following assumptions :

- we consider frequencies  $\omega = \omega_0 \pm \Omega$  centered around a carrier frequency  $\omega_0$ , with  $\Omega \in [-2\pi B, +2\pi B] \ll \omega_0$  where  $B$  is the bandwidth. This is valid since the bandwidth  $B$ , generally up to tens of GHz, is small compared to  $\omega_0/2\pi$  which is hundreds of THz for optical frequencies.
- we consider a single spatial mode, i.e. we drop the spatial dependence of the field and consider only one transverse mode function  $\mathbf{f}(\mathbf{r})$ , the fundamental Gaussian mode imposed by the laser source and/or spatial filtering elements. This is valid since the spatial envelope of the beam does not vary significantly over the considered bandwidth. The spatial mode function is then factored out of the integrals over frequency.
- we consider the electric field operator to only be dependent on time  $t$ , having projected the field onto the transverse mode function and integrated over the transverse plane, as well as setting the propagation coordinate  $z = 0$  for simplicity.

Upon these assumptions, the electric field operator reduces to a time-dependent operator (Heisenberg picture) expressed as

$$\hat{E}(t) = \mathcal{E}_0 \left[ \cos\left(\omega_0 t - \frac{\pi}{2}\right) \int_{-\infty}^{\infty} \frac{d\Omega}{2\pi} (\hat{a}_+ + \hat{a}_-^\dagger) e^{-i\Omega t} + \sin\left(\omega_0 t - \frac{\pi}{2}\right) \int_{-\infty}^{\infty} \frac{d\Omega}{2\pi} i(\hat{a}_-^\dagger - \hat{a}_+) e^{-i\Omega t} \right] \quad (\text{I.5})$$

where we defined the sideband annihilation operators as  $\hat{a}_+[\Omega] \equiv \hat{a}[\omega_0 + \Omega]$  and  $\hat{a}_-[\Omega] \equiv \hat{a}[\omega_0 - \Omega]$ . The field amplitude per photon at the carrier frequency is given by  $\mathcal{E}_0 = \sqrt{\hbar\omega_0/2\varepsilon_0 c A}$ , where  $A$  is the effective cross-sectional area of the beam and  $c$  the speed of light in vacuum. The explicit relationship between the discrete mode operator  $\hat{a}_\ell$  and the continuous mode operator  $\hat{a}[\omega]$  (and thus their hermitian conjugate) is given in the Appendix A.

**Note:** Although the electric field operator is written in the Heisenberg picture, the annihilation and creation operators  $\hat{a}[\omega]$  and  $\hat{a}[\omega]^\dagger$  are Schrödinger like operators, i.e. time independent operators. This is because we already factored out the time dependence  $e^{-i\omega t}$  associated to each frequency mode when writing our annihilation/creation operators. As seen later on, the time dependence of the field operator defined through the Fourier transform arises from the superposition of many frequency modes, leading to beating at frequency  $\Omega$ . This is the heart of the two-photon formalism, where a time dependent field Heisenberg like operator is built from the superposition of Schrödinger like annihilation/creation operators at different frequencies. In the literature, the Schrödinger like operators are sometimes written as  $\hat{a}_\omega$  to draw a parallel between the discrete mode case  $\hat{a}_\ell$ , but we will stick to the

$\hat{a}[\omega]$  notation to avoid confusion with time dependent operators.

When writing annihilation operators, we will often drop the frequency dependence to lighten the notation, but it is implicit that they depend on frequency i.e.  $\hat{a} \equiv \hat{a}[\omega]$ , such that it applies to both sideband operators  $\hat{a}_+$  and  $\hat{a}_-$ .

### Commutation Relations

As demonstrated in the Appendix, the continuous annihilation and creation operators satisfy the following commutation relations:

$$[\hat{a}[\omega], \hat{a}^\dagger[\omega']] = 2\pi \delta(\omega - \omega'), \quad [\hat{a}[\omega], \hat{a}[\omega']] = 0, \quad [\hat{a}^\dagger[\omega], \hat{a}^\dagger[\omega']] = 0.$$

such that the sideband operators satisfy

$$[\hat{a}_\pm[\Omega], \hat{a}_\pm^\dagger[\Omega']] = 2\pi \delta(\Omega - \Omega'), \quad [\hat{a}_\pm[\Omega], \hat{a}_\mp[\Omega']] = 0, \quad [\hat{a}_\pm^\dagger[\Omega], \hat{a}_\pm^\dagger[\Omega']] = 0.$$

### Quadrature Operators

We describe the phase-space properties of a field mode using hermitian quadrature operators. These are linear combinations of the annihilation and creation operators that correspond to measurable observables of the electromagnetic field. Here again, we won't write explicitly the frequency dependence, but it is implicit in the following i.e.  $\hat{\mathbf{u}} \equiv \hat{\mathbf{u}}[\Omega]$  and  $\hat{\mathbf{a}} \equiv \hat{\mathbf{a}}[\Omega]$ . The two most common quadratures are defined as follows:

$$\hat{\mathbf{u}} \equiv \begin{pmatrix} \hat{a}_1 \\ \hat{a}_2 \end{pmatrix} = \boldsymbol{\Gamma} \hat{\mathbf{a}} \quad \text{with} \quad \boldsymbol{\Gamma} \equiv \begin{pmatrix} 1 & 1 \\ -i & i \end{pmatrix} \quad \text{and} \quad \hat{\mathbf{a}} \equiv \begin{pmatrix} \hat{a}_+ \\ \hat{a}_-^\dagger \end{pmatrix} \quad (\text{I.6})$$

where we defined the field vector  $\hat{\mathbf{a}}$  and the transfer matrix  $\boldsymbol{\Gamma}$ , later used to switch from *one-photon* to *two-photon* description of optical elements. Mathematically, the integral bounds are the detection bandwidth, but we can safely extend it to infinity. The electric field operator can then be recasted as

$$\hat{E}(t) = \mathcal{E}_0 \left[ \cos\left(\omega_0 t - \frac{\pi}{2}\right) \int_{-\infty}^{\infty} \frac{d\Omega}{2\pi} \hat{a}_1[\Omega] e^{-i\Omega t} + \sin\left(\omega_0 t - \frac{\pi}{2}\right) \int_{-\infty}^{\infty} \frac{d\Omega}{2\pi} \hat{a}_2[\Omega] e^{-i\Omega t} \right]. \quad (\text{I.7})$$

where it is now explicit that the electric field features two orthogonal components oscillating at the carrier frequency  $\omega_0$ , with amplitudes given by the quadrature operators  $\hat{a}_1$  and  $\hat{a}_2$ .

### Fourier Transform

We now come to the aforementioned building of a time-dependent field operator from the superposition of many frequency modes. This is done through the Fourier transform defined as

$$\begin{aligned}\hat{\mathbf{a}}(t) &= \int_{-\infty}^{+\infty} \frac{d\Omega}{2\pi} e^{-i\Omega t} \hat{\mathbf{a}}[\Omega] \\ \hat{\mathbf{a}}[\Omega] &= \int_{-\infty}^{+\infty} dt e^{i\Omega t} \hat{\mathbf{a}}(t)\end{aligned}\quad (\text{I.8})$$

In this definition, a notable property is that the hermitian conjugate in the time domain translates to a frequency inversion in the Fourier domain:

$$[\hat{a}(t)]^\dagger = \hat{a}^\dagger(t), \quad [\hat{a}_+]^\dagger = \hat{a}_-. \quad (\text{I.9})$$

It then follows that the quadrature operators in the time domain are effectively Hermitian operators, as expected for observables, while the frequency domain quadrature operators satisfy

$$\hat{a}_1^\dagger[\Omega] = \hat{a}_1[-\Omega], \quad \hat{a}_2^\dagger[\Omega] = \hat{a}_2[-\Omega]. \quad (\text{I.10})$$

### Commutation Relations in vector form

The matrix form commutator in both time and frequency space reads

$$[\hat{\mathbf{a}}, \hat{\mathbf{a}}^\dagger] = \sigma_z \times \begin{cases} \delta(t - t') \\ 2\pi\delta(\Omega - \Omega'). \end{cases} \quad (\text{I.11})$$

with  $\sigma_z$  the Pauli Z matrix, and where it is implicit that we evaluate both at different frequencies or times respectively. An arbitrary rotated quadrature pair is obtained by

$$\hat{\mathbf{u}}_\phi \equiv \mathbf{R}(\phi) \hat{\mathbf{u}} = \mathbf{R}(\phi) \Gamma \hat{\mathbf{a}} \quad \text{with} \quad \mathbf{R}(\phi) \equiv \begin{pmatrix} \cos \phi & \sin \phi \\ -\sin \phi & \cos \phi \end{pmatrix}. \quad (\text{I.12})$$

and where we identify the useful identity

$$\mathbf{R}(\phi) \Gamma = \begin{pmatrix} e^{-i\phi} & e^{i\phi} \\ -ie^{-i\phi} & ie^{i\phi} \end{pmatrix}.$$

The commutators of the rotated quadrature operators read

$$[\hat{\mathbf{u}}_\phi, \hat{\mathbf{u}}_\phi^\dagger] = 2i \mathbf{J} \begin{cases} \delta(t - t') \\ 2\pi\delta(\Omega - \Omega') \end{cases} \quad \text{with } \mathbf{J} \equiv \begin{pmatrix} 0 & 1 \\ -1 & 0 \end{pmatrix}. \quad (\text{I.13})$$

This identity would not be true had we considered large sideband frequencies  $\Omega \sim \omega_0$  i.e. it would feature corrections in all  $\mathbf{J}$  terms, including diagonal.

### Linearization of the optical field

Let's now consider a quantum state living in this continuous mode space  $|\psi\rangle$ . We can always linearize the field operators around their mean value, which is particularly useful when dealing with intense fields featuring small quantum fluctuations around a large classical amplitude. This is the case for coherent and squeezed states, which are introduced right below. The annihilation operator is then be decomposed as

$$\hat{a} = \bar{a} + \delta\hat{a} \quad (\text{I.14})$$

where  $\bar{a} = \langle\psi|\hat{a}|\psi\rangle \in \mathbb{C}$  is the mean complex amplitude of the quantum state, and  $\delta\hat{a}$  represents quantum fluctuations with  $\langle\psi|\delta\hat{a}|\psi\rangle = 0$ . Note this decomposition is valid for any quantum state, including coherent and squeezed states. We note  $\bar{a}$  to distinguish it from the complex amplitude  $\alpha$  of a coherent state introduced below, which is a specific case of this decomposition. The field vector is then expressed as

$$\hat{\mathbf{a}} = \begin{pmatrix} \bar{a}_+ \\ \bar{a}_-^* \end{pmatrix} + \begin{pmatrix} \delta\hat{a}_+ \\ \delta\hat{a}_-^\dagger \end{pmatrix} = \bar{\mathbf{a}} + \delta\hat{\mathbf{a}} \quad (\text{I.15})$$

and it then follows that the quadrature operators can also be expressed as

$$\hat{\mathbf{u}}_\phi = \mathbf{R}(\phi) \boldsymbol{\Gamma} (\bar{\mathbf{a}} + \delta\hat{\mathbf{a}}) = \bar{\mathbf{u}}_\phi + \delta\hat{\mathbf{u}}_\phi. \quad (\text{I.16})$$

For the vacuum state  $|0\rangle$ , we have  $\bar{a}_\pm = 0$  and thus  $\hat{\mathbf{a}} = \delta\hat{\mathbf{a}}$ . Since we will always consider fluctuations around the mean value, we will systematically use the notation  $\delta\hat{a}$  to refer to the annihilation operator, unless specified otherwise, as well as assume the vacuum state as the reference when we write average values as  $\langle \cdot \rangle \equiv \langle 0 | \cdot | 0 \rangle$ . All the above definitions and properties thus apply to the fluctuation operators (commutation relations, Fourier transforms, etc.).

### Amplitude and Phase Quadratures

Considering the mean field amplitude  $\bar{\alpha} = |\bar{\alpha}|e^{i\bar{\varphi}}$ , we will often refer to the amplitude and phase quadratures, defined respectively as the quadratures at angles  $\phi = \bar{\varphi}$  and  $\phi = \bar{\varphi} + \pi/2$ . As the angle  $\bar{\varphi}$  defines the mean field phase relative to a reference (e.g. a local oscillator), we will assume without loss of generality that  $\bar{\varphi} = 0$ , such that the amplitude and phase quadratures correspond to  $\hat{a}_1$  and  $\hat{a}_2$  respectively. We will then relabel them as

$$\delta\hat{p} \equiv \delta\hat{a}_{\phi=0} = \delta\hat{a}_1, \quad \delta\hat{q} \equiv \delta\hat{a}_{\phi=\pi/2} = \delta\hat{a}_2. \quad (\text{I.17})$$

### Noise Spectral Density Matrix

A central concept in this thesis is the two-sided Noise Spectral Density matrix of the quadrature fluctuations, which characterizes the second-order statistical properties of the quantum state in the frequency domain. Namely, it describes the spectral distribution of the variances and covariances of the quadrature fluctuations. For a given quadrature angle  $\phi$ , it is defined as

$$\begin{aligned} \mathbf{S}_\phi[\Omega] &= \frac{1}{2} \int \frac{\delta\Omega'}{2\pi} \langle \{\delta\hat{\mathbf{u}}_\phi, \delta\hat{\mathbf{u}}_\phi^\dagger\} \rangle \\ &= \frac{1}{2} \int \frac{\delta\Omega'}{2\pi} \mathbf{R}(\phi) \langle \{\delta\hat{\mathbf{u}}, \delta\hat{\mathbf{u}}^\dagger\} \rangle \mathbf{R}(-\phi) \\ &= \frac{1}{2} \int \frac{\delta\Omega'}{2\pi} \mathbf{R}(\phi) \begin{pmatrix} \langle \{\delta\hat{p}, \delta\hat{p}^\dagger\} \rangle & \langle \{\delta\hat{p}, \delta\hat{q}^\dagger\} \rangle \\ \langle \{\delta\hat{q}, \delta\hat{p}^\dagger\} \rangle & \langle \{\delta\hat{q}, \delta\hat{q}^\dagger\} \rangle \end{pmatrix} \mathbf{R}(-\phi) \end{aligned} \quad (\text{I.18})$$

where  $\{\hat{A}, \hat{B}\} = \hat{A}\hat{B} + \hat{B}\hat{A}$  denotes the anticommutator, implicitly evaluated at frequencies  $\Omega$  and  $\Omega'$ , and integrated over  $\Omega'$ . The diagonal elements of the noise spectral density matrix correspond to the power spectral densities of the quadrature fluctuations, while the off-diagonal elements represent the cross-spectral densities between different quadratures. The noise spectral density matrix is a Hermitian matrix, reflecting the physical properties of the quantum state. We will particularly focus on the amplitude and phase quadrature noise spectral density matrix, obtained by setting  $\phi = 0$ , and we will denote it as  $\mathbf{S}[\Omega] \equiv \mathbf{S}_{\phi=0}[\Omega]$ . The subscripts will then denote whether we refer to the transmitted or reflected fields of an optical cavity, the output spectrum of a squeezer, etc. For completeness we introduce the single-sided noise spectral density matrix, defined as

$$\bar{\mathbf{S}}_\phi[\Omega] = \frac{1}{2} (\mathbf{S}_\phi[\Omega] + \mathbf{S}_\phi[-\Omega]) \quad (\text{I.19})$$

such that the variance of a quadrature operator can be retrieved by integrating the single-sided noise spectral density over positive frequencies only (as one would with a real signal in

a spectrum analyzer). A generalized version of the Heisenberg uncertainty relation can be expressed in terms of the noise spectral density matrix as

$$\det \mathbf{S}_\phi[\Omega] \geq 1 \quad (\text{I.20})$$

which sets a fundamental limit on the simultaneous knowledge of the quadrature fluctuations at a given frequency  $\Omega$ .

### Vacuum state

For the vacuum state  $|0\rangle$ , we derive the noise spectral density matrix using the commutation relations and the fact that  $\langle \delta\hat{a} \rangle = 0$  (see Annexe A). The calculation yields

$$\mathbf{S}_{\text{vac}}[\Omega] = \begin{pmatrix} 1 & 0 \\ 0 & 1 \end{pmatrix} \quad (\text{I.21})$$

for any angle  $\phi$  and frequency  $\Omega$ . This result indicates that the vacuum state has equal fluctuations in both quadratures, with no correlations between them, as expected for a minimum uncertainty state. The noise spectral density matrix of the vacuum state serves as a reference point for comparing other quantum states, such as coherent and squeezed states, which exhibit different fluctuation properties.

### Linear Optical Systems

As we will develop further in the next section, the output fields of various optical systems can be expressed in a general linear form as

$$\delta\hat{\mathbf{u}}_{\text{out}} = \mathbf{T} \delta\hat{\mathbf{u}}_{\text{in}} + \mathbf{L} \delta\hat{\mathbf{u}}_{\text{vac}}. \quad (\text{I.22})$$

where  $\mathbf{T}$  and  $\mathbf{L}$  are  $2 \times 2$  frequency-dependent transfer matrices. The input and vacuum fields are assumed to be in the vacuum state, as well as being uncorrelated such that

$$\begin{aligned} \langle \delta\hat{\mathbf{u}}_{\text{in}} \delta\hat{\mathbf{u}}_{\text{in}}^\dagger \rangle &= 2\pi\delta(\Omega + \Omega') \mathbf{S}_{\text{in}}[\Omega] \\ \langle \delta\hat{\mathbf{u}}_{\text{vac}} \delta\hat{\mathbf{u}}_{\text{vac}}^\dagger \rangle &= 2\pi\delta(\Omega + \Omega') \mathbf{1} \\ \langle \delta\hat{\mathbf{u}}_{\text{in}} \delta\hat{\mathbf{u}}_{\text{vac}}^\dagger \rangle &= \mathbf{0} \end{aligned} \quad (\text{I.23})$$

Computing the noise spectra is then straightforward :

$$\mathbf{S}_{\text{out}}[\Omega] = \mathbf{T} \mathbf{S}_{\text{in}} \mathbf{T}^\dagger + \mathbf{L} \mathbf{L}^\dagger \quad (\text{I.24})$$

with  $\mathbf{S}_{\text{vac}} = \mathbf{1}$  as seen above. For an arbitrary quadrature angle  $\phi$ , we simply rotate the transfer matrices as

$$\mathbf{T}_\phi = \mathbf{R}(\phi) \mathbf{T} \mathbf{R}(-\phi), \quad \mathbf{L}_\phi = \mathbf{R}(\phi) \mathbf{L} \mathbf{R}(-\phi)$$

such that

$$\mathbf{S}_{\text{out},\phi}[\Omega] = \mathbf{T}_\phi \mathbf{S}_{\text{in},\phi} \mathbf{T}_\phi^\dagger + \mathbf{L}_\phi \mathbf{L}_\phi^\dagger \quad (\text{I.25})$$

### Graphical Representation of Gaussian States

Gaussian states can actually be pictured in a 2D space, where the two axes correspond to the two quadratures  $\hat{a}_1$  and  $\hat{a}_2$ . In the case where the mean phase is zero, these quadratures correspond to the amplitude and phase quadratures  $\hat{p}$  and  $\hat{q}$ . The quantum state can then be represented as a 2D Gaussian distribution centered around the mean values of the quadratures, with the shape and orientation of the distribution characterized by the off-diagonal elements of the noise spectral density matrix. The uncertainties in the quadratures are represented by the widths of the Gaussian distribution along each axis, while correlations between the quadratures are represented by the tilt of the distribution. This graphical representation provides an intuitive way to visualize and understand the properties of Gaussian quantum states, such as coherent and squeezed states, in terms of their quadrature fluctuations and correlations.

#### I.1.3 Coherent and Squeezed States

We now turn to standard optical quantum states, in particular Gaussian states i.e. full positive in Wigner function representations such as coherent and squeezed states, that we will denote in braket notation as  $|\alpha\rangle$  and  $|\alpha, r, \theta\rangle$ .

##### Coherent States:

The monochromatic coherent state  $|\alpha\rangle$  is an eigenstate of the annihilation operator:

$$\hat{a}_+ |\alpha\rangle = \alpha \delta(\Omega) |\alpha\rangle \quad (\text{I.26})$$

where  $\alpha = |\alpha| e^{i\bar{\varphi}}$  is a complex number representing the mean coherent amplitude. In this notation, the angle  $\bar{\varphi}$  is the mean angle of the distribution, used to describe the relative phase to a reference (e.g. a local oscillator), as in Fig I.2. The  $\hat{a}$  linear decomposition above (Eq.I.14) then yields  $\alpha = \bar{\alpha}$  for a coherent state. A generic multimode coherent state is generated by the displacement operator  $\hat{D}(\alpha)$  such that

$$|\alpha\rangle = \hat{D}(\alpha) |0\rangle \quad (\text{I.27})$$

where the general expression for the displacement operator acting on the vacuum state is given by

$$\hat{D}(\alpha) = \exp\left(\int \frac{d\Omega}{2\pi} [\alpha(\Omega)\hat{a}_-^\dagger - \alpha^*(\Omega)\hat{a}_+]\right) \quad (\text{I.28})$$

which collapses to

$$\hat{D}(\alpha) = \exp\left(\frac{1}{2\pi} [\alpha\hat{a}_-^\dagger[\omega_0] - \alpha^*\hat{a}_-[\omega_0]]\right) \quad (\text{I.29})$$

when defining a monochromatic coherent state  $\alpha(\Omega) = \alpha\delta(\Omega)$ , that is a coherent state at the carrier frequency only. Upon the action of this displacement operator, the sideband operator is transformed as

$$D^\dagger(\alpha)\hat{a}_+ D(\alpha) = \hat{a}_+ + \alpha\delta(\Omega) \quad (\text{I.30})$$

such that we can verify the eigenvalue equation (Eq.I.26) straightforwardly as

$$\begin{aligned} \hat{a}_+ |\alpha\rangle &= D(\alpha)(D^\dagger(\alpha)\hat{a}_+ D(\alpha))|0\rangle \\ &= \hat{D}(\alpha)(\alpha\delta(\Omega) + \hat{a}_+)|0\rangle \\ &= \alpha\delta(\Omega)|\alpha\rangle \end{aligned}$$

**Expectation values:** Using the quadrature vector  $\hat{\mathbf{u}}_\phi$  (Eq.I.12), and the  $\mathbf{R}\Gamma$  identity, the expectation values in a coherent state are

$$\langle \hat{D}^\dagger \hat{\mathbf{u}}_\phi \hat{D} \rangle = \mathbf{R}(\phi) \langle \hat{D}^\dagger \hat{\mathbf{u}} \hat{D} \rangle = 2\delta(\Omega) \begin{pmatrix} \text{Re}(|\alpha|e^{i(\bar{\varphi}-\phi)}) \\ \text{Im}(|\alpha|e^{i(\bar{\varphi}-\phi)}) \end{pmatrix} \quad (\text{I.31})$$

such that the components reduce to  $2\text{Re}(\alpha)$  and  $2\text{Im}(\alpha)$  if  $\phi = 0$ , and to  $2|\alpha|$  and 0 if  $\phi = \bar{\varphi}$ , or equivalently if we set  $\bar{\varphi} = \phi = 0$  as mentioned earlier (such that  $\hat{\mathbf{u}}$  corresponds to the amplitude and phase quadratures). We also notice the delta function at  $\Omega = 0$ , indicating that the coherent state has a non-zero mean field only at the carrier frequency.

**Spectrum:** For a coherent state, the fluctuations are identical to that of the vacuum state, seen directly from Eq.I.30. Since the fluctuation operators are unchanged by the displacement, the noise spectral density matrix remains that of the vacuum:

$$\mathbf{S}_{\text{coh}}[\Omega] = \mathbf{S}_{\text{vac}} = \begin{pmatrix} 1 & 0 \\ 0 & 1 \end{pmatrix} \quad (\text{I.32})$$

for any angle  $\phi$  and frequency  $\Omega$ . Relating to the linear optical systems introduced, this is equivalent to having identity transfer matrices  $\mathbf{T} = \mathbf{1}$  and  $\mathbf{L} = \mathbf{0}$ , such that no additional noise is added to the input vacuum fluctuations. Coherent states only differ from vacuum by their non-zero mean field amplitudes at the carrier frequency  $\Omega = 0$ , symbolized by the

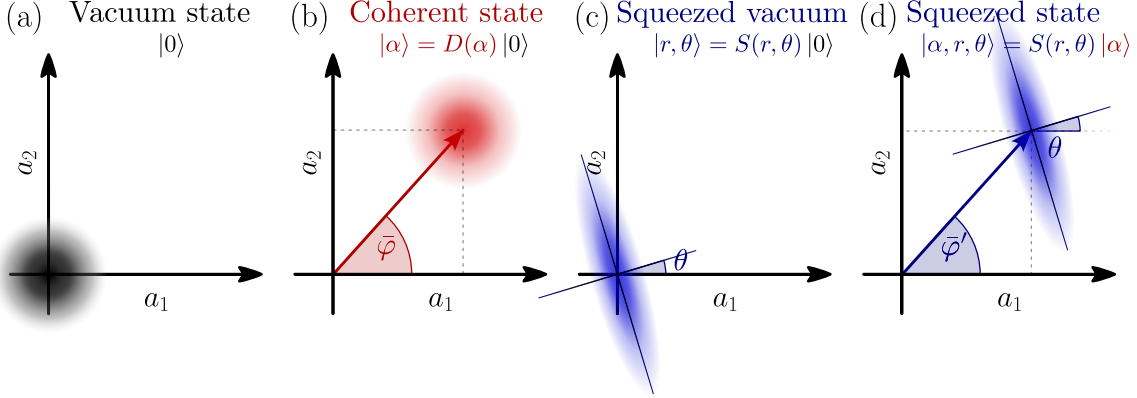


Fig. I.2 Phase-space representations of Gaussian quantum states. 2D cuts of the Wigner function in the quadrature plane ( $a_1[\Omega]$ ,  $a_2[\Omega]$ ) at a given frequency. (a) vacuum state: a circular Gaussian centered at the origin, featuring equal quantum fluctuations in both  $a_1$  and  $a_2$  quadratures. (b) coherent state: a displaced circular Gaussian, showing a shift in phase space along an angle  $\varphi$  with vacuum fluctuations. This corresponds to either the carrier ( $\Omega = 0$ ), or a sideband frequency with a non zero modulation. (c) vacuum squeezed state: an elliptical Gaussian centered at the origin, with reduced noise along a rotated quadrature and increased noise in the orthogonal direction. (d) bright squeezed state: an ellipse shifted away from the origin, combining anisotropic fluctuations and a nonzero mean amplitude. The displacement angle  $\varphi$  and squeezing angle  $\theta$  are independent.

delta function in the expectation values above.

### Squeezed States:

Squeezed states  $|\alpha, r, \theta\rangle$  are quantum Gaussian states of light in which the noise (variance) of one quadrature is reduced below the vacuum level, at the expense of increased noise in the conjugate quadrature. A generic squeezed state is characterized by three parameters: the displacement amplitude  $\alpha$ , the squeezing parameter  $r$ , and the squeezing angle  $\theta$ . The so-called 'bright' squeezed state is generated by applying both a displacement and a squeezing operation to the vacuum state:

$$|\alpha, r, \theta\rangle = \hat{S}(r, \theta)\hat{D}(\alpha)|0\rangle \quad (\text{I.33})$$

where the squeezing operator  $\hat{S}(r, \theta)$  is defined as

$$\hat{S}(r, \theta) = \exp\left(r \int_{-\infty}^{\infty} \frac{d\Omega}{2\pi} \left[ e^{-i2\theta(\Omega)} \hat{a}_+ \hat{a}_- - e^{i2\theta(\Omega)} \hat{a}_+^\dagger \hat{a}_-^\dagger \right] \right) \quad (\text{I.34})$$

where we assumed the squeezing parameter  $r$  to be frequency-independent. This operator describes the process of parametric down-conversion, where pairs of photons are created

or annihilated in the sideband modes  $\hat{a}_\pm$  with a phase relation determined by the squeezing angle  $\theta(\Omega)$ . We can then write the action of the squeezing operator on the sideband operators as

$$\hat{S}^\dagger \hat{a}_+ \hat{S} = \hat{a}_+ \cosh r - e^{i2\theta(\Omega)} \hat{a}_-^\dagger \sinh r \quad (\text{I.35})$$

and similarly for  $\hat{a}_-$ . This transformation shows how the squeezing operator mixes the annihilation and creation operators, leading to modified quadrature fluctuations in the squeezed state. Applying both transformations (displacement and squeezing) to the field vector, we have

$$\hat{D}^\dagger \hat{S}^\dagger \hat{a}_+ \hat{S} \hat{D} = \hat{a}_+ \cosh r - e^{i2\theta} \hat{a}_-^\dagger \sinh r + \gamma \delta(\Omega) \quad (\text{I.36})$$

with  $\gamma = \alpha \cosh r - \alpha^* e^{i2\theta} \sinh r = |\gamma| e^{i\bar{\varphi}'}$  the displaced amplitude at the carrier frequency. We stress that the phase  $\bar{\varphi}'$  generally differs from the displacement angle  $\bar{\varphi}$  of the coherent amplitude  $\alpha$ .

**Expectation values:** Similarly as in a coherent state, but this time from Eq.I.36, we can derive the expectation values of the quadrature vector in a bright squeezed state as

$$\langle \hat{D}^\dagger \hat{S}^\dagger \hat{\mathbf{u}}_\phi \hat{S} \hat{D} \rangle = \mathbf{R}(\phi) \langle \hat{D}^\dagger \hat{S}^\dagger \hat{\mathbf{u}} \hat{S} \hat{D} \rangle = 2\delta(\Omega) \begin{pmatrix} \text{Re}(|\gamma| e^{i(\bar{\varphi}' - \phi)}) \\ \text{Im}(|\gamma| e^{i(\bar{\varphi}' - \phi)}) \end{pmatrix} \quad (\text{I.37})$$

indicating that the mean field is shifted by the displaced amplitude  $\gamma$  at the carrier frequency  $\omega_0$ .

**Spectrum:** We identify the field fluctuation transformation under the squeezing and displacement operators from Eq.I.36:

$$\hat{D} \hat{S}^\dagger \delta \hat{\mathbf{a}} \hat{S} \hat{D} = \begin{pmatrix} \cosh r & -e^{i2\theta(\Omega)} \sinh r \\ -e^{-i2\theta(\Omega)} \sinh r & \cosh r \end{pmatrix} \delta \hat{\mathbf{a}} \quad (\text{I.38})$$

such that the quadrature fluctuations read

$$\hat{D}^\dagger \hat{S}^\dagger \delta \hat{\mathbf{u}} \hat{S} \hat{D} = \mathbf{T} \delta \hat{\mathbf{u}} \quad (\text{I.39})$$

where we defined the transfer matrix

$$\begin{aligned} \mathbf{T} &= \begin{pmatrix} \cosh r - \sinh r \cos 2\theta(\Omega) & -\sinh r \sin 2\theta(\Omega) \\ -\sinh r \sin 2\theta(\Omega) & \cosh r + \sinh r \cos 2\theta(\Omega) \end{pmatrix} \\ &= \mathbf{R}(-\theta) e^{-r\sigma_z} \mathbf{R}(\theta) \end{aligned}$$

Using the linear optical system formalism introduced earlier, we identify the transfer matrices

$\mathbf{T}$  and  $\mathbf{L} = \mathbf{0}$  (no additional noise). The noise spectral density matrix of a bright squeezed state is then computed as

$$\mathbf{S}_{\text{sqz}}[\Omega] = \mathbf{T}\mathbf{S}_{\text{vac}}\mathbf{T}^\dagger = \mathbf{T}\mathbf{T}^\dagger. \quad (\text{I.40})$$

Explicitly, this yields

$$\begin{aligned} \mathbf{S}_{\text{sqz}}[\Omega] &= \mathbf{R}(-\theta)e^{-2r\sigma_z}\mathbf{R}(\theta) \\ &= \begin{pmatrix} \cosh 2r - \sinh 2r \cos 2\theta(\Omega) & -\sinh 2r \sin 2\theta(\Omega) \\ -\sinh 2r \sin 2\theta(\Omega) & \cosh 2r + \sinh 2r \cos 2\theta(\Omega) \end{pmatrix}. \end{aligned} \quad (\text{I.41})$$

This result shows how the squeezing parameter  $r$  and squeezing angle  $\theta$  influence the quadrature fluctuations in the squeezed state. The diagonal elements of the noise spectral density matrix represent the variances of the quadrature fluctuations, while the off-diagonal elements represent the correlations between the quadratures. At an arbitrary measurement angle  $\phi$ , the noise spectral density matrix is given by

$$\begin{aligned} \mathbf{S}_{\text{sqz},\phi}[\Omega] &= \mathbf{R}(\phi)\mathbf{S}_{\text{sqz}}[\Omega]\mathbf{R}(-\phi) \\ &= \mathbf{R}(\phi - \theta)e^{-2r\sigma_z}\mathbf{R}(\theta - \phi). \end{aligned} \quad (\text{I.42})$$

such that measuring along the squeezing angle  $\phi = \theta(\Omega)$  yields the minimum variance in the first quadrature.

To obtain a reduction over the whole band, one can then either use a frequency-dependent squeezing angle  $\theta(\Omega)$  and a fixed measurement quadrature  $\phi$ , or inversely if the squeezing angle is fixed, one can rotate the measurement quadrature  $\phi$ . These two techniques are known as frequency dependent squeezing [1] and variational readout [Vyatchanin1993, 1] respectively. Frequency dependent squeezing is the focus of our work here, and will be detailed in Chapter II.

**Amplitude and Phase squeezed states:** Considering a displaced squeezed state, two special cases are of interest: the amplitude squeezed state where  $\theta = \bar{\varphi}$  and the phase squeezed state where  $\theta = \bar{\varphi} + \pi/2$ . In the first case, the amplitude quadrature  $\hat{p}$  is squeezed, while the phase quadrature  $\hat{q}$  is anti-squeezed. In the second case, the phase quadrature is squeezed, while the amplitude quadrature is anti-squeezed. The covariance matrices for these states can be derived from Eq. (I.109) by setting  $\psi = 0$  or  $\psi = \pi/2$ , respectively.

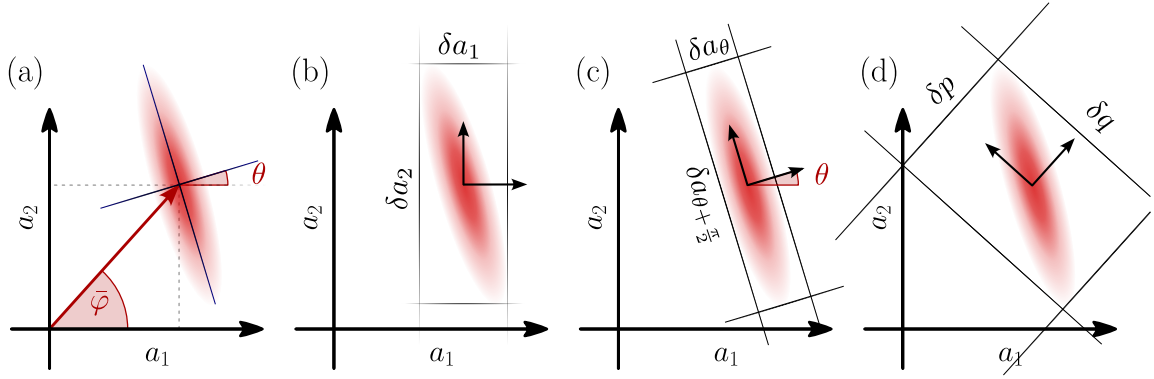


Fig. I.3 Phase-space representations of bright squeezed states with the different quadratures choices. (a) generic bright squeezed state. (b) projection of the quantum noise on the standard quadratures  $(a_1, a_2)$ . (c) projection of the quantum noise on the ellipse major axes quadratures  $(a_\theta, a_{\theta+\pi/2})$ , with  $\theta$  the ellipse angle with respect to the standard quadratures. (d) projection of the quantum noise on the amplitude and phase quadratures  $(p, q)$ .

#### I.1.4 Classical Modulations

A key ingredient in our study is the concept of sidebands generated by classical modulations of a coherent field. These sidebands are frequency components that appear around the carrier frequency of the field due to the modulation process. We will consider two types of classical modulations: amplitude modulation (AM) and phase modulation (PM). These are instrumental in experimental physics, as they notably allow to extract science signals and usable error signals to stabilize and lock various parameters of an optical setup, such as the length of a cavity or the phase of a local oscillator. Additionally, as we will see later, the optomechanical interaction itself can be seen as a phase modulation of the intracavity field by the mechanical motion, generating sidebands and noises that carry information about the mechanical position.

**Amplitude Modulation (AM)** : Let the classical amplitude be modulated at  $\Omega_{\text{mod}}$  in amplitude:

$$\alpha(t) = \bar{\alpha} (1 + \epsilon_a \cos(\Omega_{\text{mod}} t)) \quad (\text{I.43})$$

with  $\epsilon_a \ll 1$ , the field amplitude modulation depth. While the DC term lives at frequency  $\omega_0$ , the modulation introduces sidebands at frequencies  $\omega_0 \pm \Omega_{\text{mod}}$ , seen by expanding the cosine:

$$\alpha(t) = \bar{\alpha} \left( 1 + \frac{\epsilon_a}{2} e^{i\Omega_{\text{mod}} t} + \frac{\epsilon_a}{2} e^{-i\Omega_{\text{mod}} t} \right) \quad (\text{I.44})$$

**Phase Modulation (PM)** : Now let the classical amplitude be modulated in phase at

frequency  $\Omega_{\text{mod}}$ :

$$\alpha(t) = \bar{\alpha} e^{i\epsilon_\phi \cos(\Omega_{\text{mod}} t)} \quad (\text{I.45})$$

with  $\epsilon_\phi \ll 1$  the field phase modulation depth. Expanding to first order in  $\epsilon_\phi$  gives:

$$\alpha(t) \approx \bar{\alpha} \left( 1 + \frac{i\epsilon_\phi}{2} e^{i\Omega_{\text{mod}} t} + \frac{i\epsilon_\phi}{2} e^{-i\Omega_{\text{mod}} t} \right) \quad (\text{I.46})$$

While the carrier term lives at frequency  $\omega_0$ , the modulation introduces sidebands at  $\omega_0 \pm \Omega_{\text{mod}}$ , both shifted in phase by  $\pi/2$  relative to the carrier.

In both cases, amplitude or phase modulations, the field contains a carrier at frequency  $\omega_0$  and two sidebands at  $\omega_0 \pm \Omega_{\text{mod}}$ . Amplitude modulation results in sidebands that are in phase with the carrier, while phase modulation produces sidebands with a  $\pm\pi/2$  phase shift relative to the carrier. We also note a general modulation process as :

$$\alpha(t) = \bar{\alpha} (1 + \varepsilon(t)) \quad (\text{I.47})$$

where  $\varepsilon(t) \in \mathbb{C}$  is a modulation function that weakly modulates the complex amplitude in time, and that features information about the modulation frequency and depth. It then follows that the linearized amplitude-phase operators can be expressed as

$$\hat{\mathbf{u}}_{\bar{\alpha}}(t) = 2|\bar{\alpha}| \begin{pmatrix} 1 \\ 0 \end{pmatrix} + 2|\bar{\alpha}| \begin{pmatrix} \text{Re}(\varepsilon(t)) \\ \text{Im}(\varepsilon(t)) \end{pmatrix} + \begin{pmatrix} \delta\hat{p}(t) \\ \delta\hat{q}(t) \end{pmatrix} \quad (\text{I.48})$$

Computing the Fourier transform for amplitude and phase modulations yields

$$\begin{aligned} \varepsilon^{AM}(\Omega) &= \frac{\epsilon_a}{2} \left( \delta(\Omega - \Omega_{\text{mod}}) + \delta(\Omega + \Omega_{\text{mod}}) \right) \\ \varepsilon^{PM}(\Omega) &= \frac{i\epsilon_\phi}{2} \left( \delta(\Omega - \Omega_{\text{mod}}) + \delta(\Omega + \Omega_{\text{mod}}) \right) \end{aligned} \quad (\text{I.49})$$

And the quadrature operators of a modulated field can be expressed as

$$\hat{\mathbf{u}}_{\bar{\alpha}}[\Omega] = 2|\bar{\alpha}| \begin{pmatrix} 1 \\ 0 \end{pmatrix} \delta(\Omega) + 2|\bar{\alpha}| \begin{pmatrix} \text{Re}(\varepsilon[\Omega]) \\ \text{Im}(\varepsilon[\Omega]) \end{pmatrix} + \begin{pmatrix} \delta\hat{p}[\Omega] \\ \delta\hat{q}[\Omega] \end{pmatrix} \quad (\text{I.50})$$

We illustrate this by computing the spectra of a coherent field modulated in amplitude. The amplitude-phase quadrature fluctuation part reads

$$\delta\hat{\mathbf{u}}_{\bar{\alpha}}[\Omega] = |\bar{\alpha}|\epsilon_a \begin{pmatrix} \delta(\Omega - \Omega_{\text{mod}}) + \delta(\Omega + \Omega_{\text{mod}}) \\ 0 \end{pmatrix} + \begin{pmatrix} \delta\hat{p}[\Omega] \\ \delta\hat{q}[\Omega] \end{pmatrix} \quad (\text{I.51})$$

such that its covariance matrix reads

$$\mathbf{S}_{\bar{\varphi}}[\Omega] = 2|\bar{\alpha}|^2 \epsilon_a^2 \left[ \delta(\Omega - \Omega_{\text{mod}}) + \delta(\Omega + \Omega_{\text{mod}}) \right] \begin{pmatrix} 1 & 0 \\ 0 & 0 \end{pmatrix} + \mathbf{1} \quad (\text{I.52})$$

As seen in the above expression, the covariance matrix display a sum of Dirac functions corresponding to a classical amplitude modulation of the field, as well as a flat vacuum noise across all frequencies.

### I.1.5 Quantum Sideband Diagram

We now have all the tools to graphically represent the quantum states of light in the frequency domain. The so-called quantum sideband diagram is a useful representation to visualize the quantum states of light, especially when dealing with modulated fields and their sidebands. In this representation, we plot the carrier frequency  $\omega_0$  at the center, and the sidebands at frequencies  $\omega_0 \pm \Omega$  on either side.

Each sideband is represented by a vector in the quadrature plane, with its length and angle determined by the amplitude and phase of the sideband as seen above. The quantum noise associated with each sideband is represented by a gaussian distribution around the tip of the vector, with its shape and orientation determined by the noise spectral density matrix of the quantum state. The additional ingredient that the sideband diagram provides is the correlation between symmetrical sidebands, represented by markers connecting the two sidebands at  $\omega_0 + \Omega$  and  $\omega_0 - \Omega$ . These correlations are crucial in understanding the properties of squeezed states, where the noise in one quadrature is reduced below the vacuum level, while the noise in the conjugate quadrature is increased. The sideband diagram allows us to visualize these correlations and their impact on the overall quantum state of light. This representation is particularly useful when analyzing the effects of optical cavities and other linear optical systems on quantum states, as they modify the amplitude and phase of the sidebands, hence the correlated/anticorrelated quadratures.

## I.2 Cavities

Optical cavities are at the heart of this work, as they are used to coherently enhance the light-matter interaction in various systems, and also to filter and manipulate quantum states of light. In this section, we review the basic properties of optical cavities, their resonance conditions, and we derive the covariance matrices of their output fields.

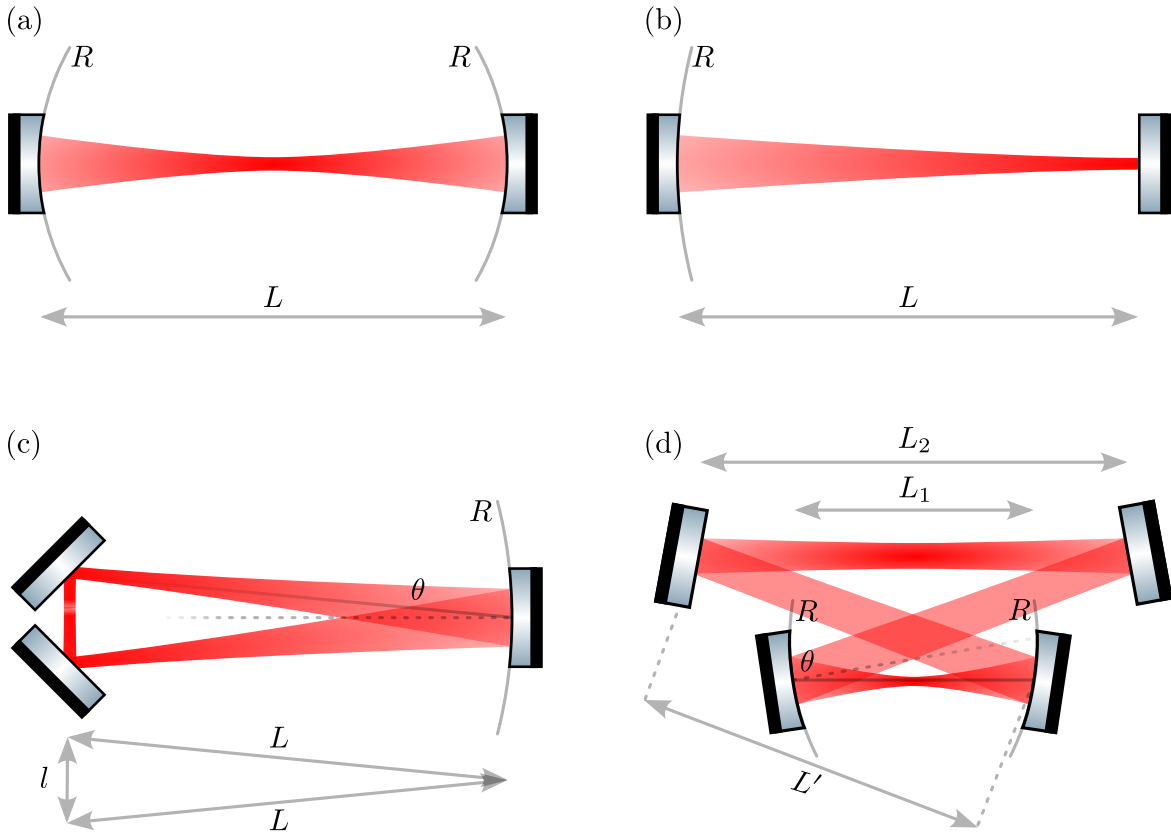


Fig. I.4 Geometries of various cavity types used in this work. (a) Linear concave-concave cavity (confocal in the  $L \sim 2R$  case). (b) Linear plano-concave cavity. (a) and (b) are both standing wave cavities. (c) Planar triangular cavity. (d) Planar bow-tie cavity. (c) and (d) are both travelling wave cavities.

### I.2.1 Cavity Geometries and Stability Conditions

An optical cavity is a structure that *traps* photons by means of reflection between two or more mirrors. They can be either standing wave cavities, where the light bounces back and forth between two mirrors, or traveling wave cavities, where the light circulates in a loop. In both cases, the cavity supports discrete resonant modes determined by its geometry and the boundary conditions imposed by the mirrors. The stability criteria of a specific cavity configuration is derived considering the round trip ABCD matrix of the cavity describing how the complex beam parameter  $q(z)$  introduced in (I.2) transforms after one round trip. The stability condition then simply reads as  $-1 < (A + D)/2 < 1$ . In the case of planar - travelling wave cavities, one needs to consider both the tangential and sagittal planes, as these cavities are astigmatic. The stricter condition, generally the sagittal plane one, then defines the stability range of the cavity.

**Linear standing wave cavities:** We first consider the two linear cavities used in this work, namely a concave-concave cavity (Fig I.13.(a)) with two identical concave mirrors, and a plano-concave cavity with one flat mirror and one concave mirror (Fig I.13.(b)). Using the ABCD formalism for a confocal cavity of length  $L$  formed by two identical mirrors of radii of curvature  $R$ , the stability condition reads

$$0 < L < 2R \quad (\text{I.53})$$

For the plano-concave cavity, the stability condition reads

$$0 < L < R \quad (\text{I.54})$$

**Planar traveling wave cavities:** We now consider a triangular cavity formed by two concave mirrors of radius of curvature  $R$  and one flat mirror (Fig I.13.(c)). The stability condition reads

$$0 < L_{rt} < 2R \cos(\theta) \quad (\text{I.55})$$

where  $L_{rt} = 2L + l$  is the cavity round trip length, and  $\theta$  is the angle of incidence of the beam onto the curved mirror. This condition is the sagittal one, and is more stringent than the tangential one.

Considering now a bow-tie cavity formed by two concave mirrors of radius of curvature  $R$  and two flat mirrors (Figure I.13.(d)), the full stability condition reads

$$0 < \left(1 - \frac{L_1 + 2L'}{R \cos \theta}\right) \left(1 - \frac{L_2}{R \cos \theta}\right) < 1 \quad (\text{I.56})$$

where  $L_1$  is the distance between the two concave mirrors,  $L_2$  the distance between the two flat mirrors, and  $L'$  the distance between a concave and a flat mirror (assuming a symmetric cavity). A simple design rule guaranteeing stability is then to set  $L_1 + 2L' < R \cos \theta$  and  $L_2 < R \cos \theta$ .

## I.2.2 Cavity Resonances

If the cavity is stable, it will then feature a discrete set of resonant modes everytime the cavity length is an integer multiple of half the wavelength  $\lambda/2$  (standing wave cavity) or the wavelength  $\lambda$  (traveling wave cavity). In the frequency domain, modes are spaced by the free spectral range  $\omega_{\text{FSR}}$  of the cavity, defined as

$$\omega_{\text{FSR}} = \frac{\pi c}{L} \quad (\text{linear cavity}), \quad \omega_{\text{FSR}} = \frac{2\pi c}{L_{rt}} \quad (\text{traveling wave cavity}) \quad (\text{I.57})$$

such that the resonant frequencies are given by

$$\omega_m = m \omega_{\text{FSR}}, \quad m \in \mathbb{N} \quad (\text{I.58})$$

and the cavity is on resonance when the input laser frequency  $\omega_0$  matches one of the resonant frequencies  $\omega_m$  i.e.  $\omega_0 = \omega_m$ . To achieve this, one can either tune the laser frequency or the cavity length. In our experiments, we use the second option by mounting one of the cavity mirrors on a piezoelectric actuator. Changing the cavity length  $L$  by  $\delta L$  shifts the resonant frequencies by

$$\delta\omega_m = -m \frac{\pi c}{L^2} \delta L = -\frac{\omega_m}{L} \delta L \quad (\text{I.59})$$

### I.2.3 Mode-Matching

A cavity also supports  $\text{TEM}_{mn}$  transverse modes, each with a specific spatial profile and resonant frequency. The resonant frequencies of these transverse modes are shifted relative to the fundamental mode by an amount that depends on the cavity geometry and the mode indices  $(m, n)$ . Coupling an incoming beam into a stable optical cavity requires that the spatial mode of the beam matches that of the cavity. This means that the mode function of the incoming beam, assumed to be a  $\text{TEM}_{00}$  Gaussian mode  $f_0(\mathbf{r})$ , must overlap with the cavity's fundamental mode  $f'_0(\mathbf{r})$ . If the basis functions are not perfectly aligned, the incoming field can be expanded in the orthonormal basis of cavity modes as

$$f_0(\mathbf{r}) = c_0 f'_0(\mathbf{r}) + \sum_{m>0} c_m f'_m(\mathbf{r}), \quad (\text{I.60})$$

where the coefficients  $c_m$  quantify the projection of the incident field onto the cavity eigenmodes. Only the component  $c_0 f'_0$  couples efficiently to the fundamental cavity mode due to the mirror geometry, while any mismatch excites higher-order transverse modes  $f'_m$ . The mode-matching procedure therefore consists in maximizing the overlap integral

$$\eta = \left| \int d^3\mathbf{r} f_0^*(\mathbf{r}) f'_0(\mathbf{r}) \right|^2, \quad (\text{I.61})$$

which ensures that essentially all the incoming photons populate the desired cavity mode, while suppressing excitation of spurious modes.

### I.2.4 Simple Cavities

We consider a single field cavity mode described by the annihilation operator  $\hat{a}$ , interacting with several independent noise inputs. The system is governed by a Hamiltonian

$$\hat{H} = -\hbar\Delta\hat{a}^\dagger\hat{a} \quad (\text{I.62})$$

with  $\Delta \equiv \omega_0 - \omega_c$  the cavity detuning to the laser frequency, and each input introduces dissipation characterized by a decay rate  $\kappa_i = T_i/\tau$ , with  $T_i$  the power transmittivity of the mirror and  $\tau = 2L/c$  the roundtrip time of the cavity. This is we consider an input coupler (mirror) with decay rate  $\kappa_1$  and an output coupler (mirror) with decay rate  $\kappa_2$ . The laser field is shone onto the cavity by the input coupler.

In the frame rotating at the laser frequency, the dynamics of  $\hat{a}$  is given by the Quantum Langevin Equation (QLE):

$$\begin{aligned} \frac{d}{dt}\hat{a}(t) &= -\frac{i}{\hbar}[\hat{a}, \hat{H}] - \frac{\kappa}{2}\hat{a}(t) + \sqrt{\kappa_1}\hat{a}_{\text{in}}(t) + \sqrt{\kappa_2}\delta\hat{a}_{\text{vac}}(t) + \sqrt{\kappa_0}\delta\hat{a}_l(t) \\ &= -\left(\frac{\kappa}{2} - i\Delta\right)\hat{a}(t) + \sqrt{\kappa_1}\hat{a}_{\text{in}}(t) + \sqrt{\kappa_2}\delta\hat{a}_{\text{vac}}(t) + \sqrt{\kappa_0}\delta\hat{a}_l(t) \end{aligned} \quad (\text{I.63})$$

where  $\kappa = \kappa_0 + \kappa_1 + \kappa_2$  is the total decay rate, with  $\kappa_0 = \mathcal{L}/\tau$  and  $\delta\hat{a}_l(t)$  the rate and fluctuation operator of additional losses. Here losses  $\mathcal{L}$  have ppm units. Another key element to deriving both steady state behaviour as well as quadrature spectra is the input-output formula given by:

$$\hat{a}_{\text{ref}} = \sqrt{\kappa_1}\hat{a} - \hat{a}_{\text{in}}, \quad \hat{a}_{\text{trans}} = \sqrt{\kappa_2}\hat{a} - \delta\hat{a}_{\text{vac}} \quad (\text{I.64})$$

for both the reflected and transmitted field. In the input-output formula, the  $\hat{a}_{\text{in}}$  refers to the field incoming on the coupler considered, which are simple vacuum fluctuations on the output coupler since we don't shine the laser by this port. Importantly, this formula describes how open quantum systems exchange information with their environment, linking the internal cavity field to the external fields. Here, the external fields are the two photon fields defined at the start of this chapter, expressed in units of  $1/\sqrt{\text{HZ}}$ , and the internal field  $\hat{a}$  is unitless. This key relation allows to compute how a discrete quantum system (the cavity mode) interacts with continuous quantum fields (the input and output fields), enabling the analysis of phenomena such as reflection, transmission, and noise properties of the cavity.

As introduced in the previous subsection, one can split the annihilation operator in a mean field part  $\alpha$  and a fluctuation part  $\delta\hat{a}(t)$  (vector form) such that this equation turns

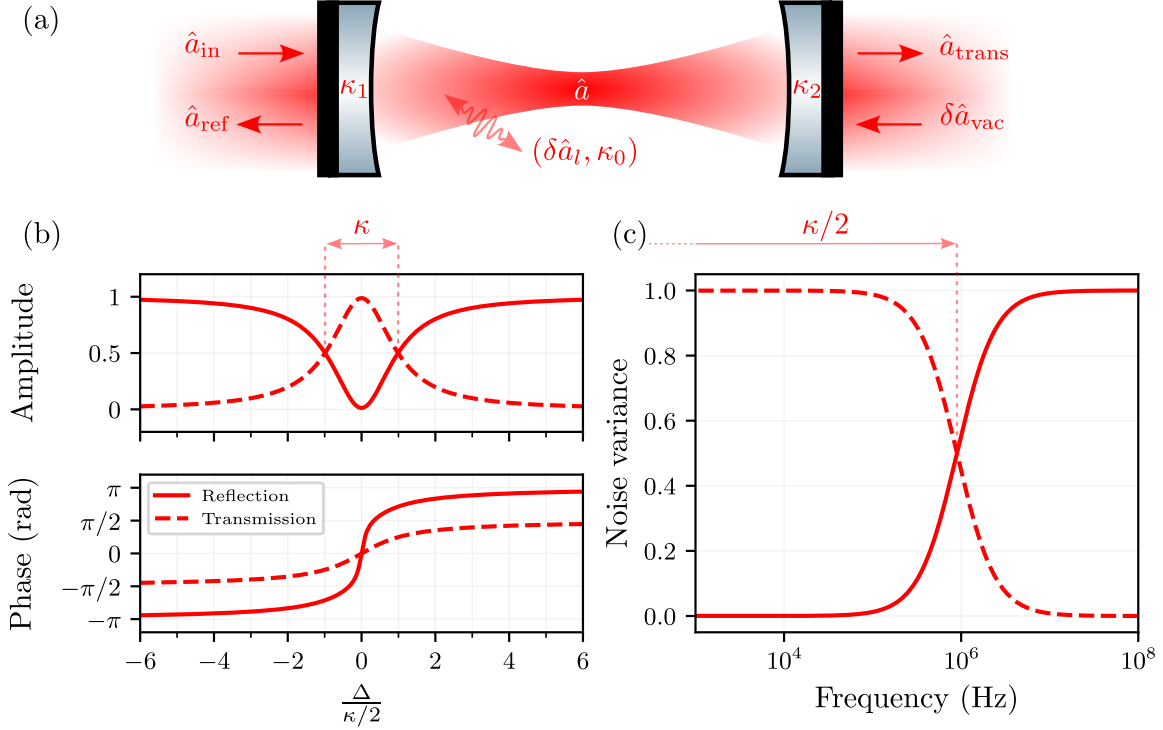


Fig. I.5 Filtering properties of optical cavities. (a) Cavity diagram and definitions.  $\hat{a}$ 's are the various fields at play.  $\kappa$ 's are the various couplings involved i.e. input and output mirrors, as well as intrinsic cavity cavity losse, with  $\delta\hat{a}$ 's the associated fluctuations. (b) Amplitude and phase response of an optical cavity as a function of the laser detuning (in cavity linewidth unit). In this case, both mirrors are identical ( $\kappa_1 = \kappa_2$ ) and cavity losses are negligible ( $\kappa_0 \ll \kappa_1$ ). (c) Transfer functions of the input classical noises as in (I.90)

into two i.e. a scalar differential equation, and an operator differentail equation, that is:

$$\begin{cases} 0 = -\left(\frac{\kappa}{2} - i\Delta\right)\bar{\alpha} + \sqrt{\kappa_1}\bar{\alpha}_{\text{in}} \\ \delta\dot{\hat{\alpha}}(t) = -\begin{pmatrix} \kappa/2 - i\Delta & 0 \\ 0 & \kappa/2 + i\Delta \end{pmatrix}\delta\hat{\alpha}(t) + \sqrt{\kappa_1}\delta\hat{a}_{\text{in}}(t) + \sqrt{\kappa_2}\delta\hat{a}_{\text{vac}}(t) + \sqrt{\kappa_0}\delta\hat{a}_l(t) \end{cases} \quad (\text{II.62})$$

**Mean field solution (Static case):** Taking the first scalar equation and expressing the mean intracavity field gives

$$\bar{\alpha} = \frac{\sqrt{\kappa_1}}{\kappa/2 - i\Delta}\bar{\alpha}_{\text{in}} \quad (\text{I.65})$$

Patching it up with the input-output formula this gives

$$\bar{\alpha}_{\text{ref}} = \left( \frac{\kappa_1}{\kappa/2 - i\Delta} - 1 \right) \bar{\alpha}_{\text{in}} \quad \bar{\alpha}_{\text{trans}} = \frac{\sqrt{\kappa_1 \kappa_2}}{\left( \kappa/2 - i\Delta \right)} \bar{\alpha}_{\text{in}}. \quad (\text{I.66})$$

The reflection and transmission coefficients are then

$$R(\Delta) = \left| \frac{\bar{\alpha}_{\text{ref}}}{\bar{\alpha}_{\text{in}}} \right|^2 = \frac{(\kappa_1 - \kappa/2)^2 + \Delta^2}{(\kappa/2)^2 + \Delta^2} \quad T(\Delta) = \left| \frac{\bar{\alpha}_{\text{trans}}}{\bar{\alpha}_{\text{in}}} \right|^2 = \frac{\kappa_1 \kappa_2}{(\kappa/2)^2 + \Delta^2}. \quad (\text{I.67})$$

The cavity linewidth (FWHM) is then given by  $\kappa/2\pi$  (Hz), as illustrated In Fig I.5.(b). We will then refer to  $\kappa/4\pi$  (HWHM) as the cavity bandwidth (Hz). Plugging back the expression of  $\kappa_i = T_i/\tau$  in the reflection coefficient, we have

$$R(\pm\infty) = 1 \quad R(0) = \left( \frac{T_1 - T_2 - \mathcal{L}}{T_1 + T_2 + \mathcal{L}} \right)^2 \quad (\text{I.68})$$

such that the relative depth of the resonance dip gives us information about the cavity losses and couplings. In particular, the resonance dip vanishes when  $T_1 = T_2 + \mathcal{L}$ , which is the so called *impedance matching* condition: no light is reflected at resonance and all of it is transmitted or lost. Similarly, the transmission coefficient reads

$$T(\pm\infty) = 0 \quad T(0) = \frac{4T_1 T_2}{(T_1 + T_2 + \mathcal{L})^2} \quad (\text{I.69})$$

We also define the cavity finesse  $\mathcal{F}$ , which is a measure of the sharpness of the resonance peaks relative to its FSR, as

$$\mathcal{F} = \frac{\omega_{\text{FSR}}}{\kappa} = \frac{\pi c}{L\kappa} = \frac{2\pi}{T_1 + T_2 + \mathcal{L}} \quad (\text{I.70})$$

which also gives the average number of round trips a photon makes before escaping the cavity i.e.  $\langle n_{rt} \rangle = \mathcal{F}/\pi$ . For a given cavity length (so same FSR), the higher the finesse, the longer the photon lifetime in the cavity  $\kappa^{-1}$ .

Measuring all these quantities then allows to fully characterize the cavity parameters  $T_1$ ,  $T_2$  and  $\mathcal{L}$ . This is done by measuring the reflection and transmission coefficients at resonance and far from resonance, as well as the cavity linewidth (or finesse).

### Mean field solution (Dynamical case):

We now let the detuning vary linearly in time, and express it in units of cavity bandwidth as  $\Delta(t) = \Delta_0 + v \frac{\kappa^2}{2} t$  where we defined  $v$  as the sweep speed in units of cavity bandwidth per

$\kappa^{-1}$ . The intracavity field yields the standard differential equation

$$\dot{\bar{\alpha}}(t) = -\left(\frac{\kappa}{2} - i\left(\Delta_0 + \frac{v\kappa^2}{2}t\right)\right)\bar{\alpha}(t) + \sqrt{\kappa_1}\bar{\alpha}_{\text{in}} \quad (\text{I.71})$$

This is solved by the means of integration factor method, such that we find

$$\begin{aligned} \alpha(t) &= \exp\left[\left(-\frac{\kappa}{2} + i\Delta_0\right)t + i\frac{v\kappa^2}{4}t^2\right] \\ &\times \left[\alpha(0) + \sqrt{\kappa_1}\bar{\alpha}_{\text{in}} \int_0^t \exp\left(\left(\frac{\kappa}{2} - i\Delta_0\right)s - i\frac{v\kappa^2}{4}s^2\right) ds\right]. \end{aligned} \quad (\text{I.72})$$

This expression describes the transient response of the intracavity field as the detuning is swept through resonance. When scanning over the cavity resonance at a rate exceeding the cavity bandwidth, photons at various detuning start to build up in the cavity without reaching the steady state value. This results in a characteristic asymmetric lineshape, where these different *colored* photons start beating against each other, leading to oscillations in the transmitted and reflected intensities. This is illustrated in Fig I.5.(c) for different sweep speeds. The above does feature an analytical formula involving error functions erf, such that can either fit the data by performing a numerical integration or the analytical formula. However if the data array feature too few points numerical integration becomes numerically costly. [figure to do](#).

The finesse-extraction procedure of Poirson *et al.* [2] can be expressed in our notation by identifying their cavity length  $d_0$  with our  $L$ , and their bandwidth  $\Omega_r$  with  $\kappa/2$ . In the fast-sweep regime—equivalent to our linear detuning sweep  $\Delta(t) = \Delta_0 + v_{\Delta}t$ —the transmitted intensity displays a sequence of maxima originating from the same interference mechanism responsible for the oscillatory behaviour in our analytical solution (Eq. (1.71)). Poirson *et al.* show that the time interval  $\Delta t$  between the first two transmitted maxima satisfies, near  $\Delta t \simeq \tau$ , the relation

$$\frac{\pi c}{L} \Delta t \simeq \frac{F}{e} \frac{I_1}{I_2}, \quad (\text{I.73})$$

which is their Eq. (21) rewritten using our notation. Since the intensity decay time is  $\tau = 2/\kappa = FL/(\pi c)$ , Eq. (I.73) links the measured ratio  $I_1/I_2$  and the peak spacing  $\Delta t$  directly to the cavity finesse. This provides an experimentally simple and robust method to determine  $F$ , fully consistent with the dynamical intracavity-field model developed here.

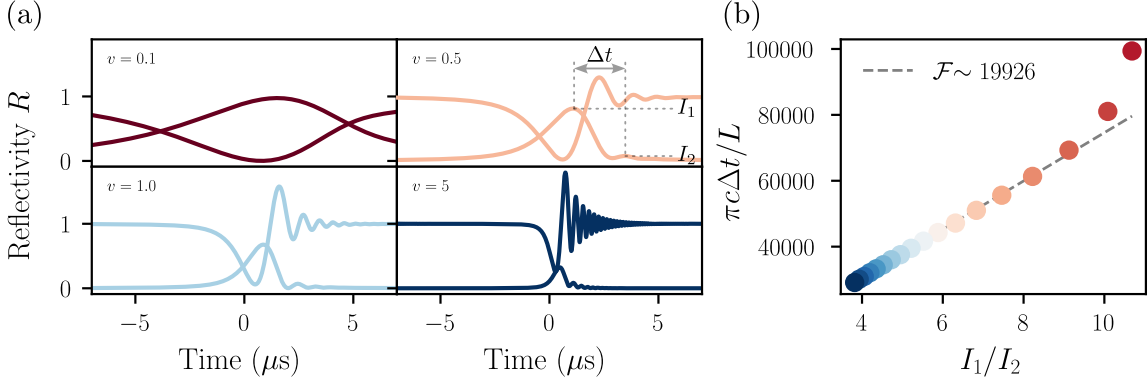


Fig. I.6 *Optical ringing effect upon a fast cavity detuning sweep.* (a) examples of optical ringing for four different sweep speeds. (b) Plotting the time interval  $\Delta t$  between the first two transmitted maxima as a function of the ratio  $I_1/I_2$  of their intensities allows to extract the cavity finesse  $\mathcal{F}$  using the relation (I.73). Here the data is simulated using the parameters of a realistic cavity i.e.  $\mathcal{F} = 20000$ ,  $L = 2\text{cm}$ . As  $v$  tends to 0, the second maximum vanishes and one recovers the lorentzian lineshape.

**Fluctuations solution:** To derive the covariance matrix we go to Fourier space such that

$$\mathbf{M}_\Delta \delta \hat{\mathbf{a}}[\Omega] = \sqrt{\kappa_1} \delta \hat{\mathbf{a}}_{\text{in}}[\Omega] + \sqrt{\kappa_2} \delta \hat{\mathbf{a}}_{\text{vac}}[\Omega] + \sqrt{\kappa_0} \delta \hat{\mathbf{a}}_{\text{l}}[\Omega] \quad (\text{I.74})$$

with

$$\mathbf{M}_\Delta = \begin{pmatrix} \kappa/2 - i(\Delta + \Omega) & 0 \\ 0 & \kappa/2 + i(\Delta - \Omega) \end{pmatrix}$$

For notational convenience, we will drop the explicit dependence on  $\Omega$  in the following. Inverting the above relation and plugging it in the input-output relations gives the reflected and transmitted fields as

$$\begin{aligned} \delta \hat{\mathbf{a}}_{\text{ref}} &= (\kappa_1 \mathbf{M}_\Delta^{-1} - \mathbf{1}) \delta \hat{\mathbf{a}}_{\text{in}} + \sqrt{\kappa_1} \mathbf{M}_\Delta^{-1} (\sqrt{\kappa_2} \delta \hat{\mathbf{a}}_{\text{vac}} + \sqrt{\kappa_0} \delta \hat{\mathbf{a}}_{\text{l}}) \\ \delta \hat{\mathbf{a}}_{\text{trans}} &= \sqrt{\kappa_2} \mathbf{M}_\Delta^{-1} (\sqrt{\kappa_1} \delta \hat{\mathbf{a}}_{\text{in}} + \sqrt{\kappa_0} \delta \hat{\mathbf{a}}_{\text{l}}) + (\kappa_2 \mathbf{M}_\Delta^{-1} - \mathbf{1}) \delta \hat{\mathbf{a}}_{\text{vac}} \end{aligned} \quad (\text{I.75})$$

where we can introduce the optical susceptibility  $\chi_c$  such that the matrix  $\mathbf{M}_\Delta^{-1}$  reads

$$\mathbf{M}_\Delta^{-1} = \begin{pmatrix} \chi_c[\Omega] & 0 \\ 0 & \chi_c^*[-\Omega] \end{pmatrix}, \quad \text{with} \quad \chi_c[\Omega] = \frac{1}{\kappa/2 - i(\Delta + \Omega)}$$

and with the same convention than that of the Fourier transform i.e. the two photon conjugate is a complex conjugation and a frequency inversion, we note that  $[\chi_c[0]]^\dagger = \chi_c^*[0]$  such that the  $\mathbf{M}_\Delta$  matrices are diagonal on resonance. Using  $\delta \hat{\mathbf{a}} = \Gamma^{-1} \delta \hat{\mathbf{u}}$  the reflected and

transmitted quadratures read

$$\begin{aligned}\delta\hat{\mathbf{u}}_{\text{ref}} &= (\kappa_1 \mathbf{\Gamma} \mathbf{M}_{\Delta}^{-1} \mathbf{\Gamma}^{-1} - \mathbf{1}) \delta\hat{\mathbf{u}}_{\text{in}} + \sqrt{\kappa_1} \mathbf{\Gamma} \mathbf{M}_{\Delta}^{-1} \mathbf{\Gamma}^{-1} (\sqrt{\kappa_2} \delta\hat{\mathbf{u}}_{\text{vac}} + \sqrt{\kappa_0} \delta\hat{\mathbf{u}}_{\text{l}}) \\ \delta\hat{\mathbf{u}}_{\text{trans}} &= \sqrt{\kappa_2} \mathbf{\Gamma} \mathbf{M}_{\Delta}^{-1} \mathbf{\Gamma}^{-1} (\sqrt{\kappa_1} \delta\hat{\mathbf{u}}_{\text{in}} + \sqrt{\kappa_0} \delta\hat{\mathbf{u}}_{\text{l}}) + (\kappa_2 \mathbf{\Gamma} \mathbf{M}_{\Delta}^{-1} \mathbf{\Gamma}^{-1} - \mathbf{1}) \delta\hat{\mathbf{u}}_{\text{vac}}\end{aligned}\quad (\text{I.76})$$

where the matrix product above reads

$$\mathbf{\Gamma} \mathbf{M}_{\Delta}^{-1} \mathbf{\Gamma}^{-1} = \frac{1}{(\kappa/2 - i\Omega)^2 + \Delta^2} \begin{pmatrix} \kappa/2 - i\Omega & -\Delta \\ \Delta & \kappa/2 - i\Omega \end{pmatrix}.$$

The structure above is the engine behind frequency-dependent squeezing. On resonance, we have

$$\mathbf{M}_0^{-1} = \frac{1}{\kappa/2 - i\Omega} \mathbf{I} \implies \mathbf{\Gamma} \mathbf{M}_0^{-1} \mathbf{\Gamma}^{-1} = \frac{1}{\kappa/2 - i\Omega} \mathbf{I}$$

causing symmetric sidebands around the carrier to be filtered identically both in amplitude and phase — so the quadrature along which these sidebands are correlated (if considering squeezed correlations) remains the same at all frequencies. The moment the cavity is detuned, the  $\mathbf{\Gamma} \mathbf{M}_{\Delta}^{-1} \mathbf{\Gamma}^{-1}$  off-diagonal terms asymmetrically mix the upper and lower sidebands; in the two-photon picture this is a frequency-dependent rotation and scaling of the  $(p, q)$  basis. The amplitude (Lorentzian) part sets how strongly each sideband passes, while the phase accrued inside the cavity sets the rotation angle that now varies with  $\Omega$ . A broadband field with a single squeezing angle at the input is therefore converted into an output whose squeezing angle “twists” with frequency: near one band it can align with the phase quadrature, and at another it can align with the amplitude quadrature. This is exactly the mechanism exploited by filter cavities in precision interferometry: by choosing bandwidth, detuning, and coupling, one tailors the rotation profile to the target noise crossover. Practically, the attainable rotation and the preserved squeezing are limited by optical loss and mode mismatch, which inject uncorrelated vacuum and partially unwind the correlations the detuned cavity imprints on sidebands.

**Note:** On resonance ( $\Delta = 0$ ), the output quadratures can then be written as

$$\begin{aligned}\delta\hat{\mathbf{u}}_{\text{ref}} &= \frac{\kappa_1 - \kappa/2 + i\Omega}{\kappa/2 - i\Omega} \delta\hat{\mathbf{u}}_{\text{in}} + \frac{\sqrt{\kappa_1 \kappa_2}}{\kappa/2 - i\Omega} \delta\hat{\mathbf{u}}_{\text{vac}} + \frac{\sqrt{\kappa_1 \kappa_0}}{\kappa/2 - i\Omega} \delta\hat{\mathbf{u}}_{\text{l}} \\ \delta\hat{\mathbf{u}}_{\text{trans}} &= \frac{\sqrt{\kappa_1 \kappa_2}}{\kappa/2 - i\Omega} \delta\hat{\mathbf{u}}_{\text{in}} + \frac{\kappa_2 - \kappa/2 + i\Omega}{\kappa/2 - i\Omega} \delta\hat{\mathbf{u}}_{\text{vac}} + \frac{\sqrt{\kappa_2 \kappa_0}}{\kappa/2 - i\Omega} \delta\hat{\mathbf{u}}_{\text{l}}\end{aligned}\quad (\text{I.77})$$

and their noise spectra are

$$\begin{aligned}\mathbf{S}_{\text{ref}}[\Omega] &= \frac{(\kappa_1 - \kappa/2)^2 + \Omega^2}{(\kappa/2)^2 + \Omega^2} \mathbf{S}_{\text{in}} + \frac{\kappa_1}{(\kappa/2)^2 + \Omega^2} (\kappa_0 \mathbf{1} + \kappa_2 \mathbf{1}) \\ \mathbf{S}_{\text{trans}}[\Omega] &= \frac{(\kappa_2 - \kappa/2)^2 + \Omega^2}{(\kappa/2)^2 + \Omega^2} \mathbf{1} + \frac{\kappa_2}{(\kappa/2)^2 + \Omega^2} (\kappa_0 \mathbf{1} + \kappa_1 \mathbf{S}_{\text{in}})\end{aligned}\quad (\text{I.78})$$

where the vacuum and loss covariance matrices are equal to  $\mathbf{1}$ . As these two vacua sum up linearly, it is equivalent to consider a single vacuum with an effective decay rate  $\kappa_2 + \kappa_0 \rightarrow \kappa_2$  to lighten the notation. We then absorb intrinsic losses into the output coupler, and consider only two ports: the input coupler with decay rate  $\kappa_1$  and the output coupler with decay rate  $\kappa_2$ . We stress that this substitution is only valid when considering the **reflected** quadratures. When focusing on the transmitted quadratures, one can perform a similar redefinition with  $\kappa_1$  i.e.  $\kappa_1 + \kappa_0 \rightarrow \kappa_1$ .

**Transfer matrices and Spectra:** Expressing the reflected and transmitted quadratures in matrix form yields

$$\begin{aligned}\delta \hat{\mathbf{u}}_{\text{ref}} &= \mathbf{T}_{\text{ref}} \delta \hat{\mathbf{u}}_{\text{in}} + \mathbf{L}_{\text{ref}} \delta \hat{\mathbf{u}}_{\text{vac}} \\ \delta \hat{\mathbf{u}}_{\text{trans}} &= \mathbf{T}_{\text{trans}} \delta \hat{\mathbf{u}}_{\text{in}} + \mathbf{L}_{\text{trans}} \delta \hat{\mathbf{u}}_{\text{vac}}\end{aligned}\quad (\text{I.79})$$

where the transfer matrices for the input and loss ports given by

$$\begin{aligned}\mathbf{T}_{\text{ref}} &= \kappa_1 \mathbf{\Gamma} \mathbf{M}_{\Delta}^{-1} \mathbf{\Gamma}^{-1} - \mathbf{1}, \quad \mathbf{L}_{\text{ref}} = \sqrt{\kappa_1 \kappa_2} \mathbf{\Gamma} \mathbf{M}_{\Delta}^{-1} \mathbf{\Gamma}^{-1} \\ \mathbf{T}_{\text{trans}} &= \sqrt{\kappa_1 \kappa_2} \mathbf{\Gamma} \mathbf{M}_{\Delta}^{-1} \mathbf{\Gamma}^{-1}, \quad \mathbf{L}_{\text{trans}} = \kappa_2 \mathbf{\Gamma} \mathbf{M}_{\Delta}^{-1} \mathbf{\Gamma}^{-1} - \mathbf{1}\end{aligned}$$

Conveniently, we introduce the complex reflectivities and transmissivities experienced by the sideband fields as

$$r_{\Delta}[\Omega] = \kappa_1 \chi_c[\Omega] - 1, \quad r'_{\Delta}[\Omega] = \kappa_2 \chi_c[\Omega] - 1, \quad t_{\Delta}[\Omega] = \sqrt{\kappa_1 \kappa_2} \chi_c[\Omega] \quad (\text{I.80})$$

Here we introduced two different reflection coefficients:  $r_{\Delta}[\Omega]$  for the input coupler, and  $r'_{\Delta}[\Omega]$  for the output coupler describing the reflection of the incoming field fluctuations on each port. The transmission coefficient  $t_{\Delta}[\Omega]$  is the same for both ports since it describes the field fluctuations transmitted from one port to the other, no matter what the direction of propagation is. We can now define the modulus and phase of the positive and negative

sideband reflectivities and transmissivities as

$$\begin{aligned} r_+ e^{i\phi_+} &= r_\Delta[\Omega] \quad , \quad r_- e^{-i\phi_-} = r_\Delta^*[-\Omega] \\ r'_+ e^{i\phi'_+} &= r'_\Delta[\Omega] \quad , \quad r'_- e^{-i\phi'_-} = r'^*_\Delta[-\Omega] \\ t_+ e^{i\theta_+} &= t_\Delta[\Omega] \quad , \quad t_- e^{-i\theta_-} = t_\Delta^*[-\Omega] \end{aligned} \quad (\text{I.81})$$

describing the amplitude filtering and dephasing underwent by a sideband at  $\Omega$  and its two-photon conjugate in both reflection and transmission. The output quadrature transfer matrices can then be expressed as

$$\mathbf{T}_{\text{ref}} = \Gamma \begin{pmatrix} r_+ e^{i\phi_+} & 0 \\ 0 & r_- e^{-i\phi_-} \end{pmatrix} \Gamma^{-1} \quad \text{and} \quad \mathbf{L}_{\text{ref}} = \Gamma \begin{pmatrix} t_+ e^{i\theta_+} & 0 \\ 0 & t_- e^{-i\theta_-} \end{pmatrix} \Gamma^{-1}$$

and in transmission as

$$\mathbf{T}_{\text{trans}} = \Gamma \begin{pmatrix} t_+ e^{i\theta_+} & 0 \\ 0 & t_- e^{-i\theta_-} \end{pmatrix} \Gamma^{-1} \quad \text{and} \quad \mathbf{L}_{\text{trans}} = \Gamma \begin{pmatrix} r'_+ e^{i\phi'_+} & 0 \\ 0 & r'_- e^{-i\phi'_-} \end{pmatrix} \Gamma^{-1}$$

We use the usual transformation for the positive and negative sideband reflectivities as

$$\begin{aligned} \bar{r} &= \frac{r_+ + r_-}{2} \quad , \quad \delta r = \frac{r_+ - r_-}{2} \\ \bar{\phi} &= \frac{\phi_+ + \phi_-}{2} \quad , \quad \delta\phi = \frac{\phi_+ - \phi_-}{2} \end{aligned} \quad (\text{I.82})$$

to finally write the reflected quadrature transfer matrices as

$$\mathbf{T}_{\text{ref}} = e^{i\delta\phi} \mathbf{R}(-\bar{\phi}) \left( \bar{r} \mathbf{1} + i \delta r \mathbf{R}(\pi/2) \right) \quad \text{and} \quad \mathbf{L}_{\text{ref}} = e^{i\delta\theta} \mathbf{R}(-\bar{\theta}) \left( \bar{t} \mathbf{1} + i \delta t \mathbf{R}(\frac{\pi}{2}) \right) \quad (\text{I.83})$$

as well as the transmitted quadrature transfer matrices

$$\mathbf{T}_{\text{trans}} = e^{i\delta\theta} \mathbf{R}(-\bar{\theta}) \left( \bar{t} \mathbf{1} + i \delta t \mathbf{R}(\frac{\pi}{2}) \right) \quad \text{and} \quad \mathbf{L}_{\text{trans}} = e^{i\delta\phi} \mathbf{R}(-\bar{\phi}) \left( \bar{r}' \mathbf{1} + i \delta r' \mathbf{R}(\frac{\pi}{2}) \right) \quad (\text{I.84})$$

such that the covariance matrices for the reflected and transmitted quadratures of a detuned cavity are given by

$$\begin{aligned} \mathbf{S}_{\text{ref}}[\Omega] &= \mathbf{T}_{\text{ref}} \mathbf{S}_{\text{in}} \mathbf{T}_{\text{ref}}^\dagger + \mathbf{L}_{\text{ref}} \mathbf{L}_{\text{ref}}^\dagger \\ \mathbf{S}_{\text{trans}}[\Omega] &= \mathbf{T}_{\text{trans}} \mathbf{S}_{\text{in}} \mathbf{T}_{\text{trans}}^\dagger + \mathbf{L}_{\text{trans}} \mathbf{L}_{\text{trans}}^\dagger \end{aligned} \quad (\text{I.85})$$

$$\mathbf{T}_r[\Omega] = \Gamma \mathbf{r}_\Delta[\Omega] \Gamma^{-1} = \frac{1}{2} \begin{pmatrix} r_+ e^{i\phi_+} + r_- e^{-i\phi_-} & i(r_+ e^{i\phi_+} - r_- e^{-i\phi_-}) \\ -i(r_+ e^{i\phi_+} - r_- e^{-i\phi_-}) & r_+ e^{i\phi_+} + r_- e^{-i\phi_-} \end{pmatrix} \quad (\text{I.86})$$

and similarly for the one photon transmission matrix

$$\mathbf{t}_\Delta[\Omega] = \sqrt{\kappa_1 \kappa_2} \mathbf{M}_\Delta^{-1} = \begin{pmatrix} t_\Delta[\Omega] & 0 \\ 0 & t_\Delta^*[-\Omega] \end{pmatrix} \quad \text{with} \quad t_\Delta[\Omega] = \frac{\sqrt{\kappa_1 \kappa_2}}{\kappa/2 - i(\Delta + \Omega)} \quad (\text{I.87})$$

such that

$$\mathbf{T}_t[\Omega] = \boldsymbol{\Gamma} \mathbf{t}_\Delta[\Omega] \boldsymbol{\Gamma}^{-1} = \frac{1}{2} \begin{pmatrix} t_\Delta[\Omega] + t_\Delta^*[-\Omega] & i(t_\Delta[\Omega] - t_\Delta^*[-\Omega]) \\ -i(t_\Delta[\Omega] - t_\Delta^*[-\Omega]) & t_\Delta[\Omega] + t_\Delta^*[-\Omega] \end{pmatrix} \quad (\text{I.88})$$

### Example 1: Mode Cleaner

Let us consider a configuration such that  $\kappa_1 = \kappa_2 \approx \kappa/2$  where we assume negligible losses  $\kappa_0 \ll \kappa_{1,2}$ . It represents a cavity where the input and output mirror transmittivities are equal, and we set the laser resonant to the cavity ( $\Delta = 0$ ), such that the transmitted quadratures are written

$$\delta \hat{\mathbf{u}}_{\text{trans}}[\Omega] = \frac{\kappa/2}{\kappa/2 - i\Omega} \delta \hat{\mathbf{u}}_{\text{in}}[\Omega] + \frac{i\Omega}{\kappa/2 - i\Omega} \delta \hat{\mathbf{u}}_{\text{vac}}[\Omega]. \quad (\text{I.89})$$

The resulting transmitted quadrature covariance matrix is given by:

$$\mathbf{S}_{\text{trans}}[\Omega] = \frac{(\kappa/2)^2}{(\kappa/2)^2 + \Omega^2} \mathbf{S}_{\text{in}} + \frac{\Omega^2}{(\kappa/2)^2 + \Omega^2} \mathbf{1} \quad (\text{I.90})$$

Now consider that the input fluctuations are above those of vacuum i.e. the input field features classical noise. We would then have  $S_{pp}^{\text{in}} > S_{pp}^{\text{vac}} = 1$  and  $S_{qq}^{\text{in}} > S_{qq}^{\text{vac}} = 1$ . One can notice that the prefactor to the input noises is a Lorentzian function - a low pass filter. Hence, the noises of the input fields are low pass filtered by the cavity, while the vacuum fluctuations are high pass filtered at precisely the same cutoff  $\kappa/2$ . The mean field of the *bright* coherent input is fully transmitted, but its super-vacuum fluctuations, potentially classically modulated, are filtered by the cavity. Taking a high finesse cavity such that the cutoff frequency is low, the transmitted field now features vacuum sidebands: it has been *clean* from classical noise. This is the principle of a *mode cleaner* cavity, which is used in many precision experiments to provide a spectrally pure laser field, as well as a spatially filtered beam such that the transmitted beam is a pure TEM<sub>00</sub>.

**Example 2: Detuned single port cavity**

We now consider a lossless single port cavity with  $\kappa_2 = 0$  and  $\kappa_1 = \kappa$ . the transfer matrix for the reflected **field** then reads

$$\kappa \mathbf{M}_\Delta^{-1} - \mathbf{1} = \begin{pmatrix} \kappa/2 + i(\Delta + \Omega) & 0 \\ \kappa/2 - i(\Delta + \Omega) & \kappa/2 - i(\Delta - \Omega) \\ 0 & \kappa/2 + i(\Delta - \Omega) \end{pmatrix}$$

where we see that the upper and lower sidebands are reflected with different amplitude  $\rho_+$  and  $\rho_-$  and phase shifts  $\phi_+$  and  $\phi_-$  when the cavity is detuned ( $\Delta \neq 0$ ). We then have :

$$\rho_+ = \left| \frac{\kappa/2 + i(\Delta + \Omega)}{\kappa/2 - i(\Delta + \Omega)} \right| = 1, \quad \rho_- = \left| \frac{\kappa/2 - i(\Delta - \Omega)}{\kappa/2 + i(\Delta - \Omega)} \right| = 1 \quad (\text{I.91})$$

$$\phi_+[\Omega] = 2 \arctan \left( \frac{\Delta + \Omega}{\kappa/2} \right), \quad \phi_-[\Omega] = 2 \arctan \left( \frac{\Delta - \Omega}{\kappa/2} \right) \quad (\text{I.92})$$

such that we can define the overall and differential phase shifts as

$$\bar{\phi}[\Omega] = \phi_+[\Omega] + \phi_-[\Omega] = \arctan \frac{4\Omega\kappa}{(\frac{\kappa}{2})^2 + \Delta^2 - \Omega^2} \quad \Delta\phi[\Omega] = \phi_+[\Omega] - \phi_-[\Omega] = \arctan \frac{4\Delta\kappa}{(\frac{\kappa}{2})^2 - \Delta^2 + \Omega^2} \quad (\text{I.93})$$

In the two-photon formalism, this asymmetric phase shift translates into a frequency-dependent rotation of the quadratures.

The transfer matrix is expressed as

$$\mathbf{T}_r[\Omega] = \frac{1}{(\kappa/2 - i\Omega)^2 + \Delta^2} \begin{pmatrix} (\kappa/2)^2 - \Delta^2 + \Omega^2 & -\kappa\Delta \\ +\kappa\Delta & (\kappa/2)^2 - \Delta^2 + \Omega^2 \end{pmatrix} \quad (\text{I.94})$$

$$\kappa \mathbf{\Gamma} \mathbf{M}_\Delta^{-1} \mathbf{\Gamma}^{-1} - \mathbf{1} = \frac{1}{(\kappa/2 - i\Omega)^2 + \Delta^2} \begin{pmatrix} (\kappa/2)^2 - \Delta^2 + \Omega^2 & -\kappa\Delta \\ +\kappa\Delta & (\kappa/2)^2 - \Delta^2 + \Omega^2 \end{pmatrix}$$

such that the covariance matrix is given by

$$\mathbf{S}_{\text{ref}}[\Omega] = \begin{pmatrix} S_{pp}^{\text{ref}}[\Omega] & S_{pq}^{\text{ref}}[\Omega] \\ S_{qp}^{\text{ref}}[\Omega] & S_{qq}^{\text{ref}}[\Omega] \end{pmatrix} \quad (\text{I.95})$$

where we won't write the full expressions of the matrix elements for brevity. The key point is that the off-diagonal terms are non zero, meaning that the reflected quadratures are correlated. This is the frequency-dependent rotation mechanism described above.

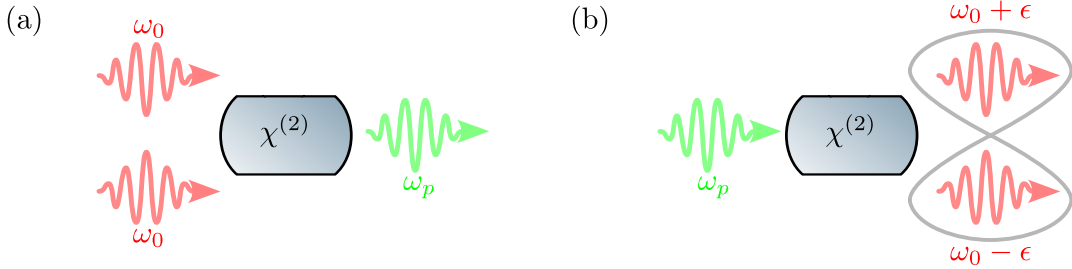


Fig. I.7 Diagrams of  $\chi^{(2)}$  non linear processes. (a) Second Harmonic Generation ( $2\omega_0 = \omega_p$ ). (b) Parametric Down Conversion. The outgoing photons are entangled.

This configuration is used in our experiment to measure the squeezing spectrum of the OPO, as the

### I.2.5 Non Linear Cavities

We now turn to the description of optical cavities in which a  $\chi^{(2)}$  medium is embedded within. This non linear medium can be used both for sum frequency generation, or difference frequency generation. The generic Hamiltonian describing a degenerate  $\chi^{(2)}$  parametric process is

$$H = \hbar\omega_p \hat{b}^\dagger \hat{b} + \hbar\omega_0 \hat{a}^\dagger \hat{a} + \frac{i\hbar\epsilon}{2} (\hat{b} \hat{a}^{\dagger 2} - \hat{b}^\dagger \hat{a}^2) \quad (\text{I.96})$$

where we assumed perfect phase matching for simplicity, that is  $\epsilon \in \mathbb{R}$ . In our experiment with squeezed light, we do use both as to first generate a pump field using a Second Harmonic Generation (SHG) scheme, then use the generated field to *pump* a degenerate Optical Parametric Oscillator (OPO). The equations of motion of both fields are very similar in their structure, yet different in their phenomenology. Here we outline the main results and predictions for both.

#### Second Harmonic Generation

The SHG scheme consists in shining a laser field at frequency  $\omega_0$  onto the cavity, and the non linear medium generates a field at frequency  $\omega_p = 2\omega_0$ , that is, two photons at  $\omega_0$  described by operator  $\hat{a}$ , are converted into a single photon at  $\omega_p$  described by operator  $\hat{b}$ . The input field is thus  $\hat{a}_{\text{in}}$  at  $\omega_0$ , while the input fields at  $\omega_p$  are vacua  $\hat{b}_{\text{in}} = \delta b_l = \delta \hat{b}_{\text{vac}}$ . We restrain the theoretical description to our experiment, where the end mirror reflectivity is  $\sim 1$  for our generated green beam, as seen in the figure below  $\kappa_{2,b} = 0$ . We will not derive the noise spectra for this scheme as they are not of interest in this work, displaying standard vacuum type fluctuations in both the pump and second harmonic field.

We rather focus on the mean field solution. The scalar part of the QLE on resonance for

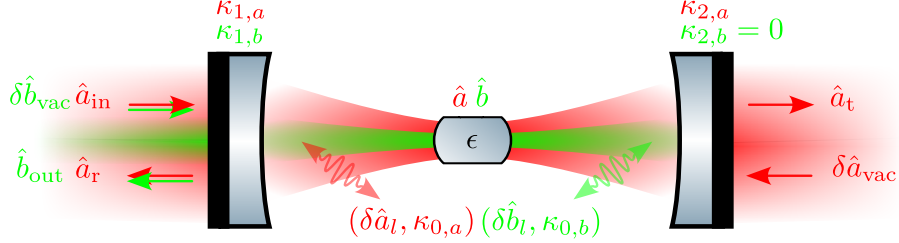


Fig. I.8 Cavity diagram for the Second Harmonic Generation.  $\hat{a}$ 's are the various fields at play,  $\kappa$ 's are the various couplings involved, with  $\delta\hat{a}$ 's the associated fluctuations, similar as in Fig I.4, now considering both the infrared pump, and the generated green beam.

both fields are given by

$$\begin{aligned} 0 &= -\frac{\kappa_a}{2} \bar{\alpha} + \epsilon \bar{\alpha}^* \bar{\beta} + \sqrt{\kappa_{1,a}} \bar{\alpha}_{\text{in}}, \\ 0 &= -\frac{\kappa_b}{2} \bar{\beta} + \frac{\epsilon}{2} \bar{\alpha}^2. \end{aligned} \quad (\text{I.97})$$

where subscript  $a$  and  $b$  refer to the  $\omega_0$  and  $\omega_p$  fields respectively. Solving for the  $\bar{\beta}$  field and computing the output field  $\bar{\beta}_{\text{out}}$  from the input mirror using the input-output relations, yields an output intensity of

$$\begin{aligned} |\bar{\beta}_{\text{out}}|^2 &= \frac{\kappa_a^2 \kappa_{1,b}^2}{4 \varepsilon^2} \left[ \left( 1 + \frac{108 \varepsilon^2 \kappa_{1,a}}{\kappa_a^3 \kappa_b} |\bar{\alpha}_{\text{in}}|^2 \left( 1 + \sqrt{1 + \frac{\kappa_a^3 \kappa_b}{54 \varepsilon^2 \kappa_{1,a} |\bar{\alpha}_{\text{in}}|^2}} \right) \right)^{1/6} \right. \\ &\quad \left. - \left( 1 + \frac{108 \varepsilon^2 \kappa_{1,a}}{\kappa_a^3 \kappa_b} |\bar{\alpha}_{\text{in}}|^2 \left( 1 + \sqrt{1 + \frac{\kappa_a^3 \kappa_b}{54 \varepsilon^2 \kappa_{1,a} |\bar{\alpha}_{\text{in}}|^2}} \right) \right)^{-1/6} \right]^4. \end{aligned} \quad (\text{I.98})$$

This cumbersome expression can be simplified in two limits. In the low input power limit, the output power scales quadratically with the input power, whereas at high powers it scales as  $|\alpha_{\text{in}}|^{4/3}$ .

**Pseudo linear behaviour:** For intermediate powers, the output power scales almost linearly with the input power, which is precisely the regime in which we will operate. The crossover between these regimes is set by the non linear gain  $\epsilon$  and the cavity decay rates  $\kappa_{a,b}$ .

### Optical Parametric Oscillation & Amplification

For this scheme, we consider a pump field with frequency  $\omega_p = 2\omega_0$ . A first key difference from the SHG scheme can be highlighted by the fact that we are now pumping at  $2\omega_0$ , such that pairs of entangled photons are generated at  $\omega_0 + \epsilon$  and  $\omega_0 - \epsilon$ , with  $\epsilon$  a sideband frequency allowed by the cavity bandwidth, hence conserving energy.

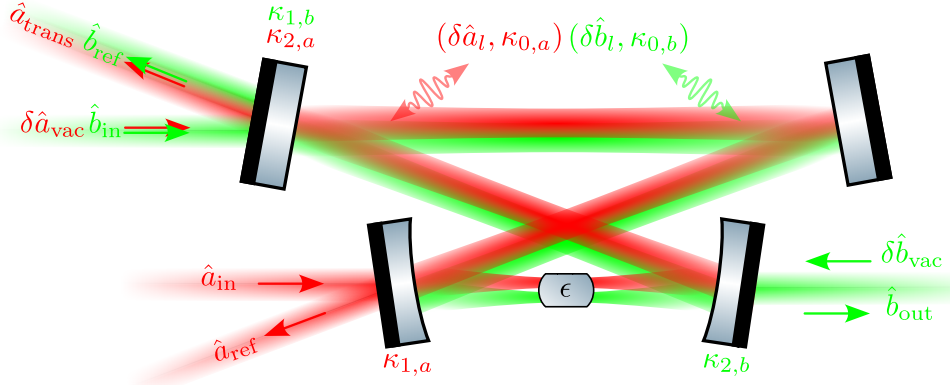


Fig. I.9 Cavity diagram for the Optical Parametric Oscillator.  $\hat{a}$ 's are the various fields at play,  $\kappa$ 's are the various couplings involved, with  $\delta\hat{a}$ 's the associated fluctuations, similar as in Fig I.4, now considering both the green pump, and the generated infrared squeezed beam. The beams are shifted for illustrative purposes but share the same optical axis in the experiment.

We further consider the pump is not *depleted*, such that we can change  $\hat{b}$  to its mean field value  $|\bar{\beta}|e^{i\bar{\varphi}_b}$ , and we disregard the  $\hat{b}$  fluctuations in the equations of motion for simplicity. A careful and complete derivations could also be carried out by keeping all terms in the equations of motion, but it is not serving our purpose here so we will these assumptions to lighten the notation. The total non linear gain is defined as  $g = \epsilon|\bar{\beta}|$ , and the QLEs for the steady state and fluctuation parts of the  $\hat{a}$  field yields:

$$\begin{cases} 0 = -\left(\frac{\kappa}{2} - i\Delta\right)\bar{a} + ge^{i\bar{\varphi}_b}\bar{a}^* + \sqrt{\kappa_1}\bar{a}_{in} \\ \delta\dot{\bar{a}}(t) = -\begin{pmatrix} \kappa/2 - i\Delta & -ge^{i\bar{\varphi}_b} \\ -ge^{-i\bar{\varphi}_b} & \kappa/2 + i\Delta \end{pmatrix}\delta\hat{a}(t) + \sqrt{\kappa_1}\delta\hat{a}_{in}(t) + \sqrt{\kappa_2}\delta\hat{a}_{vac}(t) \end{cases} \quad (\text{I.99})$$

**Mean field solution (Static case):** Assuming a real input field  $\bar{a}_{in} = |\bar{a}_{in}|$ , the transmitted field is given by:

$$\bar{a}_t = \frac{\sqrt{\kappa_1\kappa_2}}{\kappa/2} \frac{1 + i\frac{\Delta}{\kappa/2} + xe^{i\bar{\varphi}_b}}{1 + \left(\frac{\Delta}{\kappa/2}\right)^2 - |x|^2} |\bar{a}_{in}| \quad (\text{I.100})$$

where we define the normalised pump parameter  $x = 2g/\kappa \in \mathbb{R}$ . This normalised pump parameter also equals the ratio of the pump field amplitude by the pump field threshold often written  $B/B_{\text{thr}}$ . For a resonant cavity, the expression reduces to the well known parametric amplification/deamplification scheme

$$\bar{\alpha}_t = \frac{\sqrt{\kappa_1 \kappa_2}}{\kappa/2} \frac{1 + xe^{i\bar{\varphi}_b}}{1 - |x|^2} |\bar{\alpha}_{\text{in}}| \quad (\text{I.101})$$

in which the amplification or deamplification processes are set by the phase of the pump  $\bar{\varphi}_b$ . In the absence of a non linear medium  $x = 0$  we recover the standard cavity results shown above. The threshold is defined at  $x = 1$ , where the rate of generation of entangled pairs exceeds the rate at which they leak from the cavity. In other words,  $x$  is unity when the round trip gain equals the round trip losses. That's precisely the point where the no depletion approximation breaks down, as illustrated by the divergence seen in transmitted field at this very value (how could one obtain a diverging field from a pump field with a finite number of photons). We also notice two special cases, when  $\bar{\varphi}_b = \{0, \pi\}$ , coinciding with the amplification and the deamplification processes respectively.

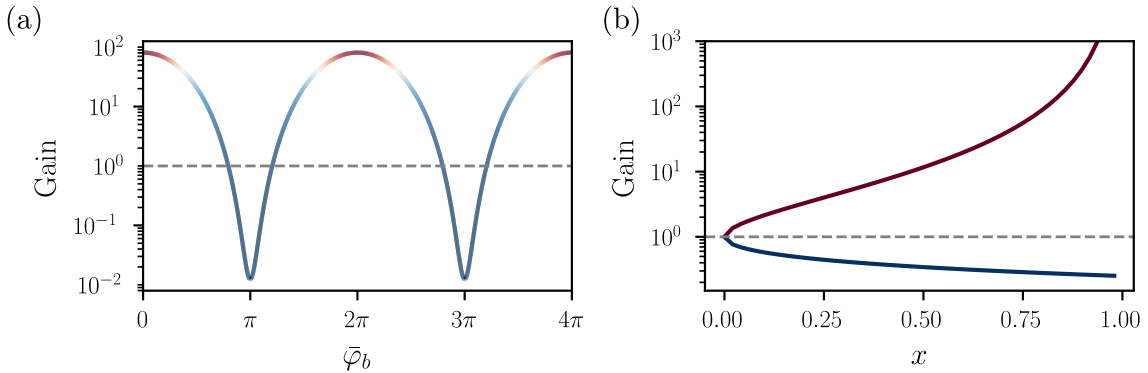


Fig. I.10 *add pump phase colorbar* Classical amplification-deamplification of an infrared seed in an Optical Parametric Oscillator below threshold. (a) Gain of the infrared seed as a function of the green pump phase. The color variations correspond to the pump phase. (b) Amplification-Deamplification of an infrared seed as a function of the normalized pump parameter  $x (< 1)$ . The colors correspond to the ones on figure (a) (its extrema).

**Fluctuations solution:** The general expression of the QLE in Fourier space is given by

$$\tilde{\mathbf{M}}_\Delta \delta \hat{\mathbf{a}}[\Omega] = \sqrt{\kappa_1} \delta \hat{\mathbf{a}}_{\text{in}}[\Omega] + \sqrt{\kappa_2} \delta \hat{\mathbf{a}}_{\text{vac}}[\Omega] \quad (\text{I.102})$$

with

$$\tilde{\mathbf{M}}_\Delta = \begin{pmatrix} \kappa/2 - i(\Delta + \Omega) & -ge^{i\bar{\varphi}_b} \\ -ge^{-i\bar{\varphi}_b} & \kappa/2 + i(\Delta - \Omega) \end{pmatrix}$$

where we defined  $\tilde{\mathbf{M}}_\Delta$  to not be confused with the matrix  $\mathbf{M}_\Delta$  defined earlier for a simple cavity. Note that a genuine *frequency dependent* squeezing angle could be obtained by detuning the OPO cavity, but the frequency range over which the squeezing angle varies is limited by the cavity bandwidth, which is typically small compared to the frequency range of interest in our experiment. This phenomenon was realised experimentally few years ago [Vahlbruch2006], but is not the focus of our work.

In the context of our work, we will assume :

- the pump phase is locked to  $\bar{\varphi}_b = \{0, \pi\}$  i.e. amplification or deamplification regime,
- the cavity is resonant  $\Delta = 0$ ,

We further normalise all frequencies to the cavity bandwidth  $\kappa/2$  such that  $\Omega \rightarrow \Omega/(\kappa/2)$  and  $g \rightarrow g/(\kappa/2) = x$ , such that the off diagonal terms below can simply be written  $\mp x$  factoring out the cavity bandwidth. We carry out the derivation for  $\bar{\varphi}_b = 0$  (amplification) for simplicity, and the  $\bar{\varphi}_b = \pi$  (deamplification) case is obtained by changing  $x$  to  $-x$  in the final expressions. The matrix QLE in Fourier space is written as

$$\tilde{\mathbf{M}}_0 \delta \hat{\mathbf{a}}[\Omega] = \sqrt{\kappa_1} \delta \hat{\mathbf{a}}_{\text{in}}[\Omega] + \sqrt{\kappa_2} \delta \hat{\mathbf{a}}_{\text{vac}}[\Omega] \quad (\text{I.103})$$

with

$$\tilde{\mathbf{M}}_0 = \frac{\kappa}{2} \begin{pmatrix} 1 - i \frac{\Omega}{\kappa/2} & -x \\ -x & 1 - i \frac{\Omega}{\kappa/2} \end{pmatrix}$$

**Transfer matrices and Spectra:** As before with a simple cavity, the transmitted quadratures at resonance are then

$$\delta \hat{\mathbf{u}}_{\text{OPO}}[\Omega] = \mathbf{T}_{\text{OPO}}[\Omega] \delta \hat{\mathbf{u}}_{\text{in}}[\Omega] + \mathbf{L}_{\text{OPO}}[\Omega] \delta \hat{\mathbf{u}}_{\text{vac}}[\Omega] \quad (\text{I.104})$$

where we defined the transfer matrices for the input and loss ports as

$$\mathbf{T}_{\text{OPO}}[\Omega] = \sqrt{\kappa_1 \kappa_2} \mathbf{\Gamma} \tilde{\mathbf{M}}_0^{-1} \mathbf{\Gamma}^{-1}, \quad \mathbf{L}_{\text{OPO}}[\Omega] = \kappa_2 \mathbf{\Gamma} \tilde{\mathbf{M}}_0^{-1} \mathbf{\Gamma}^{-1} - \mathbf{1}....$$

After a bit of algebra, the covariance matrix of the transmitted field at  $\bar{\varphi}_b = 0$  is then

computed as

$$\mathbf{S}_{\text{OPO}}^0[\Omega] = \begin{pmatrix} 1 + \frac{\kappa_2}{\kappa} \frac{4x}{(1-x)^2 + \left(\frac{\Omega}{\kappa/2}\right)^2} & 0 \\ 0 & 1 - \frac{\kappa_2}{\kappa} \frac{4x}{(1+x)^2 + \left(\frac{\Omega}{\kappa/2}\right)^2} \end{pmatrix} \quad (\text{I.105})$$

On a side note, when deriving the noise spectra for the intracavity field, the maximum amount of squeezing is limited to 3dB, while the transmitted field can feature arbitrarily high squeezing levels. This is interpreted as additional correlations between vacuum fluctuations being reflected at the output port of the OPO and the squeezed field leaking from this very same output port, allowing for strong squeezing.

**The perfect squeezer:** Starting from (I.105), in the idealized limit of perfect escape efficiency ( $\eta_{\text{esc}} = 1$ ) and for analysis frequencies much smaller than the cavity bandwidth ( $\Omega/\kappa \rightarrow 0$ ), the expression simplifies to

$$\mathbf{S}_{\text{OPO}}^0[\Omega] = \begin{pmatrix} \frac{(1+x)^2}{(1-x)^2} & 0 \\ 0 & \frac{(1-x)^2}{(1+x)^2} \end{pmatrix} \quad (\text{I.106})$$

Introducing the standard squeezing parameter  $r$  through the relation  $x = \tanh \frac{r}{2}$ , one can rewrite the numerator and denominator as

$$1 + \tanh \frac{r}{2} = \frac{e^{+\frac{r}{2}}}{\cosh \frac{r}{2}}, \quad 1 - \tanh \frac{r}{2} = \frac{e^{-\frac{r}{2}}}{\cosh \frac{r}{2}},$$

such that

$$\frac{(1 \pm \tanh \frac{r}{2})^2}{(1 \mp \tanh \frac{r}{2})^2} = \left( \frac{e^{\pm \frac{r}{2}}}{e^{\mp \frac{r}{2}}} \right)^2 = e^{\pm 2r}.$$

Thus when  $\bar{\varphi}_b = \{0, \pi\}$ , in the lossless, low-frequency limit the transmitted noise levels reduce to the well-known parametric result

$$\mathbf{S}_{\text{OPO}}^0[\Omega] = \begin{pmatrix} e^{+2r} & 0 \\ 0 & e^{-2r} \end{pmatrix} \quad \text{and} \quad \mathbf{S}_{\text{OPO}}^\pi[\Omega] = \begin{pmatrix} e^{-2r} & 0 \\ 0 & e^{+2r} \end{pmatrix} \quad (\text{I.107})$$

where we can now establish that an amplified field ( $\bar{\varphi}_b = 0$ ) corresponds to a squeezed phase quadrature and an anti-squeezed amplitude quadrature, while a deamplified field ( $\bar{\varphi}_b = \pi$ ) corresponds to a squeezed amplitude quadrature and an anti-squeezed phase quadrature. Later on, we will use this idealized expression to describe how squeezed light interacts with

a mechanical resonator whose frequency is much smaller than the OPO bandwidth.

**Losses:** Squeezing is very sensitive to optical losses, which couple uncorrelated vacuum fluctuations into the squeezed field and degrade the squeezing level. The escape efficiency  $\eta_{\text{esc}} = \kappa_2/\kappa$  of the OPO cavity is one such loss mechanism, but there are many others in a real experiment: propagation losses, mode-mismatch, non-unity quantum efficiency of the photodetectors, etc. One can then distinguish between *intracavity* losses, which are accounted for in the escape efficiency, and *extracavity* losses, which we denote by  $\eta_{\text{ext}}$  and lump all other loss mechanisms into a single effective loss. The effect of these losses can be modeled as a beam-splitter mixing the squeezed field with vacuum fluctuations, such that the lossy covariance matrix is given by

$$\mathbf{S}_{\text{det}}[\Omega] = (1 - \eta) \mathbf{S}_{\text{OPO}}^{\bar{\varphi}_b}[\Omega] + \eta \mathbf{1} \quad (\text{I.108})$$

This expression is actually true for any Gaussian state suffering from losses.

**Frequency dependence:** Similarly to what was seen earlier considering general quantum states, squeezing at an arbitrary angle  $\theta$  can be obtained by rotating the covariance matrix. However, one can now make the squeezing angle frequency dependent above as

$$\mathbf{S}_{\text{OPO}}^{\theta}[\Omega] = \mathbf{R}(\theta[\Omega]) \mathbf{S}_{\text{OPO}}^0[\Omega] \mathbf{R}^{\dagger}(\theta[\Omega]). \quad (\text{I.109})$$

where  $\theta[]$  The  $\mathbf{S}[\Omega]$  can either be the full cavity one, or the idealized one. As already mentionned, the mechanical frequencies of interest will be deep in the OPO bandwidth such that we will use the ideal squeezer expression (I.107) in addition with extrinsic losses (I.108). The explicit of the covariance matrix at a frequency dependent angle is then

$$\mathbf{S}_{\text{OPO}}^{\theta}[\Omega] = \begin{pmatrix} \cosh 2r + \sinh 2r \cos 2\theta[\Omega] & -\sinh 2r \sin 2\theta[\Omega] \\ -\sinh 2r \sin 2\theta[\Omega] & \cosh 2r - \sinh 2r \cos 2\theta[\Omega] \end{pmatrix} \quad (\text{I.110})$$

### I.2.6 Optomechanical Cavities

We now turn to standard optomechanical cavities. As in the simple FP case, we consider a cavity mode, in which we now allow one of the the coupler (traditionnaly the output coupler), to be itself a *mechanical* harmonic oscillator with annihilation operator  $\hat{c}$ , effective mass  $m$ , angular frequency  $\Omega_m$  and damping rate  $\Gamma_m$ . In canonical optomechanical systems the mechanics operators are usually denoted as  $\hat{b}$  but in our case it would be redundant with the operators describing the pump field in non linear systems. The position can be expressed in terms of our bosonic operators as  $\hat{x} = x_0(\hat{c} + \hat{c}^{\dagger})$  with  $x_0 = \sqrt{\hbar/(2m\Omega_m)}$  the resonator's

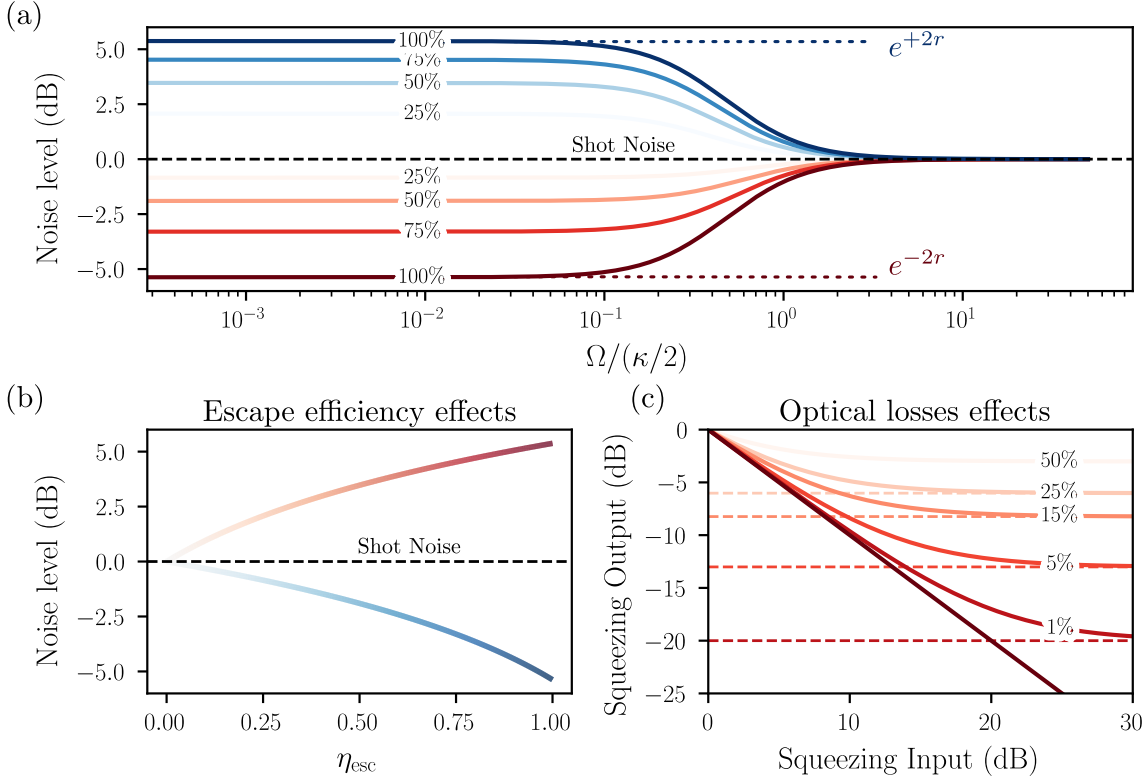


Fig. I.11 Squeezing degradation properties of a non perfect OPO. (a) Squeezing-Antisqueezing levels obtained as a function of frequency (in cavity linewidth unit). The squeezing-antisqueezing levels are maximised at 100% escape efficiency and inside the cavity linewidth (see dark red and dark blue curves). (b) Squeezing-antisqueezing levels as a function of the escape efficiency. (c) Output Squeezing level as a function of the Input Squeezing level (right at the OPO output) considering various optical loss values (extrinsic losses).

zero point fluctuations.

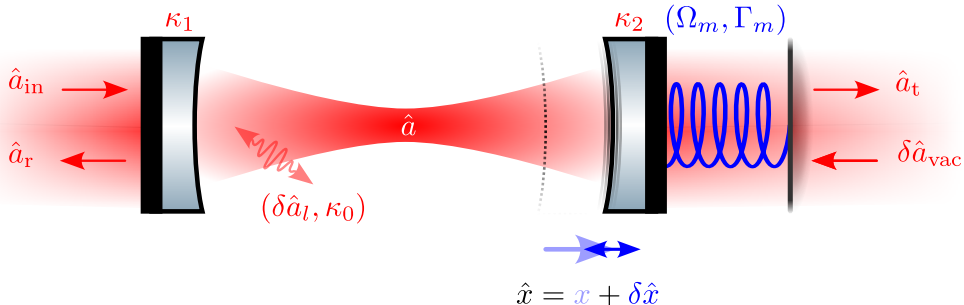


Fig. I.12 Diagram generic optomechanical system.  $\hat{a}$ 's are the various fields at play,  $\kappa$ 's are the various couplings involved, with  $\delta\hat{a}$ 's the associated fluctuations.  $\hat{x}$  is the quantum position operator of the mechanical resonator which linearly shifts the cavity resonance frequency.

## Mechanics & Radiation Pressure Force

The equation of motion of such an oscillator are given by

$$m \ddot{x} = -m \Omega_m^2 \hat{x} - m \Gamma_m \dot{\hat{x}} + \hat{F} \quad (\text{I.111})$$

where  $\hat{F}$  is the total force acting on the oscillator. In Fourier space, we recover the standard linear response form

$$\hat{x}[\Omega] = \chi[\Omega] \hat{F}[\Omega] \quad \text{with} \quad \chi[\Omega] = \frac{1}{m(\Omega_m^2 - \Omega^2 - i\Gamma_m \Omega)} \quad (\text{I.112})$$

where  $\chi[\Omega]$  is the susceptibility linearly relating the position  $\hat{x}[\Omega]$  to the external force  $\hat{F}[\Omega]$ . This susceptibility can also be written as

$$\chi[\Omega] = |\chi[\Omega]| e^{i\phi_m[\Omega]} \quad (\text{I.113})$$

with

$$\text{with } \phi_m[\Omega] = \arctan\left(\frac{\Gamma_m \Omega}{\Omega_m^2 - \Omega^2}\right) \quad \text{and} \quad |\chi[\Omega]| = \frac{1}{m \sqrt{(\Omega_m^2 - \Omega^2)^2 + (\Gamma_m \Omega)^2}}.$$

Similarly to the simple Fabry-Perot cavity (being a driven damped harmonic oscillator too), we can define the analog of the Finesse, namely the quality factor, defined as

$$Q = \frac{\Omega_m}{\Gamma_m} \quad (\text{I.114})$$

which is the number of oscillations before the resonator's energy is damped by a factor  $1/e$ . On resonance, the susceptibility is purely imaginary and reads  $\chi[\Omega_m] = -iQ/(m\Omega_m^2)$ .

As before, the position is also linearized considering small quantum fluctuations compared to its mean value, such that we write  $\hat{x} = x + \delta\hat{x}$ . Importantly, the total position fluctuation  $\delta\hat{x} = \sum \delta\hat{x}_i$  is the sum of individual fluctuations that can arise from various sources, such as a the zero point fluctuations, thermal fluctuations or radiation pressure induced fluctuations. In the following we will only consider a radiation pressure induced fluctuations  $\delta\hat{x}_{\text{RPN}}$ , such that  $\delta\hat{x} = \delta\hat{x}_{\text{RPN}}$ .

Due to the continuous yet discrete photon *hits* at a rate exceeding the resonator frequency, the resonator *feels* an effective force. This radiation pressure force is expressed as

$$\hat{F} = 2 \frac{\hbar k_L}{\tau_c} \hat{a}^\dagger \hat{a} = 2 \frac{\hbar k_L}{\tau_c} |\bar{\alpha}|^2 + 2 \frac{\hbar k_L}{\tau_c} |\bar{\alpha}| \delta\hat{p} + \mathcal{O}(\delta\hat{a}^\dagger \delta\hat{a}) \quad (\text{I.115})$$

where  $k_L = 2\pi/\lambda$  is the laser wavevector, and  $\tau_c = 2L/c$  is the cavity round-trip time, and we neglect second order terms. This force then features a static component shifting

the resonator away from its equilibrium position, that be the  $x$  component, as well as a fluctuating component  $\delta\hat{F} \propto \delta\hat{p}$  jittering the resonator around its mean displacement, that's  $\delta\hat{x}_{\text{RPN}}$ . The position mean value and its fluctuations under radiation pressure can therefore be expressed to first order as

$$x = \frac{2\hbar k_L |\bar{\alpha}|^2}{\tau_c} \chi[0], \quad \delta\hat{x}_{\text{RPN}}[\Omega] = \frac{2\hbar k_L |\bar{\alpha}|}{\tau_c} \chi[\Omega] \delta\hat{p}[\Omega]. \quad (\text{I.116})$$

### Optomechanical QLE

Considering an optomechanical cavity of length  $L$  at rest, such that the mean resonator position is initially 0, the bare cavity free spectral range is given by  $\omega_{\text{FSR}} = \pi c/L$  and the cavity frequency  $\omega_c = N\omega_{\text{FSR}}$ . Injecting light inside this cavity then shifts the mechanical resonator position as seen above, which in turn changes the cavity length  $L \rightarrow L+x$ , thus its frequency. Writing the Hamiltonian, we simply Taylor expand to first order in  $\hat{x}$  the cavity frequency  $\omega_c(\hat{x}) = \omega_c + \hat{x} \partial\omega_c/\partial x$  such that we have:

$$\hat{H} = -\hbar\Delta\hat{a}^\dagger\hat{a} + \hbar G\hat{x}\hat{a}^\dagger\hat{a} + \hbar\Omega_m\hat{c}^\dagger\hat{c} \quad (\text{I.117})$$

where  $G = \partial\omega_c/\partial x = -\omega_c/L$ . One can also identify a useful identity by considering the radiation pressure force (I.115) and the Hamiltonian above, such that

$$\hat{F}_{\text{rad}} = -\frac{\partial\hat{H}}{\partial\hat{x}} = -\hbar G\hat{a}^\dagger\hat{a} \quad \Rightarrow \quad G = -2\frac{k_L}{\tau_c} \quad (\text{I.118})$$

consistent with our previous expression of  $G$  such that we rewrite the position fluctuation as  $\delta\hat{x}_{\text{tot}}[\Omega] = -\hbar G|\bar{\alpha}|\chi[\Omega]\delta\hat{p}[\Omega]$ . Plugging in the QLE and ignoring vacuum and loss fluctuations for notational simplicity, the field's equation are written as

$$\begin{cases} 0 = -\left(\frac{\kappa}{2} - i\bar{\Delta}\right)\bar{\alpha} + \sqrt{\kappa_1}|\bar{\alpha}_{\text{in}}| \\ \delta\dot{\hat{\mathbf{a}}}(t) = -\begin{pmatrix} \kappa/2 - i\bar{\Delta} & 0 \\ 0 & \kappa/2 + i\bar{\Delta} \end{pmatrix} \delta\hat{\mathbf{a}}(t) + iG\bar{\alpha}\delta\hat{x} \begin{pmatrix} +1 \\ -1 \end{pmatrix} + \sqrt{\kappa_1}\delta\hat{\mathbf{a}}_{\text{in}}(t) + \sqrt{\kappa_2}\delta\hat{\mathbf{a}}_{\text{vac}}(t) \end{cases} \quad (\text{I.119})$$

where we introduced the radiation pressure induced detuning  $\bar{\Delta} = \Delta - Gx$  - that is, the mean resonator displacement shifts the cavity frequency, hence the detuning - and where we assume the input field to be real.

This so called *dispersive* coupling, where the cavity frequency  $\omega_c(x)$  depends linearly on the resonator's position to firs order, is the hallmark of the optomechanical interaction. In the canonical model, the cavity linewidth  $\kappa$  do not depend on the resonator's position.

**Mean field solution & Bistability:** Writing the mean intracavity amplitude by keeping

the *unperturbed* detuning  $\Delta$  for clarity and substituting for the static displacement  $x$ , we get

$$\bar{\alpha} = \frac{\sqrt{\kappa_1}}{\kappa/2 - i\left(\Delta - \frac{\hbar G^2 |\bar{\alpha}|^2}{m_{\text{eff}} \Omega_m^2}\right)} |\bar{\alpha}_{\text{in}}| \quad (\text{I.120})$$

where the  $|\bar{\alpha}|^2$  dependence in disguise in the mean mechanical displacement is the root of the bistable behaviour of optomechanical cavities. We show the induced hysteresis in figure ...

For moderate injected powers, this is the standard intracavity field formula where we simply relabel  $\Delta - Gx \rightarrow \Delta$  to lighten the notation. When resonant, the intracavity field does not pick up any phase and is real i.e.  $\bar{\alpha} = |\bar{\alpha}| = 2\sqrt{\kappa_1}/\kappa |\bar{\alpha}_{\text{in}}|$ .

Optomechanical cavities do display optical ringdowns too, as detailed in the cavity sub-part above, but this is a purely optical phenomenon: the mechanics plays no role in the optical ringdown (to first order?).

**Fluctuations solution:** As previously, going to Fourier space now yields

$$\mathbf{M}_{\bar{\Delta}} \delta \hat{\mathbf{a}}[\Omega] = i G \bar{\alpha} \delta \hat{x}[\Omega] \begin{pmatrix} +1 \\ -1 \end{pmatrix} + \sqrt{\kappa_1} \delta \hat{\mathbf{a}}_{\text{in}}[\Omega] + \sqrt{\kappa_2} \delta \hat{\mathbf{a}}_{\text{vac}}[\Omega] \quad (\text{I.121})$$

where we injected the mean field solution (??) in our equations assuming moderate input power to ignore bistable behaviour. We focus on the resonant case to derive our noise spectra, such that  $\mathbf{M}_0 = (\kappa/2 - i\Omega)\mathbf{I}$  and the intracavity quadratures are

$$\delta \hat{\mathbf{u}}[\Omega] = \frac{2G|\bar{\alpha}|}{\kappa/2 - i\Omega} \delta \hat{x}[\Omega] \begin{pmatrix} 0 \\ 1 \end{pmatrix} + \frac{\sqrt{\kappa_1}}{\kappa/2 - i\Omega} \delta \hat{\mathbf{u}}_{\text{in}}[\Omega] + \frac{\sqrt{\kappa_2}}{\kappa/2 - i\Omega} \delta \hat{\mathbf{u}}_{\text{vac}}[\Omega] \quad (\text{I.122})$$

Writing explicitly our amplitude-phase quadratures then gives

$$\begin{aligned} \delta \hat{p}[\Omega] &= \frac{\sqrt{\kappa_1}}{\kappa/2 - i\Omega} \delta \hat{p}_{\text{in}}[\Omega] + \frac{\sqrt{\kappa_2}}{\kappa/2 - i\Omega} \delta \hat{p}_{\text{vac}}[\Omega] \\ \delta \hat{q}[\Omega] &= \frac{2G|\bar{\alpha}|}{\kappa/2 - i\Omega} \delta \hat{x}[\Omega] + \frac{\sqrt{\kappa_1}}{\kappa/2 - i\Omega} \delta \hat{q}_{\text{in}}[\Omega] + \frac{\sqrt{\kappa_2}}{\kappa/2 - i\Omega} \delta \hat{q}_{\text{vac}}[\Omega] \end{aligned} \quad (\text{I.123})$$

This expression highlights the fact that only the phase is affected by the resonator position fluctuations. Physically, this can be understood by considering first that a fluctuating field amplitude leads to a fluctuating radiation pressure force, which in turn *shakes* the mechanical resonator, which changes the phase of the field reflected. The reciprocal process does not happen: a fluctuating phase does not lead to a fluctuating radiation pressure force, hence the output amplitude fluctuations are unaffected by the mechanics.

Importantly, considering the field reflected off the cavity, we define the displacement to phase fluctuation transduction  $\mathcal{C}[\Omega]$  such that

$$\delta\hat{q}_{\text{ref}}[\Omega] = \mathcal{C}[\Omega] \delta\hat{x}[\Omega] \quad \text{with} \quad \mathcal{C}[\Omega] = \frac{2\sqrt{\kappa_1}G|\bar{\alpha}|}{\kappa/2 - i\Omega} = \frac{\kappa_1}{\kappa} \frac{16\mathcal{F}\sqrt{\bar{I}_{\text{in}}}}{\lambda(1 - i2\Omega/\kappa)} \quad (\text{I.124})$$

where we plugged in useful experimental parameters  $\mathcal{F}$ ,  $\lambda$  and  $\bar{I}_{\text{in}}$ . The prefactor  $\kappa_1/\kappa$  is the analog of the escape efficiency for optomechanical cavities, and is unity for single port cavities. We stress that the total phase fluctuations are the sum of various contributions, including the input phase fluctuations, the vacuum fluctuations entering from the loss port, and the position induced phase fluctuations, whether they arise from radiation pressure or other sources. This transduction factor will be used later to express the displacement sensitivity/spectra in terms of experimental parameters.

Plugging in the position fluctuations derived earlier ((I.116) and (I.115)) in the intracavity phase fluctuations we get

$$\begin{aligned} \delta\hat{q}[\Omega] &= \frac{\mathcal{C}^2[\Omega]}{2\kappa_1} \hbar\chi[\Omega] \left( \sqrt{\kappa_1} \delta\hat{p}_{\text{in}}[\Omega] + \sqrt{\kappa_2} \delta\hat{p}_{\text{vac}}[\Omega] \right) \\ &\quad + \frac{1}{\kappa/2 - i\Omega} \left( \sqrt{\kappa_1} \delta\hat{q}_{\text{in}}[\Omega] + \sqrt{\kappa_2} \delta\hat{q}_{\text{vac}}[\Omega] \right) \end{aligned} \quad (\text{I.125})$$

such that we can readily express the intracavity quadratures in matrix form as

$$\delta\hat{\mathbf{u}}[\Omega] = \begin{pmatrix} \frac{1}{\kappa/2 - i\Omega} & 0 \\ \frac{\mathcal{K}[\Omega]}{\kappa_1} & \frac{1}{\kappa/2 - i\Omega} \end{pmatrix} \left( \sqrt{\kappa_1} \delta\hat{\mathbf{u}}_{\text{in}}[\Omega] + \sqrt{\kappa_2} \delta\hat{\mathbf{u}}_{\text{vac}}[\Omega] \right). \quad (\text{I.126})$$

with

$$\mathcal{K}[\Omega] = \frac{\mathcal{C}^2[\Omega]}{2} \hbar\chi[\Omega] = \left( \frac{\kappa_1}{\kappa} \right)^2 \frac{128\hbar\mathcal{F}^2\bar{I}_{\text{in}}}{\lambda^2(1 - i2\Omega/\kappa)^2} \chi[\Omega]$$

We then obtain the reflected and transmitted quadrature fluctuations

$$\begin{aligned} \delta\hat{\mathbf{u}}_{\text{ref}} &= \mathbf{T}_{\text{ref}}\delta\hat{\mathbf{u}}_{\text{in}} + \mathbf{L}_{\text{ref}}\delta\hat{\mathbf{u}}_{\text{vac}} \\ \delta\hat{\mathbf{u}}_{\text{trans}} &= \mathbf{T}_{\text{trans}}\delta\hat{\mathbf{u}}_{\text{in}} + \mathbf{L}_{\text{trans}}\delta\hat{\mathbf{u}}_{\text{vac}}. \end{aligned} \quad (\text{I.127})$$

where we defined the transfer matrices

$$\mathbf{T}_{\text{ref}} = \begin{pmatrix} \frac{\kappa_1}{\kappa/2 - i\Omega} - 1 & 0 \\ \mathcal{K}[\Omega] & \frac{\kappa_1}{\kappa/2 - i\Omega} - 1 \end{pmatrix} \quad \mathbf{L}_{\text{ref}} = \begin{pmatrix} \frac{\sqrt{\kappa_1\kappa_2}}{\kappa/2 - i\Omega} & 0 \\ \sqrt{\frac{\kappa_2}{\kappa_1}} \mathcal{K}[\Omega] & \frac{\sqrt{\kappa_1\kappa_2}}{\kappa/2 - i\Omega} \end{pmatrix}$$

$$\mathbf{T}_{\text{trans}} = \begin{pmatrix} \frac{\sqrt{\kappa_1\kappa_2}}{\kappa/2 - i\Omega} & 0 \\ \sqrt{\frac{\kappa_2}{\kappa_1}} \mathcal{K}[\Omega] & \frac{\sqrt{\kappa_1\kappa_2}}{\kappa/2 - i\Omega} \end{pmatrix} \quad \mathbf{L}_{\text{trans}} = \begin{pmatrix} \frac{\kappa_2}{\kappa/2 - i\Omega} - 1 & 0 \\ \frac{\kappa_2}{\kappa_1} \mathcal{K}[\Omega] & \frac{\kappa_2}{\kappa/2 - i\Omega} - 1 \end{pmatrix}$$

**Convergence to VIRGO/LIGO notation:** To sanity check this expression, we need to make sure we recover the standard expressions used in the LIGO/VIRGO community. This is we will assume the mechanical resonator is free, that is  $\Omega_m \rightarrow 0$  and  $\Gamma_m \rightarrow 0$ . The susceptibility then reduces to  $\chi[\Omega] = 1/M\Omega^2$ , and we will consider sideband frequencies  $\Omega \ll \kappa/2$  such that all terms in  $\Omega/(\kappa/2)$  can be neglected. We also consider a single port cavity such that  $\kappa_1 = \kappa$  and  $\kappa_2 = 0$ . The reflected quadrature fluctuations then read

$$\delta \hat{\mathbf{u}}_{\text{ref}} = \begin{pmatrix} 1 & 0 \\ \frac{32\omega_0 P_{\text{in}}}{ML^2\kappa^2\Omega^2} & 1 \end{pmatrix} \delta \hat{\mathbf{u}}_{\text{in}}. \quad (\text{I.128})$$

In GW papers, the pre factor will often be 8 (and not 32) as they use the cavity half width at half maximum rather than  $\kappa$ . We indeed recover the standard expression used in the GW community, which is a good sanity check of our derivation. We do stress however that this expression is only valid for a free mass, and that the full expression including the mechanical resonance is required to describe optomechanical cavities in general.

**Reflected spectra:** We can now compute the covariance matrix of the reflected quadratures, assuming vacuum fluctuations both at the input and at the loss port. We additionally consider a quasi single port cavity for simplicity  $\kappa_1 \gg \kappa_2$ , such that  $\kappa_1 \sim \kappa$ , as well as the bad cavity limit  $\Omega \ll \kappa/2$ . The reflected covariance matrix is then given by

$$\mathbf{S}_{\text{ref}} = \mathbf{T}_{\text{ref}} \mathbf{S}_{\text{in}} \mathbf{T}_{\text{ref}}^\dagger = \begin{pmatrix} 1 & \mathcal{K}[\Omega] \\ \mathcal{K}^*[\Omega] & 1 + |\mathcal{K}[\Omega]|^2 \end{pmatrix} \quad (\text{I.129})$$

where the off-diagonal entries are complex conjugates of each other, ensuring the covariance matrix is Hermitian as required. The diagonal terms are the amplitude and phase noise spectra respectively, while the off-diagonal terms quantify correlations between amplitude and phase. The presence of these correlations is the hallmark of optomechanical/ponderomotive squeezing i.e. using the non linear response of the resonator to squeeze light. This effect is

not seen nor sought in our experiment, but is a very active field of research in the optomechanics community.

One now sees two essential components in the reflected phase spectrum. The first is the direct phase fluctuations, which is simply shot noise seen as 1. The second is the back-action term  $\propto |\mathcal{K}[\Omega]|^2$ , which is the phase fluctuations induced by the resonator motion driven by radiation pressure fluctuations.

## I.3 Detection

Having layed out the theoretical framework to describe the optical fields interacting with our various cavities, we now turn to the detection schemes used to probe these fields. To detect the optical field reflected or transmitted from these optical systems, we will use two main techniques: direct detection and balanced homodyne detection.

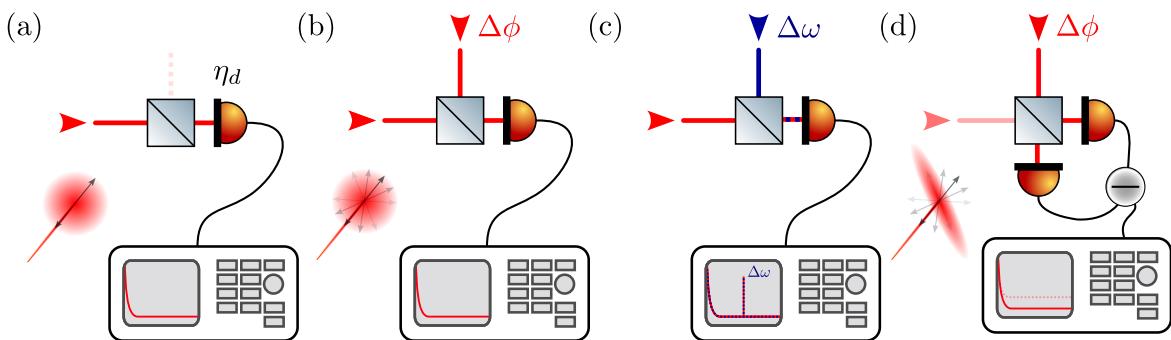


Fig. I.13 coucou

### I.3.1 Direct detection

Direct detection consists in measuring the intensity of the optical field impinging on a photodiode. We will detail three cases: the single field case, where only the signal field is incident on the photodiode, the case where a local oscillator (LO) field is added to the signal field, and finally the case where two beams at different slightly different wavelengths are incident on the photodiode.

**Single field:** The photocurrent operator, originating from the photoelectric effect is given by

$$\hat{I} = e \hat{a}^\dagger \hat{a} \quad (\text{I.130})$$

with  $e$  the electron charge. We introduce the quantum efficiency of the photodiode  $\eta_d$  to account for non unity detection efficiency, such that the detected field operator is written as

$$\hat{a} \rightarrow \sqrt{\eta_d} \hat{a} + \sqrt{1 - \eta_d} \hat{a}_{\text{vac}}$$

where  $\hat{a}_{\text{vac}}$  are vacuum fluctuations entering due to non unity detection efficiency. Assuming a real mean field  $\bar{\alpha}$ , photocurrent operator then reads

$$\hat{I} = \eta_d e \left( |\bar{\alpha}|^2 + \bar{\alpha} \delta p + \sqrt{\eta_d(1 - \eta_d)} \bar{\alpha} \delta p_{\text{vac}} \right) \quad (\text{I.131})$$

where we neglected second order terms. The photocurrent fluctuations in Fourier space are then given by

$$\delta \hat{I}[\Omega] = \eta_d e \bar{\alpha} \left( \delta p[\Omega] + \sqrt{\frac{1 - \eta_d}{\eta_d}} \delta p_{\text{vac}}[\Omega] \right) \quad (\text{I.132})$$

such that the photocurrent noise spectrum is

$$S_{II}[\Omega] = \eta_d^2 e^2 |\bar{\alpha}|^2 \left( S_{pp}[\Omega] + \frac{1 - \eta_d}{\eta_d} \right) \quad (\text{I.133})$$

where  $S_{pp}[\Omega]$  is the amplitude quadrature noise spectrum of the incident field. This expression highlights that direct detection is only sensitive to amplitude quadrature fluctuations.

**Two fields:** Let's now consider an auxiliary field at the same frequency  $\hat{a}_{\text{LO}}$ , called the local oscillator (LO), which is a coherent field dephased from our real signal field  $\hat{a}$  by a phase  $\phi_{\text{LO}}$  such that the total field impinging on the photodiode is  $\hat{a}_{\text{tot}} = \hat{a} + \hat{a}_{\text{LO}}$ . So far, we do not consider the LO to be consequently stronger than the signal field, as we will do in the homodyne detection. This coherent addition can be performed using a beam-splitter or a polarizing beam-splitter, depending on the experimental implementation. The mean field of the total field is then given by  $\bar{\alpha}_{\text{tot}} = \bar{\alpha} + |\bar{\alpha}_{\text{LO}}| e^{i\phi_{\text{LO}}}$ , and its fluctuations are  $\delta \hat{a}_{\text{tot}} = \delta \hat{a} + \delta \hat{a}_{\text{LO}}$ . For simplicity we will assume a quantum efficiency of 1 in the following. The photocurrent operator mean values is then given by

$$\bar{I} = e \left( |\bar{\alpha}|^2 + |\bar{\alpha}_{\text{LO}}|^2 + 2|\bar{\alpha}||\bar{\alpha}_{\text{LO}}| \cos \phi_{\text{LO}} \right) \quad (\text{I.134})$$

where we see the interference term between the signal and the LO: scanning the LO phase  $\phi_{\text{LO}}$  (with a piezoelectric actuator) will lead to interference fringes on the mean photocurrent, which can be used to lock the LO phase. We won't developp the full expression of the photocurrent fluctuation spectrum here (see Annexe B), as they feature a cumberstone linear combination of the amplitude and phase quadrature noise spectra of both the signal

and the LO fields, as well as cross correlation terms between the two fields (if any), which is not very interesting experimentally. However, we can already sense that adding a LO field allows to access phase quadrature fluctuations of the signal field, which was not possible with direct detection alone.

Let's consider 'slow' (hence low frequency) classical fluctuations of the LO phase  $\delta\phi_{\text{LO}}(t)$  around a mean value  $\bar{\phi}_{\text{LO}}$ , such that  $\phi_{\text{LO}}(t) = \bar{\phi}_{\text{LO}} + \delta\phi_{\text{LO}}(t)$  with  $\delta\phi_{\text{LO}}(t) \ll 1$ . Developing the photocurrent to first order in these classical fluctuations, the mean photocurrent fluctuations then reads

$$\delta\bar{I}(t) \propto \delta\phi_{\text{LO}}(t) \quad (\text{I.135})$$

such that slow phase fluctuations of the LO are directly transduced into photocurrent fluctuations. The classical phase noise of the LO can therefore pollute the photocurrent noise spectrum at low frequency, as well as limit the lock stability of the LO phase. Let's now consider the case where the LO is phase modulated at a frequency  $\Omega_{\text{mod}}$  as seen previously

$$\alpha_{\text{LO}}(t) \approx \bar{\alpha}_{\text{LO}} \left( 1 + i\epsilon_\phi \cos(\Omega_{\text{mod}} t) \right)$$

such that the mean photocurrent fluctuations are now given by

$$\delta\bar{I}(t) \propto \cos(\Omega_{\text{mod}} t) \delta\phi_{\text{LO}}(t) \quad (\text{I.136})$$

so that the LO phase noise is spectrally only transduced around the modulation frequency  $\Omega_{\text{mod}}$ . Demodulating the photocurrent at  $\Omega_{\text{mod}}$  then yields an error signal proportional to the LO phase fluctuations, which can be used to lock the LO phase to a desired value  $\bar{\phi}_{\text{LO}}$ , while rejecting low frequency phase noise of the LO.

**Two fields at different frequencies:** Finally, let's consider the case where the signal and LO fields are at slightly different wavelengths/frequencies, such that  $\hat{a}$  is at frequency  $\omega_0$  and  $\hat{a}_{\text{LO}}$  at frequency  $\omega_0 + \omega_{\text{beat}}$ . The total field impinging on the photodiode is then written as  $\hat{a}_{\text{tot}} = \hat{a} + \hat{a}_{\text{LO}} e^{-i\omega_{\text{beat}}t}$  since our operators are defined in a frame rotating at  $\omega_0$ . The mean photocurrent is then given by

$$\bar{I} = e \left( |\bar{\alpha}|^2 + |\bar{\alpha}_{\text{LO}}|^2 + 2|\bar{\alpha}||\bar{\alpha}_{\text{LO}}| \cos(\omega_{\text{beat}} t + \phi_{\text{LO}}) \right) \quad (\text{I.137})$$

where we see that the interference term now oscillates at the beat frequency  $\omega_{\text{beat}}$ . Demodulating the photocurrent at a frequency  $\omega_{\text{ref}} \sim \omega_{\text{beat}}$ , phase  $\tilde{\phi}$ , and low pass filtering the

photocurrent then gives

$$\bar{I}_{\text{demod}} \propto \cos((\omega_{\text{beat}} - \omega_{\text{ref}})t + \phi - \tilde{\phi}). \quad (\text{I.138})$$

This very signal can then be used to lock the frequency of an auxiliary laser to the desired frequency offset  $\omega_{\text{ref}}$  from the main laser. However, this signal featuring many zero crossings, one needs to tune the auxiliary laser frequency close enough to the desired offset so that it ensures the feedback loop locks to the correct zero crossing. This is generally done manually by scanning the auxiliary laser frequency until the right zero crossing is found, confirmed by monitoring the beatnote on a spectrum analyzer.

### I.3.2 Balanced Homodyne Detection

Balanced homodyne detection (HD) is a common technique to measure arbitrary quadratures of an optical field with high sensitivity. It consists in mixing the signal field  $\hat{a}$  with a strong local oscillator (LO) field  $\hat{a}_{\text{LO}}$  on a 50:50 beam-splitter, and detecting the two output ports with identical photodiodes. The beamsplitter operation reads

$$\begin{cases} \hat{a}_{\text{out},1} = \frac{1}{\sqrt{2}}(\hat{a} + \hat{a}_{\text{LO}}) \\ \hat{a}_{\text{out},2} = \frac{1}{\sqrt{2}}(\hat{a} - \hat{a}_{\text{LO}}) \end{cases} \quad (\text{I.139})$$

The two photodiodes then measure the photocurrents  $\hat{I}_1 = e \hat{a}_{\text{out},1}^\dagger \hat{a}_{\text{out},1}$  and  $\hat{I}_2 = e \hat{a}_{\text{out},2}^\dagger \hat{a}_{\text{out},2}$ . The BHD photocurrent is then defined as the difference between the two photocurrents  $\hat{I}_{\text{BHD}} = \hat{I}_1 - \hat{I}_2$ , which reads

$$\hat{I}_{\text{HD}} = e (\hat{a}_{\text{LO}}^\dagger \hat{a} + \hat{a}^\dagger \hat{a}_{\text{LO}}) \quad (\text{I.140})$$

Assuming a real mean field for the signal  $\bar{\alpha}$  and a phase shifted LO mean field  $\bar{\alpha}_{\text{LO}} = |\bar{\alpha}_{\text{LO}}| e^{i\phi_{\text{LO}}}$ , we can linearize the HD photocurrent to first order in the fluctuations as

$$\hat{I}_{\text{HD}} = 2e |\bar{\alpha}_{\text{LO}}| |\bar{\alpha}| \cos \phi_{\text{LO}} + e |\bar{\alpha}_{\text{LO}}| (\cos \phi_{\text{LO}} \delta \hat{p} + \sin \phi_{\text{LO}} \delta \hat{q}) \quad (\text{I.141})$$

where we recognise the mean photocurrent term in  $2e |\bar{\alpha}_{\text{LO}}| |\bar{\alpha}| \cos \phi_{\text{LO}}$  as in the two fields direct detection case. This slowly varying mean photocurrent can be used to lock the LO phase  $\phi_{\text{LO}}$  to a desired value, as previously described, with a piezoelectric actuator and phase modulation/demodulation scheme if needed. The HD photocurrent fluctuations in Fourier space are then given by

$$\delta \hat{I}_{\text{HD}}[\Omega] = e |\bar{\alpha}_{\text{LO}}| (\cos \phi_{\text{LO}} \delta \hat{p}[\Omega] + \sin \phi_{\text{LO}} \delta \hat{q}[\Omega]) \quad (\text{I.142})$$

such that the HD photocurrent noise spectrum reads

$$S_{II}^{\text{HD}}[\Omega] = e^2 |\bar{\alpha}_{\text{LO}}|^2 (\cos^2 \phi_{\text{LO}} S_{pp}[\Omega] + \sin^2 \phi_{\text{LO}} S_{qq}[\Omega] + 2 \sin \phi_{\text{LO}} \cos \phi_{\text{LO}} S_{pq}[\Omega]) \quad (\text{I.143})$$

where  $S_{pp}[\Omega]$ ,  $S_{qq}[\Omega]$  and  $S_{pq}[\Omega]$  are respectively the amplitude, phase and cross correlation noise spectra of the signal field. By tuning the LO phase  $\phi_{\text{LO}}$ , one can therefore measure arbitrary quadratures of the signal field with high sensitivity thanks to the strong LO field amplifying the signal fluctuations. This is the main advantage of HD over direct detection, where only amplitude quadrature fluctuations can be measured. To calibrate the HD detection efficiency, one can block the signal field, such that the LO now probes vacuum fluctuations only. This reference is then used to evaluate the squeezing level of the signal field when unblocked.

The practical implementation of these detection schemes and the associated locks are detailed in chapter 3.



## Chapter II

# Theory: Squeezed Light & Optomechanics

This chapter will cover the elementary concepts required to describe an membrane based optomechanical system in a quantum regime. We will first recall basics on optical field quantization as well describing coherent and squeezed light field, to then turn to the more specific frequency dependent squeezed light field. Secondly, we will cover the mathematical description of a mechanical resonator interacting with a generic coherent optical field, highlighting the differences with the seminal optomechanical system of a mirror on a spring. Finally, we will derive the equations of motions of a membrane based optomechanical system with frequency dependent squeezed optical fields.

**Contents**

---

<b>II.1 Squeezed Light and Optomechanics . . . . .</b>	<b>57</b>
II.1.1 Standard Quantum Limit . . . . .	57
II.1.2 Frequency Independent Squeezing in Optomechanical Cavities . . . . .	60
II.1.3 Frequency Dependent Squeezing in Optomechanical Cavities . . . . .	63
II.1.4 Filter Cavities for Frequency Dependent Squeezing . . . . .	64
<b>II.2 Cavity Optomechanics with Membrane based systems . . . . .</b>	<b>65</b>
II.2.1 Classical Description . . . . .	65
II.2.2 Quantum Description . . . . .	69

---

## II.1 Squeezed Light and Optomechanics

We will now introduce the concept of Standard Quantum Limit (SQL) in the context of optomechanical measurements, and show how frequency dependent squeezed light can be used to surpass this limit.

For the rest of this section we will assume the following

- A cavity on resonance:  $\Delta = 0$ .
- A single port optomechanical cavity:  $\kappa_1 \sim \kappa$ .
- The unresolved sideband regime:  $(\Omega, \Omega_m) \ll \kappa/2$ .

### II.1.1 Standard Quantum Limit

The question of interest is now:

**what is the best displacement sensitivity one can achieve?**

We start by recalling the reflected phase fluctuation of an optomechanical cavity from section I.2.5 under the aforementioned assumptions:

$$\delta\hat{q}_{\text{ref}}[\Omega] = \delta\hat{q}_{\text{in}}[\Omega] + \mathcal{K}[\Omega] \delta\hat{p}_{\text{in}}[\Omega] \quad \text{with} \quad \mathcal{K}[\Omega] = \frac{\mathcal{C}^2}{2} \hbar\chi[\Omega] = \frac{128\mathcal{F}^2\bar{I}_{\text{in}}}{\lambda^2} \hbar\chi[\Omega]$$

where  $\mathcal{C}$  is now positive and frequency independent. The resulting reflected phase spectrum reads

$$S_{qq}^{\text{ref}}[\Omega] = S_{qq}^{\text{in}}[\Omega] + |\mathcal{K}[\Omega]|^2 S_{pp}^{\text{in}}[\Omega] + 2 \operatorname{Re} [\mathcal{K}[\Omega] S_{pq}^{\text{in}}[\Omega]]$$

The phase to displacement transduction relation with an optomechanical escape efficiency of 1:

$$\delta\hat{q}_x = \mathcal{C}\delta\hat{x}[\Omega] = \frac{16\mathcal{F}\sqrt{\bar{I}_{\text{in}}}}{\lambda} \delta\hat{x}[\Omega]$$

Using these two relations, we can then express displacement fluctuations in terms of input amplitude and phase fluctuations, assuming the reflected field is a perfect probe of the mechanical resonator position fluctuations i.e.  $\delta\hat{q}_{\text{ref}}[\Omega] = \delta\hat{q}_x[\Omega]$ . This treatment is formally equivalent to considering the output phase as a statistical estimator of the position fluctuations being a stationary random process as done in quantum measurement theory [3]. We then write

$$\delta\hat{x}[\Omega] = \mathcal{C}^{-1} \delta\hat{q}_{\text{in}}[\Omega] + \frac{\mathcal{C}}{2} \hbar\chi[\Omega] \delta\hat{p}_{\text{in}}[\Omega] \tag{II.1}$$

such that the associated displacement spectrum reads

$$S_{xx}[\Omega] = \mathcal{C}^{-2} S_{qq}^{\text{in}}[\Omega] + \left( \frac{\mathcal{C}}{2} \hbar |\chi[\Omega]| \right)^2 S_{pp}^{\text{in}}[\Omega] + \hbar |\chi[\Omega]| \operatorname{Re} \left[ e^{i\phi_m[\Omega]} S_{pq}^{\text{in}}[\Omega] \right] \quad (\text{II.2})$$

We then identify three contributions to the displacement spectrum:

- The first term is the laser shot noise (or imprecision noise) scaling inversely with the input power  $\bar{I}_{\text{in}}$ , arising from the input phase fluctuations  $S_{qq}^{\text{in}}[\Omega]$  and given by

$$S_{xx}^{\text{SN}}[\Omega] = \frac{\lambda^2}{256\mathcal{F}^2 \bar{I}_{\text{in}}} S_{qq}^{\text{in}}[\Omega] \quad (\text{II.3})$$

- The second term is the radiation pressure noise (or backaction noise) scaling linearly with the input power  $\bar{I}_{\text{in}}$ , arising from the input amplitude fluctuations  $S_{pp}^{\text{in}}[\Omega]$  driving the mechanical resonator via radiation pressure given by

$$S_{xx}^{\text{RPN}}[\Omega] = \frac{64\mathcal{F}^2 \bar{I}_{\text{in}}}{\lambda^2} \hbar^2 |\chi[\Omega]|^2 S_{pp}^{\text{in}}[\Omega] \quad (\text{II.4})$$

- The third term is a correlation term between amplitude and phase fluctuations  $S_{pq}^{\text{in}}[\Omega]$ , which can be non-zero for arbitrary squeezed states as seen in the previous section and given by

$$S_{xx}^{\text{cor}}[\Omega] = \hbar |\chi[\Omega]| \operatorname{Re} \left[ e^{i\phi_m[\Omega]} S_{pq}^{\text{in}}[\Omega] \right] \quad (\text{II.5})$$

And we write the total displacement spectrum as the sum of these three contributions

$$S_{xx}[\Omega] = S_{xx}^{\text{SN}}[\Omega] + S_{xx}^{\text{RPN}}[\Omega] + S_{xx}^{\text{cor}}[\Omega] \quad (\text{II.6})$$

We now consider vacuum/coherent fluctuations such that  $S_{qq}^{\text{in}}[\Omega] = S_{pp}^{\text{in}}[\Omega] = 1$  and  $S_{pq}^{\text{in}}[\Omega] = 0$ , so that the displacement spectrum simplifies to

$$S_{xx}[\Omega] = \mathcal{C}^{-2} + \left( \frac{\mathcal{C}}{2} \hbar |\chi[\Omega]| \right)^2 \quad (\text{II.7})$$

and we look at what noise dominates the displacement spectrum around the mechanical resonance  $\Omega \sim \Omega_m$ . In this frequency range, there are two frequencies at which the displacement noise contributions are equal, given by the condition  $S_{xx}^{\text{SN}}[\Omega] = S_{xx}^{\text{RPN}}[\Omega]$ , leading to the frequency  $\Omega_{\text{SQL}}$  defined as

$$\Omega_{\text{SQL}}^{\pm} = \sqrt{\Omega_m^2 - \frac{\Gamma_m^2}{2}} \pm \frac{1}{2} \sqrt{\Gamma_m^4 - 4\Gamma_m^2 \Omega_m^2 + \left( \frac{\hbar \mathcal{C}^2}{m} \right)^2} \quad (\text{II.8})$$

and consistent with the LIGO/Virgo notation [[harry\\_advanced\\_2010](#), [aasi\\_enhanced\\_2013](#)]. Over the frequency range of interest  $\Omega \in [\Omega_m - \Omega_{SQL}, \Omega_m + \Omega_{SQL}]$ , the displacement noise is dominated by the radiation pressure noise, while outside this range, the noise is dominated by the shot noise. However, for every sideband frequency, there exists an optimal input power  $\bar{I}_{in}^{SQL}[\Omega]$  at which both contributions are equal, minimizing the total displacement noise. This limit is called the Standard Quantum Limit (SQL) and is a direct consequence of Heisenberg's uncertainty principle applied to continuous position measurements [[braginsky\\_quantum\\_1992](#), 3]. This SQL intensity is given by

$$S_{xx}^{SN}[\Omega] = S_{xx}^{RPN}[\Omega] \implies \bar{I}_{in}^{SQL}[\Omega] = \frac{\lambda^2}{128\mathcal{F}^2\hbar|\chi[\Omega]|} \quad (\text{II.9})$$

such that plugging back in this SQL intensity in (II.7) gives the SQL displacement spectrum as

$$S_{xx}^{SQL}[\Omega] = \hbar|\chi[\Omega]| \implies S_{xx}^{SN}[\Omega] + S_{xx}^{RPN}[\Omega] \geq \hbar|\chi[\Omega]| \quad (\text{II.10})$$

which is the fundamental limit to continuous position measurements with coherent light. We also note that for high Q resonators,  $\Omega_{SQL} \gg \Gamma_m$ , so approximating the susceptibility by its real part holds over a relatively large frequency range but fails at resonance where the susceptibility is purely imaginary.

### Thermal Noise

Thermal noise is a major limitation in optomechanical experiments, as it can mask the quantum effects one aims to observe. The mechanical resonator is indeed coupled to a thermal bath at temperature  $T$ , which drives the resonator into a thermal state with mean phonon occupation number  $\bar{n}_{th} = k_B T / (\hbar\Omega_m)$  in the high temperature limit  $k_B T \gg \hbar\Omega_m$ . The position fluctuations induced by this thermal force is given by

$$S_{xx}^{th}[\Omega] = \frac{2\hbar}{1 - e^{-\hbar\Omega/k_B T}} \text{Im } \chi[\Omega] \simeq 2m\Gamma_m k_B T |\chi[\Omega]|^2 \quad \text{if } k_B T \gg \hbar\Omega \quad (\text{II.11})$$

where we used the identity  $\text{Im } \chi[\Omega] = m\Gamma_m \Omega |\chi[\Omega]|^2$ . At  $T = 0K$ , this reduces to the zero point fluctuations spectrum  $S_{xx}^{ZPF}[\Omega] = m\Gamma_m \hbar\Omega_m |\chi[\Omega]|^2 < S_{xx}^{SQL}[\Omega]$ , such that is often neglected in the total displacement spectrum. However, at finite temperature, the thermal noise can be much larger than the SQL. Therefore, the total displacement spectrum now reads

$$S_{xx}[\Omega] = S_{xx}^{SN}[\Omega] + S_{xx}^{RPN}[\Omega] + S_{xx}^{cor}[\Omega] + S_{xx}^{th}[\Omega] \quad (\text{II.12})$$

In order to experimentally probe these quantum limits without being limited by various technical noises, one would then need:

- A high finesse cavity, such that the shot noise  $S_{xx}^{\text{SN}} \propto \mathcal{F}^{-2}$  level is low, and the radiation pressure noise  $S_{xx}^{\text{RPN}} \propto \mathcal{F}^2$  is high. One should however ensure the cavity bandwidth  $\kappa$  is still much larger than the mechanical frequency  $\Omega_m$ . This can be ensured by tuning the cavity length  $L$  and mirror transmissions.
- A low mass, low frequency, high quality factor mechanical resonator, such that the susceptibility modulus at resonance  $|\chi[\Omega_m]| = Q/m\Omega_m^2$  is high, and it comes out of the shot noise level significantly.
- A low temperature environment, such that the thermal noise  $S_{xx}^{\text{th}} \propto T$  is low and does not mask the quantum effects. This can be ensured by cryogenic cooling of the mechanical resonator, as well as using high quality factor resonators to reduce the mechanical linewidth  $\Gamma_m$ .

We now want to derive the displacement spectrum of an optomechanical system driven by a squeezed light field, whether frequency independent or dependent.

### II.1.2 Frequency Independent Squeezing in Optomechanical Cavities

We first recall the (idealized) covariance matrices for both a phase squeezed field and an amplitude squeezed field

$$\mathbf{S}_{\text{OPO}}^0[\Omega] = \begin{pmatrix} e^{+2r} & 0 \\ 0 & e^{-2r} \end{pmatrix}, \quad \mathbf{S}_{\text{OPO}}^\pi[\Omega] = \begin{pmatrix} e^{-2r} & 0 \\ 0 & e^{+2r} \end{pmatrix}$$

For a phase squeezed field, the displacement spectrum reads

$$S_{xx}^0[\Omega] = \mathcal{C}^{-2}e^{-2r} + \left(\frac{\mathcal{C}}{2}\hbar|\chi[\Omega]|\right)^2 e^{+2r} \quad (\text{II.13})$$

while for an amplitude squeezed field, the displacement spectrum reads

$$S_{xx}^\pi[\Omega] = \mathcal{C}^{-2}e^{+2r} + \left(\frac{\mathcal{C}}{2}\hbar|\chi[\Omega]|\right)^2 e^{-2r} \quad (\text{II.14})$$

We then see that phase squeezing reduces the shot noise contribution but increases the radiation pressure noise contribution, while amplitude squeezing reduces the radiation pressure noise contribution but increases the shot noise contribution. The input cross correlations being zero, this is completely equivalent to the coherent state with a rescaled input intensity  $e^{\pm 2r}\bar{I}_{\text{in}}$  (hidden in  $\mathcal{C}$ ) for phase/amplitude squeezing respectively. However, neither of these two configurations can reduce both contributions simultaneously, and therefore cannot improve the SQL limit. This is illustrated in figure II.2.

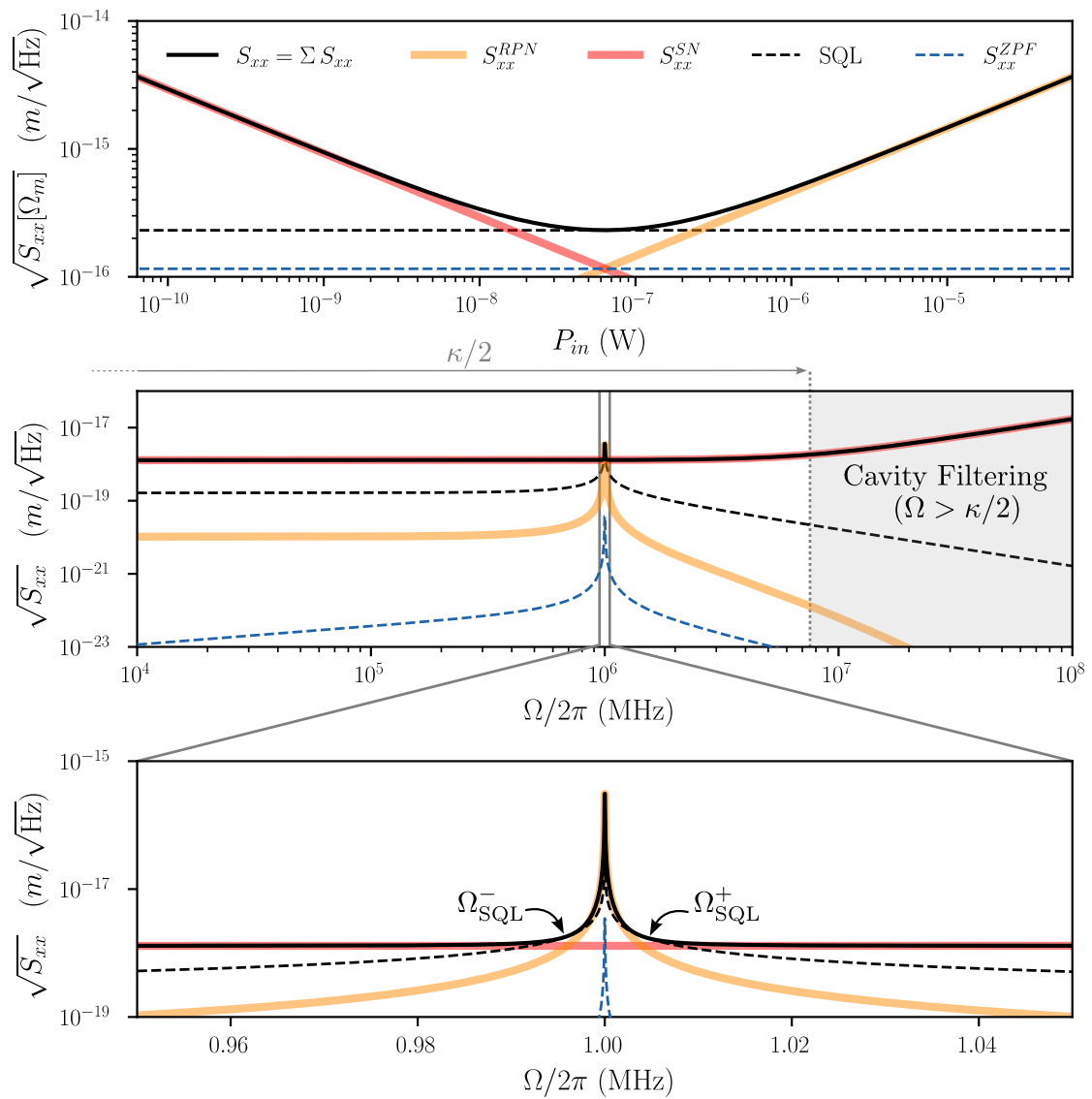


Fig. II.1 DYes

Now consider an input squeezed state with a frequency independent squeezing angle  $\theta = \pi/4$  with covariance matrix

$$\mathbf{S}_{\text{OPO}}^{\pi/4}[\Omega] = \begin{pmatrix} \cosh 2r & -\sinh 2r \\ -\sinh 2r & \cosh 2r \end{pmatrix}.$$

The resulting displacement spectrum then reads

$$S_{xx}^{\pi/4}[\Omega] = \left( C^{-2} + \left( \frac{C}{2} \hbar |\chi[\Omega]| \right)^2 \right) \cosh 2r - \hbar |\chi[\Omega]| \sinh 2r \cos \phi_m[\Omega] \quad (\text{II.15})$$

and we seek the frequency range where the displacement spectrum is below the SQL, i.e.  $S_{xx}^{\pi/4}[\Omega] < S_{xx}^{\text{SQL}}[\Omega]$ . This condition is satisfied when

$$\tanh r < \cos \phi_m[\Omega] < 1 \quad (\text{II.16})$$

Because  $\tanh r$  tends to 1 as  $r$  increases, the frequency range where the displacement spectrum is below the SQL decreases with increasing squeezing factor  $r$ . Furthermore, due to the interplay between quadrature correlations and the projection of the  $\pi/4$  ellipse onto the output quadrature axis, acting as an effective increase of the shot noise floor with effective intensity  $\bar{I}_{\text{in}} \cosh^{-1} r$ , there is an effective range of  $r$  above which the displacement spectrum is always above the SQL (for a fixed input intensity). This is illustrated in figure II.2.

Additionally, and as seen in Fig ..., the optimal angle to maximally reduce the displacement spectrum varies with frequency, being 0 at frequencies outside the resonator's bandwidth,  $\pi/2$  at the mechanical resonance frequency  $\Omega_m$ , and about  $\pm\pi/4$  at  $\Omega_m \pm \Omega_{\text{SQL}}$ .

This motivates the use of frequency dependent squeezed states to reduce the displacement spectrum below the SQL over a broad frequency range, where every sideband frequency needs to be rotated by a different angle to minimize the displacement spectrum. More specifically, sideband noises contributing to both shot noise and radiation pressure noise need to be correlated in a frequency dependent manner to optimally cancel the total displacement noise in the vicinity of the mechanical resonance.

### II.1.3 Frequency Dependent Squeezing in Optomechanical Cavities

We now consider a squeezed state with a frequency dependent angle whose covariance matrix is given by

$$\mathbf{S}_{\text{OPO}}^{\theta}[\Omega] = \begin{pmatrix} \cosh 2r + \sinh 2r \cos 2\theta[\Omega] & -\sinh 2r \sin 2\theta[\Omega] \\ -\sinh 2r \sin 2\theta[\Omega] & \cosh 2r - \sinh 2r \cos 2\theta[\Omega] \end{pmatrix}$$

The resulting displacement spectrum then reads

$$\begin{aligned} S_{xx}[\Omega] = & \mathcal{C}^{-2}(\cosh 2r - \sinh 2r \cos 2\theta[\Omega]) \\ & + \left(\frac{\mathcal{C}}{2}\hbar|\chi[\Omega]|\right)^2 (\cosh 2r + \sinh 2r \cos 2\theta[\Omega]) \\ & - \hbar|\chi[\Omega]| \sinh 2r \sin 2\theta[\Omega] \cos \phi_m[\Omega] \end{aligned} \quad (\text{II.17})$$

As shown in the annex, picking the squeezing angle as

$$2\theta[\Omega] = \arctan \left[ \frac{2|\mathcal{K}[\Omega]| \cos \phi_m[\Omega]}{1 - |\mathcal{K}[\Omega]|^2} \right] \quad (\text{II.18})$$

minimizes the displacement spectrum at every sideband frequency, leading to

$$\begin{aligned} S_{xx}[\Omega] = & \cosh 2r \left( \mathcal{C}^{-2} + \left( \frac{\mathcal{C}}{2}\hbar|\chi[\Omega]|\right)^2 \right) \\ & - \sinh 2r \sqrt{\left( \mathcal{C}^{-2} - \left( \frac{\mathcal{C}}{2}\hbar|\chi[\Omega]|\right)^2 \right)^2 + \left( \hbar|\chi[\Omega]| \cos \phi_m[\Omega] \right)^2}. \end{aligned} \quad (\text{II.19})$$

This broadband reduction of the displacement spectrum below the SQL is illustrated in figure ???. However, for a resonant optomechanical cavity i.e.  $\Delta = 0$ , it is impossible to beat the SQL at the mechanical resonance, where the susceptibility is purely imaginary  $\phi_m[\Omega_m] = \pi/2$ .

**Convergence to VIRGO/LIGO notation:** We once again show that this general treatment converges to the one used in the context of gravitational wave detectors. In the free mass regime,  $\mathcal{K}[\Omega]$  is real, such that  $\phi_m[\Omega] = 0$ . One can then rewrite the optimal squeezing angle as

$$2\theta[\Omega] = \arctan \left[ \frac{2\mathcal{K}[\Omega]}{1 - \mathcal{K}^2[\Omega]} \right] = 2 \arctan \mathcal{K}[\Omega] \quad (\text{II.20})$$

where we used the identity  $\arctan 2x/(1 - x^2) = 2 \arctan x \pmod{\pi}$ , such that this comes down to the expression used in the context of gravitational wave detectors [harry\_advanced\_2010,

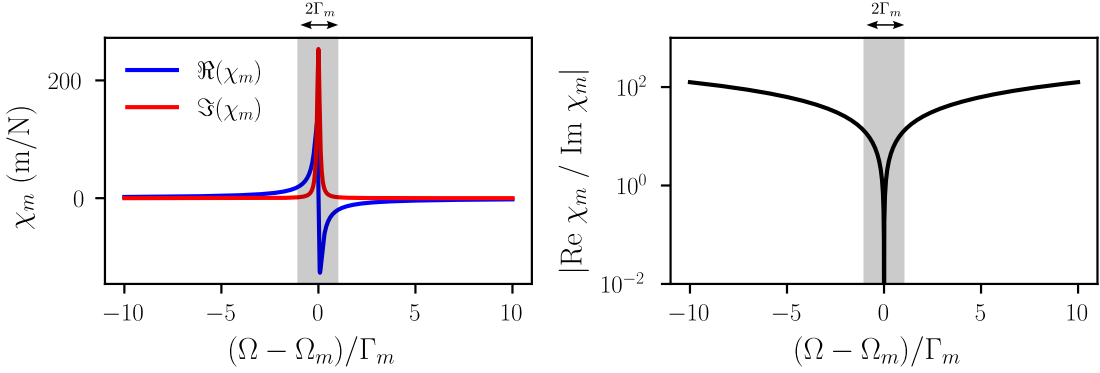


Fig. II.2 DYes

**aasi\_enhanced\_2013].** Furthermore, the mechanical frequency and damping rate will be significantly smaller than the  $\hbar\mathcal{C}^2/m$  term such that using the free-mass susceptibility  $\chi[\Omega] = -1/m\Omega^2$  boils down the the SQL frequency to the known expression

$$\Omega_{\text{SQL}} = \sqrt{\frac{\hbar\mathcal{C}^2}{2m}} \implies \kappa[\Omega] = \left(\frac{\Omega_{\text{SQL}}}{\Omega}\right)^2 \quad (\text{II.21})$$

The displacement spectrum then reduces to the common expression

$$S_{xx}[\Omega] = \mathcal{C}^{-2} \left(1 + \left(\frac{\Omega_{\text{SQL}}}{\Omega}\right)^2\right) e^{-2r} \quad (\text{II.22})$$

which is the free-mass approximation result used in the GW community.

#### II.1.4 Filter Cavities for Frequency Dependent Squeezing

To generate frequency dependent squeezed states, one can use a detuned optical cavity called a filter cavity [4]. The principle is to reflect a frequency independent squeezed state off a single sided detuned cavity, such that only the sidebands resonant with the cavity will undergo a phase shift, effectively rotating the squeezing ellipse by a frequency dependent angle. The transfer matrix for a single sideband from a detuned single port cavity was given by

$$\kappa M_{\Delta}^{-1}[\Omega] - \mathbf{1} = \begin{pmatrix} \frac{\kappa/2 + i(\Delta + \Omega)}{\kappa/2 - i(\Delta + \Omega)} & 0 \\ 0 & \frac{\kappa/2 - i(\Delta - \Omega)}{\kappa/2 + i(\Delta - \Omega)} \end{pmatrix}$$

We recall from section II.1.4 that the reflected quadratures from a detuned cavity are

given by

$$\mathbf{T}_r[\Omega] = \frac{1}{(\kappa/2 - i\Omega)^2 + \Delta^2} \begin{pmatrix} (\kappa/2)^2 - \Delta^2 + \Omega^2 & -\kappa\Delta \\ +\kappa\Delta & (\kappa/2)^2 - \Delta^2 + \Omega^2 \end{pmatrix}$$

such that the phase picked up by sidebands at frequency  $\Omega$  is given by

$$\phi_{fc}[\Omega] = \arctan\left(\frac{2\Delta\kappa}{\kappa^2/4 - \Delta^2 + \Omega^2}\right) \quad (\text{II.23})$$

## II.2 Cavity Optomechanics with Membrane based systems

### II.2.1 Classical Description

To gain intuition and derive elementary parameters used in the next section, we first describe the classical fields propagating in a three mirror cavity where a membrane with complex amplitude reflection and transmission coefficients  $r_m = |r_m|e^{i\phi_r}$  and  $t_m = |t_m|e^{i\phi_t}$  is placed between two high reflectivity mirrors of amplitude reflection coefficients  $\sim -1$ . The membrane splits the cavity in two sub-cavities of lengths  $L_1$  and  $L_2$ , with  $L = L_1 + L_2$  the total cavity length. The membrane is initially at mean position  $x = 0$ , and is modelled as a thin dielectric slab of thickness  $d$  and refractive index  $n$ , with amplitude reflection and transmission coefficients  $r_m$  and  $t_m$  given by [thompson\_strong\_2008]

$$r_m = \frac{(n^2 - 1) \sin knd}{2in \cos knd + (n^2 + 1) \sin knd}, \quad t_m = \frac{2n}{2in \cos knd + (n^2 + 1) \sin knd}. \quad (\text{II.24})$$

In the lossless case, we will assume the index of refraction  $n$  is real, such that  $|r_m|^2 + |t_m|^2 = 1$ . The right-moving mean field amplitudes in the left and right sub-cavities are denoted  $\bar{\alpha}_L$  and  $\bar{\alpha}_R$ , while the left-moving mean field amplitudes are denoted  $\bar{\alpha}'_L$  and  $\bar{\alpha}'_R$ . The cavity fields are then related by

$$\begin{aligned} \bar{\alpha}_R &= t_m \bar{\alpha}_L + r_m \bar{\alpha}'_R \\ \bar{\alpha}'_L &= t_m \bar{\alpha}'_R + r_m \bar{\alpha}_L. \end{aligned} \quad (\text{II.25})$$

In this case, energy conservation i.e.  $|\bar{\alpha}_L|^2 + |\bar{\alpha}'_R|^2 = |\bar{\alpha}'_L|^2 + |\bar{\alpha}_R|^2$  imposes that  $2(\phi_t - \phi_r) = \pi$  such that we can chose  $r_m = |r_m|$  and  $t_m = i|t_m|$ . We rewrite the the cavity fields by injecting the identities  $\bar{\alpha}_L = -\bar{\alpha}'_L e^{2ikL_1}$  and  $\bar{\alpha}'_R = -\bar{\alpha}_R e^{2ikL_2}$  such that we get the useful system

$$\begin{aligned} (1 + |r_m|e^{2ikL_2})\bar{\alpha}_R &= -i|t_m|e^{2ikL_1}\bar{\alpha}'_L \\ (1 + |r_m|e^{2ikL_1})\bar{\alpha}'_L &= -i|t_m|e^{2ikL_2}\bar{\alpha}_R. \end{aligned} \quad (\text{II.26})$$

### Resonance Frequencies

By eliminating the right and left fields in the above system, we arrive at the transcendental equation [5]

$$-\cos kL = |r_m| \cos(k\Delta L), \quad \text{with} \quad \Delta L = L_2 - L_1. \quad (\text{II.27})$$

Following the method in Sankey et al. [6], we now proceed to derive the cavity resonance frequencies as a function of the membrane position  $x$  around its mean position  $x = 0$ . We will also always consider a long cavity such that  $L \gg \lambda, x$ . The cavity sublengths considering a non zero mean membrane position are then  $L_1 \rightarrow L_1 + x$  and  $L_2 \rightarrow L_2 - x$ . It follows that  $\Delta L \rightarrow \Delta L - 2x$ . We will consider the effect of this displacement on the cavity wavenumbers/frequencies as a perturbation  $k(x) = k_N + \delta k(x)$  with  $k_N = N\pi/L$ , that is the membrane displacement does not change the longitudinal mode index  $N$  but modulates it by at most  $\pi/L$  (or equivalently by one empty cavity FSR in the frequency domain). We will omit the  $x$  dependency in both  $k$  and  $\delta k$  for ease of notation. It then follows that terms in  $k L$  and  $k x$  can be expanded as

$$\cos(kL) = (-1)^N \cos(\delta k L) \quad \text{and} \quad \cos(kx) \sim \cos(k_N x)$$

where we assumed that  $\delta k x \sim 0$ . The transcendental equation becomes

$$(-1)^{N+1} \cos(\delta k L) = |r_m| \cos(k_N \Delta L) \left[ \cos(\delta k \Delta L) \cos(2k_N x) + \sin(\delta k \Delta L) \sin(2k_N x) \right] \quad (\text{II.28})$$

and where we simplified the sines terms already equal to zero. We will now consider the Membrane At The Edge (MATE) model where  $L_1 \sim L \gg L_2 \rightarrow \Delta L \sim L$ . Solving for  $\delta k$  reinjecting in the dispersion relation  $\omega_c(x) = ck(x)$  leads to

$$\omega_c(x) \simeq \omega_{FSR} \left( N + \frac{1}{\pi} \arctan \left( -\frac{1 + |r_m| \cos 2k_N x}{|r_m| \sin 2k_N x} \right) \right) \quad (\text{II.29})$$

where  $\omega_{FSR} = \pi c/L$  is the empty cavity free spectral range. When the laser is resonant with the cavity, we then substitute  $N\omega_{FSR}$  and  $k_N$  by  $\omega_0$  and  $k$  the laser angular frequency and wavenumber. Taking the derivatives of these resonance frequencies with respect to the membrane position  $x$  gives the linear and quadratic dispersive optomechanical couplings  $G^{(1)}(x) = \partial\omega_c/\partial x$  and  $G^{(2)}(x) = \partial^2\omega_c/\partial x^2$  as

$$\begin{aligned} G^{(1)}(x) &= \frac{2|r_m|k_N\omega_{FSR}}{\pi} \frac{|r_m| + \cos(2k_N x)}{1 + |r_m|^2 - 2|r_m| \cos(2k_N x)} \\ G^{(2)}(x) &= -\frac{4|r_m|k_N^2\omega_{FSR}}{\pi} \frac{|r_m|(1 - |r_m|^2) \sin(2k_N x)}{(1 + |r_m|^2 - 2|r_m| \cos(2k_N x))^2} \end{aligned} \quad (\text{II.30})$$

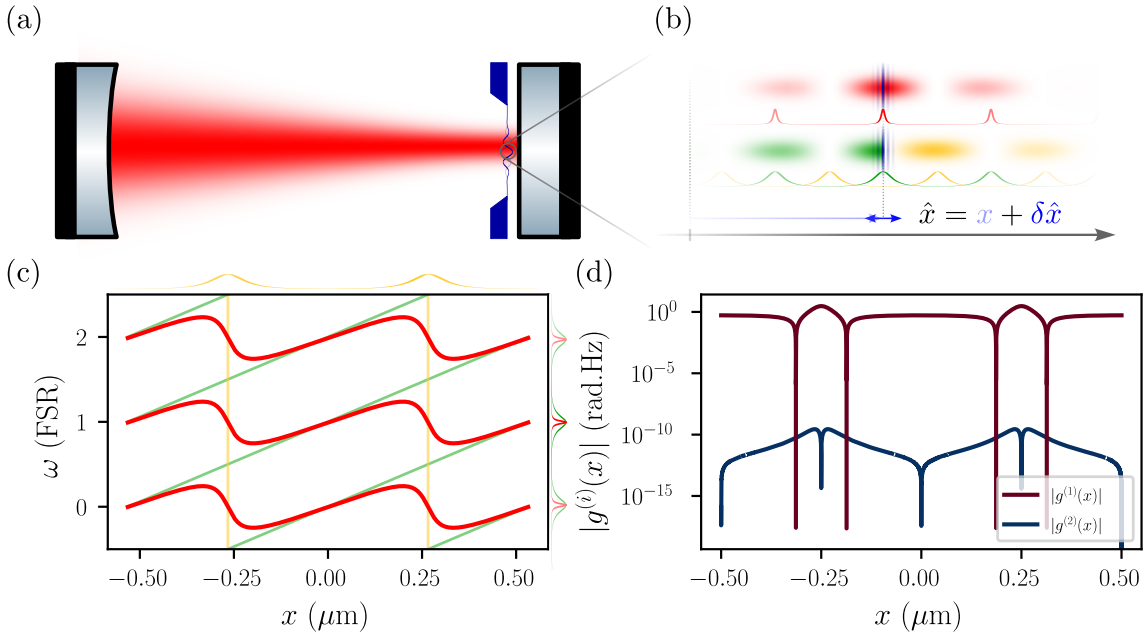


Fig. II.3  $rrlist = 0.7, L = 3e-2,$

### Cavity transmission and reflection

From the system in (II.26), and having derived just above the resonant cavity wavevectors  $k$ , we can compute the power ratio of the two sub-cavity fields as a function of  $x$  when the MATE system is on resonance. This is

$$\frac{|\bar{\alpha}_R|^2}{|\bar{\alpha}'_L|^2} = \frac{P_R}{P_L} = \frac{1 + 2|r_m| \cos(2kL_1 + 2kx) + |r_m|^2}{1 - |r_m|^2}. \quad (\text{II.31})$$

with  $P_{L,R} \propto |\bar{\alpha}_{L,R}|^2$ . It then follows that the the power fraction leaking from the left and right mirrors, i.e. the resonant reflection and transmission coefficients  $R(\Delta = 0, x)$  and  $T(\Delta = 0, x)$  are given by

$$\begin{aligned} R(\Delta = 0, x) &= \frac{|t_1|^2 P_L}{|t_1|^2 P_L + |t_2|^2 P_R} \\ &= \frac{|t_1|^2 (1 - |r_m|^2)}{|t_1|^2 (1 - |r_m|^2) + |t_2|^2 (1 + |r_m|^2 + 2|r_m| \cos 2kx)} \\ T(\Delta = 0, x) &= \frac{|t_2|^2 P_R}{|t_1|^2 P_L + |t_2|^2 P_R} \\ &= \frac{|t_2|^2 (1 + |r_m|^2 + 2|r_m| \cos 2kx)}{|t_1|^2 (1 - |r_m|^2) + |t_2|^2 (1 + |r_m|^2 + 2|r_m| \cos 2kx)} \end{aligned} \quad (\text{II.32})$$

and we get the expected relation  $R(\Delta = 0, x) + T(\Delta = 0, x) = 1$ .

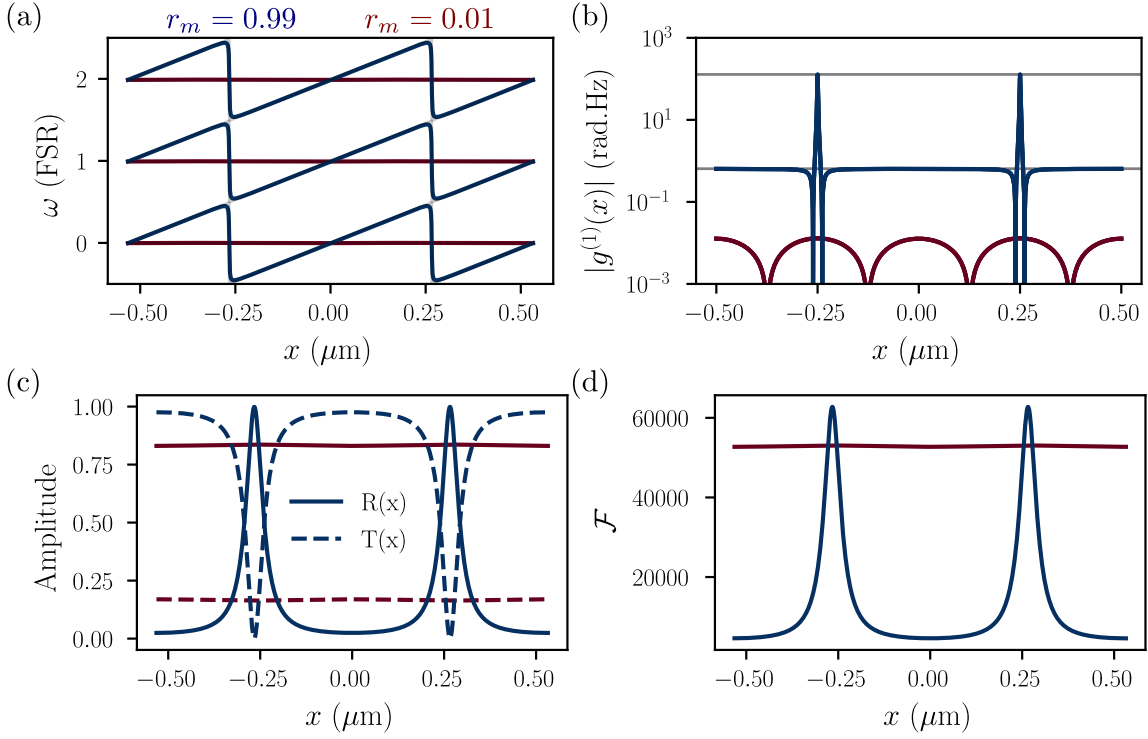


Fig. II.4  $rrlist = [0, 0.1, 0.9]$ ,  $T1 = 100\text{ppm}$ ,  $T2=20\text{ppm}$ ,  $L = 2e-2$ ,

### Cavity Linewidth and Finesse

Here, and similarly as in the next section detailing the quantum description of the MATE system, we can derive the cavity linewidth and finesse considering two different approaches. The first one, best for high membrane reflectivities, consists in considering two coupled sub-cavities, each with their own low linewidth/ high finesse, coupled by photon transmission through the membrane. The second one, appropriate for MATE geometries and low membrane reflectivities, consists in considering the whole cavity as a single optical mode, where the back short cavity act as an effective mirror with position dependent reflectivity. We will derive both and compare them.

To derive the position dependent cavity linewidth  $\kappa(x)$  and finesse  $\mathcal{F}(x)$  in the two cavity approach, we once again resort to the Sankey et al. method [6]. The total energy stored in the cavity is given by

$$E = \frac{2(L_1 + x)}{c} P_L + \frac{2(L_2 - x)}{c} P_R \quad (\text{II.33})$$

and the rate at which energy leaves the cavity

$$\partial_t E = -|t_1|^2 P_L - |t_2|^2 P_R = -\kappa(x) E. \quad (\text{II.34})$$

such that the cavity energy decay rate is given by

$$\begin{aligned}\kappa(x) &= -\frac{\partial_t E}{E} = \frac{c(|t_1|^2 + |t_2|^2 P_R/P_L)}{2(L_1+x) + 2(L_2-x)P_R/P_L} \\ &= \frac{c|t_1|^2(1-|r_m|^2) + c|t_2|^2(1+|r_m|^2 + 2|r_m|\cos 2kx)}{2(L_1+x)(1-|r_m|^2) + 2(L_2-x)(1+|r_m|^2 + 2|r_m|\cos 2kx)}.\end{aligned}\quad (\text{II.35})$$

We can then derive the cavity finesse as

$$\mathcal{F}(x) = \frac{\pi c}{L\kappa(x)}. \quad (\text{II.36})$$

add comparison with effective mirror approach

In the single cavity, effective mirror approach, the membrane acts as a position dependent mirror modifying the cavity resonance frequency as derived above. The back cavity then acts as an effective mirror with complex reflection coefficient given by

$$r_{\text{eff}}(x) = r_m + \frac{t_m^2 r_2 e^{2ik(L_2-x)}}{1 - r_m r_2 e^{2ik(L_2-x)}} \quad (\text{II.37})$$

such that the resulting cavity finesse is given by

$$\mathcal{F}(x) \sim \frac{2\pi}{|t_1|^2 + (1 - |r_{\text{eff}}(x)|^2)} \quad (\text{II.38})$$

and the associated linewidth  $\kappa(x) = \pi c / L\mathcal{F}(x)$ .

### II.2.2 Quantum Description

We now turn to the quantum description of the membrane based optomechanical system. A question that naturally arises is how to describe best this three mirror cavity quantum mechanically: should we consider two independent optical modes in each subcavity, coupled by photon tunneling through the membrane? Or should we consider the whole cavity as a single optical mode, whose resonance frequency is modified by the membrane position (and given above)?

#### Two Cavity Mode Model

We start by looking at the two cavity model. Using the same tools as in section II.2, we can derive the QLE of a membrane based optomechanical system. The membrane position now turns into an operator such that  $\hat{x} \propto \hat{c} + \hat{c}^\dagger$  with  $\hat{c}$  the mechanical annihilation operator as in the previous section. As seen above, the membrane position modifies the resonance

frequencies of the two subcavities, such that they both depend on the membrane position as  $\omega_L(x)$  and  $\omega_R(x)$  but with inverse trend: when one cavity shortens and its FSR increases, the other lengthens and its FSR decreases. To first order, we can linearize the resonance frequencies as

$$\omega_L(\hat{x}) \simeq \omega_L + G_L \hat{x}, \quad \omega_R(\hat{x}) \simeq \omega_R + G_R \hat{x}, \quad (\text{II.39})$$

with  $\omega_{L,R}$  the unperturbed resonance frequencies of the subcavities and  $G_L = \omega_L/L_1$  and  $G_R = -\omega_R/L_2$  their respective optomechanical couplings. The whole system features a network of optical modes varying linearly with the membrane position, coupled by the membrane transmission.

In Vincent Dumont's PhD work, quadratic points (where  $G^{(1)} = 0$  and  $G^{(2)} \neq 0$ ) were the centerfold of the study, in the high membrane reflectivity regime [**dumont\_cavity\_2017**]. It was then sufficient to consider two optical modes coupled by photon tunneling through the membrane.

However, in our case, we focus on the sole dispersive coupling regime in the MATE configuration, and we additionally consider a low membrane reflectivity. The optimal point to do so is when the first long cavity is on resonance, and when the short one is anti-resonant. With a lowered reflectivity, the coupling between subcavity modes increases, leading to larger mode splittings at the avoided crossings, until the two subcavities are fully hybridized into new cavity modes spanning both subcavities [**thompson\_strong\_2008**, **thompson\_coupling\_2013**].

The short cavity being precisely at an anti-node, it is equally probable for the tunneled photons from the long cavity to populate two short cavity modes on either side of the anti-node. We then need to describe the system by a single long cavity mode coupled to two short cavity modes, as illustrated in figure II.5. We introduce the annihilation operators  $\hat{a}_L$  for the long cavity mode, and  $\hat{a}_{R+}$  and  $\hat{a}_{R-}$  for the two short cavity modes on either side of the anti-node. The Hamiltonian of this system can then be written as

$$\begin{aligned} \hat{H} &= \hbar(\omega_L + G_L x) \hat{a}_L^\dagger \hat{a}_L + \hbar(\omega_{R-} - G_R x) \hat{a}_{R-}^\dagger \hat{a}_{R-} + \hbar(\omega_{R+} - G_R x) \hat{a}_{R+}^\dagger \hat{a}_{R+} & (= \hat{H}_\gamma) \\ &+ \hbar\Omega_m \hat{c}^\dagger \hat{c} & (= \hat{H}_m) \\ &+ \hbar G_L \hat{a}_L^\dagger \hat{a}_L \delta\hat{x} - \hbar G_R (\hat{a}_{R+}^\dagger \hat{a}_{R+} + \hat{a}_{R-}^\dagger \hat{a}_{R-}) \delta\hat{x} & (= \hat{H}_{\text{OM}}) \\ &- \hbar J [\hat{a}_L^\dagger (\hat{a}_{R+} + \hat{a}_{R-}) + (\hat{a}_{R+}^\dagger + \hat{a}_{R-}^\dagger) \hat{a}_L] & (= \hat{H}_{\text{tun}}) \end{aligned}$$

where  $J = c|t_m|/2\sqrt{L_1 L_2}$  is the photon tunneling rate through the membrane [**thompson\_strong\_2008**],

and where we linearized the position as before as  $\hat{x} = x + \delta\hat{x}$ . The first line describes the free evolution of the subcavity modes, the second one the mechanical resonator, the third the optomechanical interaction between the membrane position and the subcavity modes, and the last the photon tunneling through the membrane. As before, the commutation relations are given by

$$[\hat{a}_L, \hat{a}_L^\dagger] = [\hat{a}_{R\pm}, \hat{a}_{R\pm}^\dagger] = [\hat{c}, \hat{c}^\dagger] = 1 \quad \text{and} \quad [\hat{a}_L, \hat{a}_{R\pm}] = [\hat{a}_L, \hat{a}_{R\pm}^\dagger] = 0$$

We will only consider the photonic part of the Hamiltonian, as to put it in matrix form such that we can diagonalize it and work in the basis of the new eigenmodes. Furthermore, we go the frame rotating at frequency  $\omega_0 = \omega_{R-} = \omega_L$  i.e. when the long cavity mode is degenerate with the left short cavity mode, such that the photonic Hamiltonian becomes

$$\hat{H}_\gamma = \hbar G_L x \hat{a}_L^\dagger \hat{a}_L - \hbar G_R \left( x + \frac{\lambda}{4} \right) \hat{a}_{R-}^\dagger \hat{a}_{R-} + \hbar \left( \omega_{FSR} - G_R \left( x - \frac{\lambda}{4} \right) \right) \hat{a}_{R+}^\dagger \hat{a}_{R+} \quad (\text{II.40})$$

and we can rewrite both the photonic and tunneling hamiltonian i.e. the photonic manifold in matrix form as

$$\hat{H}_\gamma + \hat{H}_{\text{tun}} = \hbar \begin{pmatrix} \hat{a}_L^\dagger & \hat{a}_{R-}^\dagger & \hat{a}_{R+}^\dagger \end{pmatrix} \mathbf{M} \begin{pmatrix} \hat{a}_L \\ \hat{a}_{R-} \\ \hat{a}_{R+} \end{pmatrix} \quad (\text{II.41})$$

with

$$\mathbf{M} = \begin{pmatrix} G_L x & -J & -J \\ -J & -G_R(x + \lambda/4) & 0 \\ -J & 0 & \omega_{FSR} - G_R(x - \lambda/4) \end{pmatrix}.$$

One could then diagonalize this  $3 \times 3$  matrix to get the new eigenmodes of the system, and rewrite the optomechanical interaction in this new basis. In the limit where the membrane transmittivity is high such that  $|t_m| \sim 1$  and  $|r_m| \ll 1$ , the tunneling rate  $J$  becomes much larger than both optomechanical couplings  $G_{L,R}x$  and the free spectral range  $\omega_{FSR}$ . The cumbersome expression of the eigenmodes is not displayed here, but is equivalent to considering an system's eigenstate described by a annihilation operator  $\hat{a}$  with optomechanical coupling  $G^{(1)}(x)$  and decay rate  $\kappa(x)$  as derived in the previous section. The system's Hamiltonian can then be written as

$$\hat{H} = \hbar \omega_c(x = \lambda/4) \hat{a}^\dagger \hat{a} + \hbar \Omega_m \hat{c}^\dagger \hat{c} + \hbar G^{(1)}(x) \hat{a}^\dagger \hat{a} \hat{x} \quad (\text{II.42})$$

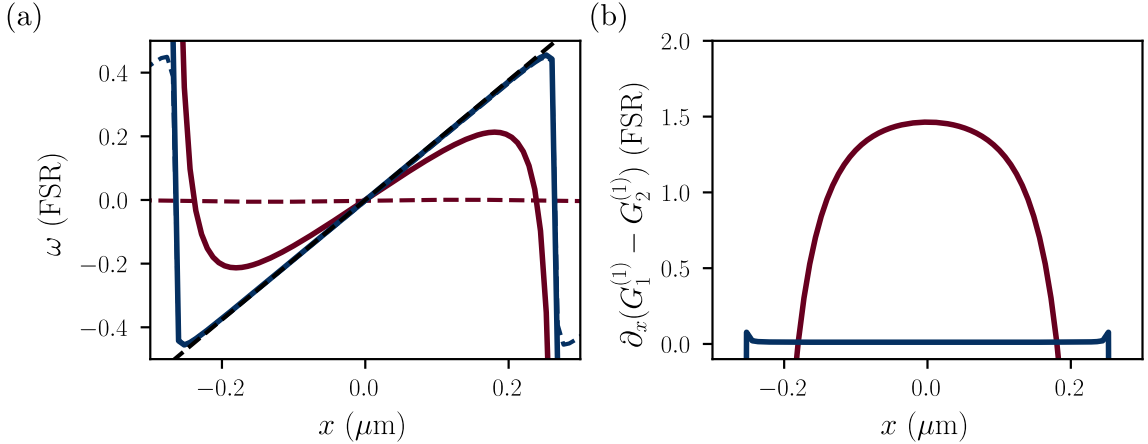


Fig. II.5 0.01, 0.99

### Single Mode Model

If the membrane is more transmissive than reflective, one could ask if the system could be described by a single optical mode, whose resonance frequency is weakly perturbed by the membrane position as derived in the previous section. In this case, the Hamiltonian of the system reads

$$\hat{H} = \hbar\omega_c(x)\hat{a}^\dagger\hat{a} + \hbar\Omega_m\hat{c}^\dagger\hat{c} \quad (\text{II.43})$$

where  $\omega_c(x)$  is given by the expression derived above. This description is then matching the two mode model in the limit of highly reflective membranes as seen in figure ??, as well as in the limit of low reflectivity membranes where the subcavities are fully hybridized.

### Comparison to Single Mode Model

Since we are interested in the dispersive coupling regime in the MATE configuration with a low reflectivity membrane, such that we will operate the system where the linear dispersive coupling is dominant over quadratic dispersive coupling and dissipative coupling, we need to compare which model is best suited to describe the system.

Obviously the two mode model breaks down in the limit of low reflectivity membranes where the subcavities are fully hybridized, and the single mode model is then more appropriate. In the opposite limit of highly reflective membranes, both models converge to the same description as seen above. Regarding the radiation pressure force acting on the membrane, in the two mode model, the radiation pressure force is given by the sum of the forces exerted by each subcavity mode as  $\hat{F}_{rp} = -\hbar G_L \hat{a}_L^\dagger \hat{a}_L + \hbar G_R (\hat{a}_{R+}^\dagger \hat{a}_{R+} + \hat{a}_{R-}^\dagger \hat{a}_{R-})$ . In the single mode model, the radiation pressure force is given by  $\hat{F}_{rp} = -\hbar \partial \omega_c(x) / \partial x \hat{a}^\dagger \hat{a}$ . In the limit

of highly reflective membranes, the two mode model radiation pressure force is then more appropriate since the optical mode is split in two subcavity modes, each exerting a force on the membrane. In the opposite limit of low reflectivity membranes where the subcavities are fully hybridized and where we focus on the dispersive coupling regime, it would genuinely be of no interest when studying radiation pressure effects, and a relevant description of the radiation pressure force is tricky to derive (because there are actually photons in both subcavities, but the model breaks down). In our middle ground case of moderately reflective membranes, we will assume the optical mode is mostly localized in the long cavity mode such that the single mode description is valid, and that the radiation pressure force is given by the derivative of the cavity resonance frequency with respect to the membrane position as seen in the textbook case of a single mirror cavity. The same QLEs as in the previous chapter can then be derived and used in our case.



## Chapter III

# Experimental Methods

This chapter essentially covers feedback control techniques used in Chapter IV and V. It is thought as a practical guide to the implementation of various locking schemes using the LKB *home grown* control software PyRPL. The chapter begins with a general introduction to feedback control, PI controllers and error signal requirements. It then details specific locking techniques used in this work, with an emphasis on experimental aspects. For in depth technical description of the PyRPL working principle, we refer the reader to Chapter III or Leonard Neuhaus thesis [[Neuhauser\\_Thesis\\_2021](#)], as well as the PyRPL documentation [[PyRPL\\_Docs](#)] and original article [[PyRPL\\_Article](#)]. Some figures are adapted from this last reference (with authorization)

## Contents

---

<b>III.1 Feedback control . . . . .</b>	<b>76</b>
III.1.1 Overview . . . . .	76
III.1.2 Proportion-Integral (PI) Controllers . . . . .	77
III.1.3 PyRPL overview . . . . .	79
III.1.4 IQ modules . . . . .	81
<b>III.2 Locking techniques . . . . .</b>	<b>83</b>
III.2.1 Temperature Lock . . . . .	84
III.2.2 Optical phase Lock . . . . .	84
III.2.3 Cavity Locks . . . . .	85
III.2.4 Offset Frequency Locks and Phase Lock Loop . . . . .	88

---

### III.1 Feedback control

A central aspect of experimental quantum optics is the ability to stabilize various parameters of an optical setup against environmental fluctuations. These parameters include cavity lengths, laser frequencies, optical phases, and temperatures of nonlinear crystals, which all undergo unwanted drifts and noise due to thermal, acoustic, and mechanical perturbations. To achieve this stabilization, feedback control systems are employed, which rely on generating an error signal that quantifies the deviation from a desired setpoint. This error signal is then processed by a controller to compute a corrective feedback signal that drives an actuator to counteract the disturbance and maintain the parameter at its target value.

#### III.1.1 Overview

A feedback control loop then aims to stabilize the behaviour of a physical system that is continuously subject to disturbances. When the system may be linearized around its operating point, its response to a harmonic perturbation at angular frequency  $\omega_0$  is fully characterized by its complex transfer function  $G(\omega)$ . We denote by  $V_{\text{exc}}(t)$  the real excitation applied to the system, taken to be sinusoidal,

$$V_{\text{exc}}(t) = A_{\text{exc}} \cos(\omega_0 t), \quad (\text{III.1})$$

with amplitude  $A_{\text{exc}}$ . In the frequency domain the system is described by its complex transfer function

$$G(\omega) = |G(\omega)| e^{i\phi(\omega)}, \quad (\text{III.2})$$

which specifies the amplitude response  $|G(\omega)|$  and the phase shift  $\phi(\omega)$  experienced by a sinusoid at frequency  $\omega$ . The relation between input and output is expressed most naturally in complex notation. Writing the excitation as the real part of a complex exponential,

$$V_{\text{exc}}(t) = \text{Re}\left\{ A_{\text{exc}} e^{i\omega_0 t} \right\} \implies V_{\text{meas}}(t) = \text{Re}\left\{ G(\omega_0) A_{\text{exc}} e^{i\omega_0 t} \right\}$$

so that explicitly

$$V_{\text{meas}}(t) = |G(\omega_0)| A_{\text{exc}} \cos(\omega_0 t + \phi(\omega_0)). \quad (\text{III.3})$$

Thus the physical output remains real, while the complex transfer function  $G(\omega_0)$  determines how the amplitude and phase of the input harmonic are modified.

### In-phase and quadrature decomposition.

It is convenient to decompose the transfer function into its in-phase (I) and quadrature (Q) components such that Eq. (III.3) can be written as

$$V_{\text{meas}}(t) = I(\omega_0) \cos(\omega_0 t) + Q(\omega_0) \sin(\omega_0 t), \quad (\text{III.4})$$

which forms the basis of IQ demodulation. By multiplying  $V_{\text{meas}}(t)$  by  $\cos(\omega_0 t)$  and  $\sin(\omega_0 t)$  and low-pass filtering the results with a filter  $H_f(\omega)$  with a cutoff frequency  $\omega_f \ll \omega_0$ , one obtains the slowly varying quadratures  $I(t)$  and  $Q(t)$ , from which the complex baseband signal

$$s_{\text{meas}}(t) = I(\omega_0) + i Q(\omega_0) \quad (\text{III.5})$$

is constructed.

Obviously, realistic excitation signals are never pure sinusoids, such that they can be decomposed into a superposition of harmonic components

$$V_{\text{exc}}(t) = \text{Re} \left\{ \int_0^\infty \frac{d\omega}{2\pi} A_{\text{exc}}(\omega) e^{i\omega t} \right\}.$$

where  $A_{\text{exc}}(\omega)$  is the complex amplitude of the component at angular frequency  $\omega$ . Demodulating the measured signal at a frequency  $\omega_0$  and low pass filtering it yields a measured signal given by

$$\begin{aligned} s_{\text{meas}}(t) &= \int_0^\infty \frac{d\omega}{2\pi} G(\omega - \omega_0) H_f(\omega) A_{\text{exc}}(\omega - \omega_0) e^{i\omega t} \\ &= I(t) + i Q(t) \end{aligned} \quad (\text{III.6})$$

such that the IQ demodulation produces time-dependent quadratures  $I(t)$  and  $Q(t)$ , whose complex combination  $s_{\text{meas}}(t)$  represents the slowly varying complex envelope.

In a feedback loop, a relevant observable derived from  $s_{\text{meas}}(t)$  is fed into the controller and is denoted  $s_{\text{in}}(t)$ . Depending on the application,  $s_{\text{in}}(t)$  may correspond to one of the quadratures, the reconstructed phase, or any real-valued function of  $(I, Q)$ .

#### III.1.2 Proportion-Integral (PI) Controllers

Now that both quadratures are accessible through the IQ demodulation, and that we obtained a signal  $s_{\text{in}}(t)$  relevant for the control task at hand, we need to extract an error signal  $\varepsilon(t)$  that quantifies the deviation from a desired setpoint at which we wish to *lock* the system.

It is typically expressed as the difference between a measured signal and its reference value:

$$\varepsilon(t) = s_{\text{in}}(t) - s_{\text{ref}}, \quad (\text{III.7})$$

where  $s_{\text{in}}(t)$  is the physical quantity monitored in the experiment, and  $s_{\text{ref}}$  is the target value.

For effective feedback stabilization, this error signal must satisfy several essential criteria listed below.

**High SNR:** Near the setpoint,  $\varepsilon(t)$  should exhibit a high SNR to ensure robust locking and minimize the influence of technical and electronic noise.

**Linearity and antisymmetry:** The error signal should be linear and antisymmetric in a neighborhood of the operating point. Small deviations from the setpoint should produce a proportional response in  $\varepsilon(t)$ , with opposite signs for deviations of opposite direction.

**Monotonicity and uniqueness:** The slope  $\partial\varepsilon/\partial x$ , where  $x$  denotes the control parameter (e.g., cavity length or laser frequency), should be monotonic and unambiguous near the lock point to avoid multiple equilibrium points and ensure stable locking behavior.

**Steep slope near the setpoint:** A steeper slope improves sensitivity to small deviations and enhances lock accuracy, although it must be balanced against potential noise amplification.

**Bandwidth compatibility:** The spectral content of  $\varepsilon(t)$  must be compatible with the bandwidth of the actuator and the dynamics of the system. For example, in the case of a piezoelectric transducer, which acts as a low-pass mechanical element, the error signal high-frequency components won't be compensated by the actuator.

A standard way to achieve this stabilization is to use a Proportion-Integral (PI) controller. The PI controller computes the feedback signal  $u(t)$  from the error signal  $\varepsilon(t)$  according to:

$$s_{\text{out}}(t) = K_P \varepsilon(t) + K_I \int_0^t \varepsilon(\tau) d\tau \quad (\text{III.1})$$

where  $K_P$  and  $K_I$  are the proportional and integral gains, respectively. The proportional term  $K_P \varepsilon(t)$  responds to the current error and primarily acts on mid-frequency deviations, enabling rapid corrections. The integral term  $K_I \int \varepsilon(\tau) d\tau$  accumulates past errors and is most effective at low frequencies, helping to eliminate long-term drifts and steady-state off-

sets.

In classical control theory, PID (Proportional-Integral-Derivative) controllers are designed to stabilize dynamic systems by combining three terms: a proportional term for immediate response, an integral term to eliminate steady-state error, and a derivative term that anticipates future error based on the rate of change. However, in practical experimental setups—particularly in quantum optics—PI control (Proportional-Integral) is typically sufficient and even preferable to full PID control. The derivative term, which acts predominantly at high frequencies, is generally unnecessary and can be counterproductive. This is because the feedback actuator is often a piezoelectric transducer, which exhibits non-zero capacitance. Combined with the finite output impedance of the control electronics, this forms a natural low-pass filter that significantly attenuates high-frequency components of the feedback signal. As a result, any derivative term—which primarily targets high-frequency correction—would be both ineffective due to this filtering and potentially harmful by injecting high-frequency noise into the loop.

Therefore, PI control offers a balanced and robust approach: the integral term suppresses low-frequency drifts (typically below a few Hz to tens of Hz), the proportional term corrects intermediate-frequency deviations (up to a few kHz), and high-frequency components (above the mechanical resonance or actuation bandwidth) are naturally filtered out and deliberately left uncorrected. This allows for stable feedback while preserving high-frequency signals—such as thermal noise or mechanical sidebands—which carry essential physical information for analysis and measurement.

### III.1.3 PyRPL overview

With the rise of digital signal processing, many feedback control systems have transitioned from analog electronics to software-based implementations. One such powerful and flexible platform is PyRPL (Python Red Pitaya Lockbox), an open-source software suite designed for real-time digital signal processing and feedback control using the Red Pitaya (RP) hardware and developed in our team. PyRPL provides a user-friendly interface for implementing various control algorithms, including PI controllers, and is now widely used in experimental physics laboratories across the world [[PyRPL\\_Article](#), [PyRPL\\_Docs](#)]. While we refer the reader to Leonhard Neuhaus' thesis [[Neuhauser\\_Thesis\\_2021](#)] and the PyRPL documentation [[PyRPL\\_Docs](#)] for an in-depth technical description of the PyRPL working principle, we will concisely summarize the main performance metrics and high abstraction blocks relevant for this work.

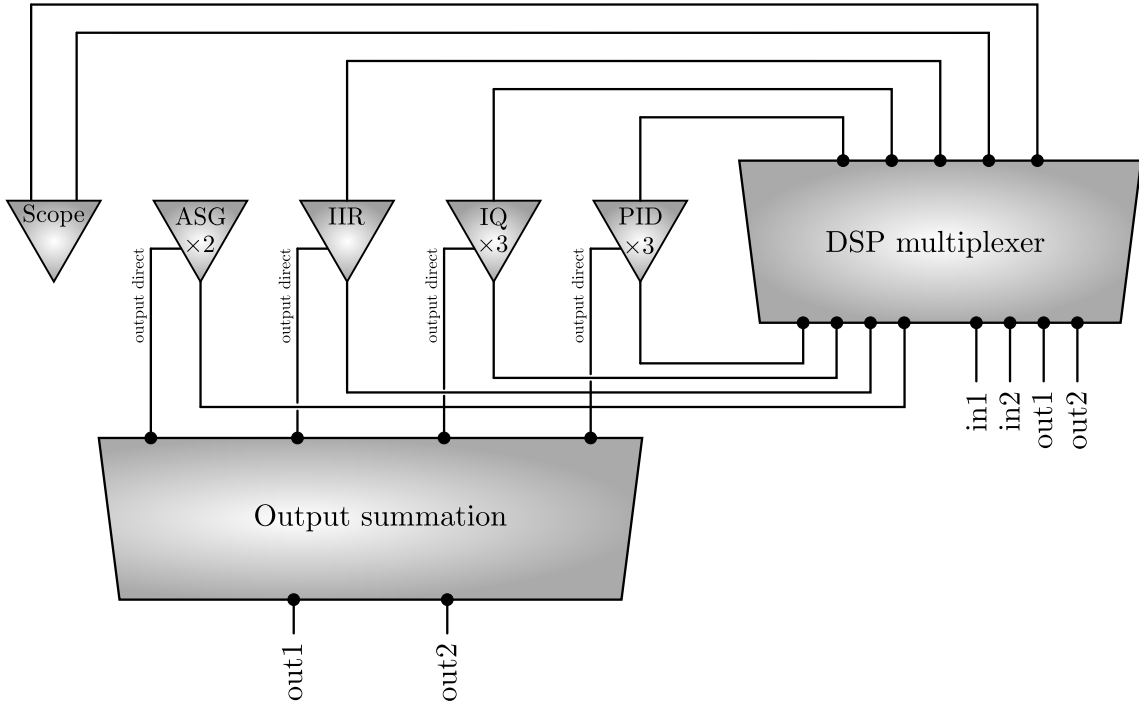


Fig. III.1 coucou

Red Pitaya is a compact FPGA-based platform that combines high-speed analog-to-digital (ADC) and digital-to-analog (DAC) converters with a powerful FPGA for real-time signal processing. The onboard ADCs and DACs operate at a 125 MHz sampling rate with 14-bit nominal resolution, which enables the digitization and synthesis of signals up to about 60 MHz according to the Nyquist criterion. In practice, the effective resolution is about 12 bits for the ADC and 11 bits for the DAC, which remains more than sufficient for precision photodetection, modulation, and error-signal processing in quantum optics. A notable limitation is the digitization noise floor, as well as the noise added from the voltage shifter, bounding the output to  $\pm 1V$ . Sensible improvement of the order of 5 dBm/Hz can be achieved in the 100 Hz - 1 MHz frequency range by unsoldering the voltage shifter circuit, as well as taking of the regulator from the board and powering the Red Pitaya with a low noise external voltage source. Taking the voltage offset off actually makes the output range 0-2V, ideal as to not feed (high voltage amplified) negative voltages to our piezoelectric actuators (which would kill them). This modification was performed on all RPs used in this work, bringing the noise floor down to 140dBm/Hz at 1MHz. In the frequency range relevant to experimental quantum optics (from a few kHz to a few hundred kHz), the RP noise floor is remarkably close—within 10–15 dB—to that of high-end laboratory lockboxes

and diagnostic instruments. Above 1 MHz, however, professional RF analyzers remain significantly quieter and cleaner. 10dB for a fraction of the cost is a fair trade off in our opinion.

PyRPL leverages this hardware to implement various digital signal processing tasks. The modules available in PyRPL are a scope, a spectrum analyser, 2 Arbitrary Signal Generators (ASG), 3 PID controllers, 3 IQ modules, an Infinite Impulse Response (IIR) filter module, and 4 pulse width modulation modules (pwm). These modules can be interconnected in a flexible manner to create complex feedback loops tailored to specific experimental needs, by simply rerouting the signal flow either in a programmatic way using the PyRPL Python API, or graphically through the PyRPL GUI. The signal flow architecture is illustrated in figure III.1, where one can see how the various modules can be interconnected. This makes PyRPL a very versatile and cheap tool for monitoring and piloting a wide range of experimental setups.

An additional experimental tricks to circumvent the number of output issues (2 DAC channels only) is to use the slow analog outputs of the RP, which need to be soldered manually to BNC/SMA outputs. These outputs send 4 0-1.8V signals synthesized from filtered pwm signals, have a sensibly noisier floor as well as a limited bandwidth (up to  $\sim$ 100kHz only), but are very useful for sending DC offsets as well as slow feedback signals. Additionally, we make extensive use of minicircuits bias tess to direct both slow and RF signals to the same output, as to be able to artificially double the number of output channels (2 RF + 2 DC).

### III.1.4 IQ modules

We now turn more specifically to the PyRPL IQ modules, which can be used for various purposes. Using the Python API or the GUI, one can select which input channel (in1 or in2) is fed to the IQ module. Similarly, one can chose to which output channel (out1 or out2) the processed signal is sent. In between, various registers allow the user to manipulate the input signal as desired. The latent available operations of the mpdule are illustrated in figure III.2. The input signal can first be high pass filtered to eventually remove DC offsets. It is then mixed with the  $\cos \omega_0 t$  and  $\sin \omega_0 t$  signals discussed above, with an additional phase shift  $\phi$  that can be set by the user. They are then lowpass filtered to yield the in-phase and quadrature components  $I(t)$  and  $Q(t)$ . Finally, these quadratures can be manipulated in various ways before being sent to the output channel, or sent to other modules such as the scope or the spectrum analyzer for diagnostic purposes.

**Filters:** setting the various registers as in fig III.3(a), one can choose to lowpass, highpass

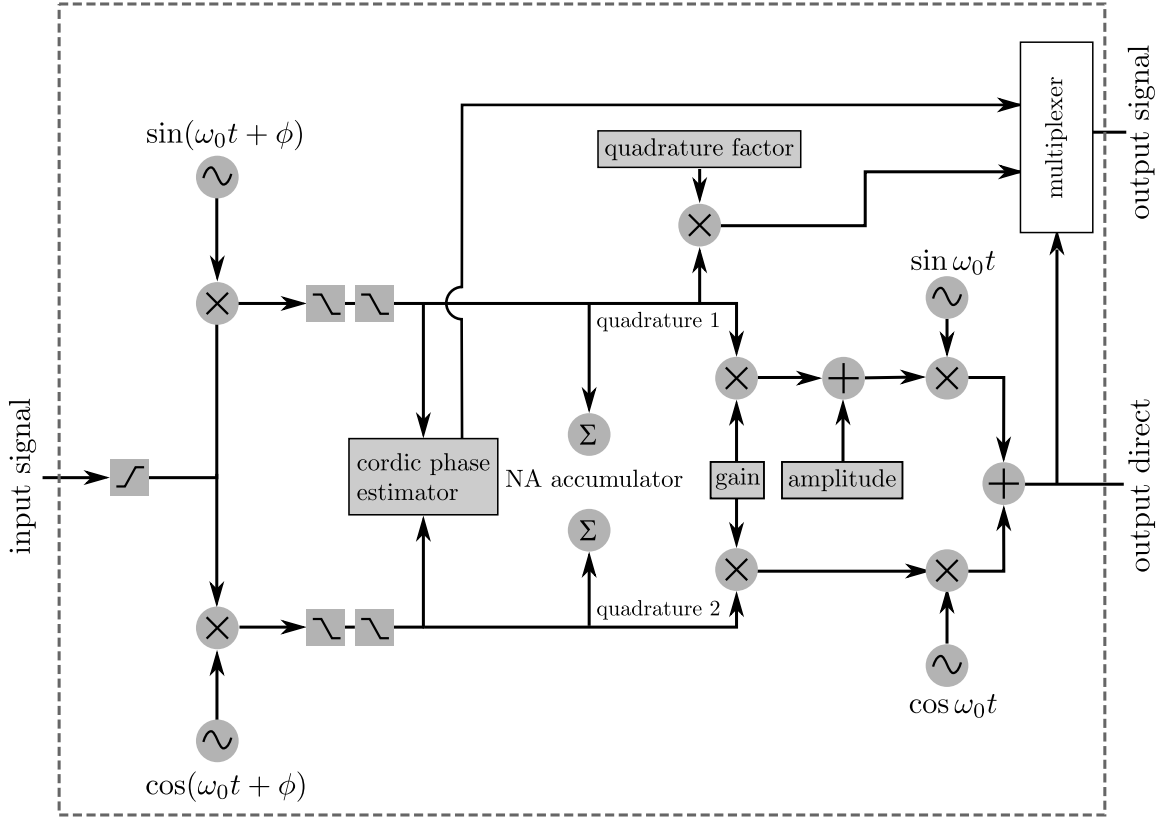


Fig. III.2 Basic working principle of the IQ module in PyRPL. One can set any register value using either the GUI or the Python API to manipulate the input signal as desired.

or bandpass an input signal by choosing the cutoff frequencies the filter orders.

**Network Analyzer:** by setting the registers as in fig III.3(b), one can use the IQ module as a network analyzer. The input signal is swept over a user-defined frequency range, and the in-phase and quadrature components are recorded at each frequency step. This allows to reconstruct the complex transfer function of a system connected to the input channel, which is very useful for characterizing the response of feedback loops.

**Phase Lock Loop:** by setting the registers as in fig III.3(c), one can use the IQ module as a phase lock loop (PLL). The phase of the input signal is continuously monitored through the IQ demodulation, and a feedback signal is generated. This error signal then needs to be routed to the PID modules to lock the phase to a desired reference value. This is particularly useful for stabilizing optical phases in interferometric setups, as well as implemental frequency offset locks and PLLs.

**Error Signals - Lock-in Detection:** by setting the registers as in fig III.3(d), one can use the IQ module to generate error signals for feedback control. The user can select which quadrature (I or Q) is sent to the output channel, as well as apply additional processing such as scaling, offsetting, or filtering. A modulation with known phase relationship to the demodulated signal can be sent off to an EOM, and AOM or a PZT to implement locks. This allows to tailor the error signal to the specific requirements of the feedback loop, ensuring optimal performance and stability.

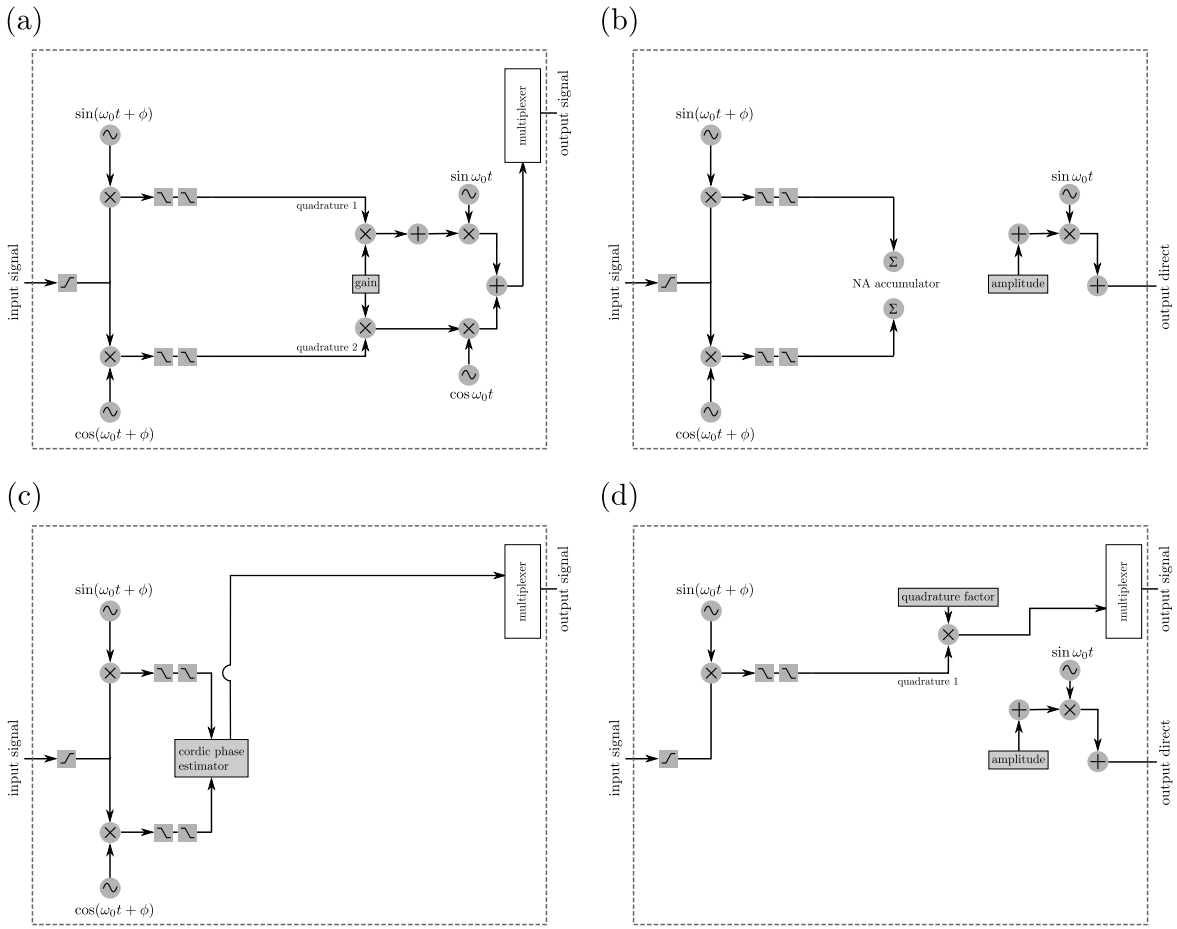


Fig. III.3 coucou

## III.2 Locking techniques

We now proceed to give a list of the various locks used in this work, along with their practical implementation as well as their error signal expression. The details of the derivations of the error signals are given in Appendix B.

### III.2.1 Temperature Lock

A first example of a PI lock used in this work is the temperature lock, which is used to stabilize the temperature of non linear crystals embedded inside optical cavities. The error signal is derived from a temperature sensor, such as a thermistor, which measures the temperature of the crystal and simply written as:

$$\varepsilon(\Delta T) \propto \Delta T \quad (\text{III.8})$$

where  $\Delta T = T_{\text{meas}} - T_{\text{set}}$ . The error signal is then fed into a PI controller, which adjusts the heating element, a peltier module in our case, to maintain the desired temperature setpoint. In the case of our SHG, temperature lock is actually performed using a commercial temperature controller provided along the PPLN crystal array provided by Covesion. Similarly, the OPO crystal temperature is stabilized using a Thorlabs temperature controller (TED???) connected to a thermistor and a peltier module, the RP just allowing us to module the lock point by feeding an offset voltage to the temperature controller.

A full PyRPL lock has however been implemented on the quantum thermometry experiment led by Tristan Briant, and the details of this implementation can be found in the thesis of Emile Ferreux. The RP wiring diagram is shown in figure III.4.

The temperature lock is crucial for maintaining the phase matching conditions in nonlinear optical processes (developped in the next section), such as second-harmonic generation or optical parametric oscillation, where the efficiency of frequency conversion depends sensitively on the crystal temperature. By stabilizing the temperature, we ensure that the nonlinear interactions remain optimal, leading to consistent and reproducible results in experiments involving squeezed light generation or other nonlinear optical phenomena.

### III.2.2 Optical phase Lock

Controlling the relative path length between two arms of an interferometer is a fundamental technique in quantum optics. The basic idea is to use the interference of light from two paths to lock the phase difference between them. Although not being the same experiential setups, Michelson interferometers, Mach-Zhender interferometers, and Local Oscillator stabilization error signals fall in the same category as they are derived from the same principle. Namely,

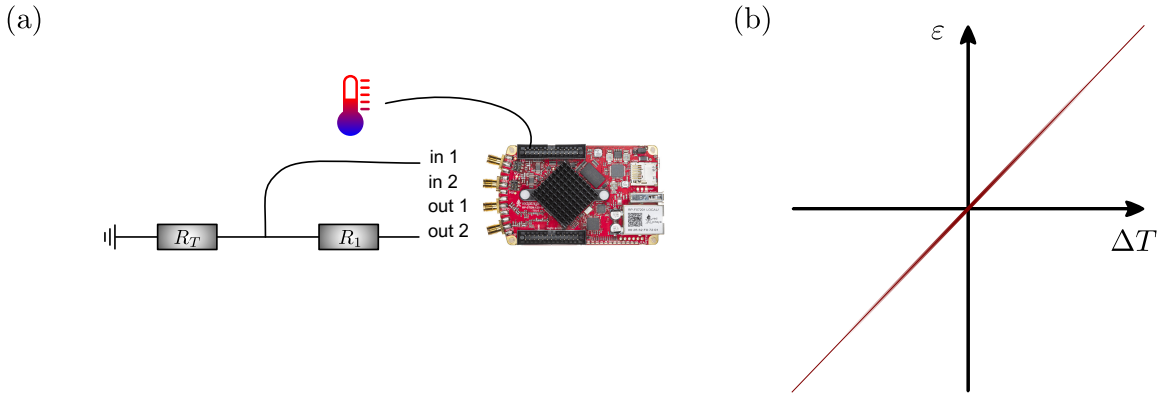


Fig. III.4 coucou

the error signal is proportional to the sine of the phase difference between the two arms:

$$\varepsilon(\Delta\phi) \propto \sin(\Delta\phi) \simeq \Delta\phi \quad (\text{III.9})$$

where  $\Delta\phi = \phi_a - \phi_b$  is the phase difference between the two optical paths. Analogically, we would need to add an adjustable voltage offset, as to be able to tune the error signal to zero at the desired phase difference, before seeding this error signal to the PI block. Digitally, this is performed by adding a constant offset to the error signal, which can be adjusted to set the desired phase difference.

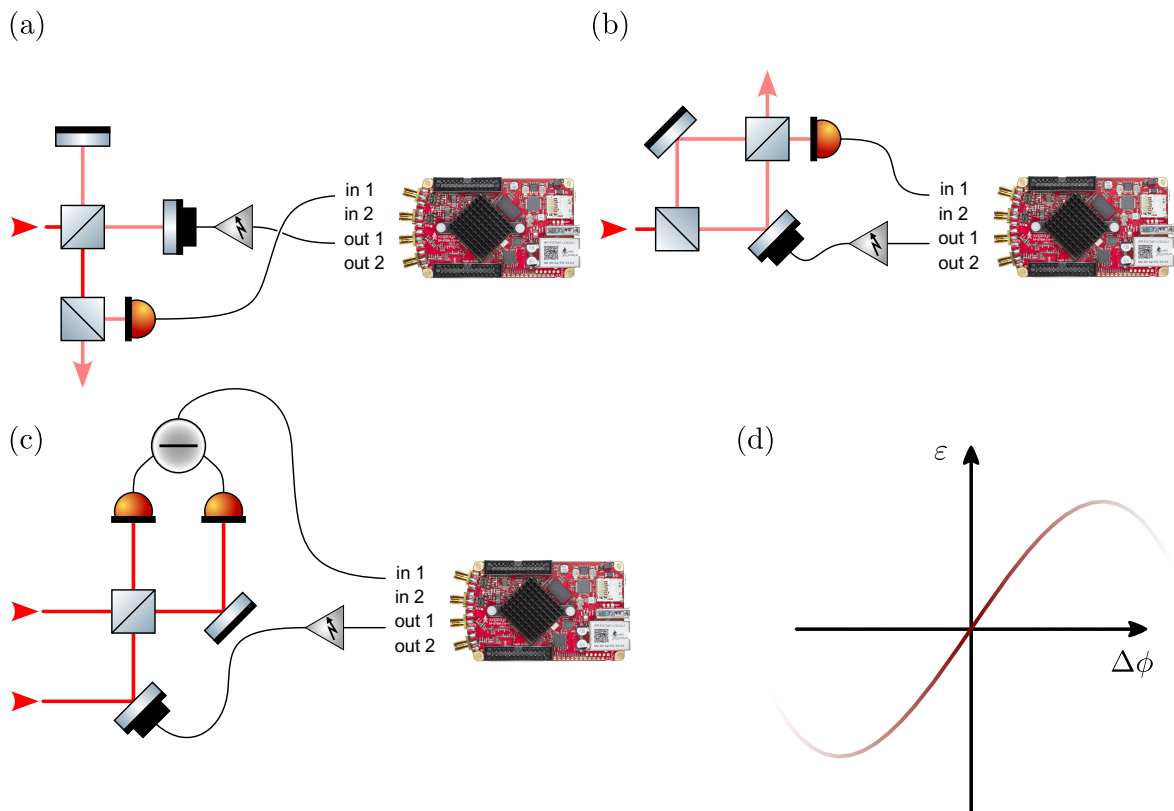
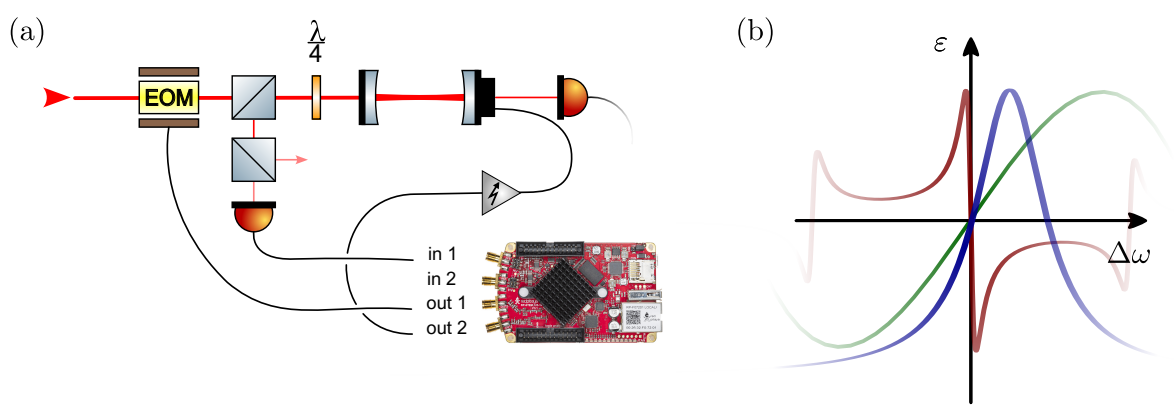
In practice, this is implemented by mounting a mirror on which one of the arms is reflected, and then using a piezoelectric transducer to control the position of the mirror, hence modulating the relative phase between the two optical paths. The piezo is then feedback controlled through a PI loop, which adjusts the voltage applied to the piezo to set the error signal to 0. The RP wiring diagram is shown in figure III.5.

### III.2.3 Cavity Locks

We now turn to the locking of optical cavities, and will develop 3 techniques used in this work: the side of fringe lock, the dither lock and the Pound-Drever-Hall (PDH) lock. The RP wiring and the typical error signal shapes are shown in figure III.6.

#### Side of Fringe

A lorentzian dip does not qualify as a valid error signal to lock the cavity on resonance, according to the requirements listed above, as it is symmetric around resonance. However,

Fig. III.5 *coucou*Fig. III.6 *coucou*

by locking the cavity on the side of the resonance fringe, one can obtain a usable error signal that is linear and antisymmetric in a small neighborhood around the lock point. This technique is known as the *side of fringe* lock. The error signal near resonance is then given by

$$\varepsilon(\Delta\omega) \propto (\Delta\omega - \Delta_{\text{lock}}) \quad (\text{III.10})$$

where the  $\Delta_{\text{lock}}$  is the detuning at which the cavity is locked. In PyRPL, calibrating the lorentzian dip in transmission or reflection allows to set the lock point in units of the cavity linewidth, which is very convenient. This would also allow to explore off resonant optomechanical effects, such as optical spring and damping.

The side of fringe lock is almost always used in this work as a preliminary step to bring the cavity close to resonance before engaging a more sophisticated lock such as PDH or dither lock. However, it is less robust and sensitive compared to other techniques, making it less suitable for long-term stabilization or high-precision applications.

### Dither lock

A first technique to lock an optical cavity on resonance is the dither lock. The basic idea is to impose a small sinusoidal modulation modulating the cavity resonant frequency, typically by applying a phase modulation using an EOM, or by modulating the cavity length using a piezoelectric actuator. Linking this to the IQ section above, we would modulate the cavity at frequency  $\omega_0 \lesssim \kappa$  with  $\kappa$  the cavity linewidth, and demodulate the reflected or transmitted signal at the same frequency using an IQ module. The error signal is then proportional to the in-phase or quadrature component of the demodulated signal, depending on the demodulation phase chosen. The error signal near resonance is then given by

$$\varepsilon(\Delta\omega) \propto \Delta\omega \quad (\text{III.11})$$

This technique is relatively simple to implement and can provide a robust lock, although it may introduce additional noise due to the imposed modulation. The modulation frequency and depth need to be carefully chosen to optimize the lock performance while minimizing the impact on the system's dynamics. This technique has the advantage of being implementable with the transmitted signal of the cavity (while PDH requires the reflected signal), since the modulation frequency is lower than the cavity linewidth (otherwise the sidebands would only be reflected).

### Pound-Drever-Hall Lock

The second method to lock an optical cavity on resonance is the Pound-Drever-Hall (PDH) technique [Black\_PDH\_2001], which can be used to lock a laser frequency to a stable optical cavity, or conversely to lock the cavity length to a stable laser frequency. The method relies on imposing phase modulation sidebands on the laser field outside the cavity bandwidth this time, typically using an electro-optic modulator (EOM), and using these sidebands as phase-stable references. Because they lie far outside the cavity linewidth ( $\Omega_{\text{mod}} \gg \kappa$ ), the sidebands are reflected nearly unchanged:  $r(\omega_\ell \pm \Omega_{\text{mod}}) \approx 1$ . In contrast, the carrier field near resonance acquires a frequency-dependent phase shift upon reflection, captured by the complex cavity reflection coefficient  $r_c(\delta)$ . The PDH error signal is obtained by detecting the reflected beam and demodulating the photocurrent at the modulation frequency, isolating the beat terms between carrier and sidebands. The resulting signal is proportional to the *imaginary part* of  $r_c(\delta)$ , which varies antisymmetrically with detuning and provides a zero-crossing error signal ideal for linear feedback. The error signal near resonance is then given by

$$\epsilon(\Delta\omega) \propto \Im(r_c(\Delta\omega)) \simeq \Delta\omega \quad (\text{III.12})$$

This imaginary component encodes the rapid phase dispersion near resonance that allows the system to discriminate the sign and magnitude of frequency deviations. In contrast, the real part of  $r_c(\delta)$ , being symmetric around resonance, does not yield a usable error signal. The PDH lock is generally preferred to the dither lock due to its superior sensitivity, larger linear range, and reduced susceptibility to technical noise.

The *demodulation phase* plays a critical role in selecting the appropriate quadrature of the signal for feedback. Since the beat signal between the carrier and sidebands has both in-phase and quadrature components, choosing the correct demodulation phase ensures that the extracted error signal aligns with the imaginary part of the reflection coefficient. A misaligned demodulation phase can lead to mixing of the symmetric (real) part into the error signal, thereby reducing sensitivity and introducing offset or distortion near the lock point. In practice, the demodulation phase is optimized empirically—either via a variable phase shifter in the electronic demodulation path or by adjusting the physical delay in the reference oscillator—to maximize the slope of the error signal at zero-crossing, corresponding to pure detection of the dispersive component.

#### III.2.4 Offset Frequency Locks and Phase Lock Loop

Finally, we discuss the implementation of frequency offset locks and phase lock loops (PLL) using the IQ modules in PyRPL. These techniques are essential for stabilizing the frequency offset and the relative phase of the beatnote between two lasers. The RP wiring diagram is

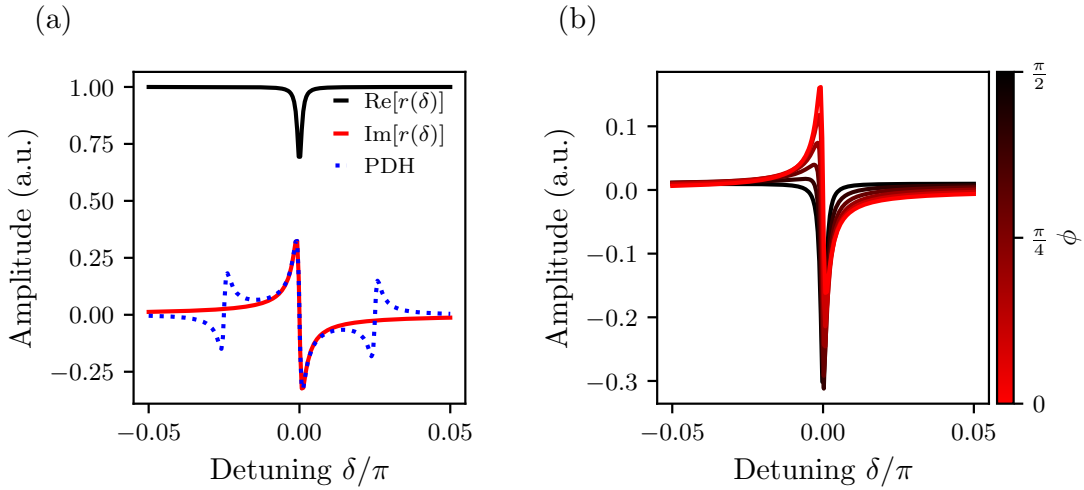


Fig. III.7 Schematic of the Pound-Drever-Hall (PDH) locking technique. The laser passes through an electro-optic modulator (EOM) generating phase modulation sidebands. The modulated beam is incident on the optical cavity, and the reflected light is detected by a photodiode (PD). The photocurrent is demodulated at the modulation frequency to produce the PDH error signal, which is fed to a PI controller driving the cavity actuator (e.g., piezo). Key components are labeled: EOM (electro-optic modulator), PD (photodiode), LO (local oscillator for demodulation), and PI (proportional-integral controller).

shown in figure III.8.

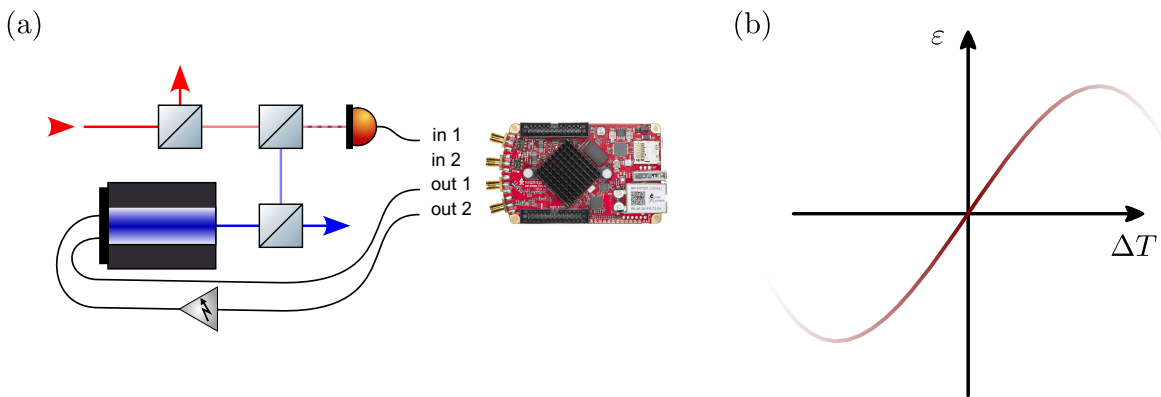


Fig. III.8 coucou

The basic principle is to detect the beatnote between two lasers on a fast photodiode, and to demodulate this signal using an IQ module at a frequency close to the desired offset frequency. The error signal is then derived from one of the quadratures of the demodulated

signal. The error signal near the lock point is then given by

$$\varepsilon(\Delta\omega_{\text{beat}}) \propto \Delta\omega_{\text{beat}} \quad (\text{III.13})$$

where  $\Delta\omega_{\text{beat}} = \omega_{\text{beat}} - \omega_{\text{ref}}$  is the deviation of the beatnote frequency from the reference frequency. This error signal is then fed into a PI controller, which adjusts the frequency of one of the lasers (typically via a piezoelectric actuator or current modulation) to maintain the desired offset frequency.

As explained before, a high voltage piezoelectric actuator has a limited bandwidth, typically up to a few kHz, due to the naturally occurring lowpass filtering effect of the piezo capacitance and the output impedance of the driving electronics. To overcome this limitation, we resort to the so called floating ground technique, which consists in locking both the piezo actuator through a standard PI loop, as well as locking the piezo ground to a higher frequency without amplifying it (or using an Operational Amplifier with high bandwidth i.e. OP27? 37?). This technique effectively extends the bandwidth of the piezo actuator up to a few tens of kHz, allowing for more robust and stable locks. Additionally, the laser current or temperature (the case here), is also locked to ensure the piezo remains in its mid-range of operation. Although not detailed in figure III.8, the temperature can be locked using the PyRPL PWM module, such that the modulated pwm signal (duty cycle) is sent to the laser temperature controller. The heating element of the laser will then naturally lowpass filter the pwm signal, providing a smooth and stable temperature control. This dual feedback approach enhances the overall stability and performance of the frequency offset lock and PLL.

## Chapter IV

# Experiments: Optomechanics

This chapter will cover the experimental methods used in the development of optomechanical three-mirror cavity systems, focusing on the design, fabrication, and characterization of mechanical resonators within optical cavities. The methods are designed to enhance the sensitivity of measurements in quantum optics and optomechanics.

### Contents

---

<b>IV.1 System Description and Setup . . . . .</b>	<b>92</b>
IV.1.1 Previous LKB work and Motivation . . . . .	92
IV.1.2 Specifications and Design . . . . .	93
IV.1.3 Flexure Actuation . . . . .	97
IV.1.4 Experimental Setup . . . . .	99
IV.1.5 Alignment Procedures . . . . .	101
<b>IV.2 Experimental Characterization . . . . .</b>	<b>102</b>
IV.2.1 Cavity Scans . . . . .	102
IV.2.2 Cavity Locking and Mechanical Characterization . . . . .	111
IV.2.3 Bistability . . . . .	115
<b>IV.3 Optomechanical Fibered Cavity . . . . .</b>	<b>116</b>
IV.3.1 Design considerations . . . . .	117
IV.3.2 Fiber mirror fabrication . . . . .	121
IV.3.3 Designs and optical layout . . . . .	123
<b>IV.4 Conclusion &amp; perspectives . . . . .</b>	<b>127</b>

---

Over the past two decades, optomechanical systems have greatly benefited from advancements in optical coating technologies, enabling the realization of high-finesse cavities ( $\mathcal{F} > 10^5$ )[coating\_review]. Simultaneously, progresses in micro/nanofabrication allowed the making of mechanical structures with high  $Q$  factors ( $> 10^6$ )[nanofab\_review]. Despite these achievements, a significant challenge remained: fabricating mechanical elements that possess both high  $Q$  and high reflectivity, as optical, mechanical and thermal effects often degrade system performance and hinder ultra-sensitive measurements[optomech\_challenges].

## IV.1 System Description and Setup

### IV.1.1 Previous LKB work and Motivation

Previous optomechanics experiments at LKB have primarily utilized Fabry–Pérot cavities with two mirrors, where the end mirror of the cavity was typically a HR mirror deposited on top of a mechanical structure featuring a mechanical mode of interest [<empty citation>].

Over Aurélien’s and Leonard’s PhD works, the group in collaboration with ONERA developed a platform based on a 1-mm-thick quartz micropillar with an effective mass of  $33 \mu\text{g}$ . The structure supports a fundamental compression mode oscillating at 3.6 MHz, with a mode shape as shown in Fig. ???. Using a dry-film photoresist technique, a  $100 \mu\text{m}$  diameter high-reflectivity mirror was deposited on one end of the pillar. Careful design of the suspension has yielded mechanical quality factors up to  $3 \times 10^6$  at room temperature and up to  $7 \times 10^7$  below 1 K. When integrated into a  $50 \mu\text{m}$ -long Fabry–Pérot cavity with a custom-fabricated coupling mirror, finesses exceeding  $10^5$  were achieved. Importantly, this compact cavity remains robust against vibrations of the dilution refrigerator and maintains alignment during cooldown, thereby providing a stable platform to study optomechanical effects in the intermediate mass regime. [limitations and why it didnt work](#)

Then over Rémi’s and Michael’s PhD, another resonator was developed in collaboration with Francesco Marin’s team, based on a suspended silicon disk. The device operates in a balanced mode, where the central disk vibrates in opposition to four surrounding counterweights. By adjusting the geometry, the resonance frequency was increased to 280 kHz, corresponding to an effective mass of about  $110 \mu\text{g}$ , bringing the system closer to the micropillar parameters. A HR mirror was then deposited on top using the same technique as the micropillar. Finesse of about  $\sim 50000$  were then reached. At cryogenic temperature, optimized designs reached mechanical quality factors on the order of  $1.2 \times 10^6$ .[limitations and why it didnt work](#)

Although the systems ended up being limited by various factors mentioned above (optical, mechanical and thermal effects) [<empty citation>], the parts designed over the years did feature a high level of passive stability as well as good thermalization properties. A pivotal solution, introduced by Regal, Kimble, Harris, and collaborators[Harris2008, 7], was to decouple these requirements by embedding a high- $Q$  mechanical resonator within a high-finesse optical cavity, using the optical field to probe and control the resonator's dynamics.

### IV.1.2 Specifications and Design

It was then decided to build on this design and extend it to a three-mirror cavity in a MATE configuration to benefit from this large linear and tunable coupling range as detailed in the previous chapter. That is the work Michael and myself undertook during my M2 internship and the following years of my PhD. This new three mirror cavity then needed to fulfill various requirements detailed in what follows.

#### High Finesse

Low loss mirrors were produced by **Jérôme DEGALLAIX** and **David HOFMAN** at the *Laboratoire des Matériaux Avancés* (LMA, Lyon) using ion-beam-sputtered (IBS) Bragg stacks made of  $\text{Ta}_2\text{O}_5$  (high index,  $n \approx 2.09$ ) and  $\text{SiO}_2$  (low index,  $n \approx 1.46$ )[AmatoPhD, LMA\_IBS]. The coatings were deposited in the LMA's *Veeco SPECTOR* chambers and subsequently annealed at  $500^\circ\text{C}$  for 10 hours to minimise both optical (absorption) and mechanical losses, following the recipe of Amato *et al.* [AmatoPhD]. <sup>1</sup>.

We supplied the LMA with a batch of substrates with various radii of curvature to explore different cavity geometries. The requested specifications are summarized in the table below. The total round-trip scatter and absorption losses are usually below 20 ppm, in agreement with the measurements reported (absoption  $\sim 0.7$ ppm, scattering  $\sim 10$ ppm)in Ref. [AmatoPhD].

Substrate type	Laseroptik ID	$R$	Front-side HR T	Back-side AR
Plane	S-00798	$\infty$ (plane)	$20 \pm 45$ ppm	$R \lesssim 100$ ppm
Plano-concave	S-00128	-25 mm	$100, 50 \pm 10$ ppm	$R \lesssim 100$ ppm
Plano-concave	S-00127	-15 mm	$100, 50 \pm 10$ ppm	$R \lesssim 100$ ppm
Plano-concave	S-00126	-10 mm	$100, 50 \pm 10$ ppm	$R \lesssim 100$ ppm

Table IV.1: Specifications of supplied Laseroptik substrates for different cavity geometries.

The quarter-wave design is centred at  $\lambda = 1064$  nm for normal incidence. After annealing, the measured mechanical loss angle of the  $\text{TiO}_2:\text{Ta}_2\text{O}_5/\text{SiO}_2$  stack is  $\phi < 4 \times 10^{-4}$  at 1 kHz

---

<sup>1</sup>Identical optics are used for the Advanced LIGO, Advanced Virgo and KAGRA interferometers[LIGO\_optics].

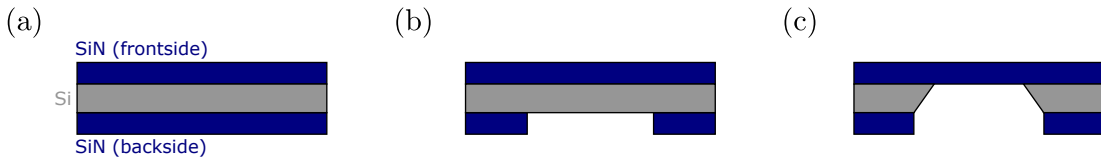


Fig. IV.1 *Fabrication steps of the SiN membrane resonator used in the MATE cavity. (a) starting from a silicon wafer coated with SiN on both sides. (b) lithography and RIE to open a square window in the top SiN layer. (c) KOH wet etching from the opened side until the cavity breaks through, leaving a free-standing SiN membrane. The membrane is then cleaned using HF to remove any residuals from the fabrication process.*

[link to mechanical damping needed](#), supporting cavity finesse in the range  $200\,000 - 500\,000$  before excess scatter or absorption dominates[**AmatoPhD**].

### High $Q$ factor

Two different square membranes were used in the MATE cavities, both made of high-stress silicon nitride ( $\text{Si}_3\text{N}_4$ ), a material known for its excellent mechanical properties, including high tensile stress and low intrinsic mechanical loss, making it ideal for optomechanical applications[**SiN\_review**], and of nominal side lengths  $l_n \times l_m = 500\,\mu\text{m} \times 500\,\mu\text{m}$ .

The first membrane was made in-house at LKB by **Thibaut Jacqmin** and **Himanshu Patange** during Himanshu's PhD work. The silicon wafer was  $350\,\mu\text{m}$  thick, and the SiN layers thicknesses was nominally 100 nm. Starting with the silicon wafer/chip coated with SiN on both sides, a photoresist is patterned by lithography to define a square window. Reactive-ion etching (RIE) then opens a square window through the top SiN layer. The exposed silicon is then wet-etched in KOH from the opened side until the cavity breaks through, leaving a released, free-standing SiN membrane spanning the opening. The membrane is then cleaned using HF to remove any residuals from the fabrication process. This very process etches the SiN layer as well, resulting in a final membrane thickness of less than 100nm. For detailed fabrication steps, refer to Himanshu's PhD thesis[**PatangePhD**]. We nonetheless succinctly display the fabrication steps in Fig IV.1.

The second membrane is a commercially Norcada® (NX10050AS)[**SiN\_review**, **Norcada\_datasheet**] SiN square membrane, specifically marketed as a *high Q* standard membrane for optomechanics applications. It features a Silicon frame of  $200\,\mu\text{m}$  thickness, and a SiN layer of nominal thickness 50 nm. Regarding the quality factor, literature reports:

- **Room temperature.** Measurements on nominally identical Norcada membranes report quality factors  $Q \sim 5 \times 10^6$  at  $\approx 1\,\text{MHz}$  in  $< 10^{-6}\,\text{mbar}$  vacuum [**SiN\_review**,

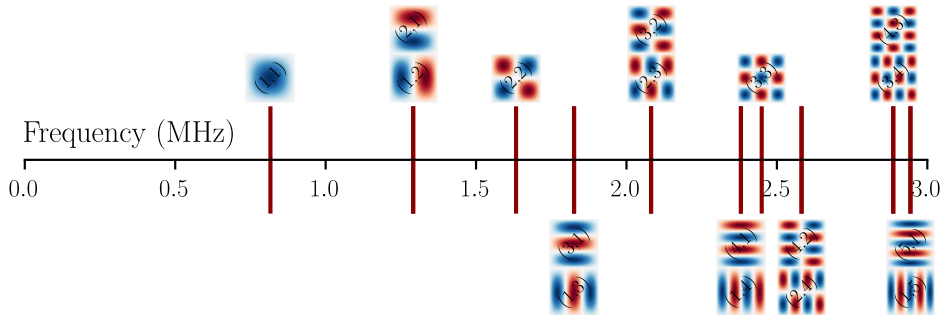


Fig. IV.2 Simulated mode shapes and frequencies of a square SiN membrane of side length  $500\mu\text{m}$  under high tensile stress ( $\sigma \sim 1\text{GPa}$ ).

[Norcada\\_datasheet](#)].

- **Cryogenic operation.** Cooling to  $T \lesssim 300\text{ mK}$  reduces internal friction by an order of magnitude, with  $Q > 10^7$  routinely observed [[SiN\\_cryogenic](#)].

The membrane's high stress, thin-film nature and dielectric composition make it fully compatible with ultra-high-vacuum environments and repeated cryogenic cycling, while introducing (a priori) negligible optical loss in the cavity. The expected mechanical mode structure can be derived from

$$f_{n,m} = \sqrt{\frac{\sigma}{4\rho} \left( \left(\frac{n}{l_n}\right)^2 + \left(\frac{m}{l_m}\right)^2 \right)} \quad (\text{IV.1})$$

with  $\rho \sim 3\text{ g/cm}^3$  the film mass density,  $\sigma \sim 1\text{ GPa}$ ,  $(n, m)$  the mode indices, and  $(l_n, l_m)$  the membrane side lengths. Considering a square membrane of identical side lengths of  $500\mu\text{m}$  yields a fundamental mode frequency at  $f_{1,1} \sim 816\text{ kHz}$ , with the two higher order modes  $(1, 2)$  and  $(2, 1)$  degenerate at  $f_{1,2} \sim f_{2,1} \sim 1.29\text{ MHz}$  etc.. We display the first few mode shapes and expected frequencies in Fig. IV.2.

### Optical alignment

The cavity is designed to be compatible with the Thorlabs® cage system. The input mirror is mounted on a 3 axis cage mount, allowing for easy alignment of the input mirror with respect to the cavity optical axis. Both the resonator and the back mirror are embedded within a custom-made holder, which is itself integrated into the cage system. The relative tilt between the resonator and the back mirror is adjusted using a set of 3 screws with a very fine thread, allowing for a fine alignment of the parallelism of the back cavity. The alignment procedure is detailed in section ??.

### Dynamical range

The input mirror is glued to a PI Ceramic® P-016.00H ring-stack piezoelectric actuator using vacuum epoxy (Torr Seal®). Driven from 0 to +1000 V it provides a longitudinal stroke of 5  $\mu\text{m}$ , a blocking force of 2.9 kN, as well as an unloaded resonance of 144 kHz, making it suitable for fast, low-noise cavity-length control.

The end-mirror–membrane assembly is mounted on a custom holder actuated by three PD080.31 piezo chips arranged mechanically in series. Each chip yields 2  $\mu\text{m}$  of travel over a drive range of -20 to +100 V; the triple stack therefore supplies roughly 6  $\mu\text{m}$  of coarse tuning while preserving high stiffness and sub-microsecond response. The effective range is lower than this owing to the fact the piezo is constrained within the holder. Furthermore, one should not constrain the piezo to much to avoid damaging it: it happened that the assembly was too tightly screwed in such that it ended up fracturing the piezo pushing against the back mirror holder. An easy workaround would be to add some elastic spacer between the piezo and the copper piece (like kapton tape for example).

Combining the 5  $\mu\text{m}$  stroke of the front P-016.00H with the 6  $\mu\text{m}$  range of the rear triple stack provides an overall cavity-length adjustment sufficient to scan few FSRs, as well as to tune the membrane position over a full wavelength, thus accessing allowing exploration of the three mirror cavity physics.

### Compactness & Stability

The entire assembly is built as a cage system using standard Thorlabs® cage parts, allowing for a compact and stable assembly. The cage system also allows for (relatively) easy alignment of the mirrors, as well as easy access to the piezo actuators.

### Vacuum and Cryogenic compatibility

The back cavity composed of the back mirror and the middle mirror is embedded inside an Oxygen Free Copper (OFHC) assembly with a circular geometry, eventually mitigating for transverse misalignment issues when going to cryogenic temperatures, the constraints compensating themselves radially with respect to the symmetry axis of the cavity assembly[[OFHC\\_review](#)]. Furthermore, the screws used to hold the assembly together are made of brass with a thermal expansion coefficient lower than that of the OFC, tightening up the cavity when reaching cryogenic temperatures. Thorlabs cage parts are compatible with moderate vacuum operation down to  $\sim 10^{-7}$  mbar if properly degreased and ultrasound cleant, but a custom cryocompatible system to hold the input mirror would be needed for

operation at cryogenic temperatures.

The initial design of the cavity was made using Autodesk Fusion 360, allowing for a detailed 3D model of the entire assembly, including the piezo actuators, the mirrors and the cage system. The design was then exported to a STEP file format, which was used to manufacture the parts using a 3 axis CNC milling machine and a digital lathe. The pieces were machined by **Carounagarane DORE** and **Gael COUPIN** at the LKB mechanical workshop with  $100\mu\text{m}$  tolerance. A detailed view of the cavity design and assembly is shown in Fig. IV.3.

#### IV.1.3 Flexure Actuation

One specificity of the MATE system is that the back cavity is significantly shorter than the front cavity, which would require high precision in both the machining of the copper pieces and the positioning of the resonator. In our case, we aim at a centimetric cavity which would require to position the membrane at roughly hundreds of microns from the back mirror, and parallel to the back mirror. Moving the membrane independently from the back mirror while maintaining a controllable tilt between both planes is therefore challenging.

A smart workaround was introduced by Jack Sankey and its group [8], where the authors introduced a flexure-tuned MATE system. The key innovation lies in actuating the membrane position by flexing its supporting silicon frame rather than translating the entire mount. This is done by mounting the back cavity in a semi-monolithic fashion, and 'locking' the silicon frame of the membrane using three screws with a fine thread, allowing for a fine adjustment of the angle of the membrane plane with respect to the back mirror plane. The piezos pushing on the back of the assembly then force the silicon frame constrained by the screws to bend, thus displacing the membrane with respect to the back mirror, as shown in Fig. IV.4. This approach preserves the cavity alignment for gentle flexures, while enabling continuous and wide-range tuning of both the membrane displacement and tilt.

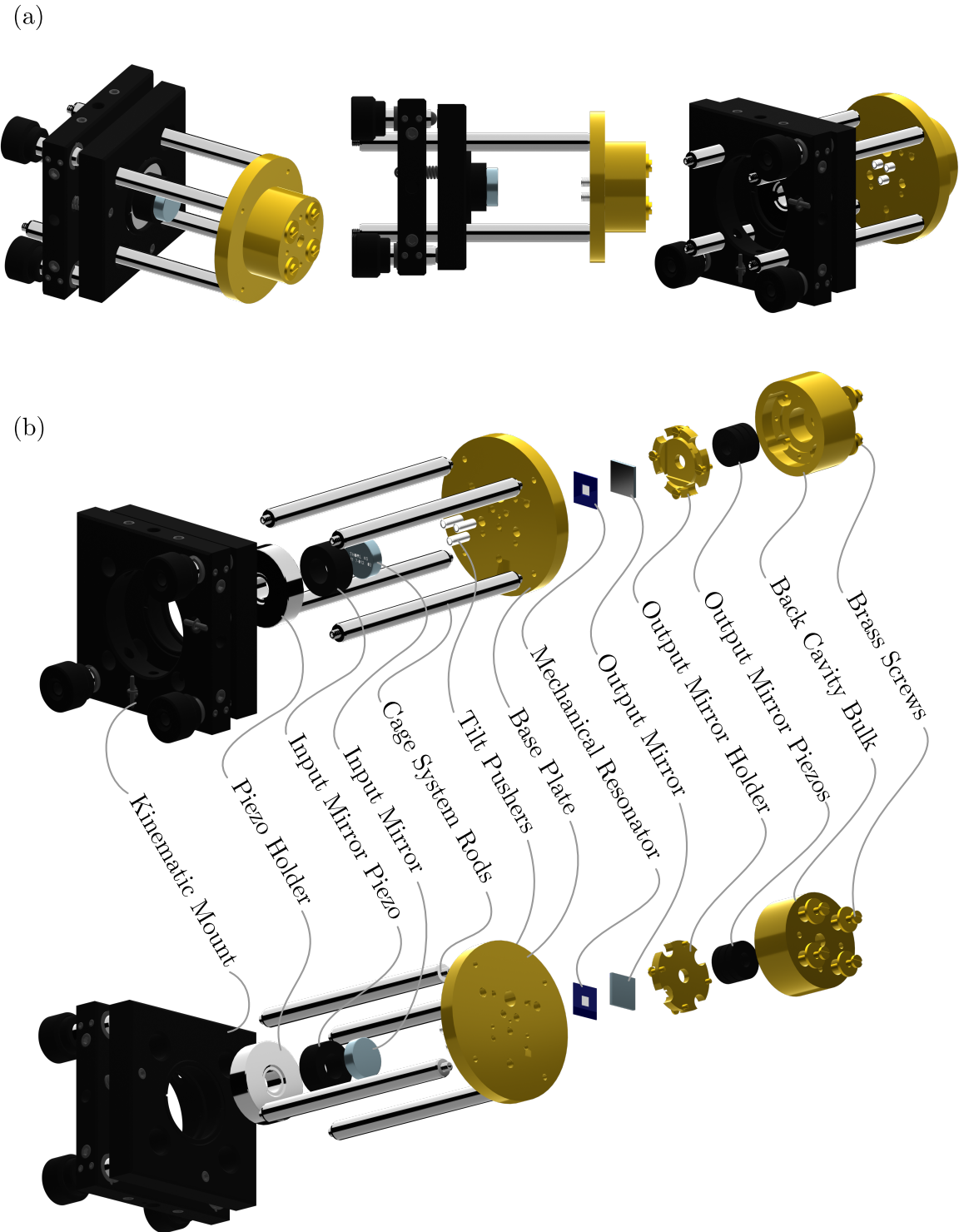


Fig. IV.3 Cavity design and assembly. (a) The figure shows the overall assembly of the MATE system from various views, highlighting the integration of the high-finesse mirrors, the membrane resonator embedded inside the back cavity copper assembly held to the input mirror Thorlabs holder through a cage system.(b) The exploded view details the arrangement of the mechanical and optical components, illustrating the modular design that facilitates alignment, stability, and compatibility with vacuum environments.

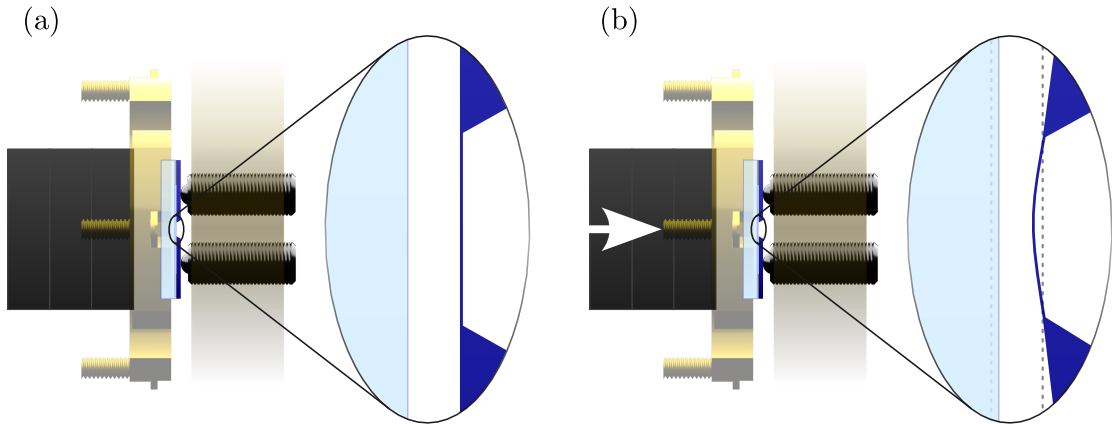


Fig. IV.4 Cavity design and assembly. (a) In this configuration (no voltage applied to the piezos), the screws are used to align the membrane plane with respect to the back mirror plane, ensuring a good parallelism between both planes. (b) Flexure tuning of the membrane position. When a voltage is applied to the piezos, they push on the back of the assembly, forcing the silicon frame to bend, thus displacing the membrane with respect to the back mirror. The two dashed lines show the initial positions of the back mirror and the membrane. This push shortens the overall cavity length (i.e. increasing the overall system's frequency), as well as the relative distance between the mirror and the membrane (i.e. changing the optomechanical coupling).

#### IV.1.4 Experimental Setup

The assembly is now to be integrated into the optical setup shown in Fig. IV.5, as well as schematically in Fig. IV.6. The source laser is a 1064nm Nd:YAG laser (Coherent Mephisto). We did not require the full optical power delivered by the laser, so a short optical path not detailed here splits the laser in 3 arms to eventually fiber couple some laser power and bring it to other experiments that would need 1064nm laser light.

The optical path then consists of :

- a first half waveplate and a beam splitter to adjust the total power injected into the experimental setup,
- a fibered electro-optics phase modulator (EOM Photline NIR-MPX-LN-10) to generate sidebands for the PDH locking of the cavity. It is polarization matched by using a fibered polarization controller to avoid Residual Amplitude Modulation noise (RAM) at the output (three blue circles on the optical layout).

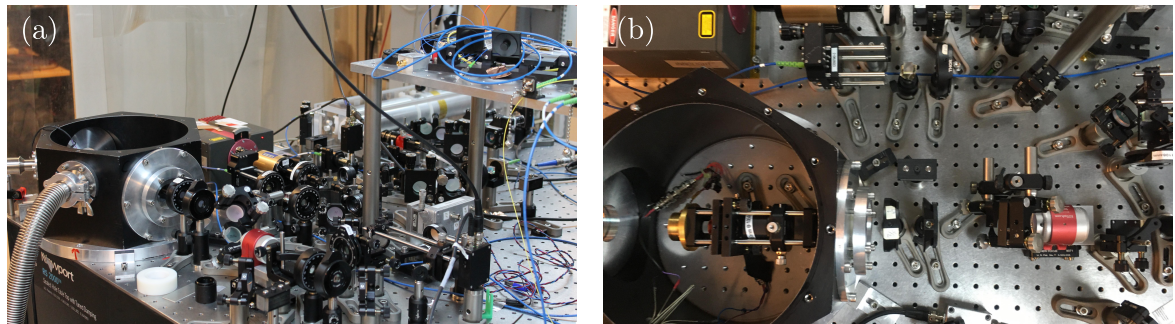


Fig. IV.5 *Pictures of the optical setup used for the MATE cavity experiments. (a) Overall view of the optical table, with the laser source in the back, the optical path in the middle, and the vacuum tank on the left. (b) Top view of the MATE cavity mounted inside the vacuum tank, with AR coated windows to allow for optical access.*

- a fiber coupler to go from a guided optical mode to a free space optical mode, with the coupler adjusted such that the outputted beam is collimated and has a waist of about 1mm,
- a quarter waveplate to compensate for ellipticity of the output beam polarization, then a half waveplate and a beam splitter to adjust the powers injected into the cavity path and the prospective LO path, respectively,
- on the cavity path, a faraday rotator to ensure the cavity reflected beam to be deflected to an output port and not back into the fiber
- a lens to mode match the laser input mode to the cavity mode, with a focal length of 40 to 60mm depending on the input mirror radii of curvature. This lens is mounted on a x-y cage system translation mount, and is mounted inside the vacuum chamber that features AR coated windows to allow for optical access yet minimal parasite reflections.
- the cavity itself.
- two photodiodes (Thorlabs ???) to detect the reflected beam and the transmitted beam, respectively, with 40mm focal length lenses to focus the beam onto the photodiodes.

The optical path was designed to be as modular as possible, allowing for easy replacement of the components if needed, as well as additions of optical elements. For this reason, it features two faint additional optical paths as seen on Fig. IV.6, one for a prospective LO, and another to deflect the reflected beam to a Homodyne Detection setup using a flip mirror. Polarization optics would also need to be added on the Homodyne Detection path to mix the LO and the reflected beam, but this was not done during this thesis.

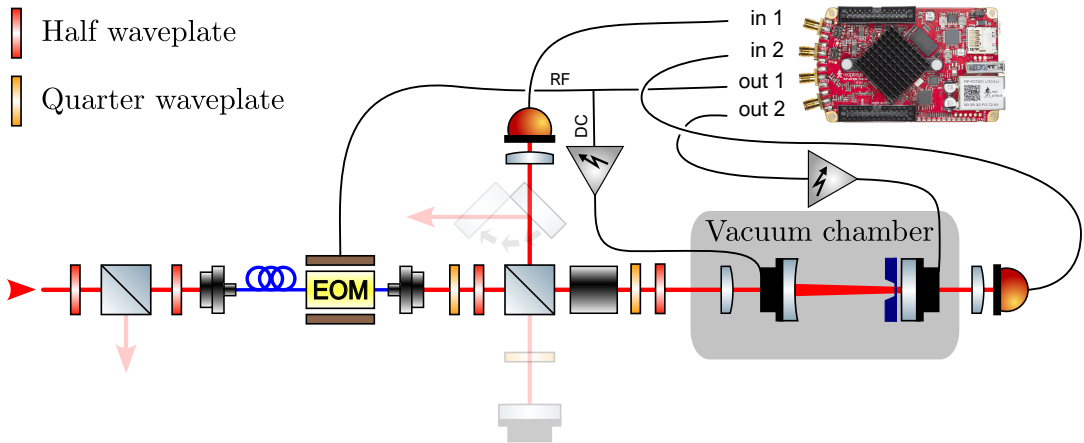


Fig. IV.6 Schematic of the optical layout used for the MATE cavity experiments. The various optical components are detailed in the main text. The transparent lines show two additional optical paths that were not used during this thesis, one for a prospective LO, and another to deflect the reflected beam to a Homodyne Detection setup using a flip mirror.

#### IV.1.5 Alignment Procedures

The optical setup is now to be aligned as to ensure a good mode matching between the laser input mode and the cavity mode. The steps are as follows, and the associated diagrams are shown in Fig. IV.7:

- **Step 1** (Fig. IV.7(a)): we position an iris diaphragm before our two injection mirrors mounted on  $(\theta_x, \theta_y)$  kinematic mounts. We then adjust the tilt of both mirrors i.e. *beam-walking*, such that the reflected beam is centered on the iris diaphragm: this is done by maximising the reflected signal on the reflection photodiode. This ensures the beam reflected by the output mirror (HR mirror) is at normal incidence. In a second time we tune the plane of the resonator using the three screws of the assembly. We monitor the Fizeau fringes in transmission with a camera (Allied Vision Alvium), and adjust the tilt such that no fringes are to be seen.
- **Step 2** (Fig. IV.7(b)): we then place the focusing lens in the optical path, and adjust its position such that we recover maximal power on the reflection photodiode. This lens is mounted on the (x-y) cage system translation mount, and positioned at a distance from the back mirror fixed by the cavity mode matching requirements (ref chap theory). The lens is then fixed in place using the cage system screws.
- **Step 3** (Fig. IV.7(c)): we add the input mirror on a  $(\theta_x, \theta_y)$  cage system mount, and adjust its position to get an input beam normal to the tangent of the concave

mirror curvature. This is also done maximising the reflected power on the reflection photodiode. The mount (and thus the mirror) was also positioned at the appropriate distance from the back mirror to ensure optimal mode matching.

- **Step 4** (Fig. IV.7(d)): We scan the cavity length using the piezo actuator mounted on the input mirror, and monitor the cavity resonances using both the reflected and transmitted photodiodes. We finally fine tune the mode match by *beam-walking* the two injection mirrors. We can also play with the collimating lens at the fiber coupler (not shown on the diagram) as to fine tune for longitudinal mode matching. The cavity is now aligned and ready for operation.

## IV.2 Experimental Characterization

### IV.2.1 Cavity Scans

Once the cavity is aligned, we can scan the cavity length by driving the front mirror piezo with a triangular or a sine wave voltage. This signal is first amplified using a high voltage amplifier made by the LKB electronic workshop, which can deliver up to 1000V. The output impedance of the amplifier is a standard 50 Ohms, but the piezo in parallel at the end of the line with capacitance of about 15 nF low pass filters the signal at  $\sim 200$  Hz. We can also modulated the back piezo actuators, in DC or AC, and a similar lowpass filtering occurs with a lower cutoff frequency  $\sim 50$ Hz (3 piezo actuators in parallel with a capacitance of around 100 nF each).

We then monitor the cavity resonances using both the reflected and transmitted photodiodes and scanning the cavity over a large range, as to mode match the cavity to the  $\text{TEM}_{00}$  mode. By beam walking, we optimally mode match the cavity such that higher order modes vanish in the photodiode noise floor and the reflected and transmitted signals are maximised, we can then perform finer scans to characterize the cavity parameters. We observed that putting the cavity under vacuum did sometimes misalign the cavity, such that even mode matching to our best ability using two mirrors outside the vacuum tank did not yield a perfect  $\text{TEM}_{00}$  match. We also saw some membranes/phononic crystals break throughout the pumping process, most likely due to dust or degazing of the setup.

Once aligned and mode matched, we can proceed to the cavity characterization. Over the course of my PhD, few *functional* cavities were mounted inside the vacuum tank. We chose to only present the results for two of these, as to display various physical effects observed. The key parameters of these two cavities are summarized in Table IV.2. Both were mounted using 100ppm input mirrors, with a concave radius of curvature of -25mm, and a plane back mirror

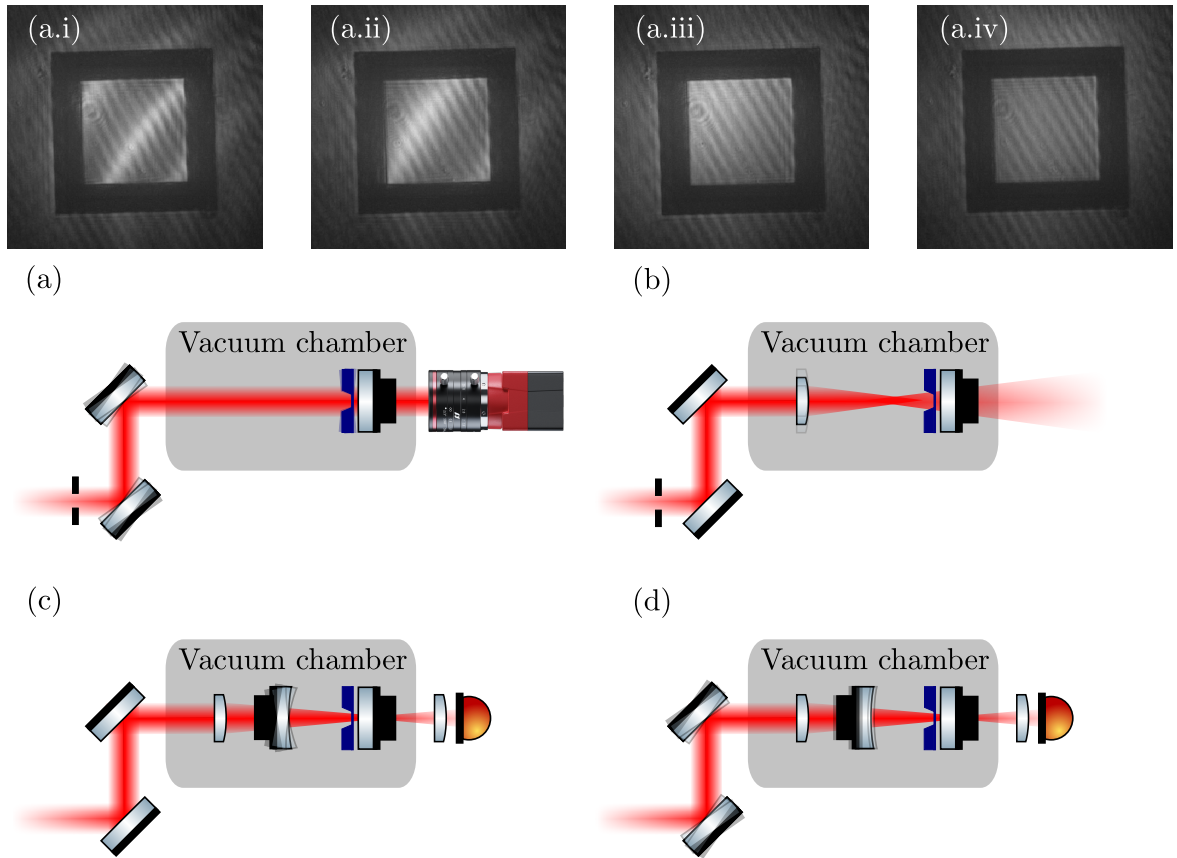


Fig. IV.7 Set up alignment procedure. (a) to (d) show the steps to align the cavity with respect to the optical path (detailed in the main text). The (a.i) to (a.iv) show what is seen on the camera for four different tilt positions where (a.iv) displays a 'good' tilt alignment: no visible fringes except for the dim fringes of the camera setup. These dim fringes are present when the beam is a normal incidence with the back mirror (use of the iris) and are believed to be interferences arising from reflections inside the camera objective as they are seen whatever the plane of focus is.

with a nominal transmission of 20ppm. Cavity I used the in-house fabricated membrane of nominal thickness 100nm, while cavity II used the commercial Norcada membrane of nominal thickness 50nm. The reason why we used the 100ppm input mirror rather than the 50ppm one was to ensure that the cavity linewidth would be larger than the mechanical resonance frequency of the membrane, such that we would be in the genuine unresolved sideband regime. Had we chosen the 50ppm mirror, the cavity linewidth would have been around 85kHz, an order of magnitude below the expected fundamental mechanical resonance frequency of the membrane at 861kHz (see above). A tradeoff is to be made here, as using a higher transmission input mirror reduces the intracavity power for a given input power,

thus reducing radiation pressure effects.

	Cavity I	Cavity II
Input mirror RoC (mm)	-25	
Back mirror RoC (mm)	$\infty$	
Nominal input mirror $T_1$ (ppm)	100	
Nominal back mirror $T_2$ (ppm)	20	
Length $L$ (mm)	17	24
FSR (GHz)	8.817	6.246

Table IV.2: Summary of relevant parameters for the two cavities used in this work.

### Cavity resonances versus membrane position

We first scan the input mirror piezo with a linear ramp  $V_{\text{SW}}$  ranging from 0 to 500V at 10-50Hz, corresponding to a displacements of around  $2\mu\text{m}$  ( $\sim 4$  FSRs). The back piezo actuating the membrane position was driven by a DC voltage  $V_{\text{DC}}$  ranging from 0 to 70V, with an associated stroke of  $4\mu\text{m}$  (3 piezos). Knowing the FSR of the cavity, we calibrate the piezo displacement as a function of the applied voltage, and fit the resonances positions using the theoretical model detailed in chapter 3. We modelled the front cavity length  $L_1$  as well as the back cavity length  $L_2$  as third order polynomials of the applied voltages  $V_{\text{SW}}$  and  $V_{\text{DC}}$  such that

$$\begin{aligned} L_1 &= a_0 + a_1 V_{\text{SW}} + a_2 V_{\text{SW}}^2 + a_3 V_{\text{SW}}^3 - \alpha V_{\text{DC}} \\ L_2 &= b_0 + b_1 V_{\text{DC}} + b_2 V_{\text{DC}}^2 + b_3 V_{\text{DC}}^3 \end{aligned} \quad (\text{IV.2})$$

where we introduced the coefficients  $a_i$  and  $b_i$  to be fitted, as well as a cross-coupling term  $\alpha V_{\text{DC}}$  to take into account the fact that the back piezo actuators does change the front cavity length since the piezo pushing the back cavity assembly bends the silicon frame.

We show a typical raw scan in Fig. IV.8(a), as well as a rescaled one in Fig. IV.8(b), where we can see a good agreement between the experimental data and the theoretical model. This fits allow us to extract the membrane reflectivity  $|r_m|$ , from which we can compute the power reflectivity and transmittivity of the membrane. This would tend towards using the single mode model as to describe radiation pressure in such a system.

Using (II.24) we can then estimate the membrane thickness to a surprisingly high accuracy with an error of less than 1nm. For cavity I, we found a thickness of  $d = 86.9$  nm, while for cavity II we found  $d = 41.1$  nm nm. For cavity I, the discrepancy with the nominal thickness of 100nm could be explained by the fabrication process used to make the membrane, i.e.

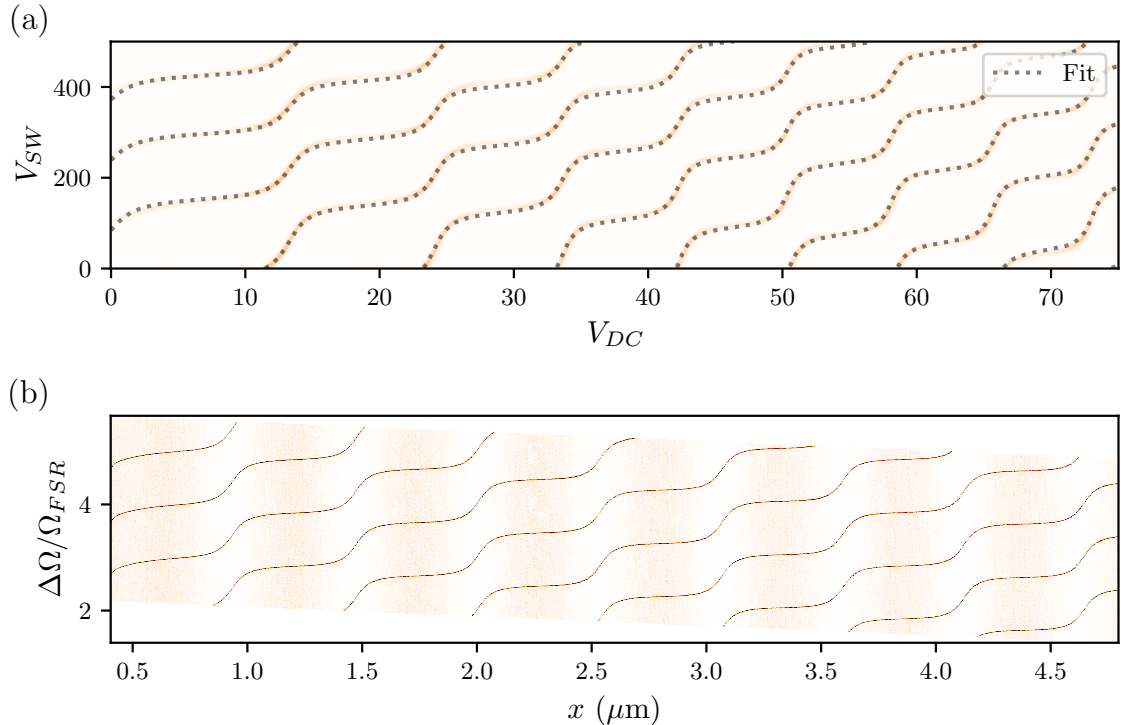


Fig. IV.8 Scans of cavity I over few FSRs. (a) Raw scan of the cavity transmission as a function of the applied voltage  $V_{SW}$  on the front piezo and  $V_{DC}$  on the back piezo. The dashed line displays the theoretical model using the fitted membrane reflectivity  $|r_m|$ . (b) Rescaled scan where the fitted polynomials are used to convert the sweep voltage into effective cavity detuning in FSR unit, and the DC voltage into effective membrane displacement in microns.

the HF cleaning step at the end of the fabrication procedure etches the SiN layer at a rate of around 1nm/s. The membrane was cleaned for around 5 minute, such that we expected a thickness of around 90nm (it etches both sides of the membrane). For cavity II, the nominal thickness was 50nm, such that the discrepancy could be explained by fabrication tolerances.

From the fitted polynomials, we then extract the transfer functions of both piezo actuators, such that each measured observable can be mapped to an effective membrane displacement  $x$  rather than the applied voltages  $V_{SW}$  and  $V_{DC}$ . This gives us a displacement map shown in Fig. IV.9, where we can extract the cavity length variations  $\Delta L = \Delta L_1(V_{SW}, V_{DC}) + \Delta L_2(V_{DC})$ .

Importantly, we see that, contrary to the model developed earlier, the back piezo actuation does change the front cavity length, with a non zero coupling coefficient  $\alpha$ . This is

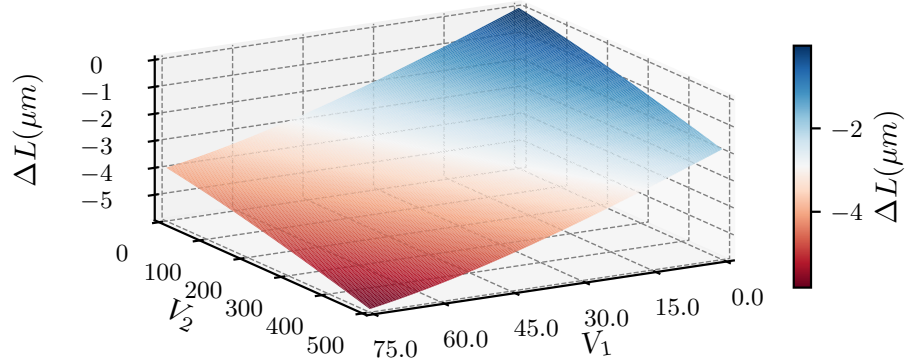


Fig. IV.9 Displacement map of cavity I. Using the fitted polynomials, we can convert the applied voltages  $V_{\text{SW}}$  and  $V_{\text{DC}}$  into effective displacements of the membrane with respect to the back mirror. The colormap shows the total cavity length variations  $\Delta L = \Delta L_1 + \Delta L_2$  as a function of both piezo voltages.

expected from the flexure tuning mechanism, where pushing on the back of the assembly bends the silicon frame, thus shortening the overall cavity length. Knowing these  $\Delta L$ s variations, a natural next step would be to compensate the action of the back piezo on the long cavity length by adding a DC component to the front piezo voltage, such that the overall cavity length remains constant when tuning the membrane position. This would allow for a better decoupling of the membrane position and the cavity length, which would be useful for various experiments.

### Slow and Fast Scans

As developed in I, scanning over a cavity resonance can be done in two different regimes, depending on the sweep rate of the cavity length with respect to the cavity linewidth. In the adiabatic limit where the sweep rate is much smaller than the cavity linewidth, the intra-cavity field adiabatically follows the input field, and the transmitted and reflected intensities follow lorentzian lineshapes. In the opposite limit where the sweep rate is much larger than the cavity linewidth, dynamical effects such as cavity ringdowns appear, where the intra-cavity field undergoes damped oscillations as the cavity length is swept over the resonance. This effect is visible both in transmission and reflection, as shown in Fig. IV.10. This effect

can be used to extract the cavity linewidth/finesse by comparing the heights of the first two rebounds in transmission to their temporal spacings, as detailed in chapter I. We will come back to this point later, particularly regarding the accuracy of the finesse estimation.

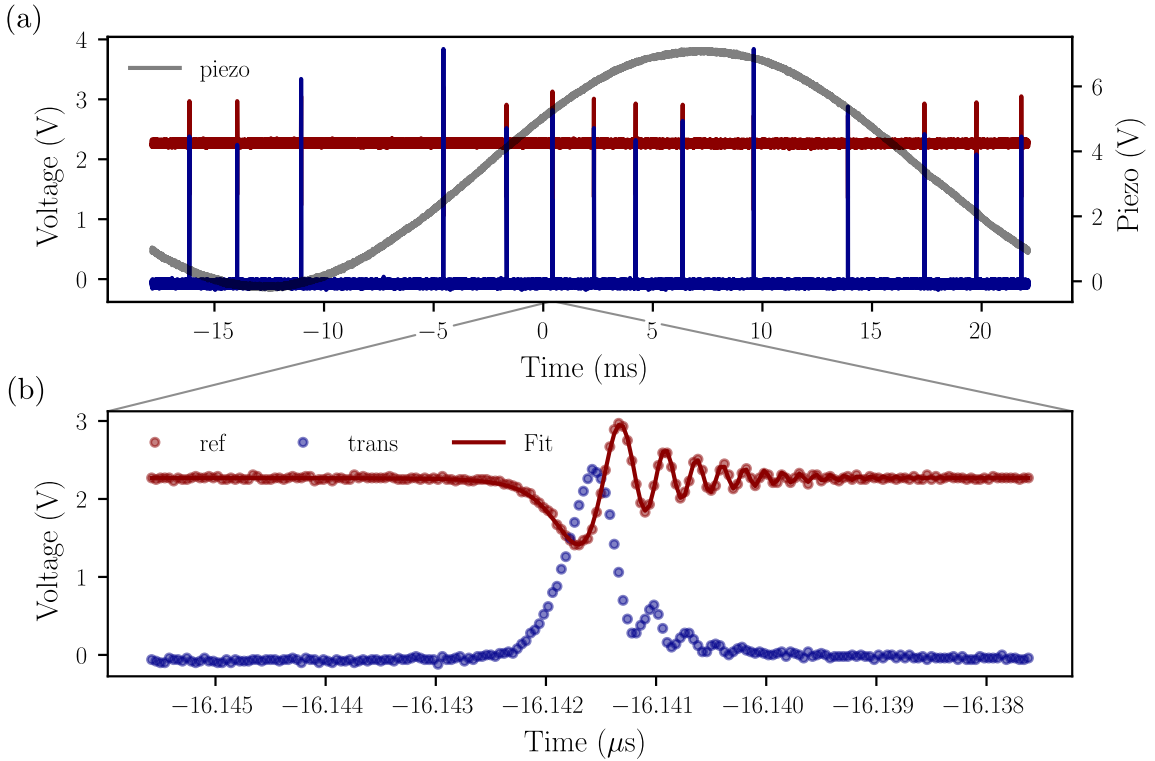


Fig. IV.10 *Larges cavity scans of cavity II showing dynamical effects such as cavity ringdowns both in transmission and reflection. The sweep rate is much larger than the cavity linewidth, such that the intracavity field cannot adiabatically follow the input field. (a) Cavity transmission and reflection swept over few FSRs. The blue curve (transmission) is eventually a single column of the 2D color plots showing the cavity scan in Fig. IV.8(a). One can then actuate the back piezo to scan the membrane position as to see the cavity resonances shift. (b) Zoom on a single resonance showing cavity ringdown effects, with the fits used to compute the cavity linewidth and finesse.*

To recover the lorentzian lineshapes, we first proceeded to apply slower sweep rates at the mHz level. This rendered the cavity sensitive to acoustic noise from the environment (the turbo pump for example), which did not yield quality lorentzian dips. We therefore kept the sweep rates at the 10-50Hz level, but drastically reduced the sweep amplitude to scan over a single resonance only. The classical EOM phase modulation sidebands is then used as a frequency reference to extract the cavity linewidth, as shown in Fig. IV.11 with a modulation frequency of 10 MHz. Having access to both transmitted and reflected

intensities, and calibrating properly the photodiode response, we then have access to the  $\eta_T$  and  $\eta_R$  outcoupling coefficients defined in chapter 3.

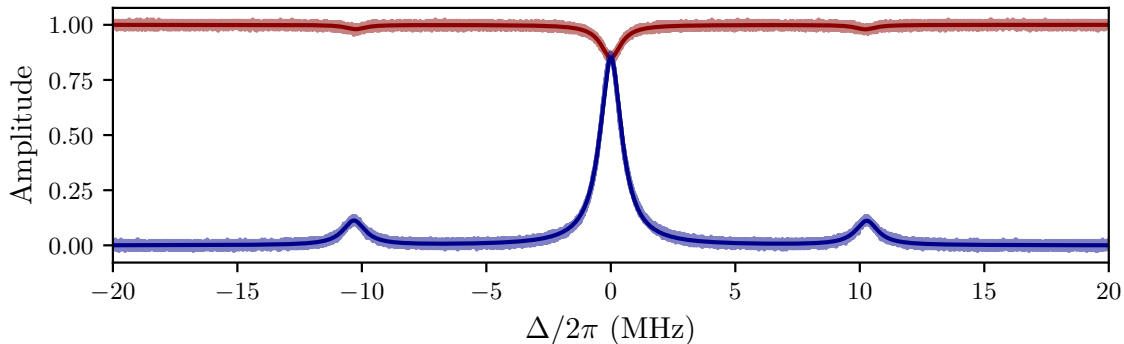


Fig. IV.11 *Small amplitude scan of cavity II over a single resonance (with membrane mounted), showing the transmitted and reflected intensities as well as the EOM sidebands used as a frequency reference to extract the cavity linewidth. The modulation frequency is set to 10 MHz. The fits (solid lines) are used to extract the cavity linewidth and finesse.*

### Finesse

We now turn to the evaluation of the system's finesse as a function of the membrane displacement. We use two different methods to evaluate the finesse of the cavity and we compare them:

- The first method would be to scan the cavity over a single resonance, and use the EOM sidebands as a frequency reference to extract the linewidth of the resonance. This method is less sensitive to piezo nonlinearities, assuming the piezo sweep is quasi linear over the resonance width.
- The second method would be to scan the cavity rapidly and observe a cavity ringdown, and compare the heights of the first two rebounds in transmission to their temporal spacings. This method is less sensitive to piezo nonlinearities, but requires a fast photodiode. Additionally we can vary the piezo sweep frequency to scan for various sweep rates and use a sine wave to sweep the cavity length such that the sweep rate is maximum at the sine zero crossing.

We then evaluate the finesse of the empty cavity as well as the cavity with the membrane inserted, at various membrane positions. This allows for an evaluation of the losses introduced by the membrane insertion, as well as their position dependence i.e. position dependent linewidths/finesse. Assuming low scattering losses and absorption as reported in

the literature for high-stress SiN membranes[SiN\_review], we can attribute these excess losses to imperfect membrane alignment, i.e. remaining tilt between the membrane plane and the back mirror plane, imperfect mode matching to the cavity mode, and clipping loss due to the finite size of the membrane. The latter is not thought to be significant given the large size of the membrane with respect to the cavity mode waist, but could still contribute to few percents of the total losses.

The second method to estimate the cavity finesse turned out to be slightly disappointing, as it didn't yield consistent and reproducible results. Furthermore, numerical integration as to fit the measured data produces divergences (due to a low number of data points), which in turn forbids a proper estimation of the finesse. The reliable method was therefore taken to be the sideband method. A typical linear regression (detailed in Chap II) is still shown as an example in Fig. IV.12, but the results shown in Fig. IV.13 are only extracted from the sideband method.

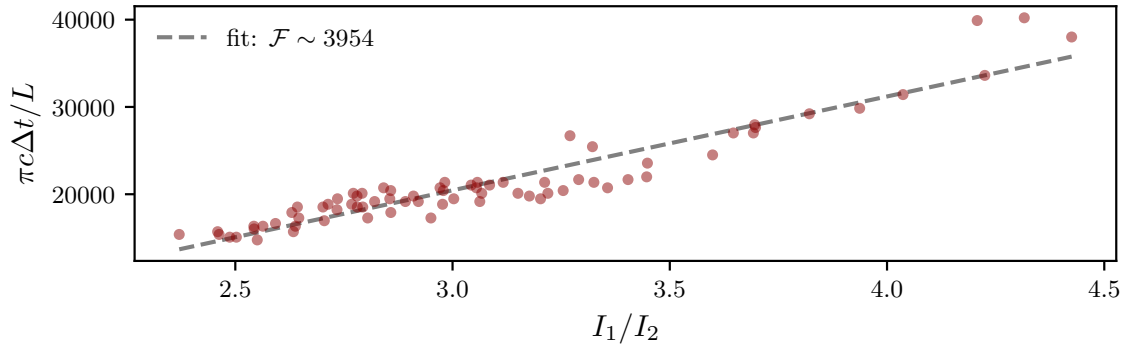


Fig. IV.12 *Finesse measurement of cavity II using the ringdwon method. The data points show a typical linear regression used to extract the cavity finesse from the heights of the first two rebounds in transmission as a function of their temporal spacing.*

The results from the first method are shown in Fig. IV.13, where we can see a good qualitative agreement with the theoretical model developed in chapter III. While cavity I featured an empty cavity finesse of 14 000, the insertion of the membrane reduced it to values ranging from 6 000 to 10 000 depending on the membrane position. Cavity II featured a lower empty cavity finesse of 12 780, which was further reduced to values ranging from 3 000 to 5 000 with the membrane inserted. These values are in line with other MIM/MATE systems reported in the literature[9, 8, 10], and could be improved by better membrane alignment (tilt and transverse position).

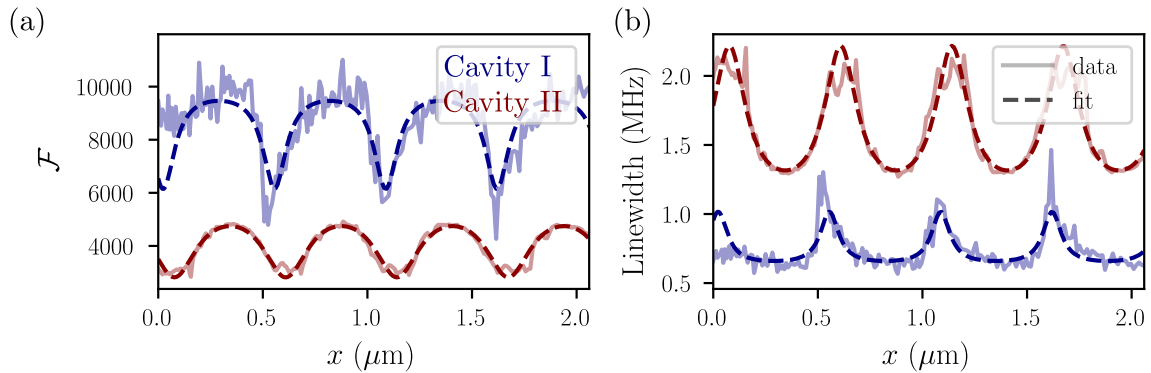


Fig. IV.13 Finesse measurement of the two cavities using the sideband method (a) and the associated linewidths (b). The finesse model in (II.35) has been changed as to account for the linear shifts underwent by all resonances as a consequence of the cavity shortening.

### Cavity outcouplings

Monitoring the cavity transmission while scanning over resonances with the input piezo allows us to extract the transmission and reflections dips of the cavity at a given position (calibrated using the scans). We then fit these position dependent outcoupling transmittivities using the model developed in chapter III. The resulting scans for both cavities are shown in Fig ...

Interestingly, the second cavity displayed anomalous dips, seen as abrupt changes in the transmittivities. These have been reported years ago in Jack Harris lab [ref], and occur when two optical modes become degenerate at a given membrane position. This was verified experimentally, as the mode matching was de facto less qualitative in the second cavity than in the first one.

### Dispersive couplings

The next essential parameters central to MATE systems are the linear and quadratic dispersive couplings, as developed in chapter II. These are computed from the rescaled scans of the cavity resonances, giving access to the first and second derivative of the peak positions (once rescaled, expressed in FSR units) with respect to the membrane position. These are plotted in Fig IV.15, and we see that, although the second cavity featured a lower finesse, it does display a larger linear dispersive coupling. Due to the different cavity geometry/constraints. These were observed to vary greatly from one cavity to another, independently of the cavity finesse.

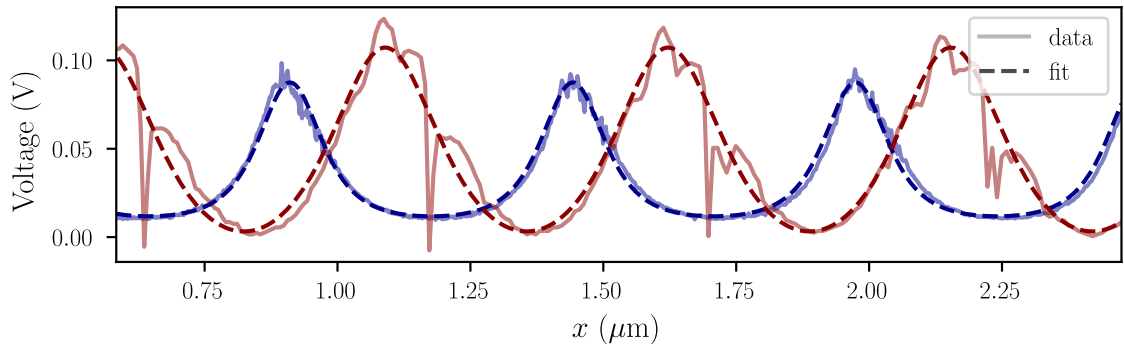


Fig. IV.14 Transmission outcoupling coefficients  $\eta_T$  extracted from the fits of the cavity resonances for both cavities I and II as a function of the membrane position.

From these various characterization sequences, we extract the key parameters of the two cavities, summarized in Table IV.3.

Empty cavity	Cavity I	Cavity II
FSR (GHz)	8.817	6.246
Finesse $\mathcal{F}$	14 000	12 780
Linewidth (kHz)	630	489
$T_1 + T_2 + \mathcal{L}$ (ppm)	449	492
Resonant reflection R(0)	0.76	0.85
$T_1$ (ppm)	421	472
$T_2 + \mathcal{L}$ (ppm)	28	19
<hr/>		
MATE cavity		
Fitted reflectivity $ r_m $	0.54	0.33
Finesse $\mathcal{F}$	6 000 - 10 000	3 000 - 5 000
Linewidth (MHz)	0.88 - 2.20	1.25 - 2.10
$T_1 + T_2 + \mathcal{L}_{\text{mem}}$ (ppm)	630 - 1570	1255 - 2095
Input power	10 μW- 50 mW	

Table IV.3: Summary of the measured parameters for the two cavities used in this work.

#### IV.2.2 Cavity Locking and Mechanical Characterization

Once the cavity was characterized, we proceeded to lock it using the PDH technique detailed in chapter III. The whole lock was done using PyRPL, as to showcase its versatility and ease of use. The analogic signal was manipulated with standard MiniCircuits® RF components, as to amplify/filter/mix the signals as needed. The overall locking sequence is shown in Fig. IV.16, where we can see the various steps needed to lock the cavity. First, performing a fine scan over a cavity resonance as to recover a lorentzian lineshape. From this, we tune

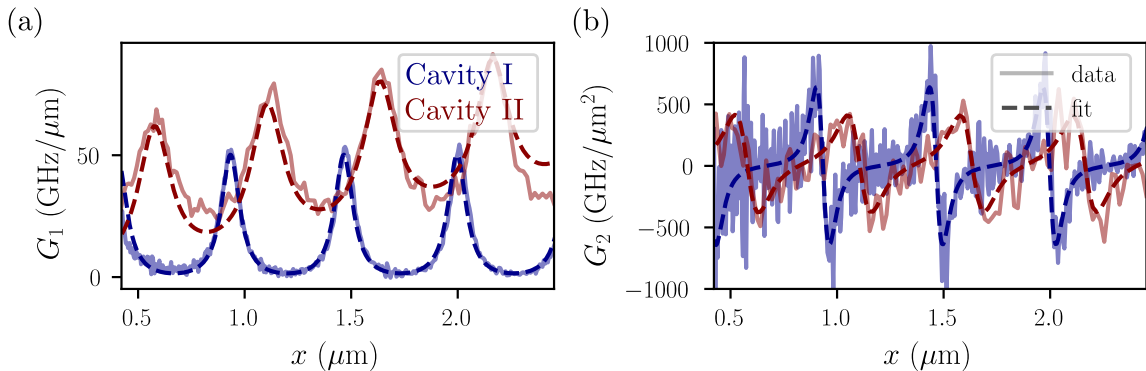


Fig. IV.15 *Linear and quadratic dispersive couplings extracted from the rescaled scans of cavity I and II. Units are given in  $\text{GHz}/\mu\text{m}$  for  $G_1$  and in  $\text{GHz}/\mu\text{m}^2$  for  $G_2$ , as rescaling by the zero point fluctuation in a cavity with a large number of photon obscures the true meaning of the vacuum optomechanical couplings.*

the error signal amplitude and demodulation phase as to optimize the PDH error signal (Fig IV.16(b)). We then engage the lock by first locking on the side of the resonance dip. It was observed that at mW powers, locking on the blue side of the resonance was not feasible. This could be explained by optomechanical heating of the membrane, as changing the side of the lock to the red side made the lock stable. Finally, we engage the PDH lock to lock onto the cavity resonance. The critical point in maintaining the lock was the input power i.e. the cavity circulating power. In terms of power range, locking at 1-50  $\mu\text{W}$  held the lock, while ramping the input power to 1-50 mW greatly perturbed the optomechanical system such that it was no possible to keep the lock. We suspect that optomechanical heating, bistability and photothermal effects were playing a significant role in the lock stability.

Keeping the optical power low, the lock held, and we could proceed to the mechanical characterization of the membrane resonator. Using a spectrum analyzer (Agilent 90A20???), we monitored the spectrum of both the reflected intensity. The membrane motion modulating the cavity resonance faster than the lock could respond, the membrane motion modulates the intracavity field intensity, which can in turn be detected in direct detection in both transmission and reflection. The resulting spectra are shown for cavity II in Fig. IV.17, where we can see the fundamental mechanical resonance at 861kHz, as well as various higher order modes. To reduce the averaging time, we used a Resolution Bandwidth (RBW) of 1kHz, which broadens the mechanical peaks, masking the true linewidth from which we could have extracted the effective mechanical quality factor.

To extract the intrinsic mechanical quality factor, we then proceeded to do mechanical ringdown measurements. Knowing the mechanical resonance frequencies from the spectra,

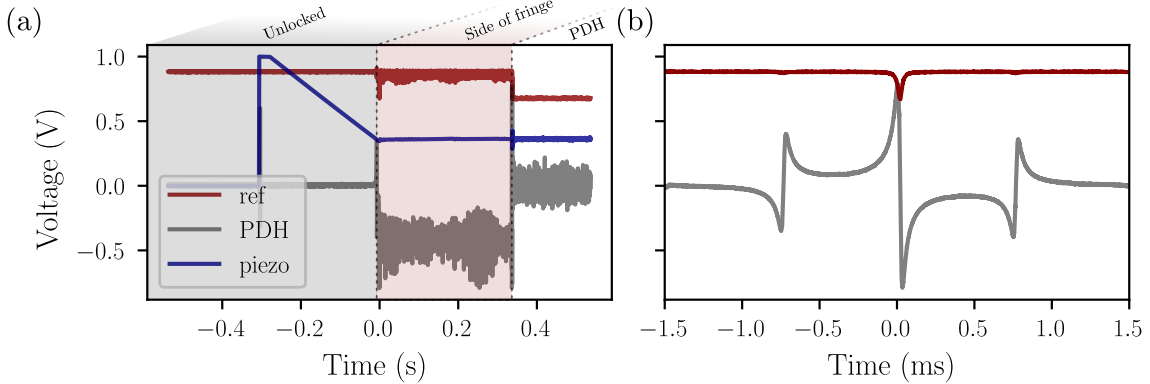


Fig. IV.16 *Lock sequence of the MATE cavity using the PDH technique. (a)* Steps of the lock sequence, where we launch the side of fringe lock at approximately -0.3s. The red pitaya then sets its output voltage to 1 and starts PID control as to lock on the 0 of the error signal, which is achieved at time 0s. Being locked at a HWHM from resonance, launching the PDH lock then brings the cavity to resonance at time  $\sim 0.35$ s. *(b)* Zoom on the error signal and reflected intensity during the lock sequence upon prior cavity scan. These traces are used to fine tune the error signal amplitude and demodulation phase as to optimize the PDH error signal.

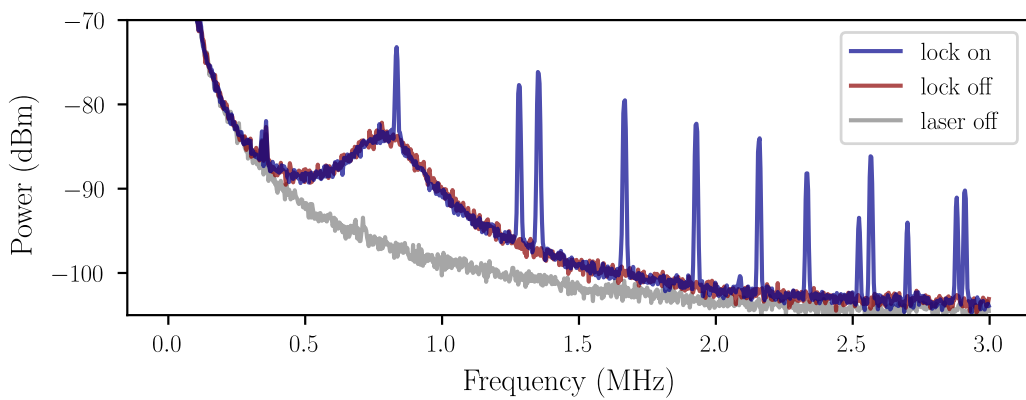


Fig. IV.17 *Reflection mechanical spectrum of cavity II, showing the fundamental mechanical resonance at 861kHz as well as various higher order modes. We observe the relaxation oscillation peak at around 1MHz, as well as the laser technical noise at low frequencies. The RBW is set to 1kHz, which broadens the mechanical linewidth.*

we drive the membrane fundamental mode using the back mirror piezo, while sweeping the cavity. Recording the reflected intensity while triggering the oscilloscope on the piezo sweep of the first mirror then yields the mechanical ringdown as shown in Fig. IV.18(a), where each column of the image corresponds to a scope acquisition. The ringup phase is visible as the red area before time zero, where the piezo drives the membrane at resonance. At time zero, the piezo drive is stopped, and the mechanical motion decays exponentially with a characteristic time related to the intrinsic mechanical quality factor. By fitting the width of these decays, we can extract the mechanical quality factor as shown in Fig. IV.18(b). For cavity II, we found a mechanical quality factor of  $Q = 12000$ , which is lower than expected from the nominal values given by Norcada (around 1 million).

The probable cause for this low mechanical quality factor is the stress applied to the membrane by the flexure mechanism. While this stress is necessary to tune the membrane position, it does reduce the mechanical quality factor by introducing additional loss channels such as clamping losses and internal friction due to bending of the membrane. This  $Q$  degradation was reported in MIM systems by Cindy Regal and coworkers, where they observed a drop from  $10^6$  down to  $10^4$  when the membrane frame was glued, adding stress to the membrane [7]. Therefore, while the flexure mechanism is necessary to tune the membrane position, it does degrade significantly the mechanical quality factor, which could be an issue for experiments requiring high  $Q_m$  such as ground state cooling or quantum limited measurements.

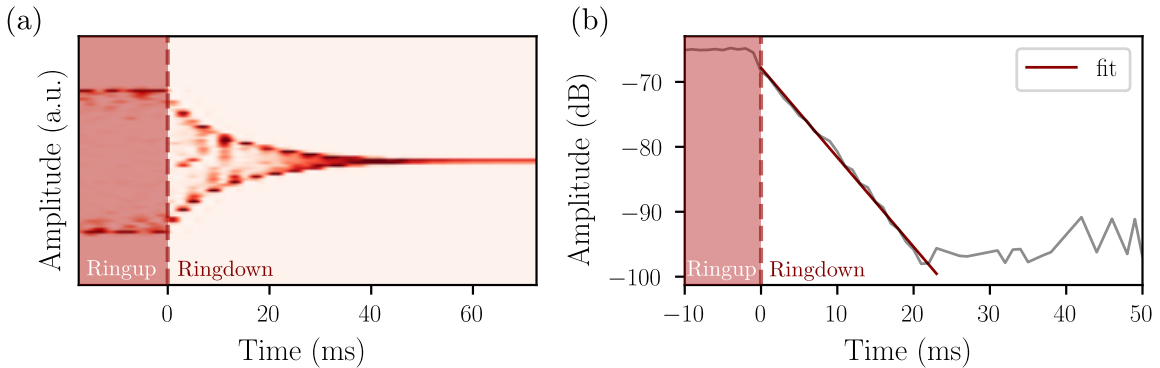


Fig. IV.18 *Ringdown sequence of the fundamental mechanical mode of cavity II. (a) 2D colormap showing the mechanical ringdown as a function of time and acquisition number. Each column corresponds to a single oscilloscope acquisition triggered on the piezo drive stopping at time 0s. The red area before time zero shows the ringup phase where the piezo drives the membrane at resonance, while after time zero the mechanical motion decays exponentially. (b) Fit of the mechanical ringdown decay used to extract the intrinsic mechanical quality factor  $Q_m$ . From this fit, we found  $Q_m = 12000$  for cavity II.*

### IV.2.3 Bistability

While characterizing the mechanical properties of cavity II, we observed an interesting bistability effect when driving the membrane at high optical powers (above 10mW input power). As shown in Fig. IV.19(a), when sweeping the resonance using the front piezo, we observed a hysteresis depending on the sweep direction. This effect is reminiscent of bistability, where photo-thermal effects or radiation pressure effects induce a shift of the cavity resonance depending on the intracavity power.

The hysteretic response observed at high input power is characteristic of an optical nonlinearity that shifts the cavity resonance proportionally to the intracavity field. In the usual optomechanical (radiation-pressure) bistability, the resonance shift is mediated by the instantaneous displacement induced by the optical force, so the nonlinearity is essentially set by the mechanical susceptibility and reacts on mechanical time scales. By contrast, photothermal bistability originates from residual absorption: intracavity power heats the membrane/coatings, leading to thermo-refractive and/or thermo-elastic changes that detune the cavity; because the temperature follows the absorbed power with a finite thermal relaxation time, the detuning acquires a delayed component, which naturally produces sweep-direction-dependent hysteresis and can also enable dynamical backaction via this phase lag (as emphasized in photothermally induced transparency experiments). In our case, the appearance of the effect only above a clear power threshold, together with the strong hysteresis and the concomitant self-sustained oscillation consistent with a delayed force, points to a thermally mediated mechanism: a fraction of the intracavity power is absorbed by the membrane, heating it and shifting its effective position/optical response, thereby shifting the cavity resonance. We therefore attribute the bistability primarily to photothermal effects rather than to pure radiation pressure. The oscillation then sits precisely at the fundamental mode frequency, where a zoom can be seen in the inset of Fig. IV.19(a), and the associated FFT spectra are shown for both sweep directions in Fig. IV.19(b).

Unfortunately, due to time constraints (and membrane breakage...), we could not further investigate this interesting phenomenon, which would require a more in-depth study of the photothermal properties of the membrane, as well as the dynamical backaction effects at play in this regime. This would be an interesting avenue for future research, as photothermal effects can be harnessed for various applications such as cooling or amplification of mechanical motion, as well as for studying nonlinear dynamics in optomechanical systems.

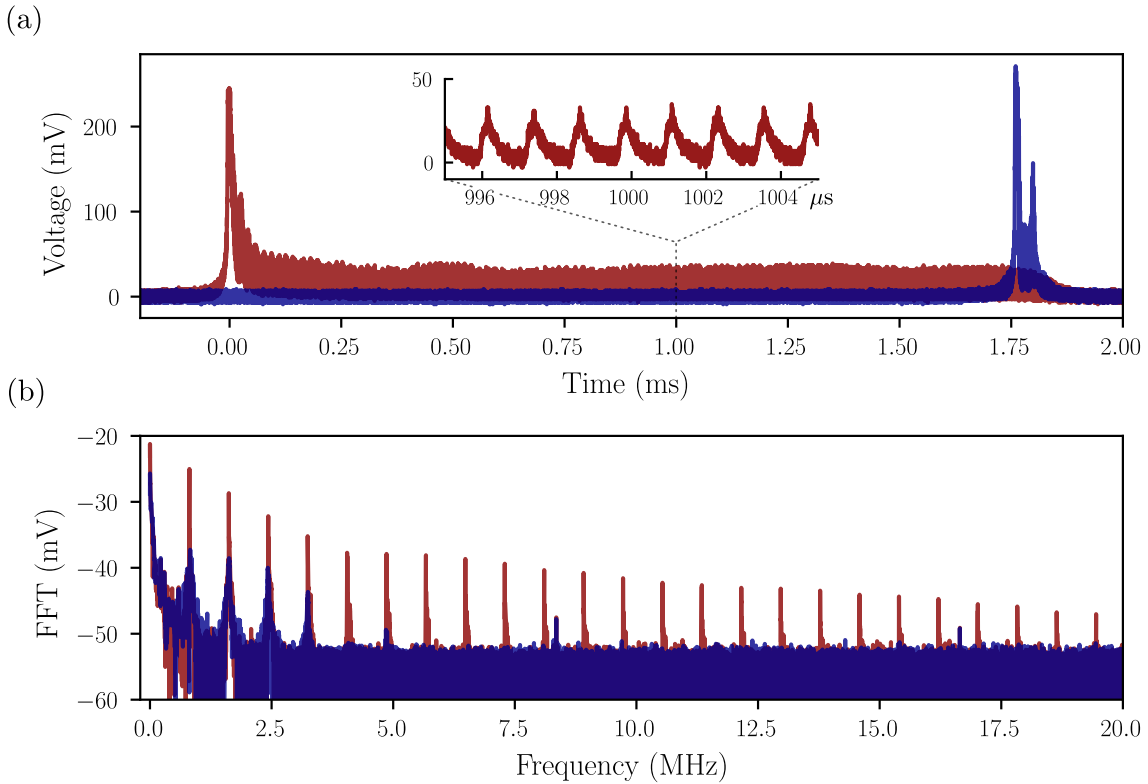


Fig. IV.19 *Bistable behavior observed in cavity II at high input power ( $> 10\text{mW}$ ). (a) Cavity transmission as a function of the front piezo voltage, showing a hysteresis depending on the sweep direction (blue: increasing voltage, orange: decreasing voltage). The inset shows a zoom on the oscillations observed at the mechanical resonance frequency. (b) FFT spectra of the transmitted intensity showing a peak at the fundamental mechanical resonance frequency and its harmonics, indicating self-sustained oscillations of the membrane motion.*

### IV.3 Optomechanical Fibered Cavity

Having characterized the MATE cavity phenomenology, we now turn to the specifications, design and preliminary steps towards the realization of a fibered optomechanical cavity using a MATE architecture.

The reasons why one would want to build a micrometer/millimeter scale optomechanical cavity are numerous. First, the small mode volume allows for a large optomechanical coupling rate  $g_0$ , as the linear dispersive couplings scale as the inverse of the cavity length. Additionally, for a fixed finesse and a fixed resonator frequency of about 1MHz, the cavity linewidth  $\kappa$  becomes easily larger than the mechanical frequency, rendering the unresolved sideband regime easily achievable. One can then boost the finesse, enhancing radiation pressure effects

while remaining in the unresolved sideband regime. Finally from an experimental point of view, it seems that free space cavities embedded within cryogenic environments tend to suffer from unwanted intensity and phase fluctuations, severe misalignment issues, and limited optical access. The beam being injected by and collected from AR coated windows, and the cryostat being subject to acoustic and vibrational noise from the environment (pumps, acoustics, etc), the cavity intracavity power fluctuates significantly, rendering stable locking and long term operation difficult. Fibered cavities, on the other hand, are more compact, easier to align and maintain aligned, and can be directly integrated within cryostats with minimal optical access requirements (only the fiber feedthroughs).

This work was carried out in collaboration with the group of **Jakob REICHEL** and **Romain LONG**, as well as with **Pierre MAHIOU** from the spin-off company Mirega, who I once again deeply thank for his patience, expertise and availability throughout our collaboration. **Amin LAKHAL**'PhD thesis will focus more extensively on this optomechanical experiment.

#### IV.3.1 Design considerations

Moving to micrometric cavities imposes stringent design constraints, as the cavity length needs to be precisely controlled and tuned, and the radii of curvature of the fiber mirrors need to be chosen as to provide a stable optical resonator while minimizing losses, which would degrade the squeezing level coupled to the cavity mode. Additionally, the membrane needs to be mounted and aligned within the small cavity volume, which imposes further constraints on the membrane assembly size and actuation mechanisms.

##### Cavity mode & coupling efficiency

In a fibred Fabry–Perot operated at micrometric lengths, the spatial mode is set by the optical constraint that the cavity eigenmode at the input mirror must efficiently overlap with the guided mode exiting the injection fiber. We denoted the waist of the cavity as  $w_0$ , and the guided mode radius of the fiber as  $w_0^f$ . We recall the waist size of the fundamental Gaussian mode in a plano-concave cavity,

$$w_0 = \sqrt{\frac{\lambda}{\pi} \sqrt{L(R - L)}},$$

where  $L$  is the cavity length and  $R$  the radius of curvature of the concave mirror. The waist as a function of the distance  $z$  from the waist reads

$$w_{\text{cav}}(z) = w_0 \sqrt{1 + \left(\frac{z}{z_R}\right)^2}, \quad z_R = \frac{\pi w_0^2}{\lambda}.$$

The coupling efficiency between the fiber mode and the cavity mode can be computed from the overlap integral between both modes, assuming perfect axial alignment and no tilt at the fiber–cavity interface [ref]. This yields the coupling efficiency

$$\epsilon \approx \frac{4}{\left(\frac{w_0^f}{w_0} + \frac{w_0}{w_0^f}\right)^2 + \frac{(z_0 - z_0^f)^2}{z_R z_R^f}}, \quad (\text{IV.3})$$

where  $z_0$  and  $z_0^f$  are the positions of the cavity waist and fiber waist respectively, and  $z_R$  and  $z_R^f$  their associated Rayleigh ranges. This expression shows that optimal coupling efficiency is obtained when both waists are matched in size and position, i.e.  $w_0 = w_0^f$  and  $z_0 = z_0^f$ .

We then have two configurations to consider, as shown in Fig. IV.20 i.e. injecting the light from the flat fiber mirror or from the curved fiber mirror. To realize the MATE system, the resonator needs to be positioned near the flat fiber interface. As seen in the coupling efficiency expression, setting  $z_0 = z_0^f$  requires the cavity waist to be located at the flat mirror, which is naturally achieved in configuration A.

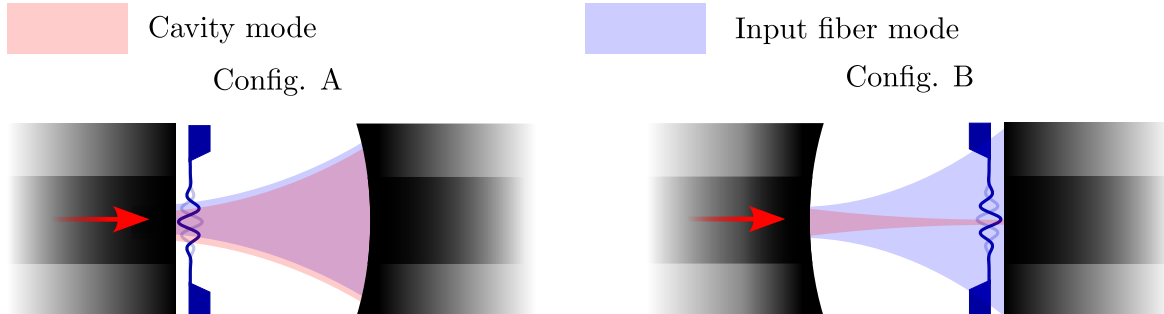


Fig. IV.20 Two possible configurations for a fibered MATE cavity. (a) shows the configuration where the membrane is mounted on the input fiber mirror, while (b) shows the configuration where the membrane is mounted on the back mirror. The overlap between the cavity mode and the input fiber mode needs to be maximized as to ensure optimal mode matching to the cavity mode. The components are not to scale.

### Choice of fibers

In order to couple a single fiber mode to the cavity mode, we need to select an appropriate fiber type. For injection, multi-mode (MM) fibers are not suitable, as the presence of higher order modes would lead to parasitic coupling to the cavity mode, reducing the effective coupling efficiency and leading to unwanted interference effects. Therefore, single mode (SM) fibers are the natural choice for this application. Hence, let's first consider a standard SM fiber at 1064nm, such as the Thorlabs SM-1060 XP. The specified mode field diameter is

$6.2\mu\text{m}$ , corresponding to a mode radius and cavity waist of  $w_0^f = w_0 = 3.1 \mu\text{m}$ . The associated Rayleigh range is  $z_R = \pi w_0^2 / \lambda \approx 28.5 \mu\text{m}$ , yielding feasible L and R values of the order of a few tens of microns. Embedding a membrane within such a short cavity length is however extremely challenging, since the Si membrane frames are typically few hundreds of microns thick. We would then need to mount the cavity around the membrane, which forbids to change the resonator at will.

In practice, this strongly motivates the use of *large mode area* (LMA) fibers for light injection: a larger mode field diameter  $2w_0^f$  allows to increase the cavity waist  $w_0$ , and therefore the Rayleigh range  $z_R$ , relaxing the constraints on the cavity length and mirror radius of curvature. This in turn allows to insert larger membrane assemblies within the cavity, while keeping the mode matching intact. A reference LMA fiber purchased by the lab is the Coherent LMA-GDF-20-125, featuring a core diameter of  $20 \mu\text{m}$  and aperture of  $\text{NA} \simeq 0.08$ , whose specified values will be used here for simulations. The normalized frequency (V-number) of such a fiber reads

$$V = \frac{2\pi a}{\lambda} \text{NA}, \quad (\text{IV.4})$$

which, at  $\lambda = 1064 \text{ nm}$ , gives  $V \simeq 3.8$ . This useful number approximates the number of modes a fiber can guide, making the LMA fiber a *few mode* fiber. The company however claims it is easily operated in single mode by properly adjusting the input coupling conditions and not constraining the fiber too tightly, or with critical bending radii. The corresponding fundamental guided-mode radius can be estimated from standard step-index formulae. Using the Marcuse-Petermann approximation,

$$w_P \simeq a \left( 0.65 + \frac{1.619}{V^{3/2}} + \frac{2.879}{V^6} - \left( 0.016 + 1.561 V^{-7} \right) \right), \quad (\text{IV.5})$$

one obtains a mode radius  $w_0^f \sim w_P \sim 8.5 \mu\text{m}$ . This sets the target cavity mode size at the injection mirror for efficient coupling, i.e.  $w_{\text{cav}}(z=0) \sim w_0^f$ . The Rayleigh range  $z_R \sim 2.2 \times 10^2 \mu\text{m}$  then gives us the order of magnitude of the cavity length and mirror radius of curvature needed to achieve good mode matching, which are now in the hundreds of microns range, making the membrane insertion more feasible.

Regarding the collection fiber, we note that even if the injection is optimally mode-matched to the cavity waist using the LMA fiber (with  $w_0^f \simeq w_0 \simeq 8.5 \mu\text{m}$ ), the cavity mode expands over the cavity length. Using  $L \simeq 500 \mu\text{m}$  and  $R \simeq 600 \mu\text{m}$  at  $1064\text{nm}$ , the beam radius at the second mirror reaches  $w(L) \approx w_0 \sqrt{1 + (L/z_R)^2} \simeq 22 \mu\text{m}$ . In other words, the output mode is roughly a factor  $\sim 2.5$  larger than the injected mode. As a re-

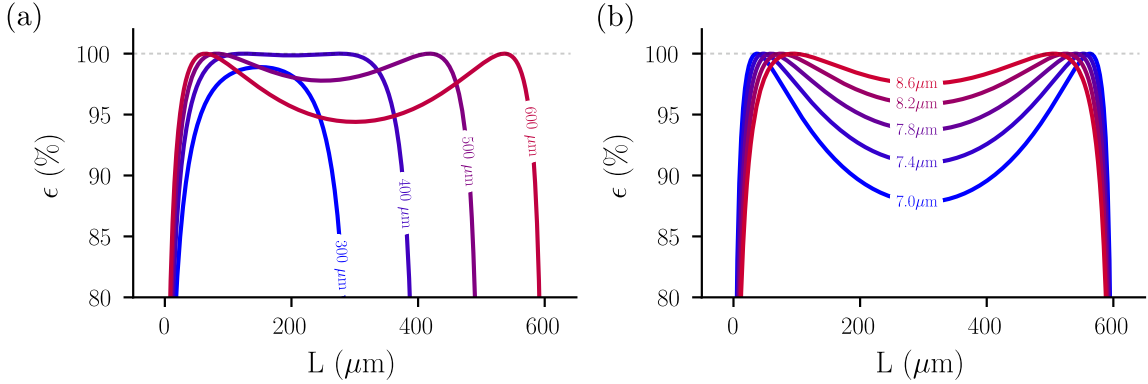


Fig. IV.21 *Coupling efficiency of the fiber mode to the cavity mode as a function of various parameters. (a) Coupling efficiency as a function of the cavity length  $L$  and the mirror radius of curvature  $R$ . The dashed line shows the optimal coupling condition. We observe a plateau of high coupling efficiency around the optimal condition, showing the robustness of the coupling to small deviations from the optimal geometry. (b) Coupling efficiency as a function of a variation in the mode field diameter of the fiber for  $R=600\mu\text{m}$ .*

sult, collecting the transmitted light back into the same LMA fiber would incur a substantial mode-mismatch loss (even under perfect alignment), whereas a large-core collection fiber can capture essentially all of the emerging power without requiring tight matching to a single transverse mode. For this reason, while injection is conveniently performed using an LMA single-mode fiber, the collection will be implemented with a MM fiber.

Using the estimated mode field diameter of the LMA fiber, we can compute the coupling efficiency as a function of the cavity length and mirror radius of curvature, as shown in Fig. IV.21(a) to seek for optimal cavity parameters. We observe a plateau of high coupling efficiency around the optimal condition, showing the robustness of the coupling to small deviations from the optimal geometry. Additionally, we plot in Fig. IV.21(b) the coupling efficiency as a function of a variation in the mode field diameter of the fiber for  $R = 600 \mu\text{m}$ . This shows that a precise knowledge of the fiber mode field diameter is not critical to achieve good mode matching, as variations of hundreds of nanometers still yield coupling efficiencies above 90%, which would result in marginal losses in terms of squeezing level coupled to the cavity mode i.e.  $\sim 0.5\text{dB}$ .

Maintaining good mode matching also requires precise alignment of the fiber in the transverse plane, as well as controlling the tilt of the fiber mirror. The coupling efficiency as

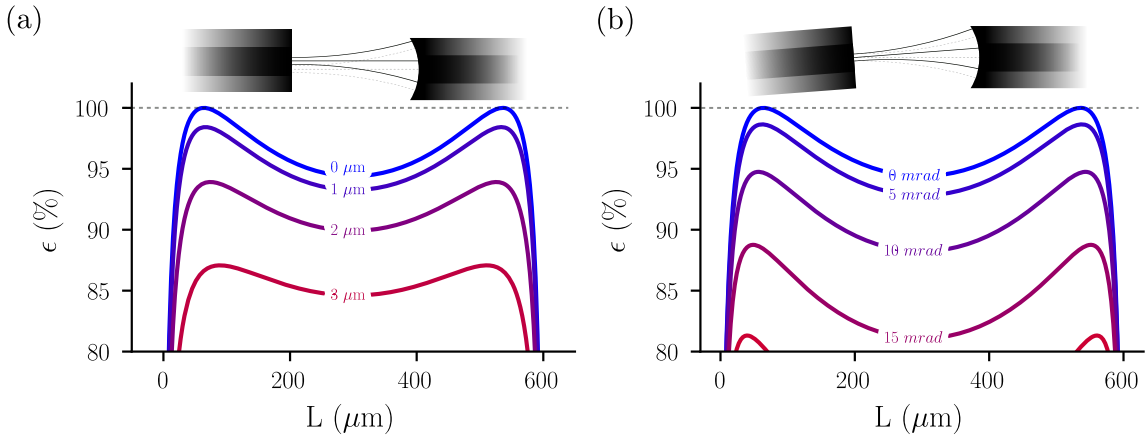


Fig. IV.22 *Coupling efficiency of the fiber mode to the cavity mode as a function of various parameters.* (b) Coupling efficiency as a function of a variation in the mode field diameter of the fiber for  $R=600\mu\text{m}$ . (c) Coupling efficiency as a function of a transverse misalignment between the fiber and the cavity mode for  $R=600\mu\text{m}$ . The positioning of the fiber should hence be precise to submicrometric precision to optimize the mode matching. (d) Coupling efficiency as a function of a tilt misalignment between the fiber and the cavity mode for  $R=600\mu\text{m}$ . The tilt should be controlled to within few mrad.

a function of a misalignment  $d$  in the transverse plane is given by [Siegman1986]

$$\epsilon(d) = \epsilon e^{-(d/d_e)^2}, \quad \text{with} \quad d_e^2 = \frac{2}{\epsilon((1/w_0^f)^2 + (1/w_0)^2)}. \quad (\text{IV.6})$$

Similarly, the coupling efficiency as a function of a tilt misalignment  $\theta$  between the fiber and the cavity mode reads [Siegman1986]

$$\epsilon(\theta) = \epsilon e^{-(\theta/\theta_e)^2}, \quad \text{with} \quad \theta_e^2 = \frac{2}{\pi^2 \epsilon ((w_0^f/\lambda)^2 + (w_0/\lambda)^2)} \quad (\text{IV.7})$$

and the general coupling efficiency becomes  $\epsilon(d, \theta) = \epsilon e^{-(d/d_e)^2} e^{-(\theta/\theta_e)^2}$ . These two expressions are plotted in Fig. IV.22(c) and (d), showing that the transverse positioning of the fiber should be precise to submicrometric precision to optimize the mode matching, while the tilt should be controlled to within few mrad. These constraints are achievable using standard fiber positioning stages such as NanoMax® stages from Thorlabs.

### IV.3.2 Fiber mirror fabrication

The fabrication of high quality fiber mirrors is a crucial step in the realization of fibered optomechanical cavities. The mirrors need to feature low surface roughness, precise radii

of curvature, and high reflectivities to achieve high finesse cavities. The fabrication process typically involves the following steps:

**Fiber preparation:** The optical fibers are first cleaved to obtain a clean and flat end face. This is typically done using a precision fiber cleaver to ensure a perpendicular cut.

**Laser machining:** The cleaved fiber end faces are then shaped using a CO<sub>2</sub> laser. By carefully controlling the laser parameters (power, duration, focus), we can create concave or flat profiles on the fiber tips. Single or multiple laser shots can be used to achieve the desired curvature and surface quality. The machined fiber tips are then characterized using interferometric profilometry to measure their surface profiles and ensure they meet the required specifications.

**Coating deposition:** After shaping, the fiber tips are coated with high-reflectivity dielectric coatings using techniques such as ion beam sputtering or electron beam evaporation. The coatings are designed to achieve the desired reflectivity at the operating wavelength.

**Characterization:** The reflectivity of the coatings are then to be measured using transmission measurements for a rough estimate. More precise measurements can be done by integrating the fiber mirrors into a test cavity and measuring the finesse and resonant reflectivity.

Over my PhD I only got to fabricate and characterize the fiber profiles, while the coating deposition and reflectivity measurements are to be taken over by **Amin LAKHAL** who designed a custom fiber holder with **Pierre MAHIOU** to coat the fibers at the LMA, following the same recipe briefly detailed earlier for the free space mirrors. There, and supervised by **Jerome DEGALLAIX** and **David HOFMAN**, he will need to develop a precise protocol to handle, clean, coat and characterize the fiber mirrors. The first trial of coating realised in 2025 was not successful.

The setup used to shape the fiber tips using the CO<sub>2</sub> laser is shown in Fig. IV.23. The system combines external pulse generation and focusing optics with a high-precision three-axis translation platform for reproducible positioning i.e. shooting path, complemented by an optical profilometer for surface metrology i.e. imaging path. The entire setup is housed in a temperature-stabilized enclosure, and includes a motorized tip/tilt stage to align the fiber facet perpendicular to the CO<sub>2</sub> beam prior to machining. The machining and profilometry beam paths are kept separate, allowing reliable shuttling between processing and measurement locations. The profilometry stage provides sub-micron lateral resolution and, through

averaging, can reach sub-nanometer height sensitivity, enabling automated centering and alignment of fiber cores before fabrication.

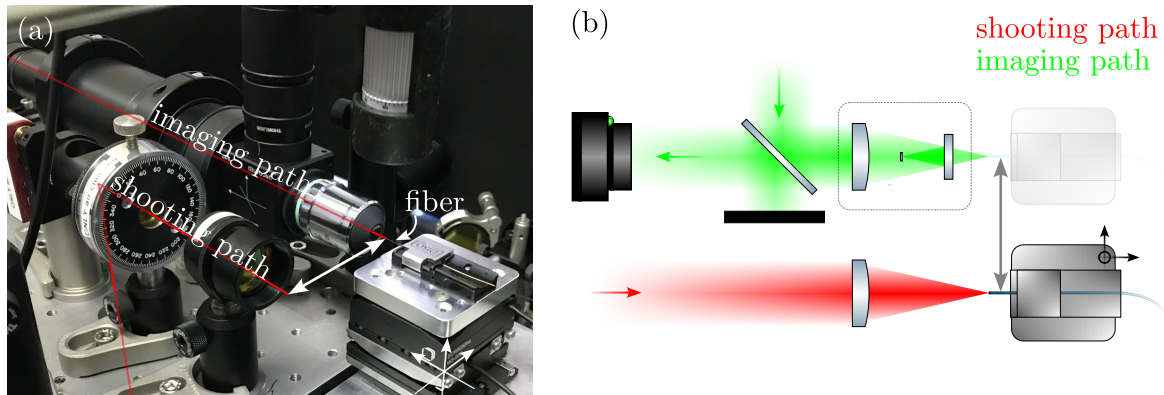


Fig. IV.23  $\text{CO}_2$  laser machining setup for fiber mirror fabrication. (a) Picture of the setup, where we can see the  $\text{CO}_2$  laser path, the imaging path, and the fiber mounted on a 3-axis translation stage. (b) Schematic of the setup, showing the  $\text{CO}_2$  laser beam focused onto the cleaved fiber tip using a lens. The fiber is mounted on a 3-axis translation stage to allow precise positioning and focusing of the laser beam. The precision translation stages allow to move the fiber in and out of the laser focus as needed, implement multiple laser shoot routines, and go back and forth between imaging and machining. The imaging part uses a 515nm LED source along with a Mirau objective to reconstruct the fiber profile interferometrically.

Using this setup under supervision of **Pierre MAHIOU**, I helped fabricating and characterizing various fiber profiles, some of which are shown in Fig. IV.24. We can see a flat fiber profile obtained after cleaving and *cleaning* the fiber tip using a defocused  $\text{CO}_2$  laser shot to remove surface roughness (a). We also see two concave profiles obtained using single (b) and multiple (c)  $\text{CO}_2$  laser shots, yielding parabolic profiles over the fiber core with radii of curvatures ranging from tens to hundreds of microns.

### IV.3.3 Designs and optical layout

Based on the design considerations detailed earlier, we can now propose various designs for the fibered MATE cavity. Additionally, and similarly to our free space MATE cavity, we need to make the system vacuum and cryo compatible, as to allow for low temperature operation. This would point towards the same material as before i.e. OFHC copper, which can be gold coated to prevent oxidation and improve thermalization. The piezo actuators used to tune the cavity length should also be cryo compatible while allowing for sufficient stroke at low temperatures. The Noliac®NAC2402-H3.4 piezo actuators would seem to pro-

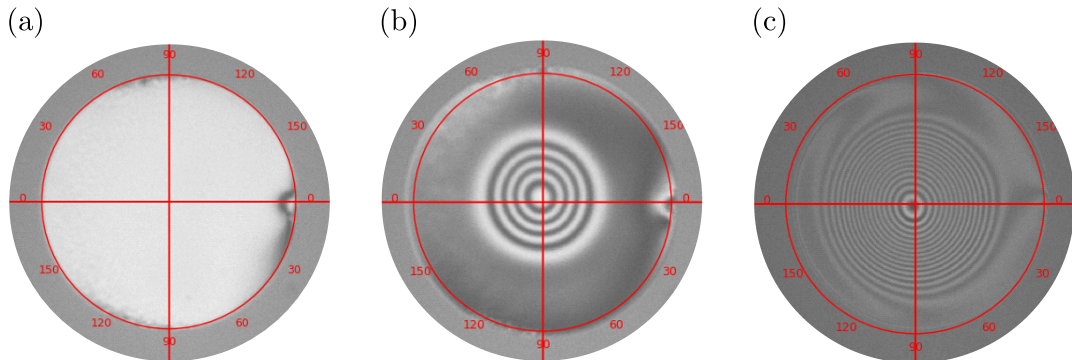


Fig. IV.24 *Interferometric readout of the fiber profiles using a LED at 515nm. Superposing the light field reflected of the fiber surface with a plane phase reference allows to reconstruct the fiber profile with nanometric accuracy.* (a) Profile of a flat fiber, that could be used as a plane mirror. The fiber is cleaved and then cleant using a CO<sub>2</sub> laser to remove surface roughness. (b) Profile of a concave fiber mirror machined using a single shot of the CO<sub>2</sub> laser. The profile yields a gaussian shape. (c) Profile of a concave fiber mirror machined using multiple shots of the CO<sub>2</sub> laser, yielding a parabolic shape.

vide sufficient displacement at cryogenic temperatures i.e.  $6\mu\text{m} \times 2 \times 20\% \sim 2.5 \mu \rightarrow 5 \text{ FSRs}$ , where  $6\mu\text{m}$  is the room temperature stroke, 2 for the two piezos, and 20% the expected displacement in bipolar operation at 10mK: they provide enough displacement as to lock the cavity on resonance with one piezo, and change the relative position of the membrane with respect to the second fiber mirror with the other.

The main challenge lies in inserting and aligning the membrane within the small cavity volume, while allowing for precise tuning of its position. The three main designs considered are shown in Fig. IV.25, where we elaborated a ferrule-based and two v-groove based designs. We now detail their respective advantages and drawbacks.

**Ferrule design** (a) allows for a (relatively) easy alignment of the cavity mirrors using ferrules hosted within ferrule holders glued to the piezos. Like in Harris or Sankey's lab, a single *dummy* fiber would first be inserted through both ferrules/holders to provide a passive alignment. They can then be glued in place. Once the ferrule holders are glued, the dummy fiber is removed and replaced by the actual fiber mirrors. The membrane is then inserted from the top of the assembly, and held in place using two fine screws, providing a mean to correct for tilt. Upon the dummy fiber removal, one would then need to insert the actual fiber mirrors without damaging them, which is challenging. It was reported that coatings on fiber tips usually thicken the fiber diameter by a few microns near the tip, which can

prevent the fiber from being inserted fully into the ferrule, leading to breakage. Removing extra material from the fiber tip by chemical means is an active area of research in some labs, but no established protocol exists yet. As seen earlier in the chapter, constraining the membrane frame too much degrades the mechanical quality factor too.

**V-groove design I** (b) uses v-grooves to host the fiber mirrors, inspired by the fiber cavities developed in Jakob Reichel's group. The v-grooves are then held/glued by their sides using silica pieces, themselves glued on the piezo actuators. The alignment is carried out using a piezoelectric fiber gripper providing force-free release and fine translation, opposed to a tilt-mounted fiber holder for angular optimization. After maximizing the cavity coupling, UV-curable glue is applied to fill the groove/channel surrounding the fiber and is cured using a small-diameter UV beam to confine curing to the adhesive and mitigate drift. The process is repeated for the second fiber, and the final assembly is completed by adding local strain-relief points and minimizing the free-standing fiber length. The Reichel group has experience with this type of design, having used it to probe fiber cavities with record finesse. The membrane is again inserted from the top and held in place using two fine screws. This design still constrains the membrane frame.

**V-groove design II** (c) aims at preserving a higher mechanical quality factor by avoiding constraining the membrane frame too much. In this design, the membrane is glued/held onto a separate piece, which is then inserted from the top and screwed onto the cavity base plate. This allows for a more flexible mounting of the membrane, potentially preserving its mechanical quality factor better than the other designs. The cavity alignment and fiber mounting is similar to design (b).

It was then decided to proceed with the V-groove design II (c), as it seemed to provide the best compromise between ease of assembly, cavity alignment, and mechanical quality factor preservation. The final design is shown in Fig. IV.26, where we can see the various components of the cavity assembly. The membrane is glued/kapton taped to the membrane holder, which is then screwed to the cavity base plate. This should avoid adding stress to the membrane frame. Attention should be paid to thermally anchor the fibers properly to the copper base plate, as to ensure good thermalization of the cavity mirrors at low temperatures.

Once the cavity aligned and the membrane inserted, both fibers are to be spliced *in-situ* to fibers on the vacuum side of our custom KF40 SQS® pigtalled feedthrough. The fibers on the atmosphere side are then coupled to the squeezed light source and HD setup, similar to the one detailed in the next chapter, with the addition of a fibered EOM for PDH locking (not shown on the figure), using the DC output of the HD for example. We show the optical

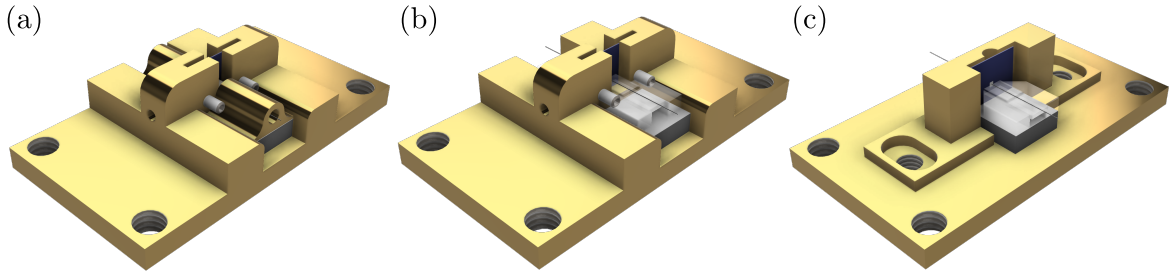


Fig. IV.25 Examples are three possible designs for the fibered MATE cavity. (a) Ferrule based design, where the membrane is inserted from the top of the assembly, then held in place by two fine screws, and where the fibers are inserted inside ferrules. (b) V-groove based design, where the fibers are held and glued in v-grooves positioned on the piezo actuators. Similarly as in (a), the membrane is inserted from the top and held in place by two fine screws. (c) V-groove based design where the membrane is glued on a separate piece, then inserted from the top and screwed to the cavity base plate. This design avoids constraining the membrane frame too much, hence preserving a higher mechanical quality factor in theory.

layout of the experiment in Fig. IV.27, where we can see the various components needed to generate, inject, lock and detect squeezed light from the fibered MATE cavity. Using non PM fibers, care must be taken to properly control and optimize the polarization state injected into the cavity, as to maximize the coupling to the fundamental cavity mode. This can be achieved using fiber polarization controllers.

Regarding the squeezed light degradation, few loss channels are to be considered. First, the mode matching to the filter cavity  $\eta_{\text{cav}}$  needs to be optimized. We estimate a realistic value to be around 90% (although it can reach up to 99% with careful alignment). Additionally, the fiber injection, MATE cavity mode match and collection efficiencies  $\eta_c$  needs to be considered. We can hope for an optimal overall coupling of about 90% too. Finally the detection efficiency  $\eta_{\text{hom}}$  which bundles the photodiode quantum efficiency, the visibility and propagation losses needs to be considered. Assuming high quality photodiodes (quantum efficiency  $\sim 99\%$ ), a good visibility ( $\sim 98\%$ ) and low propagation losses ( $\sim 99\%$ ), we can expect an overall detection efficiency of about 95%. The total efficiency then reads  $\eta_{\text{tot}} = \eta_{\text{cav}} \times \eta_c \times \eta_{\text{hom}} \sim 0.81$ , which would lead to a degradation of about 1.15dB of squeezing for an initial level of 6dB injected into the cavity. This shows that achieving high overall efficiencies is crucial to observe significant squeezing levels at the output of the cavity. On the other hand, pushing the initial squeezing level higher than 6dB would help rendering the experiment more resilient to losses.

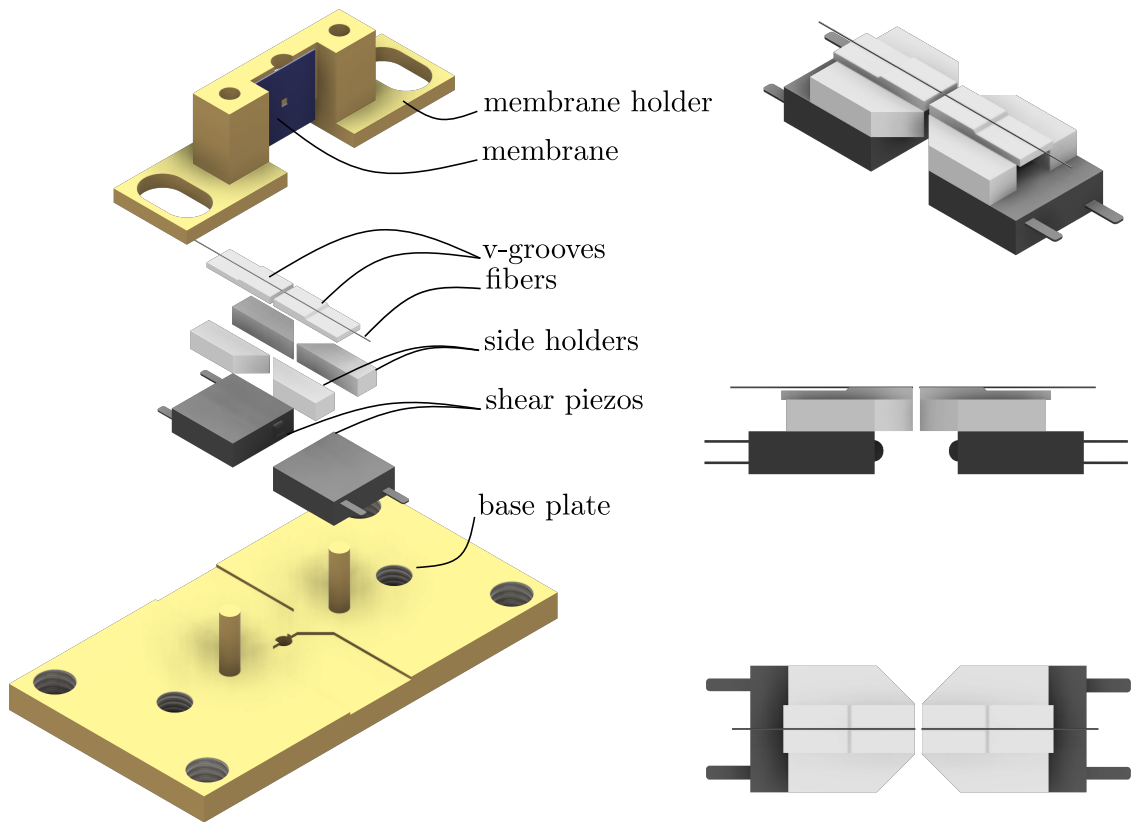


Fig. IV.26 CAD model of the fibered MATE cavity assembly. (left) The membrane is glued/kapton taped to the membrane holder, which is then inserted and screwed to the cavity base plate. The fibered cavity is mounted on two piezo actuators used to tune the cavity length and the membrane position. (right) The fibers are held and glued in v-grooves positioned on the piezo actuators. Various views of the assembly are shown.

#### IV.4 Conclusion & perspectives

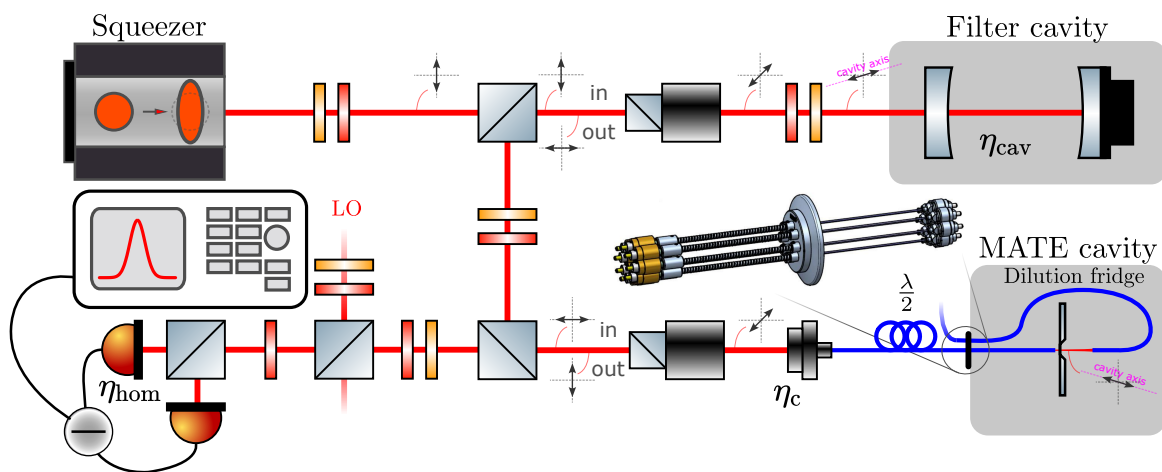


Fig. IV.27 Prospective optical layout for the fibered MATE cavity experiment. The squeezed light source is similar to the one detailed in the next chapter. The frequency dependent bright squeezed field is injected into the MATE cavity using an LMA fiber, while the transmitted light is collected using a MM fiber. Not displayed here is a fibered EOM used to generate the PDH sidebands for locking the cavity. The PDH error signal would be obtained by demodulating the DC output of the HD, while the AC output would be used to monitor the mechanical spectrum.

# Chapter V

## Experiments: Squeezed Light

This chapter will cover the experimental methods used in the development of frequency-dependent squeezing in optomechanical systems, focusing on the generation of squeezed light, optical locking techniques, and quadrature measurement methods. The methods are designed to enhance the sensitivity of measurements in quantum optics and optomechanics.

### Contents

---

V.1	Optical Setup Overview	130
V.2	Cavity Resonances and Locks	133
V.2.1	IRMC Cavity	133
V.2.2	SHG Cavity	135
V.2.3	OPO Cavity	141
V.3	Squeezed State Detection	145
V.3.1	Configuration I	145
V.3.2	Configuration II	147
V.4	Filter Cavity Concept	148
V.4.1	Virgo Filter Cavity	149
V.4.2	Lock and thermal effects	151
V.4.3	Filter cavity for tabletop experiments	153
V.5	Conclusion & perspectives	153

---

## V.1 Optical Setup Overview

The generation and manipulation of squeezed light is a complex process that requires a carefully designed optical setup. Over the course of **Sheon CHUA** postdoctoral work at the lab, **Michael CROQUETTE** PhD work, and my own PhD work, we have developed a versatile setup aiming at producing both bright and vacuum squeezed states of light using an Optical Parametric Oscillator (OPO) below threshold. Squeezing experiments being very prone to losses, noises, or any type of imperfection, the optical table is protected from air currents and temperature fluctuations using a custom-made cabin (inspired from the lab of **Julien LAURAT** and **Alban URVOY**), and the optics were initially mounted in two boxes such that they could be transported easily between different labs, or stacked on top of each other to save space (inspired from **Roman SCHNABEL** lab). Pictures of the setup are shown in

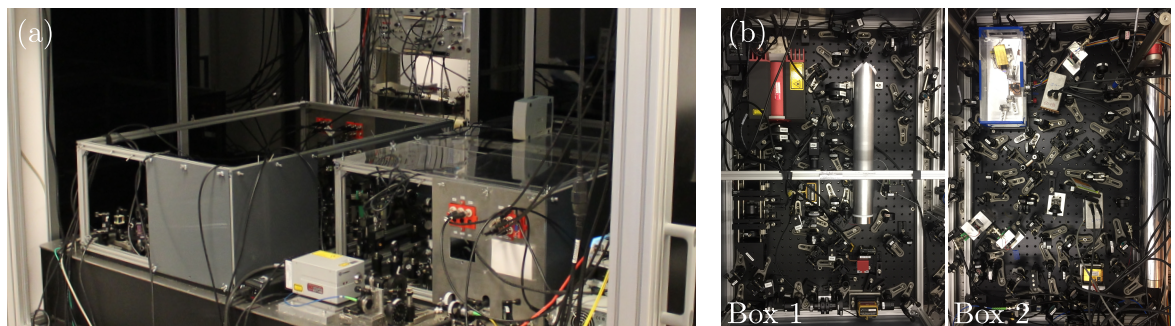


Fig. V.1 *Pictures of the optical setup for squeezed light generation and detection.*  
 (a) *Overview of the experiment inside the cabin.* (b) *Top view of the two boxes containing the optics for squeezed light generation and detection.*

We first provide a general overview of the optical setup used to generate and manipulate squeezed light. Two lasers are used in this setup, to give flexibility as to produce bright squeezing directly from the OPO (one laser only), or produce vacuum squeezing to be mixed with a bright coherent field (two lasers). Both lasers are 1064nm Nd:YAG lasers (Coherent Mephisto and Mephisto S) as in the previous chapter. The full optical layout is shown in figure V.2. The dashed box on the right part of the squeezing setup is the one to be changed to implement both configurations, as shown in figure V.3. The experiment was designed as to easily switch between the two configurations. Throughout this chapter, we will refer to three different optical cavities common to the two configurations: the infrared mode cleaner (IRMC) cavity, the SHG cavity, and the OPO cavity. Each of these cavities is central to the generation and manipulation of squeezed light, and their characterization is detailed in the following sections.

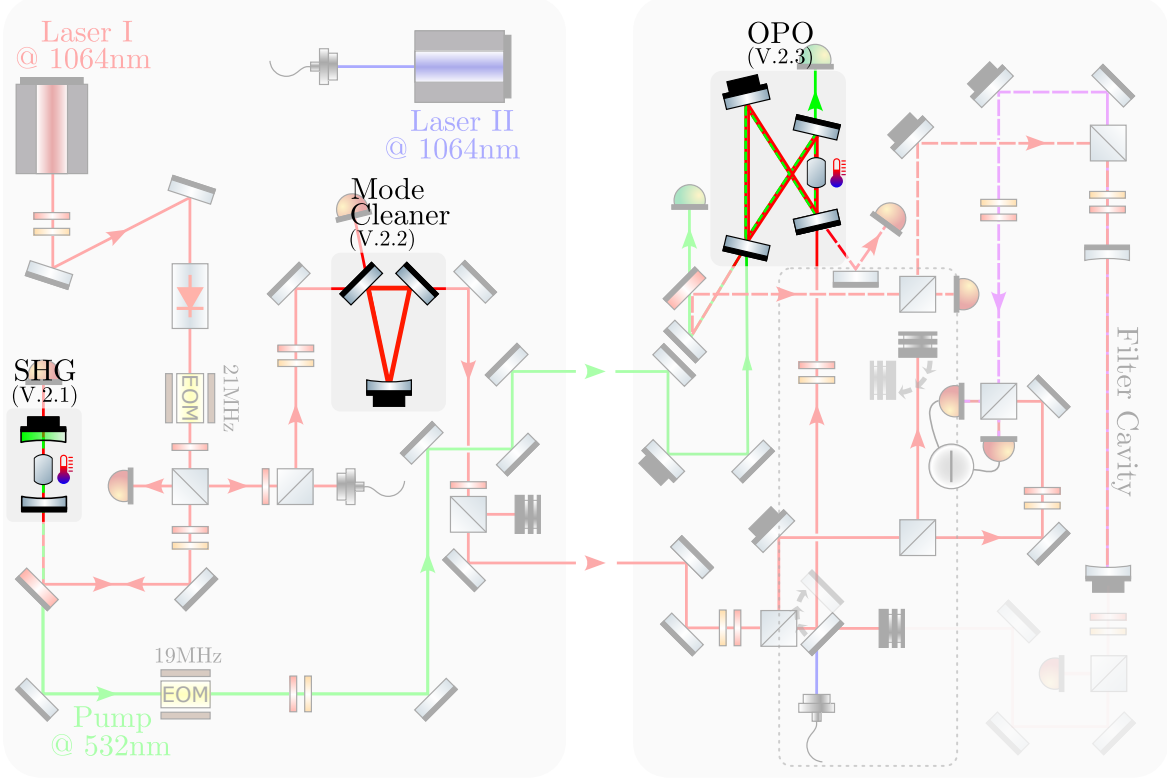


Fig. V.2 Optical layout for squeezed light generation and detection. The setup includes two Nd:YAG lasers, an IRMC cavity for spatial filtering, a SHG cavity to produce the pump beam at 532 nm, and an OPO cavity for squeezing generation. The homodyne detection setup is used to measure the squeezed states. Key components such as electro-optic modulators (EOMs), piezoelectric transducers (PZTs), and photodiodes (PDs) are indicated for locking and detection purposes.

To generate bright squeezed light from an OPO, we now detail the two different configurations implemented in this setup, as shown in figure V.3. The only notable modification between the two configurations lies in the way the OPO is seeded and locked, and in what the piezo actuators are used for.

### Configuration I: bright squeezing from OPO

The first one uses a single laser source, where the main laser beam is split into two paths. It is shown in figure V.3(a). The IR beam outputted from the IRMC cavity is split in two paths: one path is the LO used in the detection, while the other one is sent to the OPO as a bright seed. Locking the pump phase then allows to select the squeezed quadrature. The piezo shown is then used to lock the LO phase.

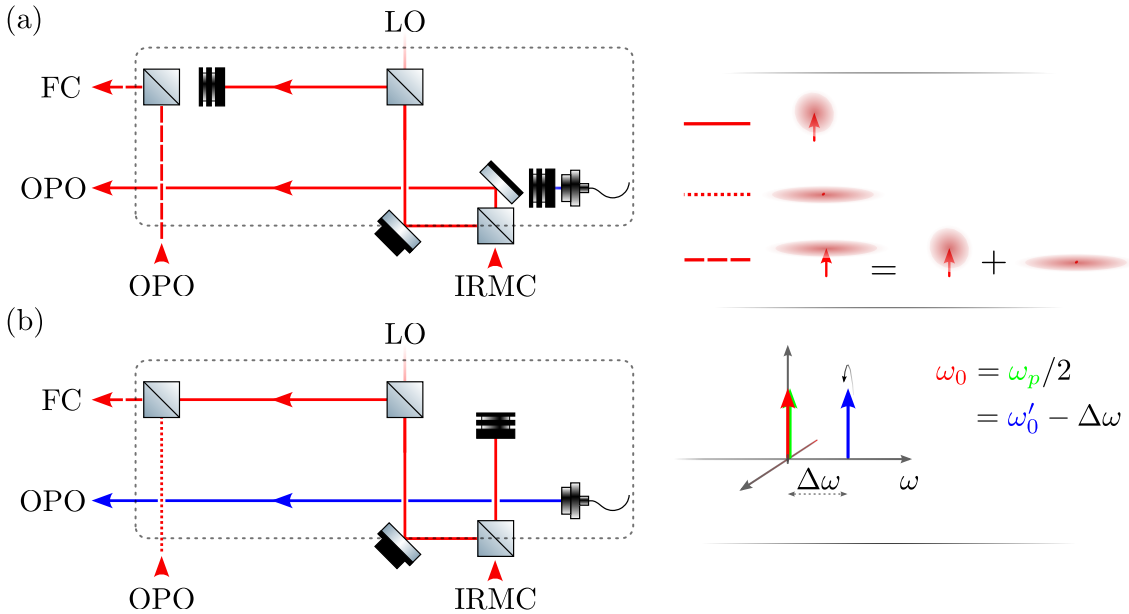


Fig. V.3 Schematic of the two configurations for squeezed light generation. (a) Configuration I: bright squeezing from OPO using a single laser source. The IR beam from the IRMC cavity is split into two paths: one for the local oscillator (LO) and one as a bright seed for the OPO. (b) Configuration II: vacuum squeezing with a bright seed using two lasers. The first laser serves as the detection LO and bright coherent state, while the second laser provides a bright coherent field detuned from the OPO resonance. The outputted vacuum squeezing is then mixed with the bright seed to generate bright squeezing.

### Configuration II: vacuum squeezing + bright seed

The second configuration employs the two lasers. Its schematic configuration is shown in figure V.3(b). The first laser is used both as a detection LO, as well as a bright coherent state to be mixed with the squeezed vacuum generated by the OPO. In this case, the piezo shown is used to lock the relative phase between the bright seed and the vacuum squeezing ellipse angle as to select the squeezed quadrature. A second piezo not displayed here is used to lock the signal quadrature to be probed by the detection. The second laser provides a bright coherent field detuned from the OPO resonance. This field, seen as a strong sideband, is injected into the OPO cavity. The photons generated from the pump beam at 532nm will then be down-converted into pairs of photons, which eventually populate the sideband mode at the second laser frequency. These correlated photons being equally distributed in the upper and lower sidebands around the first laser frequency (since the pump was generated from it), demodulating the IR signal leaking from the cavity at the PLL frequency and twice the PLL frequency allows to extract two error signals. The first one, at the PLL frequency, gives us the phase of the pump with respect to the bright seed, while the second one,

at twice the PLL frequency, gives us access to the quadrature angle of the squeezed vacuum with respect to the bright seed. Hence, we lock the pump phase using the first error signal, while the second error signal is used to lock the homodyne angle to the optimal squeezing quadrature.

The second configuration is more complex to implement, but is meant to render the squeezing generation more robust to low-frequency noises. It was studied over Michael Croquette's PhD thesis [[croquette\\_thesis](#)] and the start of mine, where we obtained 3dB of vacuum squeezing and 1.5dB of bright squeezing. These results will quickly be summarized in section V.3.2, but we will mainly focus on the first configuration in the rest of this chapter V.3.1, as it is simpler to implement and optimize.

## V.2 Cavity Resonances and Locks

### V.2.1 IRMC Cavity

The first cavity presented is the infrared mode cleaner (IRMC) cavity. The purpose of this cavity is to spatially filter the laser beam, ensuring a high-quality TEM00 mode profile, as well as *cleaning* the IR beam from any excess classical noise as developed in Chapter I. It is a three mirror - *travelling wave* Fabry-Pérot resonator with a total round-trip length of  $L = 84$  cm, corresponding to a free spectral range of  $\text{FSR} = 357$  MHz. The input and output coupler have a radius of curvature of  $\text{RoC} = -2$  m, while the middle mirror is flat. With a measured optical linewidth of  $\kappa/2\pi = 52$  kHz, the finesse reaches a value of  $\mathcal{F} \sim 7000$ , which ensures significant filtering of laser frequency noise and intensity noise above the cavity linewidth. The associated round-trip losses are estimated to be around 900 ppm, dominated by the input coupler transmission of  $T_1 = 666$  ppm. The cavity parameters are summarized in Table V.1.

This cavity is mounted in a aluminium housing to make it as monolithic as possible. The optimal alignment of the cavity is found by first making sure the laser beam goes through the first two mirrors without being clipped. This is most easily done by positioning a IR camera in transmission of the cavity rather than a photodiode. Once the beam is well centered on the first two mirrors, we adjust the angle of the output coupler to center the beam on the concave/second mirror. We then adjust the position of the concave mirror such that the first reflection spot coincides with the input beam on the input coupler surface. Finally, we adjust the angle of the input coupler to superpose the consecutive round-trip spots with the input beam reflected from the input coupler surface. This is most easily done in the far-field limit, such that great angular precision can be achieved doing so. A characteristic elliptic

Specifications	
Length (cm)	84.0
FSR (MHz)	357
$T_1^{\text{spec}}$ (ppm)	475
$T_2^{\text{spec}}$ (ppm)	475
RoC (m)	-2
Measurements	
Finesse $\mathcal{F}$	6812
Linewidth (kHz)	52
$T_1 + T_2 + \mathcal{L}$ (ppm)	922
Resonant reflection $R(0)$	0.44
$T_1$ (ppm)	767
$T_2 + \mathcal{L}$ (ppm)	155

Table V.1: IRMC parameter table summary.

shape formed by the multiple spots appears as one converges to the optimal alignment, seen both in reflection on an IR card and in transmission on the IR camera. Once the cavity is pre-aligned, we position a photodiode in both reflection and transmission of the cavity, and scan the cavity length. One can then beam walk the input beam as to maximise the coupling to the TEM00 mode of the cavity, observed as the highest and narrowest resonance peak in transmission. Triggering the oscilloscope on the PZT ramp, we measure the cavity linewidth and finesse, as well as the resonant reflection to estimate the various cavity parameters.

The cavity is then locked using a standard PDH technique, with a preliminary side-of-fringe lock to bring the cavity close to resonance. The input beam is phase-modulated at  $\Omega_{\text{mod}} = 21$  MHz using a free space EOM (New Focus IR 4003). The cavity length is swept, and the detected reflected beam is manipulated with PyRPL to generate the PDH error signal. The finesse being relatively high, we observed cavity ringing effects when scanning the cavity length resonance too quickly, as already seen in the previous chapter. The cavity length was then swept over gently at 0.5 Hz as to recover the expected lorentzian resonance peaks in reflection.

Once locked, the intensity noise spectra of the reflected and transmitted beam are measured in direct detection. We then renormalize the transmitted spectra by the known  $R(0)$  to yield equivalent optical powers. The results are shown in figure V.4, where we observe significant noise suppression above the cavity bandwidth (half linewidth) of 26 kHz. This is notably seen in the attenuation of the laser relaxation oscillation peak around 1 MHz. However, at low frequencies, the intensity noise is amplified, most likely due to the feedback loop. Above 2 MHz, the intensity noise reaches the shot noise level, indicating that the

IRMC effectively filters classical intensity noise from the laser. At the membrane fundamental mode frequency of  $\sim 850$  kHz, the laser intensity noise is suppressed by approximately 20 dB, which is beneficial for optomechanical experiments. It does however not reach the shot noise level, indicating that further improvements in the cavity locking or laser stabilization may be necessary for optimal performance.

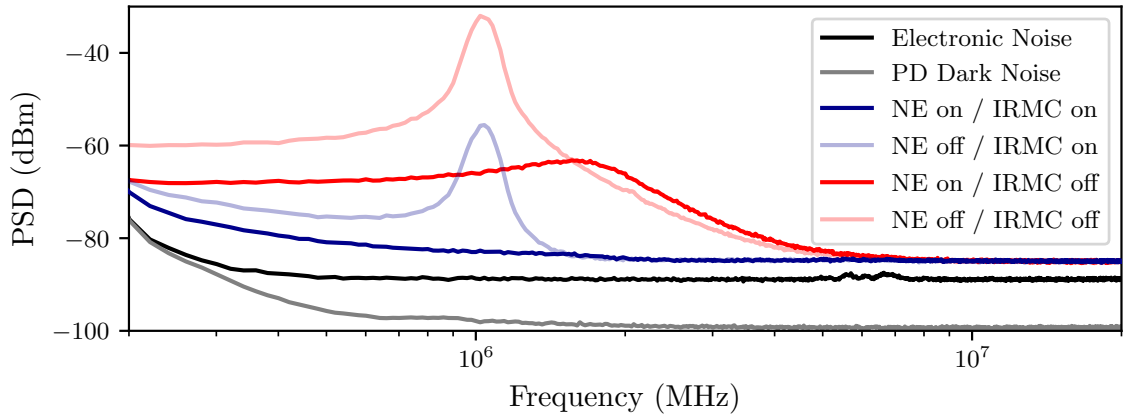


Fig. V.4 Noise spectra of the IRMC transmitted beam in direct detection, showing significant suppression of classical intensity noise above the cavity linewidth. We show the curves for unfiltered IR beams with and without the laser noise eater on, where we see the relaxation oscillation peak being significantly attenuated and shifted up in frequency when the noise eater is on. The relaxation oscillation peak around 1 MHz is notably attenuated upon IRMC filtering. However, low-frequency noise is amplified, likely due to feedback effects. Above 2 MHz, the intensity noise reaches the shot noise level, indicating effective filtering of classical noise by the IRMC.

The IRMC beam is now directed to the homodyne detection setup to measure the phase noise of the transmitted beam. The results are shown in figure V.5, where we observe a linear variation of the phase noise with the LO power, confirming that the detected noise is indeed shot noise limited. The residual classical noises below 2 MHz are effectively killed by the HD detection, and we deduce a clearance of approximately 10dB up to 10 MHz, which is satisfactory for squeezing measurements.

### V.2.2 SHG Cavity

In order to generate a stable 532 nm pump beam for the OPO, we implemented and characterized a linear SHG cavity. The cavity is designed to resonantly enhance an incoming IR field at 1064 nm, and convert it to its second harmonic at 532 nm using a periodically poled lithium niobate (PPLN) crystal as the nonlinear medium. The crystal is a Covington

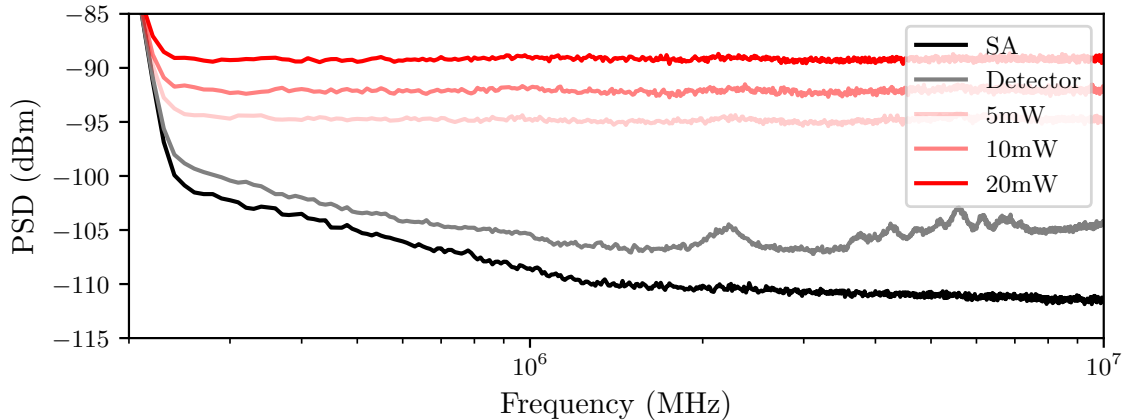


Fig. V.5 Noise spectra of the IRMC transmitted beam in homodyne detection, showing shot noise limited behavior across the measured frequency range. The phase noise scales linearly with the LO power, confirming the shot noise dominance. A clearance of approximately 10 dB is observed up to 10 MHz, indicating effective suppression of residual classical noise by the homodyne detection scheme.

$1 \times 10 \times 10\text{mm}^3$  MgO:PPLN SHG crystal with five different quasi-phase-matching gratings in the bulk, with poling periods ranging from  $6.83\text{\mu m}$  to  $6.96\text{\mu m}$  and apertures of  $1\text{mm}^2$ . The crystal is temperature controlled using a Covision® temperature controller to achieve optimal phase matching for SHG, with a temperature stabilized to  $10\text{mK}$  precision. The crystal and its oven are then positioned at the center of the SHG cavity. The cavity features two mirrors with radii of curvature -250mm, ensuring that the crystal length is shorter than the Rayleigh range of the cavity mode, thus minimizing diffraction losses. The output coupler is HR coated for both IR and green wavelengths, while the input coupler has a transmission of 10% at  $1064\text{nm}$  and less than 1% at  $532\text{nm}$ . These characteristics are summarized in table V.2. It results in a theoretical cavity finesse of approximately 60 at  $1064\text{nm}$ , while the finesse at  $532\text{nm}$  would be around 1, as no cavity buildup is desired at this wavelength. The reflected IR and green beams are then separated on a dichroic mirror before being sent to their respective detection systems, as seen in figure V.6(a).

This cavity is first aligned without the crystal to find the optimal cavity mode. Taking off the input coupler, we center the beam on the output coupler, and adjust its angle to retro-reflect the beam back onto itself, using two irises for example. We then re-insert the input coupler and adjust its angle to superpose the input beam with the retro-reflected beam from the output coupler. Once the cavity is pre-aligned, we insert the PPLN crystal and adjust its position to recover the cavity resonance peaks, as well as placing a photodiode in transmission to monitor resonances on an oscilloscope. One can then beam walk the input

Specifications	
Length (cm)	9
FSR (GHz)	3.3
Specified $T_1$ @1064nm	10%
Specified $T_2$ @1064nm	0.5%
Specified $T_1$ @532nm	>99%
Specified $T_2$ @532nm	<0.1%
Roc input/output (mm)	-250
Measurements	
Finesse IR $\mathcal{F}$	30
Linewidth (MHz)	111
$T_1 + T_2 + \mathcal{L}$ (ppm)	$\sim 2.10^6$

Table V.2: SHG cavity parameter table summary.  
The specified values are taken from the PhD thesis  
of M. Croquette [**croquette\_thesis**].

beam as to maximize the coupling to the TEM00 mode of the cavity, observed as the highest and narrowest resonance peak in transmission. Doing so, and if the IR beam passes through one of the PPLN gratings (and not in between), we observe green flashes by eye, indicating successful SHG every time the cavity comes to resonance.

Initial characterization was performed by scanning the cavity length around resonance using a piezoelectric transducer on which the cavity output coupler was glued. The input infrared power was maintained at approximately 100 mW. The transmitted IR signal and the generated green output were simultaneously monitored on fast photodiodes. Typical traces of the transmitted IR beam are shown in Fig. V.6(b)–(c). As the cavity length is swept, the cavity exhibits sharp IR resonance peaks, corresponding to successive TEM00 modes of the cavity. At the same time, the green output rises only in coincidence with infrared resonances, confirming that efficient SHG occurs exclusively under resonant build-up of the fundamental field. The actual IR finesse was measured to be  $\mathcal{F} = 30$ , where the discrepancy is attributed to poor knowledge of the mirror parameters, as well as optical losses from the non linear medium. The polarization of the input beam is controlled by half and quarter waveplates as to maximize the output green power, and the symmetry of the resonance peaks in the scans further indicates negligible birefringence in the PPLN crystal.

This cavity is first aligned without the crystal in order to identify the optimal cavity mode. After removing the input coupler, the beam is centered on the output coupler and its angle is adjusted to retro-reflect the beam back onto itself (e.g., using two irises). The input coupler is then re-inserted and aligned so as to overlap the incident beam with the

retro-reflected beam from the output coupler, providing a robust pre-alignment of the cavity. The PPLN crystal is subsequently inserted and its position is adjusted to recover the cavity resonances, while a transmission photodiode is used to monitor the resonance peaks on an oscilloscope. Final coupling is optimized by beam-walking the input beam to maximize the TEM00 coupling, identified as the highest and narrowest transmission resonance; when the infrared beam is correctly routed through one of the PPLN gratings (and not between gratings), green flashes are observed at resonance, indicating efficient SHG. Initial characterization is then performed by scanning the cavity length around resonance using a piezoelectric transducer bonded to the output coupler, while maintaining an input infrared power of approximately 100, mW. The transmitted infrared signal is monitored on a fast photodiode (see typical trace in Fig. V.6(b)), showing sharp infrared resonance peaks with green output occurring only in coincidence with these resonances, consistent with SHG taking place exclusively under resonant build-up of the fundamental field. The infrared finesse is measured to be  $\mathcal{F}_{\text{IR}} = 30$ , with the discrepancy attributed to imperfect knowledge of the mirror parameters and additional intracavity losses introduced by the nonlinear medium. The input polarization is adjusted using half- and quarter-waveplates to maximize the generated green power, and the observed symmetry of the resonance peaks further suggests negligible birefringence in the PPLN crystal.

Modulating the input IR beam at  $\Omega_{\text{mod}} = 21 \text{ MHz}$  using the same free space EOM as for the IRMC cavity (New Focus<sup>®</sup> IR 4003), we manipulated the detected IR signal into a PDH error signal suitable for locking the cavity length to resonance, with a preliminary side-of-fringe lock as usual. A typical lock trace is shown in Fig. V.6(c), where both the transmitted IR power and the generated green power are monitored on an oscilloscope. The first striking observation is the drift of the transmitted IR and reflected green power away from their nominal peak heights. This effect is attributed to thermal effects in the PPLN crystal: upon locking, the intracavity IR power stabilizes at a relatively high intensity, leading to heating of the crystal due to residual absorption. This heating causes a change in the refractive index and physical dimensions of the crystal, thereby shifting the optimal quasi phase matching temperature (the oven would need to be locked to a lower temperature as to compensate for this extra optical heating). As a result, the cavity drifts away from the optimal resonance, necessitating a manual tuning of the temperature setpoint to recover maximum green output. Keeping the IR power at about 200mW, we could then scan the crystal temperature to find the optimal phase-matching condition for SHG. The results are shown in Fig V.7(a), where we found a maximum green output of around 100 mW at a crystal temperature of  $\sim 58^\circ\text{C}$  for the  $6.90 \mu\text{m}$  grating, sufficient to pump the OPO below threshold. The conversion efficiency usually follows a sinc-squared dependence on temperature. Due to the high IR power build-up in the cavity, thermal effects are observed, which distort the expected  $\text{sinc}^2$  shape

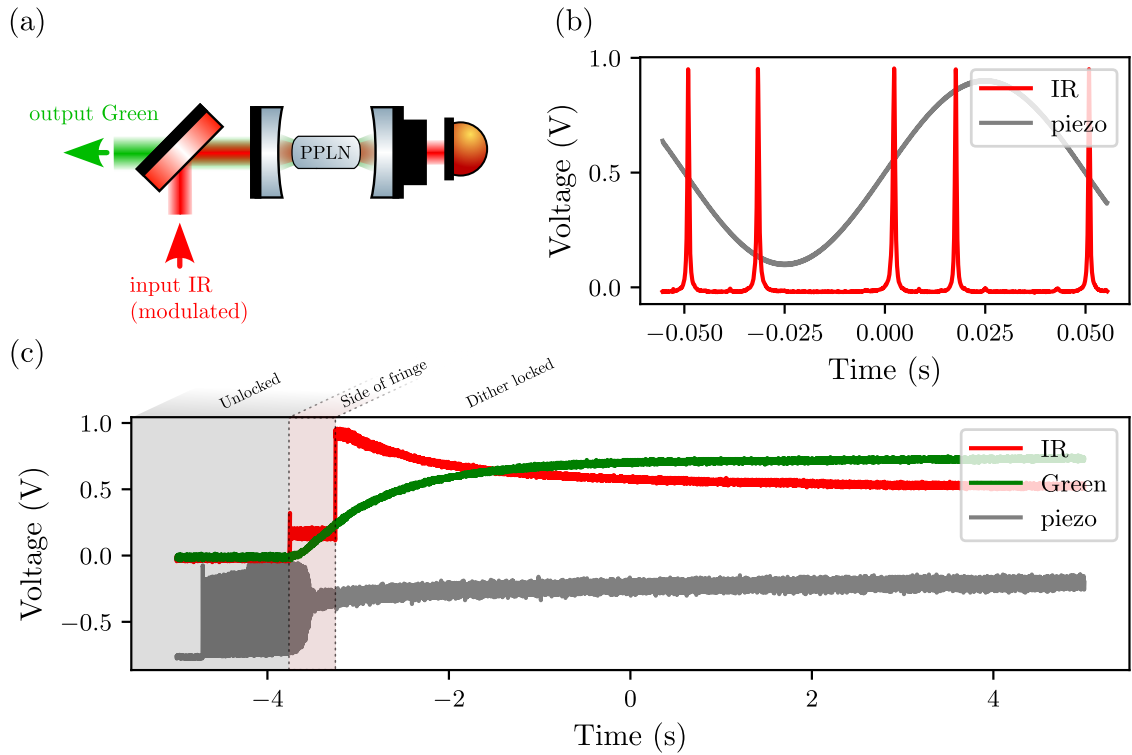


Fig. V.6 Overview of the SHG cavity locking: (a) Schematic of the PDH lock setup used to stabilize the SHG cavity length to resonance. The temperature of the PPLN crystal is locked via a commercial temperature controller from Covington<sup>®</sup>. (b) Cavity scan at low input IR power, showing the IR resonances onto which the cavity is locked. A PDH error signal, not displayed here, is tuned as to lock the cavity (c) Cavity lock as seen on the scope, showing the transmitted IR power (red) and the generated green power (green). We observe a drift away from the nominal peak height, due to thermal effects in the crystal. More precisely, the heating of the crystal changes the effective optical length of the cavity, hence shifting the resonance condition. This needs to be tuned by the experimenter.

as reported in ... The side lobes of the  $\text{sinc}^2$  curve are seen when scanning the temperature over a larger range, but we only show the central peak here. The symmetric  $\text{sinc}^2$  shape is however recovered when injecting an order of magnitude less IR power, but not useful to our purpose as it does not provide sufficient power for the OPO. To measure our SHG conversion efficiency, we varied the input IR power while keeping the crystal temperature at the optimal phase-matching point by tuning the temperature slightly at each new IR power injected to maximise the output green power. The results are shown in Fig V.7(b), where we observe a pseudo-linear dependence of the green output power with respect to the input IR power. From a linear fit, we extract a conversion efficiency of approximately 54%, which is (very) satisfactory for our application, and rather high compared to similar setups in the

literature [eckardt\_high-efficiency\_2019, kourogi\_high-efficiency\_2020].

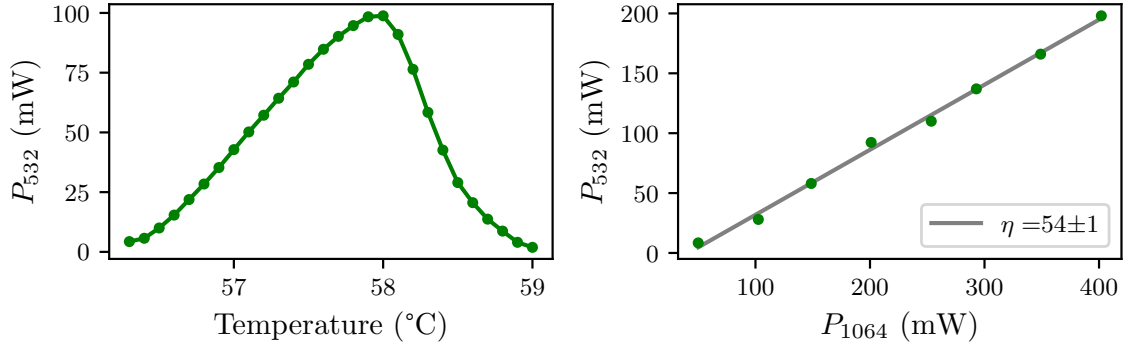


Fig. V.7 *Output power of the SHG cavity varying against different parameters:* (a) *Output green power measured against the crystal temperature, showing the phase-matching curve at high input IR power. A hysteresis is observed due to thermal effects.* (b) *Output green power as a function of the IR input power, showing pseudo linear behavior. The SHG conversion efficiency is extracted from a linear fit, yielding a value of 54%*

We can now place a photodiode on the path of the outgoing green beam to monitor its intensity noise spectrum. The results are shown in figure V.8, where we observe significant excess intensity noise above the shot noise level for frequencies in the range Hz-10MHz. We identify the peak at 2MHz as the relaxation oscillation frequency of the IR laser transduced to the second harmonics field. This excess noise will severely limit the achievable squeezing level from the OPO, as classical pump noise is known to degrade squeezing generation. We can however expect to achieve squeezing above the 2MHz band.

We now have a *clean* TEM00 IR beam from the IRMC cavity outputting up to 200mW, as well as a stable TEM00 532nm green pump beam from the SHG cavity delivering up to 200mW. Both beams are now directed to the OPO cavity for squeezing generation. Further improvements of the experimental setup could include a Mach-Zehnder (MZ) interferometer after the SHG cavity to stabilize the green power sent to the OPO, as thermal effects in the PPLN crystal can lead to fluctuations in the output power over time [ref], as well as a mode cleaner cavity for the green beam too, to ensure a high-quality spatial mode and suppress any classical noise from the SHG process and cavity locking. However, these improvements were not implemented in the current setup, and it is thought that these would alter the (relative) simplicity of the setup without significantly lowering classical noises.

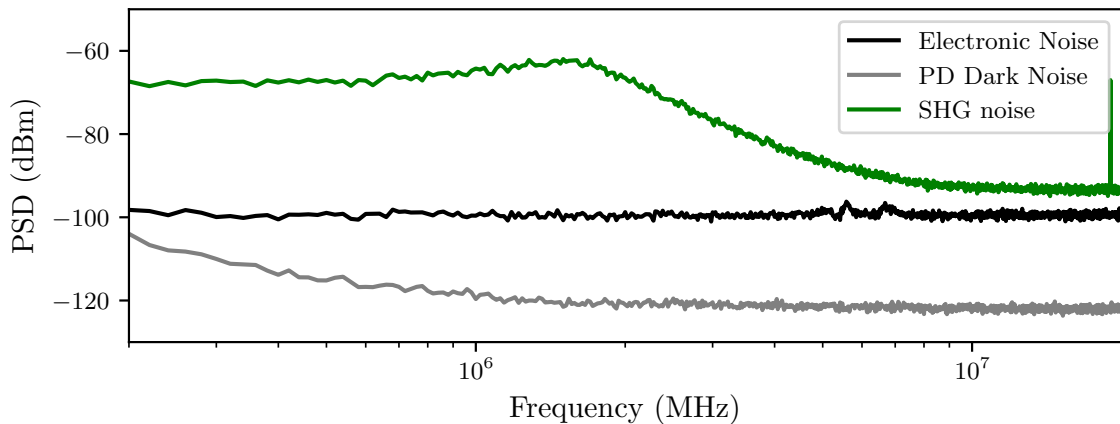


Fig. V.8 *Intensity noise spectrum of the SHG output beam, showing significant excess noise above the shot noise level across the measured frequency range. The relaxation oscillation peak at 2 MHz is notably transduced from the fundamental IR laser to the second harmonic field, indicating that classical pump noise may limit squeezing performance in the OPO. The noise floor is not the same as for the previous figure because the RBW is different.*

### V.2.3 OPO Cavity

The final cavity is the Optical Parametric Oscillator (OPO) cavity, which is the core of the squeezed light generation setup. The OPO is bow-tie travelling-wave cavity designed to be resonant for both the fundamental IR field at 1064 nm and the pump field at 532 nm. The cavity contains a periodically poled potassium titanyl phosphate (PPKTP) crystal as the nonlinear medium for parametric down-conversion. The crystal is a Raicol®  $1 \times 5 \times 11.2$  mm<sup>3</sup> PPKTP crystal with a poling period of  $9.0\text{ }\mu\text{m}$ , designed for type-I phase matching at room temperature. It has been coated on both sides to be anti-reflective at both 1064 nm and 532 nm by Laseroptik®, and is mounted in a temperature-controlled oven to maintain phase-matching conditions, with a temperature stability of 100mK. The crystal further features a wedge angle on one face to allow for gross tuning of the quasi-phase-matching condition by displacing the crystal using the 4 axis mount the whole assembly is held on (Newport® 9071-M). The fine tuning of the phase-matching is achieved by adjusting the crystal temperature.

The cavity is formed by two concave mirrors with a radius of curvature of 25 mm, as well as two flat mirrors. One of the flat mirrors is mounted on a PZT actuator to allow for cavity length tuning and locking. The angle of the bow tie cavity needs to be as small as possible to optimize the mode matching (reduces astigmatism), while keeping a sufficient distance between the mirrors to accommodate the crystal mount. To align the cavity, we follow a similar procedure as for the IRMC cavity (and any travelling wave cavity for that matter).

Using the pump beam as a proxy (because seeable with the eye), we first center the beam on the first two (flat) mirrors without clipping, then adjust the angle of the second mirror to center the beam on the first concave mirror. We similarly adjust the position of this mirror to center the beam on the second concave mirror, and then adjust its angle to reflect it onto the input beam spot on the input coupler surface. Finally, we adjust the angle of the input coupler to superpose the consecutive round-trip spots with the input beam reflected from the input coupler surface, once again in the far-field limit for better precision (and watch out for that typical elliptical shape). Once the cavity is pre-aligned, we position a photodiode in both reflection and transmission of the cavity, and scan the cavity length. One can then beam walk the input beam as to maximise the coupling to the TEM00 mode of the cavity as usual. We then insert back the crystal mount and adjust its position to recover the cavity resonance peaks. This step can be very tricky and time-consuming, as the crystal mount can easily clip the beam if not well centered. Injecting the IR beam from the IRMC output, we then beam walk the input beam to maximize the coupling to the TEM00 mode of the cavity. To achieve co-resonance, we then proceed to the gross tuning of the quasi-phase-matching condition by displacing the crystal laterally using the 4 axis mount while scanning the cavity length, by periodically beam walking the two beams to remain optimally matched to the fundamental mode. We can then proceed to the cavity characterization.

The mirror coatings of the OPO cavity were selected with the primary objective of maximizing the escape efficiency of the squeezed field at 1064 nm, while maintaining a pump resonance at 532 nm that is sufficiently robust for stable operation. As seen before in chapter I, this motivates an overcoupled design at 1064 nm, in which the desired output coupler dominates the total round-trip dissipation. Writing the effective round-trip loss rate for the down-converted field as the sum of the output coupling and parasitic losses, we recall the definition of the escape efficiency  $\eta_{\text{esc}}$ :

$$\eta_{\text{esc}} = \frac{\kappa_2}{\kappa} = \frac{T_2^{1064}}{T_2^{1064} + T_1^{1064} + \mathcal{L}},$$

where  $T_1^{1064}$  is the power transmittivity of the 1064 nm output coupler and  $\mathcal{L}$  denotes the additional loss. Experimentally, we measured  $T_{\text{out}}^{1064} + \mathcal{L} \approx 7.5\%$ . Assuming additional losses on the order of a few hundred ppm, we get an estimated escape efficiency of  $\eta_{\text{esc}} \approx 99.2\%$ .

On the pump side (532 nm), the coating strategy is intentionally different. The pump resonance was designed to be low finesse ( $\mathcal{F}_{532} \approx 8.5$ ) with a large pump input coupler ( $T_{\text{in}}^{532} \approx 74\%$ ). A broad pump resonance improves operational robustness by reducing sensitivity to cavity-length fluctuations and simplifying acquisition and locking, while still enabling sufficient circulating pump power to reach threshold (measured  $P_{\text{th}} \approx 80 \text{ mW}$ ). It however jitters

the coresonance, seen as abrupt variations of the seed amplification/deamplification traces, too fast to be corrected by the temperature control. Overall, the combined coating choices implement a consistent design philosophy: *minimize parasitic loss and enforce overcoupling at 1064 nm to maximize escape efficiency and preserve squeezing, while keeping the pump resonance forgiving and efficiently driven at 532 nm to ensure stable, reproducible operation.* The measured parameters of the OPO cavity are summarized in Table V.3.

Specifications	
Length (cm)	27.2
FSR (GHz)	1.1
RoC (mm)	-38
Measurements	
IR Finesse $\mathcal{F}_{1064}$	84
IR Linewidth (MHz)	13
IR resonant reflection $R^{1064}(0)$	0.97
IR input coupler $T_1^{1064}$	0.02%
IR output coupler $T_2^{1064} + \mathcal{L}$	7.5%
Pump Finesse $\mathcal{F}_{532}$	8.5
Pump Linewidth (MHz)	130
Pump resonant reflection $R^{532}(0)$	0.87
Pump input coupler $T_1^{532}$	74%
Pump output coupler $T_2^{532} + \mathcal{L}$	3%
OPO threshold $P_{\text{th}}$	80.2 mW
escape efficiency	99.2%

Table V.3: OPO cavity parameter table summary.

The cavity length is now swept using the PZT actuator to observe the resonances at both wavelengths. The input pump beam is phase-modulated at  $\Omega_{\text{mod}} = 19 \text{ MHz}$  (New Focus® IR 4001), and the transmitted and reflected signals are manipulated with PyRPL to generate a PDH error signal suitable for locking the cavity length to resonance, with a preliminary side-of-fringe lock as usual. Once locked, we proceed to the fine-tuning of the quasi phase-matching condition by adjusting the crystal temperature to maximize the amplification/deamplification of the seed. Fig V.9(a) shows a typical scan of the cavity length below threshold, where we observe the co-resonance of both the pump and IR beams. Above threshold, as seen in Fig V.9(b), the IR resonance peak height increases significantly due to the onset of parametric oscillation, indicating that the pump power has exceeded the threshold value, such that IR photons are generated at every pump resonance (which is not the case below threshold). This is a clear signature of OPO operation.

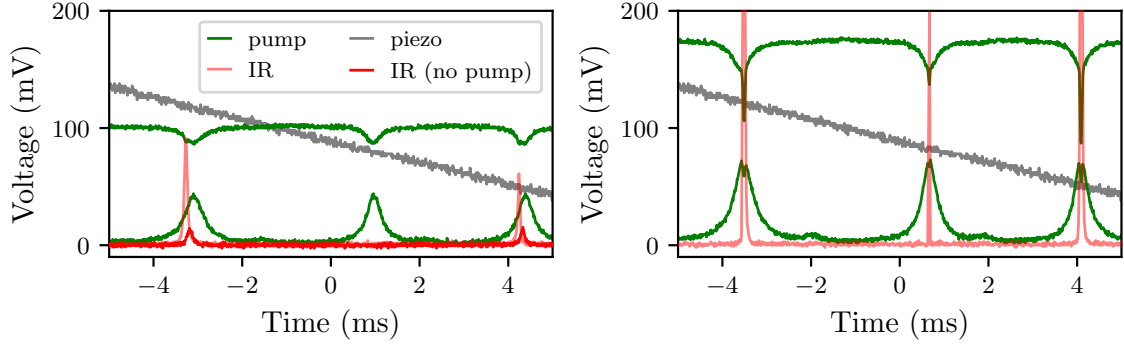


Fig. V.9 OPO resonances observed by scanning the cavity length. (a) co-resonance of the pump and IR beam below threshold i.e. no oscillation is observed (b) resonance of the IR beam above threshold, showing the onset of parametric oscillation as the pump power exceeds the threshold value.

To precisely estimate the OPO threshold power, we measure the amplified and deamplified output IR power when seeding the OPO with the IR seed. By sweeping the pump power from zero to above threshold while keeping the seed power constant, we record the extrema of the typical gain curve shown in Fig V.10(a). The curve obtained is fitted using the standard OPO gain model [bachor\_guide\_2004], and we find a threshold power of  $P_{\text{th}} = 104.85 \text{ mW}$  for the amplification data, and  $P_{\text{th}} = 80.29 \text{ mW}$  for the deamplification data.

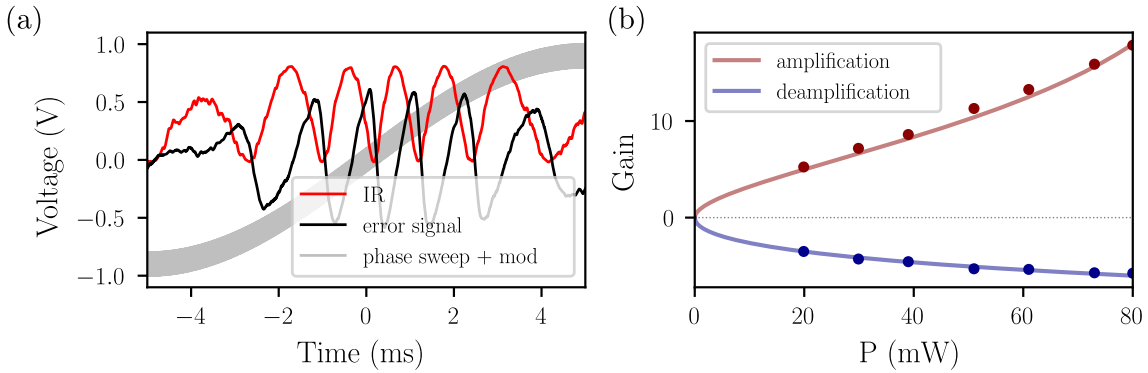


Fig. V.10 Fitted  $P_{\text{th}}$  for amplification: 104.85 & Fitted  $P_{\text{th}}$  for deamplification: 80.29

We then need to lock the pump phase to stabilize the squeezed quadrature angle. When seeding the OPO with a bright coherent field from the IRMC output, we detect the transmitted IR beam on a photodiode by placing a 99:1 beamsplitter and directing the 1% port to a fast photodiode in direct detection while the 99% port is sent to the homodyne detec-

tion setup. We then implement a dithering lock technique by modulating the pump phase at  $\sim 50\text{kHz}$  using the PZT mounted mirror in the pump path. The detected IR signal is demodulated at the dither frequency with a variable phase shift to generate an error signal proportional to the derivative of the amplified/deamplified output power with respect to the pump phase. This error signal is then fed to a PyRPL PID module before seeding it back to the PZT actuator to lock the pump phase to the deamplification phase. The error signal is shown in Fig V.10(a), where we observe a clear zero-crossing at the deamplification point. Once locked and optimized, we can proceed to the noise study of the resulting bright squeezed state.

## V.3 Squeezed State Detection

### V.3.1 Configuration I

In order to characterise the generated squeezed states from the OPO, we direct the transmitted squeezed beam to the homodyne detection setup. We first calibrate the shot noise level by blocking the OPO output beam and measuring the homodyne noise spectrum for various LO powers, as seen in Fig V.5. The homodyne detection is carefully balanced to ensure maximum common mode rejection of classical noises, and the LO power is set to about 10mW for optimal clearance above the electronic noise floor, 10dB in our case. The common mode rejection ratio is measured to be at least 10dB across the measured frequency range using the attenuation of the LO intensity noise when both photodiodes are illuminated. A proper calibration of the CMRR would be needed to be more precise (using a proper AM tone), but this is sufficient for a preliminary characterization.

The circuit of the homodyne detection was elaborated by **L. Neuhaus** in his PhD thesis [[neuhaus\\_thesis\\_2021](#)], and features two output channels. The first one, a DC-100kHz output, is used to monitor the DC level of the homodyne signal, useful for alignment and mode matching optimization. The second output channel is a RF output, AC coupled (1-100MHz), which is sent to a spectrum analyser to measure the noise spectrum of the detected quadrature. The LO phase can be scanned using a PZT actuator on which one of the homodyne mirrors is glued, or locked to a specific quadrature using a dithering lock technique similar to the one used for the OPO pump phase lock. Injecting the bright squeezed beam from the OPO of about  $10\mu\text{W}$ , the visibility of the detection is optimized by adjusting the LO mode matching and alignment, as well as the relative angle of the two polarizations using a half-wave plate before the PBS. A visibility of 98% is achieved, which is satisfactory. The beam splitter used to mix the signals being very angle dependent as well as polarization dependent, we need to carefully adjust both the angle of incidence and the polarization of

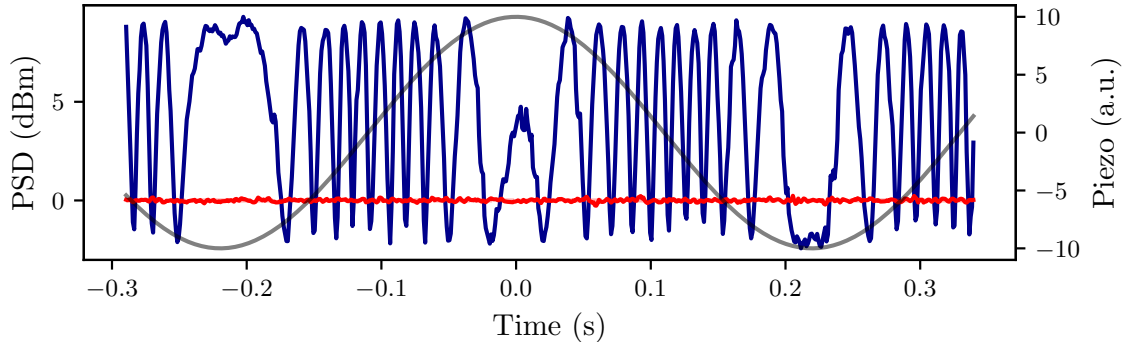


Fig. V.11 Fitted  $P_{th}$  for amplification: 104.85 & Fitted  $P_{th}$  for deamplification: 80.29

the incoming beams to maximize the visibility. A trick is to slightly ellipticize the beams using a quarter waveplate, as to converge to the optimal balance more easily.

Once optimally balanced, we seed the OPO with a pump of 60mW, expecting a squeezing-antisqueezing level of -5.3-12.6 dB respectively, uncorrected for detection losses, from the standard OPO squeezing model. We then measure the noise at 10MHz while slowly scanning the LO phase. The results are shown in Fig V.11, where we observe clear squeezing and anti-squeezing levels as the LO phase is scanned. We measure a squeezing level of 1.6dB and an anti-squeezing level of about 9.0dB at 10MHz. These values are rather modest, and can be attributed to several factors including residual classical pump noise from the SHG cavity, imperfect mode matching and visibility in the homodyne detection, as well as parasitic losses in the OPO cavity and detection chain. Further optimization of these parameters could lead to improved squeezing performance in future experiments. The LO phase is then locked to the squeezed quadrature using the dithering lock technique described earlier, and we can proceed to the spectral analysis of the squeezing level. The resulting spectra are shown in Fig V.12, where we observe that the pump noise from the SHG cavity limits the squeezing level at low frequencies, with squeezing only observed above 2MHz where the pump noise reaches the shot noise level. We also identify the relaxation oscillation of the seed beam at 1MHz i.e. residual from IRMC and enhanced by the homodyne detection scheme, as well as the downconcereted relaxation oscillation at twice the frequency, confirming the occurence of second order nonlinear processes in the OPO cavity.

Further characterization of the squeezing level at various pump powers and analysis frequencies could be performed to better understand the limitations of the current setup. Placing the IRMC cavity before the SHG cavity to filter the pump beam could significantly

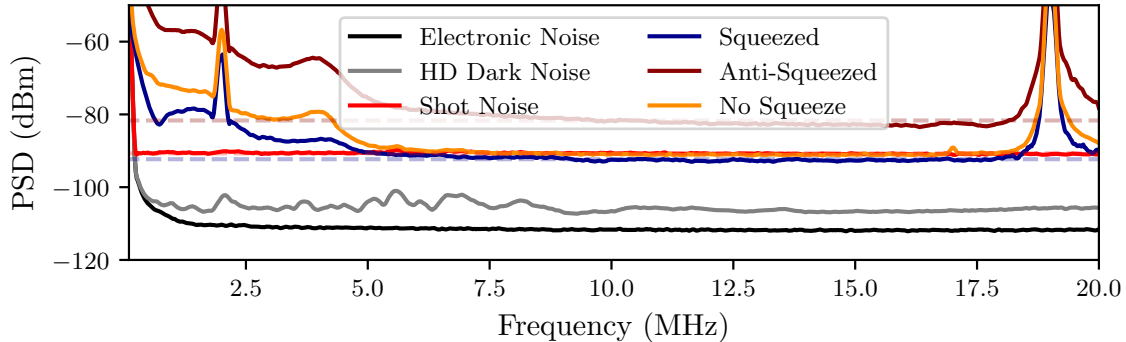


Fig. V.12 Fitted  $P_{th}$  for amplification: 104.85 & Fitted  $P_{th}$  for deamplification: 80.29

reduce classical pump noise and improve squeezing performance at low frequencies. Additionally, implementing a mode cleaner cavity for the green pump beam could enhance spatial mode quality and further suppress classical noise contributions. Overall, while the current setup demonstrates the generation of squeezed states, there is room for optimization to achieve higher bright squeezing levels suitable for subSQL optomechanical experiments.

### V.3.2 Configuration II

We now turn to the second configuration, in which the OPO is not seeded by a bright coherent field, but rather operated in the vacuum squeezing regime. The data presented here were acquired at the end of M. Croquette's PhD thesis [[croquette\\_thesis](#)], and I participated in the data analysis and interpretation of the results. We briefly discuss them here for completeness, but redirect the reader to his thesis for a more detailed account.

In this configuration, the squeezed vacuum states generated by the OPO are directly sent to the homodyne detection setup without any bright seed. The homodyne detection is configured similarly as before, with the LO power set to about 10mW and the visibility maximized. A coherent control field (CCF) is then needed to lock both the OPO pump phase and the LO phase to the squeezed quadrature. The CCF is a weak coherent field injected into the OPO cavity at a frequency offset of about ten MHz from the main laser frequency. The PLL to do so has been described in section ??, and is implemented using PyRPL. The seed is initially injected into the cavity to mode match the cavity. Then, using fiber components, we change the seed for the CCF which is now detuned by an amount of the order of the OPO bandwidth such that CCF photons do see the non-linear gain of the OPO. The OPO is then locked, and the LO phase is swept to observe the squeezing and anti-squeezing levels as seen in Fig V.13(a). We observe a squeezing level of 3dB and an

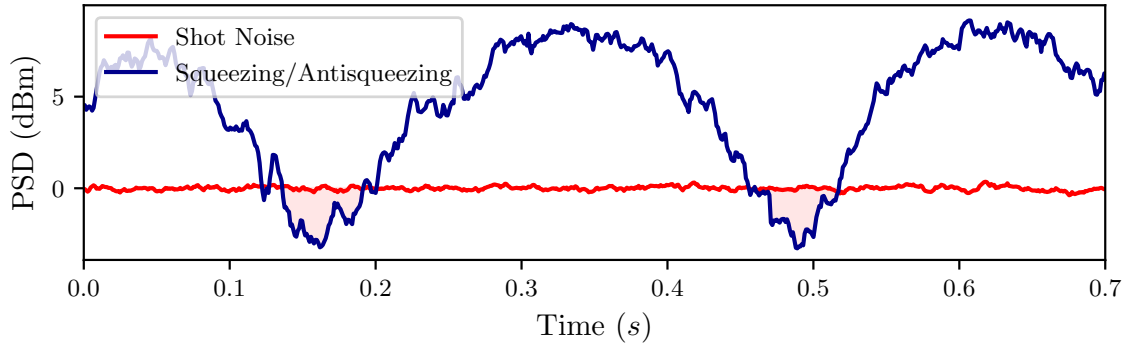


Fig. V.13 Squeezing and antisqueezing levels while varying the pump phase. These levels are obtained at 500kHz analysis frequency.

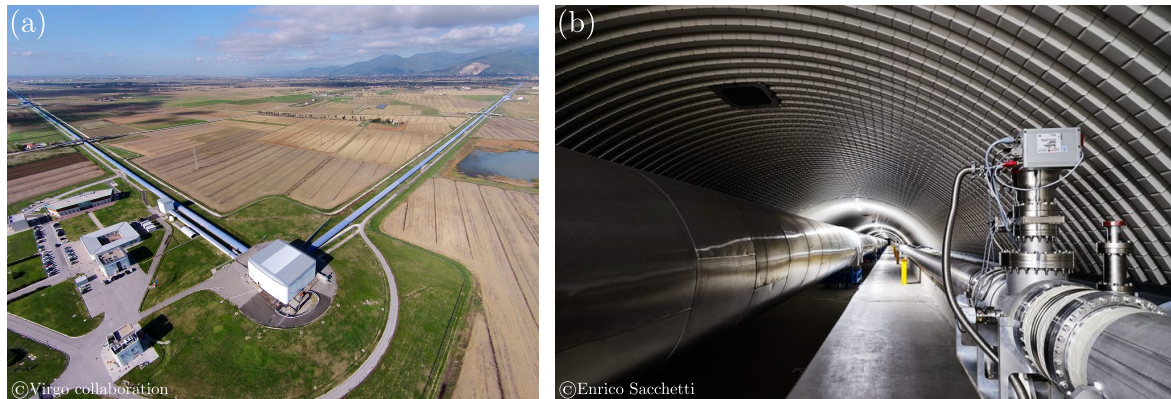


Fig. V.14 (a) Aerial view of Virgo site. (b) Picture of the filter cavity vacuum tank, housing the 285m long Fabry-Perot cavity in parallel to the North arm of the interferometer.

antisqueezing level of 9dB at 500kHz analysis frequency.

#### V.4 Filter Cavity Concept

As detailed in the previous chapters, the generation of squeezed states of light alone cannot provide a reduction of quantum noise across a broad frequency range in interferometric measurements, nor allow subSQL measurements of a mechanical resonator embedded within a resonant optical cavity. To achieve this, the squeezed states must be manipulated in a frequency-dependent manner to optimally reduce quantum noise at each frequency of interest. This is accomplished by reflecting the squeezed states off a detuned optical cavity.

Over the course of my PhD, I was lucky enough to collaborate the Virgo collaboration to help characterizing their filter cavity (FC), designed to provide frequency-dependent squeez-

ing for the Advanced Virgo gravitational wave detector. Although drastically different in scale compared to our tabletop OPO setup, the underlying principles remain the same, and it was a great opportunity to gain insight into the challenges of implementing frequency-dependent squeezing in interferometers.

This part will briefly summarize the work done on the Virgo FC, focusing on the thermal effects encountered when implementing a bichromatic lock. This work was carried out under the supervision of **Jean Pierre ZENDRI**, and in collaboration with **Luis Diego BONAVENA** and **Yuhang ZHAO** from the Virgo collaboration. No extensive reviews of the optical setup nor the detailed characterization of the cavity will be provided here, as they are out of the scope of this thesis. For further details on the Virgo filter cavity and its characterization, I refer the reader to the PhD thesis of **Luis Diego BONAVENA** [[bonavena\\_thesis\\_2024](#)], as well as the associated publications [[bonavena\\_frequency-dependent\\_2023](#), [bonavena\\_characterization\\_2024](#)].

#### V.4.1 Virgo Filter Cavity

The Virgo FC aims to implement frequency-dependent squeezing in the Advanced Virgo gravitational wave detector, enhancing its sensitivity to gravitational waves. The cavity is a 285m long Fabry-Perot cavity located in Cascina, in the North arm of the interferometer. The cavity is designed to provide a frequency-dependent rotation of the squeezed quadrature at about 25Hz, where the radiation pressure noise and shot noise contributions are equivalent for the Virgo interferometer. The FC is mounted inside a vacuum tank, and is formed by two dual coating mirrors treated by the LMA, with input mirror IR transmittivity of 562ppm and an end mirror transmittivity of 3ppm, leading to a finesse of about 10000 at 1064nm, as well as a green transmittivity of both mirrors of 2.7%, leading to a finesse of about 120 at 532nm. The reflected IR beams are then directed towards a standard HD detection setup. A picture of the cavity tank as well as an aerial view of the Virgo site are shown in Fig V.14.

The vacuum squeezed light source developed for Virgo is similar to the one described earlier. It outputs squeezing level as high as 8.5dB down to the Hz level. When characterizing the filter cavity, a retro-reflector used induces a stray light bump below 20Hz i.e. scattered light coupled to seismic noises, and limits the achievable FDS squeezing level at low frequencies. It produces FDS squeezing levels of about 5dB which is subsequently injected into the FC. The FDS curve obtained by the Virgo collaboration in 2023 is shown in Fig V.15, showing a frequency-dependent rotation of the squeezed quadrature at about 90Hz, limited by the stray light bump at low frequencies.

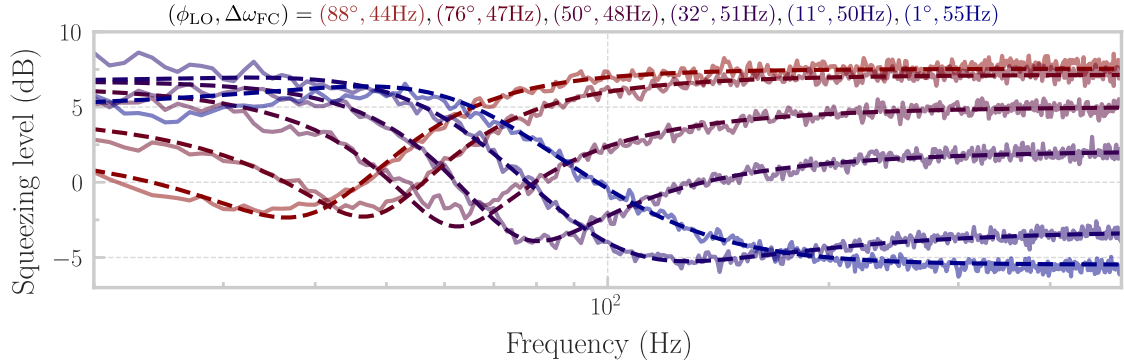


Fig. V.15 Frequency-dependent squeezing levels obtained by the Virgo collaboration in 2023, showing a rotation of the squeezed quadrature at about 90Hz. The low frequency squeezing level is limited by a stray light bump below 20Hz. Although the green beam detuning is kept constant at 45Hz, the fitted detuning of the FDS traces varies by about 20% over time, attributed various effects, including thermal effects.

The setup to lock the FC involves two IR lasers, that we will refer to as the main laser and the sub carrier laser (SC).

**The main laser:** The first one is an IR laser (1064nm) at frequency  $\omega_0$ , which is used to pump the SHG cavity in order to generate a green beam at frequency  $\omega_p = 2\omega_0$  (532nm). This green beam is then separated in two paths. The first path is used to pump the OPO cavity below threshold to generate the vacuum squeezed states at  $\omega_0$ . The second path is frequency shifted using an AOM to generate a beam at frequency  $\omega'_p = \omega_p + \Delta\omega_p$ , phase modulated and subsequently injected into the filter cavity for locking. Demodulation of the reflected signal generates a PDH error signal at 532nm.

**The SC laser:** The second laser is another IR laser at frequency  $\omega'_0 = \omega_0 + \Delta\omega_0$ , phase locked to the main laser with an offset frequency of  $\Delta\omega_0$ . This SC laser is used to probe the filter cavity at IR wavelength, by injecting it into the cavity after being phase modulated to generate a PDH error signal.

The two lasers are phase/frequency locked using a PLL scheme, such that the detuning of the SC laser with respect to both the green beam and the squeezed beam is kept constant at  $\Delta\omega_0$ . Importantly, injecting the *bright* SC laser into the setup saturates the HD detection, such that it is currently not possible to measure HD spectra with the SC laser on.

#### V.4.2 Lock and thermal effects

##### Naive GR lock

The first locking scheme implemented for the Virgo FC involves locking the cavity length to the green beam only, using a standard PDH technique. The green beam at frequency  $\omega'_p$  is injected into the cavity, and the reflected signal used for the lock. The detuning of the squeezed beam with respect to the cavity resonance is then set by adjusting the frequency offset  $\Delta\omega_p$  introduced by the AOM. To circumvent the issue of the stray light bump at low frequency, the detuning was set to 180Hz, where the squeezing level is not significantly affected. The reflected FDS beam is then directed towards the HD detection. The LO is derived from the main laser, and the homodyne detection is performed similarly as described in section V.3.1. By scanning the LO phase and recording the AC noise spectrum, the squeezing levels can be measured and the optimal LO phase can be locked.

Operating this setup for tens of hours (even days), it was observed that the squeezing minima drifted over time, with a characteristic period of about 24 hours. A typical trace of such a drift with both the FC and the HD angle locked (at a  $\pi/2$  phase) over more than ten hours is shown in Fig V.16. The clear drift of the FDS minimum over time, points towards bichromatic detuning of the filter cavity. Recording the temperature of both cavity mirrors continuously, it was realized that these detuning drifts were correlated with temperature fluctuations of the end mirrors, as shown in Fig V.17. This effect was attributed to thermal effects, and notably to a sensitive change in the phase picked up by both beam upon reflection on the end cavity mirror (the 3ppm one), changing the effective optical length of the cavity as seen by both wavelengths. This effect was further confirmed by performing controlled temperature variations of the end mirror, and measuring the corresponding variation in cavity detuning.

##### Bichromatic lock

To circumvent these thermal effects, a more robust locking scheme was implemented, relying on bichromatic locking of the cavity to both the green beam and the SC laser. This scheme ensures that the cavity remains at coresonance for both wavelengths, thereby stabilizing the detuning of the squeezed beam with respect to the cavity resonance. Both the SC laser at  $\omega'_0$  and the green beam at  $\omega'_p$  are injected into the cavity to achieve coresonance. Upon coresonance, the squeezed beam would be locked at the right detuning, since its detuning with respect to the SC beam is set by the PLL. The green beam at frequency  $\omega'_p$  is once again obtained by frequency shifting the green beam generated from the main laser using the AOM. The AOM is driven by a VCO, and the name of the game is to lock the VCO frequency by adjusting the seeded offset voltage. The cavity being continuously locked to

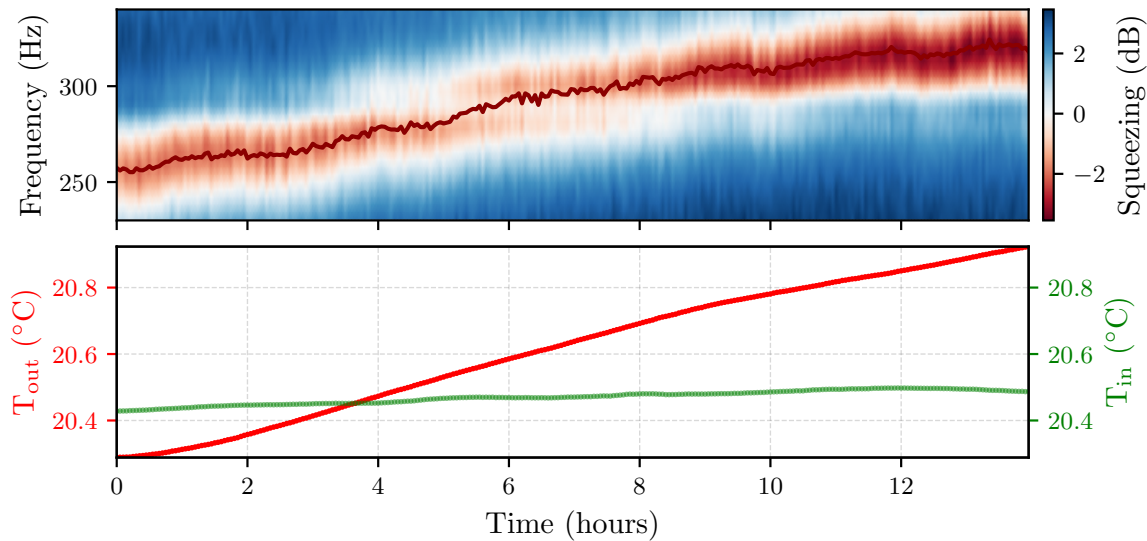


Fig. V.16 Observation of thermally induced detuning drifts over time, correlated with temperature fluctuations of the end cavity mirror. The data were recorded on the 11th of January 2023. (top) FDS HD traces recorded over more than 10 hours, showing the drift of the squeezed quadrature minimum (red) with respect to the shot noise level (white). Blue areas indicate antisqueezing regions. (bottom) Temperatures of the input (green) and end (orange) cavity mirrors over the same time period.

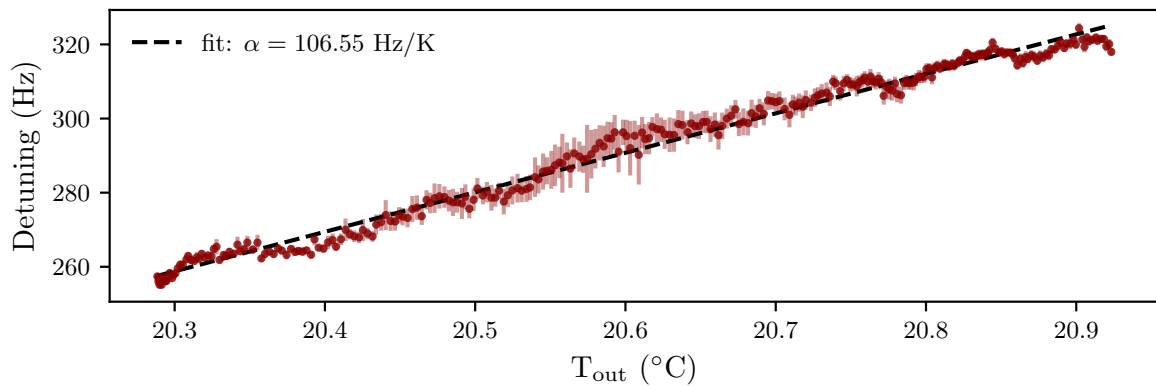


Fig. V.17 Frequency of the squeezed quadrature minimum against FC end mirror temperature for the same data batch, showing a clear correlation between temperature variations and detuning drifts.

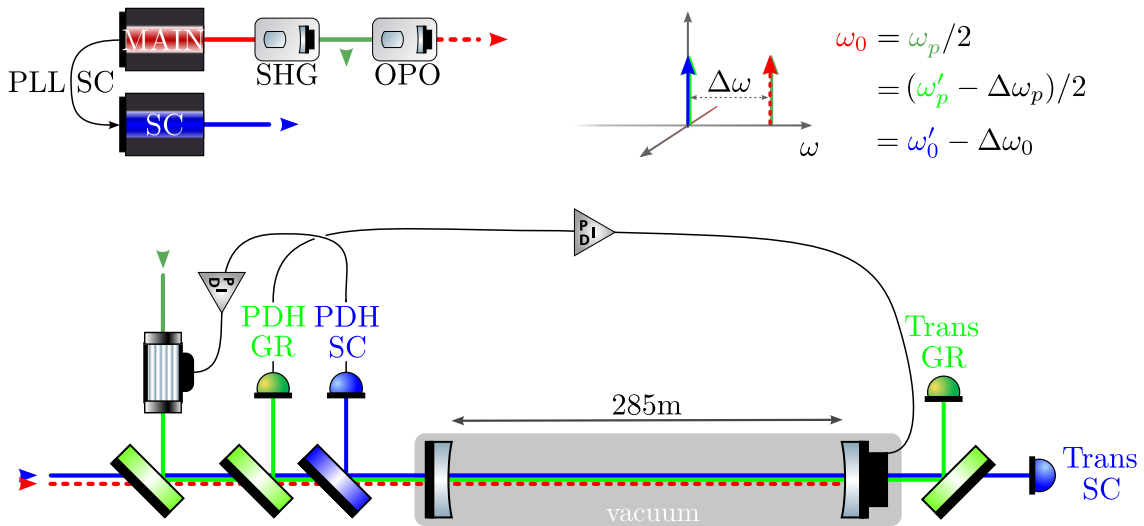


Fig. V.18 *Full schematic of the bichromatic locking scheme implemented for the Virgo filter cavity. The cavity length is locked to the green beam using a standard PDH technique, while the VCO offset frequency is adjusted using the SC PDH error signal to achieve coresonance for both wavelengths. The naive lock presented in the main text is done by simply locking the cavity length to the green beam only (no PID block on the AOM).*

the green beam while changing the VCO offset, the correct VCO offset yields coresonance. The error signal being fed back to the VCO is therefore the SC PDH error signal, which monitors the detuning of the cavity with respect to the SC laser. The PID controller output seeking to minimize this error signal is then used to adjust the VCO offset voltage, thereby locking the cavity to coresonance. The schematic of the locking setup is shown in Fig V.18.

Thermally induced bichromatic detuning of the cavity was then further confirmed operating this setup for a long period of time upon forced temperature variations of the end mirror. The probe of this detuning over time is now the seeded VCO voltage, which directly indicates the detuning of the cavity with respect to the SC laser. We refer the reader to the associated publication [bonavena\_frequency-dependent\_2023] for further details on this locking scheme and an extensive analysis of the thermal effects encountered.

#### V.4.3 Filter cavity for tabletop experiments

### V.5 Conclusion & perspectives



# **Conclusion**

This chapter will cover the summary of the work done, the conclusions drawn from the experiments, and the perspectives for future research in optomechanical systems. It will highlight the key findings, their implications for quantum optics, and potential directions for further exploration.

**Summary of Work**

**Outlooks**

**Final Remarks**



# Appendix A: Two-photon derivations

## Field Quantization

### From discrete to continuous modes

We consider the quantised electromagnetic field in a volume  $V$  along a single polarization direction. We assume the field to be a gaussian beam such that the quantization volume is written as  $\mathcal{V} = \mathcal{A}L$ , with  $\mathcal{A}$  the effective mode cross-sectional area, normal to the propagation direction  $z$ . The electric field operator can be written as

$$\hat{\mathbf{E}}(\mathbf{r}, t) = i \sum_{\ell} \sqrt{\frac{\hbar\omega_{\ell}}{2\varepsilon_0\mathcal{V}}} \left[ \hat{a}_{\omega_{\ell}} \mathbf{f}_{\ell}(\mathbf{r}) e^{-i\omega_{\ell}t} - \hat{a}_{\omega_{\ell}}^{\dagger} \mathbf{f}_{\ell}^*(\mathbf{r}) e^{+i\omega_{\ell}t} \right], \quad (\text{V.1})$$

The index  $\ell$  then labels the different modes, discrete at this point. The bosonic operators satisfy the canonical commutation relations

$$[\hat{a}_{\omega_{\ell}}, \hat{a}_{\omega_{\ell'}}^{\dagger}] = \delta_{\ell\ell'}, \quad [\hat{a}_{\omega_{\ell}}, \hat{a}_{\omega_{\ell'}}] = [\hat{a}_{\omega_{\ell}}^{\dagger}, \hat{a}_{\omega_{\ell'}}^{\dagger}] = 0.$$

We consider a the polarization along the  $\hat{\mathbf{x}}$  direction where the hat denotes the unit vector and not an operator. The mode function can then be written as  $\mathbf{f}_{\ell}(\mathbf{r}) = f_{\ell}(\mathbf{r})\hat{\mathbf{x}}$ . We consider 1D wavevectors along the  $+z$  direction i.e. positive  $k_{\ell}$  only, such that in the limit of quantization volumes tending to infinity i.e.  $L \rightarrow \infty$ , the discrete sum over k modes turns into an integral over frequencies

$$\sum_{\ell}(\dots) \rightarrow \frac{L}{2\pi} \int_0^{\infty} dk(\dots) = \frac{1}{\Delta f} \int_0^{\infty} \frac{d\omega}{2\pi}(\dots) \quad \text{with} \quad \Delta f = \frac{c}{L}$$

using the dispersion relation  $\omega = c|k|$ . We then simply relabel  $\hat{a}_{\omega_\ell} \rightarrow \hat{a}_\omega$ ,  $f_\ell(\mathbf{r}) \rightarrow f(\mathbf{r}, \omega)$  and plug back into the original expression to have

$$\hat{\mathbf{E}}(\mathbf{r}, t) = i \int_0^\infty \frac{d\omega}{2\pi} \sqrt{\frac{\hbar\omega}{2\varepsilon_0\mathcal{A}c}} \left[ \lim_{L \rightarrow \infty} \frac{\hat{a}[\Omega]}{\sqrt{\Delta f}} f(\mathbf{r}, \omega) e^{-i\omega t} - \lim_{L \rightarrow \infty} \frac{\hat{a}^\dagger[\Omega]}{\sqrt{\Delta f}} f^*(\mathbf{r}, \omega) e^{+i\omega t} \right] \hat{\mathbf{x}},$$

and we can define the continuous bosonic operators as

$$\hat{a}[\omega] = \lim_{L \rightarrow \infty} \frac{\hat{a}_\omega}{\sqrt{\Delta f}} \quad \text{and} \quad \hat{a}^\dagger[\omega] = \lim_{L \rightarrow \infty} \frac{\hat{a}_\omega^\dagger}{\sqrt{\Delta f}}$$

such that the electric field operator reads

$$\hat{\mathbf{E}}(\mathbf{r}, t) = i \int_0^\infty \frac{d\omega}{2\pi} \mathcal{E} \left[ \hat{a}[\omega] f(\mathbf{r}, \omega) e^{-i\omega t} - \hat{a}^\dagger[\omega] f^*(\mathbf{r}, \omega) e^{+i\omega t} \right] \hat{\mathbf{x}}, \quad \text{with} \quad \mathcal{E} = \sqrt{\frac{\hbar\omega}{2\varepsilon_0\mathcal{A}c}}.$$

### Commutation relations

Using standard complex analysis techniques, the kronecker delta can be expressed as

$$\delta_{\ell\ell'} = \int_{-\pi}^{+\pi} dt \frac{e^{i(\ell-\ell')t}}{2\pi}.$$

Upon the aforementioned assumptions, we can introduce the frequency spacing  $\Delta\omega = 2\pi\Delta f$  such that the discrete angular frequencies are written as  $\omega_\ell = \ell\Delta\omega$ . It then follows that  $\ell - \ell' = (\omega_\ell - \omega_{\ell'})/\Delta\omega$ . By changing the variable of integration from  $t$  to  $t' = t/\Delta\omega$ , we can rewrite the kronecker delta as

$$\delta_{\ell\ell'} = \int_{-L/2c}^{+L/2c} dt' \Delta f e^{i(\omega_\ell - \omega_{\ell'})t'}.$$

We can then see that in the limit of  $L \rightarrow \infty$  i.e.  $\Delta\omega \rightarrow 0$ , the integral limits tend to infinity and the kronecker delta turns into a dirac delta such that

$$\lim_{L \rightarrow \infty} \frac{\delta_{\ell\ell'}}{\Delta f} = \int_{-\infty}^{+\infty} dt' e^{i(\omega - \omega')t'} = 2\pi\delta(\omega - \omega').$$

where we relabeled  $\omega_\ell \rightarrow \omega$  and  $\omega_{\ell'} \rightarrow \omega'$ . The commutation relations for the continuous bosonic operators then read which satisfy the commutation relations

$$[\hat{a}[\omega], \hat{a}^\dagger[\omega']] = \lim_{L \rightarrow \infty} \frac{[\hat{a}_{\omega_\ell}, \hat{a}_{\omega_{\ell'}}^\dagger]}{\Delta f} = 2\pi\delta(\omega - \omega'), \quad [\hat{a}[\omega], \hat{a}[\omega']] = [\hat{a}^\dagger[\omega], \hat{a}^\dagger[\omega']] = 0.$$

## Two photon formalism

### Quadratures

We will now consider mode field frequencies  $\omega = \omega_0 + \Omega$  around a carrier frequency  $\omega_0$ , such that the integral term becomes

$$\int_0^\infty \frac{d\omega}{2\pi}(\dots) \rightarrow \int_{-\omega_0}^\infty \frac{d\Omega}{2\pi}(\dots) \sim \int_{-B}^B \frac{d\Omega}{2\pi}(\dots) \sim \int_{-\infty}^\infty \frac{d\Omega}{2\pi}(\dots)$$

where  $B$  is the detection bandwidth, which is always much smaller than the optical frequency  $\omega_0$ . We can then safely extend the integral limits to infinity. Assuming that the mode function  $f(\mathbf{r}, \omega)$  does not vary significantly over the bandwidth  $B$ , we can approximate it by its value at the carrier frequency  $f(\mathbf{r}, \omega_0) \equiv f(\mathbf{r})$ . Pulling out this term from the integral, one can then project the electric field operator onto both the proper polarization axis and this mode function such that the electric field operator becomes spatially independent and reads

$$\hat{E}(t) = i\mathcal{E}_0 \int_0^\infty \frac{d\Omega}{2\pi} \left[ \hat{a}_+ e^{-i(\omega_0+\Omega)t} - \hat{a}_+^\dagger e^{+i(\omega_0+\Omega)t} + \hat{a}_- e^{-i(\omega_0-\Omega)t} - \hat{a}_-^\dagger e^{+i(\omega_0-\Omega)t} \right] \quad (\text{V.2})$$

with  $\mathcal{E}_0 = \sqrt{\hbar\omega/2\varepsilon_0\mathcal{A}c}$ , and where we additionally split the integral term in two, introducing negative and positive sideband frequencies whose annihilation and creation operators are written as

$$\hat{a}_\pm \equiv c_\pm \hat{a}[\omega_0 \pm \Omega] \quad \text{and} \quad \hat{a}_\pm^\dagger \equiv c_\pm \hat{a}^\dagger[\omega_0 \pm \Omega] \quad \text{with} \quad c_\pm = \sqrt{\frac{\omega_0 \pm \Omega}{\omega_0}}.$$

The commutators then read

$$[\hat{a}_\pm, \hat{a}_\pm^\dagger] = 2\pi c_\pm^2 \delta(\Omega - \Omega'), \quad [\hat{a}_\pm, \hat{a}_\mp] = [\hat{a}_\pm^\dagger, \hat{a}_\mp^\dagger] = 0$$

$$[\hat{a}_\pm, \hat{a}_\mp^\dagger] = 2\pi c_+ c_- \delta(\Omega + \Omega'), \quad [\hat{a}_\pm, \hat{a}_\mp] = [\hat{a}_\pm^\dagger, \hat{a}_\mp^\dagger] = 0$$

Computing expectation values for these operators in vacuum yields  $\langle \hat{a}_\pm \rangle = \langle \hat{a}_\pm^\dagger \rangle = \langle 0 | \hat{a}_\pm^\dagger \hat{a}_\pm | 0 \rangle = 0$  and  $\langle 0 | \hat{a}_\pm \hat{a}_\pm^\dagger | 0 \rangle = 2\pi c_\pm^2 \delta(0)$ , which is consistent with the fact that no photons are present in these modes. We then regroup the terms along common quadratures  $\cos \omega_0 t$  and  $\sin \omega_0 t$  such that we get

$$\begin{aligned} \hat{E}(t) = i\mathcal{E}_0 & \left[ \cos \omega_0 t \int_0^\infty \frac{d\Omega}{2\pi} \left[ (\hat{a}_+ - \hat{a}_-^\dagger) e^{-i\Omega t} + (\hat{a}_- - \hat{a}_+^\dagger) e^{+i\Omega t} \right] \right. \\ & \left. - i \sin \omega_0 t \int_0^\infty \frac{d\Omega}{2\pi} \left[ (\hat{a}_+ + \hat{a}_-^\dagger) e^{-i\Omega t} + (\hat{a}_- + \hat{a}_+^\dagger) e^{+i\Omega t} \right] \right] \end{aligned}$$

We now define the two-photon quadrature operators as

$$\hat{p}[\Omega] = \hat{a}_+ + \hat{a}_-^\dagger, \quad \hat{q}[\Omega] = i(\hat{a}_-^\dagger - \hat{a}_+)$$

such that the electric field operator reads

$$\begin{aligned} \hat{E}(t) &= \mathcal{E}_0 \left[ \cos\left(\omega_0 t - \frac{\pi}{2}\right) \int_0^\infty \frac{d\Omega}{2\pi} [\hat{p}[\Omega] e^{-i\Omega t} + \hat{p}^\dagger[\Omega] e^{+i\Omega t}] \right. \\ &\quad \left. + \sin\left(\omega_0 t - \frac{\pi}{2}\right) \int_0^\infty \frac{d\Omega}{2\pi} [\hat{q}[\Omega] e^{-i\Omega t} + \hat{q}^\dagger[\Omega] e^{+i\Omega t}] \right] \end{aligned} \quad (\text{V.3})$$

where we used the fact that  $\hat{p}^\dagger[\Omega] = \hat{p}[-\Omega]$  and  $\hat{q}^\dagger[\Omega] = \hat{q}[-\Omega]$ . The  $\pi/2$  phase shifts originate from the leading factor  $i$  in the electric-field operator. Had the field operator been written without that prefactor (and without the minus sign in the creation-term), the resulting cosine and sine components would contain no such phase offset. The commutation relations for these quadrature operators read

$$\begin{aligned} [\hat{p}[\Omega], \hat{q}^\dagger[\Omega']] &= [\hat{q}[\Omega], \hat{p}^\dagger[\Omega']] = 4\pi i \delta(\Omega - \Omega') \\ [\hat{p}[\Omega], \hat{p}^\dagger[\Omega']] &= [\hat{q}[\Omega], \hat{q}^\dagger[\Omega']] = 4\pi \frac{\Omega}{\omega_0} \delta(\Omega - \Omega') \sim 0 \quad \text{if } \Omega \ll \omega_0 \\ [\hat{p}[\Omega], \hat{q}[\Omega']] &= [\hat{p}^\dagger[\Omega], \hat{q}^\dagger[\Omega']] = 0. \end{aligned}$$

In the limit where the sideband frequencies are small compared to the carrier frequency i.e.  $\Omega \ll \omega_0$ , we can approximate these prefactors by  $c_\pm \sim 1$ .

### Expectations values in vacuum

We now proceed to evaluate the first and second momenta of our field operators in the vacuum state  $|0\rangle$ . As expected, the annihilation and creation operators have zero mean in vacuum, such that

$$\langle 0 | \hat{a}_+ | 0 \rangle = \langle 0 | \hat{a}_-^\dagger | 0 \rangle = 0$$

so it follows that

$$\langle 0 | \hat{p}[\Omega] | 0 \rangle = \langle 0 | \hat{q}[\Omega] | 0 \rangle = 0.$$

Building the two-photon quadrature column vector as

$$\hat{\mathbf{u}}[\Omega] = \begin{pmatrix} \hat{p}[\Omega] \\ \hat{q}[\Omega] \end{pmatrix}, \quad \text{we have} \quad \langle \hat{\mathbf{u}}[\Omega] \rangle = \begin{pmatrix} 0 \\ 0 \end{pmatrix}$$

where we see that, for a vacuum state, the full operator  $\hat{\mathbf{u}}[\Omega]$  actually equates the fluctuating part  $\delta\hat{\mathbf{u}}[\Omega] = \hat{\mathbf{u}}[\Omega] - \langle \hat{\mathbf{u}}[\Omega] \rangle$  since the mean value is zero. In the following, we will assume

that expectation values are always computed in the vacuum state unless otherwise specified (we will omit the  $|0\rangle$  notation for clarity). We only wrote the results for the  $\hat{a}_+$  and  $\hat{a}_-^\dagger$  operators as there are the ones composing the  $\hat{p}$  and  $\hat{q}$  quadratures, but the same results hold for the other sideband operators as well. We can then compute the second momenta of the annihilation and creation operators, yielding

$$\langle 0 | \hat{a}_-^\dagger \hat{a}_- | 0 \rangle = \langle 0 | \hat{a}_+ \hat{a}_- | 0 \rangle = \langle 0 | \hat{a}_-^\dagger \hat{a}_+^\dagger | 0 \rangle = 0$$

$$\langle 0 | \hat{a}_\pm \hat{a}_\pm^\dagger | 0 \rangle = 2\pi\delta(\Omega - \Omega') .$$

Using these relations, we can compute the second momenta for the two-photon quadrature operators as

$$\begin{aligned} \langle 0 | \hat{p}[\Omega] \hat{p}^\dagger[\Omega'] | 0 \rangle &= \langle 0 | \hat{a}_+ \hat{a}_+^\dagger + \hat{a}_+ \hat{a}_- + \hat{a}_-^\dagger \hat{a}_+^\dagger + \hat{a}_-^\dagger \hat{a}_- | 0 \rangle \\ &= 2\pi\delta(\Omega - \Omega') , \\ \langle 0 | \hat{q}[\Omega] \hat{q}^\dagger[\Omega'] | 0 \rangle &= 2\pi\delta(\Omega - \Omega') . \end{aligned}$$

as well as

$$\langle 0 | \hat{p}[\Omega] \hat{q}^\dagger[\Omega'] | 0 \rangle = -\langle 0 | \hat{q}^\dagger[\Omega] \hat{p}[\Omega'] | 0 \rangle = i2\pi\delta(\Omega - \Omega') .$$

Using the expression for the symmetrized double sided covariance matrix given in the main text, we can compute the covariance matrix for the two-photon quadrature operators in vacuum as

$$\begin{aligned} \mathbf{S}[\Omega] &= \frac{1}{2} \int \frac{\delta\Omega'}{2\pi} \langle \{ \delta\hat{\mathbf{u}}[\Omega], \delta\hat{\mathbf{u}}^\dagger[\Omega'] \} \rangle \\ &= \frac{1}{2} \int \frac{\delta\Omega'}{2\pi} \begin{pmatrix} \langle \{\hat{p}[\Omega], \hat{p}^\dagger[\Omega']\} \rangle & \langle \{\hat{p}[\Omega], \hat{q}^\dagger[\Omega']\} \rangle \\ \langle \{\hat{q}[\Omega], \hat{p}^\dagger[\Omega']\} \rangle & \langle \{\hat{q}[\Omega], \hat{q}^\dagger[\Omega']\} \rangle \end{pmatrix} \\ &= \frac{1}{2} \int \frac{\delta\Omega'}{2\pi} \begin{pmatrix} 2 \cdot 2\pi\delta(\Omega - \Omega') & 0 \\ 0 & 2 \cdot 2\pi\delta(\Omega - \Omega') \end{pmatrix} \\ &= \begin{pmatrix} 1 & 0 \\ 0 & 1 \end{pmatrix} = \mathbf{1} . \end{aligned}$$

The vacuum state then features vacuum fluctuations of unity in both quadratures, across all sideband frequencies  $\Omega$ , and no correlations between the quadratures.

### States and Operators in the Two-Photon Formalism

In a similar fashion as in the single-mode case, we can define the displacement operator as

$$\hat{D}(\alpha) = \exp \left( \int_{-\infty}^{\infty} \frac{d\Omega}{2\pi} [\alpha(\Omega) \hat{a}_-^\dagger - \alpha^*(\Omega) \hat{a}_+] \right)$$

as well as a squeezing operator

$$\hat{S}(r, \theta) = \exp \left( r \int_{-\infty}^{\infty} \frac{d\Omega}{2\pi} [e^{-i2\theta(\Omega)} \hat{a}_+ \hat{a}_- - e^{i2\theta(\Omega)} \hat{a}_+^\dagger \hat{a}_-^\dagger] \right)$$

where  $r$  is the squeezing factor and  $\theta(\Omega)$  the squeezing angle. Here we assumed the squeezing parameter to be frequency independent, but one can easily generalize to a frequency dependent squeezing parameter  $r(\Omega)$ . Using the sidebands annihilation operators defined previously, we can compute the action of the displacement and squeezing operators on the annihilation operator as

$$\begin{aligned} \hat{D}^\dagger(\alpha) \hat{a}_+ \hat{D}(\alpha) &= \hat{a}_+ + \alpha(\Omega), \\ \hat{S}^\dagger(r, \theta) \hat{a}_+ \hat{S}(r, \theta) &= \hat{a}_+ \cosh r - e^{i2\theta(\Omega)} \hat{a}_-^\dagger \sinh r. \end{aligned}$$

We consider a intial vacuum state  $|0\rangle$ , and we displace it by a coherent amplitude  $\alpha(\Omega) = \alpha\delta(\Omega)$  i.e. a carrier, monochromatic field of complex amplitude  $\alpha$  sitting at frequency 0 (we are in the frame rotating at  $\omega_0$  already since we factored out the  $e^{-i\omega_0 t}$  term). The displacement operator then acts on the two photon quadrature operators as

$$\begin{aligned} \hat{D}^\dagger(\alpha) \hat{p}[\Omega] \hat{D}(\alpha) &= \hat{p}[\Omega] + 2 \operatorname{Re}\{\alpha\} \delta(\Omega), \\ \hat{D}^\dagger(\alpha) \hat{q}[\Omega] \hat{D}(\alpha) &= \hat{q}[\Omega] + 2 \operatorname{Im}\{\alpha\} \delta(\Omega). \end{aligned}$$

or in matrix form

$$\hat{D}^\dagger(\alpha) \hat{\mathbf{u}}[\Omega] \hat{D}(\alpha) = \hat{\mathbf{u}}[\Omega] + 2 \begin{pmatrix} \operatorname{Re}\{\alpha\} \\ \operatorname{Im}\{\alpha\} \end{pmatrix} \delta(\Omega).$$

In a similar fashion, the squeezing operator acts as

$$\begin{aligned} \hat{S}^\dagger(r, \theta) \hat{p}[\Omega] \hat{S}(r, \theta) &= \hat{p}[\Omega] (\cosh r - \sinh r \cos 2\theta) - \hat{q}[\Omega] \sin 2\theta \sinh r, \\ \hat{S}^\dagger(r, \theta) \hat{q}[\Omega] \hat{S}(r, \theta) &= \hat{q}[\Omega] (\cosh r + \sinh r \cos 2\theta) - \hat{p}[\Omega] \sin 2\theta \sinh r. \end{aligned}$$

and its matrix form reads

$$\hat{S}^\dagger(r, \theta) \hat{\mathbf{u}}[\Omega] \hat{S}(r, \theta) = \mathbf{S}(r, \theta) \hat{\mathbf{u}}[\Omega], \quad \text{with} \quad \mathbf{S}(r, \theta) = \begin{pmatrix} \cosh r - \sinh r \cos 2\theta & -\sin 2\theta \sinh r \\ -\sin 2\theta \sinh r & \cosh r + \sinh r \cos 2\theta \end{pmatrix}.$$

The state resulting from applying both operators onto the vacuum is written as

$$|\psi\rangle = \hat{S}(r, \theta) \hat{D}(\alpha) |0\rangle$$

and describes a squeezed coherent state, or bright squeezed state. One can then set the coherent amplitude to 0 as to get a vacuum squeezed state, or set the squeezing parameter to 0 to get a coherent state. This is one of the most generic gaussian state one can define in quantum optics. We write the operator product as  $\hat{D}\hat{S}$  and we drop the  $\Omega$  dependencies to lighten the notation, such that applying them to the field operators yields

$$\begin{aligned} \hat{D}^\dagger \hat{S}^\dagger \hat{a}_+ \hat{S} \hat{D} &= \hat{a}_+ \cosh r - e^{i2\theta} \hat{a}_-^\dagger \sinh r + \gamma \delta(\Omega) \\ \hat{D}^\dagger \hat{S}^\dagger \hat{a}_-^\dagger \hat{S} \hat{D} &= \hat{a}_-^\dagger \cosh r - e^{-i2\theta} \hat{a}_+ \sinh r + \gamma^* \delta(\Omega). \end{aligned}$$

as well as the quadratures

$$\begin{aligned} \hat{D}^\dagger \hat{S}^\dagger \hat{p} \hat{S} \hat{D} &= \hat{p}(\cosh r - \cos 2\theta \sinh r) - \hat{q} \sin 2\theta \sinh r + 2 \operatorname{Re}\{\gamma\} \delta(\Omega), \\ \hat{D}^\dagger \hat{S}^\dagger \hat{q} \hat{S} \hat{D} &= \hat{q}(\cosh r + \cos 2\theta \sinh r) - \hat{p} \sin 2\theta \sinh r + 2 \operatorname{Im}\{\gamma\} \delta(\Omega). \end{aligned}$$

where we introduced the scalar part of these transformed operators as

$$\begin{aligned} \gamma &= \alpha \cosh r - \alpha^* e^{i2\theta} \sinh r, \\ \gamma^* &= \alpha^* \cosh r - \alpha e^{-i2\theta} \sinh r. \end{aligned}$$

The matrix form then reads

$$\hat{D}^\dagger \hat{S}^\dagger \hat{\mathbf{u}} \hat{S} \hat{D} = \mathbf{S}(r, \theta) \hat{\mathbf{u}} + 2 \begin{pmatrix} \operatorname{Re}\{\gamma\} \\ \operatorname{Im}\{\gamma\} \end{pmatrix} \delta(\Omega).$$

The mean values is then straightforward to compute

$$\begin{aligned} \langle \hat{D}^\dagger \hat{S}^\dagger \hat{\mathbf{u}} \hat{S} \hat{D} \rangle &= \mathbf{S}(r, \theta) \langle \hat{\mathbf{u}} \rangle + 2 \begin{pmatrix} \operatorname{Re}\{\gamma\} \\ \operatorname{Im}\{\gamma\} \end{pmatrix} \delta(\Omega) \\ &= 2 \begin{pmatrix} \operatorname{Re}\{\gamma\} \\ \operatorname{Im}\{\gamma\} \end{pmatrix} \delta(\Omega). \end{aligned}$$

such that the fluctuating part reads

$$\delta \hat{\mathbf{u}} = \hat{D}^\dagger \hat{S}^\dagger \hat{\mathbf{u}} \hat{S} \hat{D} - \langle \hat{D}^\dagger \hat{S}^\dagger \hat{\mathbf{u}} \hat{S} \hat{D} \rangle = \mathbf{S}(r, \theta) \hat{\mathbf{u}} \quad \text{and} \quad \delta \hat{\mathbf{u}}^\dagger = \hat{\mathbf{u}}^\dagger \mathbf{S}(r, \theta).$$

where we used the fact that the squeezing matrix is symmetric, i.e.  $\mathbf{S} = \mathbf{S}^T$ . The covariance matrix for this squeezed coherent state then reads

$$\begin{aligned} \mathbf{S}[\Omega] &= \frac{1}{2} \int \frac{\delta\Omega'}{2\pi} \langle \{\delta \hat{\mathbf{u}}[\Omega], \delta \hat{\mathbf{u}}^\dagger[\Omega']\} \rangle \\ &= \frac{1}{2} \int \frac{\delta\Omega'}{2\pi} \langle \{\mathbf{S}(r, \theta) \hat{\mathbf{u}}[\Omega], \hat{\mathbf{u}}^\dagger[\Omega'] \mathbf{S}(r, \theta)\} \rangle \\ &= \mathbf{S}(r, \theta) \left( \frac{1}{2} \int \frac{\delta\Omega'}{2\pi} \langle \{\hat{\mathbf{u}}[\Omega], \hat{\mathbf{u}}^\dagger[\Omega']\} \rangle \right) \mathbf{S}(r, \theta) \\ &= \mathbf{S}(r, \theta) \cdot \mathbf{1} \cdot \mathbf{S}(r, \theta) = \mathbf{S}(r, \theta)^2 \\ &= \begin{pmatrix} \cosh 2r - \sinh 2r \cos 2\theta & -\sin 2\theta \sinh 2r \\ -\sin 2\theta \sinh 2r & \cosh 2r + \sinh 2r \cos 2\theta \end{pmatrix}. \end{aligned}$$

such that the expectation values are computed as

$$\begin{aligned} \langle \hat{a}_+ \rangle &= \gamma \delta(\Omega) \\ \langle \hat{a}_-^\dagger \rangle &= \gamma^* \delta(\Omega) \\ \langle \hat{p} \rangle &= 2 \operatorname{Re}\{\gamma\} \delta(\Omega) \\ \langle \hat{q} \rangle &= 2 \operatorname{Im}\{\gamma\} \delta(\Omega). \end{aligned}$$

and we compute the expectation value of our two-photon annihilation operator as

$$\langle \hat{a}_+ \rangle = \alpha \delta(\Omega) \quad \text{and} \quad \langle \hat{a}_-^\dagger \rangle = \alpha^* \delta(\Omega)$$

as well as their second momenta as

The electric field operator finally reads

$$\hat{\mathbf{E}}(\mathbf{r}, t) = i \sqrt{\frac{\hbar\omega_0}{\varepsilon_0 \mathcal{A}c}} \left[ \int_{-\infty}^{\infty} \frac{d\Omega}{2\pi} \left[ \hat{a}_\Omega e^{-i(\omega_0 + \Omega)t} - \hat{a}_\Omega^\dagger e^{+i(\omega_0 + \Omega)t} \right] \right] \quad (\text{V.4})$$

such that the classical part of the electric field reads

We start from the standard single-mode field quantization in terms of annihilation and

creation operators  $\hat{a}$  and  $\hat{a}^\dagger$ :

$$\hat{E}(t) = \sqrt{\frac{\hbar\omega_0}{2\varepsilon_0}} (\hat{a}e^{-i\omega_0 t} + \hat{a}^\dagger e^{i\omega_0 t}).$$

and we now make our bosonic operators time-dependent,  $\hat{a} \rightarrow \hat{a}(t)$ , to account for sidebands around the carrier frequency  $\omega_0$ . Using the Fourier transform convention

$$\hat{a}(t) = \int_{-\infty}^{+\infty} \frac{d\Omega}{2\pi} \hat{a}[\Omega] e^{-i\Omega t},$$

we rewrite the field operator as

$$\hat{E}(t) = \sqrt{\frac{\hbar\omega_0}{2\varepsilon_0}} \int_{-\infty}^{+\infty} \frac{d\Omega}{2\pi} (\hat{a}[\Omega] e^{-i(\omega_0+\Omega)t} + \hat{a}^\dagger[\Omega] e^{i(\omega_0+\Omega)t}).$$

$$\hat{p}[\Omega] = 2|\alpha|(\delta[\Omega] + \text{Re}\{\varepsilon[\Omega]\}) + \delta\hat{p}[\Omega], \quad (\text{V.5})$$

$$\hat{p}[\Omega] \hat{p}[\Omega'] = 4|\alpha|^2 (\delta[\Omega]S[\Omega'] + \delta[\Omega]\text{Re}\{\varepsilon[\Omega']\} + \delta[\Omega']\text{Re}\{\varepsilon[\Omega]\} + \text{Re}\{\varepsilon[\Omega]\}\text{Re}\{\varepsilon[\Omega']\}) + \delta\hat{p}[\Omega] \delta\hat{p}[\Omega'], \quad (\text{V.6})$$

$$\langle \dots \rangle = 4|\alpha|^2 (\delta(\Omega)\delta(\Omega') + \frac{\varepsilon}{2}\delta(\Omega)\delta(\Omega' - \Omega_m) + \frac{\varepsilon}{2}\delta(\Omega)\delta(\Omega' + \Omega_m)) \quad (\text{V.7})$$

$$+ \frac{\varepsilon}{2}\delta(\Omega')\delta(\Omega - \Omega_m) + \frac{\varepsilon}{2}\delta(\Omega')\delta(\Omega + \Omega_m) \quad (\text{V.8})$$

$$+ \frac{\varepsilon^2}{4} [\delta(\Omega - \Omega_m)\delta(\Omega' + \Omega_m) + \delta(\Omega - \Omega_m)\delta(\Omega' - \Omega_m) \quad (\text{V.9})$$

$$+ \delta(\Omega + \Omega_m)\delta(\Omega' + \Omega_m) + \delta(\Omega + \Omega_m)\delta(\Omega' - \Omega_m)] \big) + \langle \delta p[\Omega] \delta p[\Omega'] \rangle. \quad (\text{V.10})$$

## Derivation of the optimal angle

### Optimal fixed homodyne angle with complex $\mathcal{K}$

Assume the measured (reflected) quadrature is

$$\delta q_r = \delta q_{\text{in}} + \mathcal{K} \delta p_{\text{in}},$$

so that, for any input covariance matrix  $S^{\text{in}}$ ,

$$S_{qq}^r = S_{qq}^{\text{in}} + |\mathcal{K}|^2 S_{pp}^{\text{in}} + 2 \text{Re}\{\mathcal{K}\} S_{pq}^{\text{in}}.$$

For an input squeezed state of strength  $R$  and angle  $\theta$ ,

$$S^{\text{in}}(r, \theta) = \begin{pmatrix} \cosh 2r + \sinh 2r \cos 2\theta & -\sinh 2r \sin 2\theta \\ -\sinh 2r \sin 2\theta & \cosh 2r - \sinh 2r \cos 2\theta \end{pmatrix}.$$

Hence

$$\begin{aligned} S_{qq}^r(\theta) &= \cosh 2r - \sinh 2r \cos 2\theta + |\mathcal{K}|^2(\cosh 2r + \sinh 2r \cos 2\theta) - 2 \operatorname{Re}\{\mathcal{K}\} \sinh 2r \sin 2\theta \\ &= (1 + |\mathcal{K}|^2) \cosh 2r - (1 - |\mathcal{K}|^2) \sinh 2r \cos 2\theta - 2 \operatorname{Re}\{\mathcal{K}\} \sinh 2r \sin 2\theta. \end{aligned} \quad (\text{V.11})$$

**Optimal fixed angle.** Differentiate (V.11) w.r.t.  $\theta$  and set to zero:

$$\frac{\partial S_{qq}^r}{\partial \theta} = 2 \sinh 2r \left[ (1 - |\mathcal{K}|^2) \sin 2\theta - 2 \operatorname{Re}\{\mathcal{K}\} \cos 2\theta \right] = 0,$$

which gives the optimal fixed readout angle

$$\tan(2\theta_{\text{opt}}) = \frac{2 \operatorname{Re}\{\mathcal{K}\}}{1 - |\mathcal{K}|^2} \quad (\text{V.12})$$

Writing  $\mathcal{K} = |\mathcal{K}|e^{i\varphi_m}$  one may also use

$$\tan(2\theta_{\text{opt}}) = \frac{2|\mathcal{K}| \cos \varphi_m}{1 - |\mathcal{K}|^2}.$$

**Minimum attained value.** Plugging the optimal angle back into (V.11) then yields

$$S_{qq,\text{min}}^r = (1 + |\mathcal{K}|^2) \cosh 2r - \sqrt{(1 - |\mathcal{K}|^2)^2 + (2 \operatorname{Re}\{\mathcal{K}\})^2} \sinh 2r, \quad (\text{V.13})$$

**Lower bound and the real- $\mathcal{K}$  case.** In the free mass limit,  $\mathcal{K}$  is purely real, so that  $\varphi_m = 0$  and  $\operatorname{Re}\{\mathcal{K}\} = |\mathcal{K}|$ . In this case, the minimum variance (V.13) reduces to

$$S_{qq,\text{min}}^r = (1 + |\mathcal{K}|^2)e^{-2r}$$

# Appendix B: Error Signals

In this appendix, we detail calculation details not mentionned in the main text regarding the detection of optical fields and error signals.

## Direct detection error signals

We describe the completely generic photocurrent obtained from direct detection of two optical fields interfering on a photodetector. We consider two fields with field operators  $\hat{a}$  and  $\hat{a}'$ , with classical amplitudes  $|\bar{\alpha}|$  and  $|\bar{\alpha}'|e^{-i(\Delta\omega t+\phi)}$  as well as fluctuations  $\delta\hat{a}$  and  $\delta\hat{a}'e^{-i(\Delta\omega t+\phi)}$  i.e.  $\bar{\alpha}$  is real. The photocurrent operator is then given by

$$\hat{I} = \left( |\bar{\alpha}| + \delta\hat{a}^\dagger + |\bar{\alpha}'|e^{i(\Delta\omega t+\phi)} + \delta\hat{a}'^\dagger e^{i(\Delta\omega t+\phi)} \right) \left( |\bar{\alpha}| + \delta\hat{a} + |\bar{\alpha}'|e^{-i(\Delta\omega t+\phi)} + \delta\hat{a}' e^{-i(\Delta\omega t+\phi)} \right)$$

We remind here the expression for the amplitude and phase quadratures for both fields

$$\delta\hat{p} = \delta\hat{a} + \delta\hat{a}^\dagger, \quad \delta\hat{q} = -i(\delta\hat{a} - \delta\hat{a}^\dagger),$$

and

$$\delta\hat{p}' = e^{-i(\Delta\omega t+\phi)}\delta\hat{a}' + e^{i(\Delta\omega t+\phi)}\delta\hat{a}'^\dagger, \quad \delta\hat{q}' = -i(e^{-i(\Delta\omega t+\phi)}\delta\hat{a}' - e^{i(\Delta\omega t+\phi)}\delta\hat{a}'^\dagger).$$

Expanding this expression and keeping only terms up to first order in the fluctuations, we find

$$\begin{aligned} \hat{I}(t) \approx & |\bar{\alpha}|^2 + |\bar{\alpha}'|^2 + 2|\bar{\alpha}||\bar{\alpha}'| \cos(\Delta\omega t + \phi) \\ & + |\bar{\alpha}|(\delta\hat{p} + \delta\hat{p}') \\ & + |\bar{\alpha}'| \cos(\Delta\omega t + \phi)(\delta\hat{p} + \delta\hat{p}') \\ & + |\bar{\alpha}'| \sin(\Delta\omega t + \phi)(\delta\hat{q} - \delta\hat{q}') \end{aligned}$$

The first line corresponds to the classical DC and beatnote terms, while the remaining lines correspond to the fluctuations. We will now explore the different detection regimes covered in the main text.

### Single field detection

Let's first consider the single field case where we get rid of all terms related to  $\hat{a}'$ . The photocurrent operator then reduces to

$$\hat{I} \approx |\bar{\alpha}|^2 + |\bar{\alpha}|\delta\hat{p}.$$

The photocurrent fluctuations are then directly proportional to the amplitude quadrature fluctuations of the input field, scaled by the classical amplitude.

### Two fields detection

Let's first consider two fields with the same frequency, i.e.  $\Delta\omega = 0$ . The photocurrent operator then reads

$$\begin{aligned}\hat{I} \approx & |\bar{\alpha}|^2 + |\bar{\alpha}'|^2 + 2|\bar{\alpha}||\bar{\alpha}'| \cos(\phi) \\ & + |\bar{\alpha}| (\delta\hat{p} + \delta\hat{p}') \\ & + |\bar{\alpha}'| \cos(\phi) (\delta\hat{p} + \delta\hat{p}') \\ & + |\bar{\alpha}'| \sin(\phi) (\delta\hat{q} - \delta\hat{q}')\end{aligned}$$

where the mean field is a simple interference between the two fields, while the fluctuations depend on both amplitude and phase quadratures of the two fields. By adjusting the relative phase  $\phi$ , one can select which quadrature is measured. For example, setting  $\phi = 0$  selects the amplitude quadratures, while setting  $\phi = \pi/2$  selects the phase quadratures. The issue is that in this case, both fields contribute to the measured quadrature fluctuations, which is not desired when probing sub shotnoise fluctuations of a signal (the LO will add its own fluctuations).

### Two fields detection with frequency offset

Now, we consider the case where the two fields have a frequency offset  $\Delta\omega \neq 0$ . The mean photocurrent then contains a beatnote at frequency  $\Delta\omega$  and reads

$$\bar{I} = |\bar{\alpha}|^2 + |\bar{\alpha}'|^2 + 2|\bar{\alpha}||\bar{\alpha}'| \cos(\Delta\omega t + \phi).$$

such that demodulating the photocurrent at frequency  $\Delta\omega' \sim \Delta\tilde{\omega}$  with phase  $\tilde{\phi}$  and low-pass filtering yields

$$\bar{I}_{\text{demod}} \approx |\bar{\alpha}||\bar{\alpha}'| \cos((\Delta\omega - \Delta\tilde{\omega})t + \phi - \tilde{\phi}).$$

This very signal can then be used to lock the frequency of an auxiliary laser to the desired frequency offset  $\Delta\tilde{\omega}$  from the main laser. However, this signal featuring many zero crossings, one needs to tune the auxiliary laser frequency close enough to the desired offset so that it

ensures the feedback loop locks to the correct zero crossing. This is generally done manually by scanning the auxiliary laser frequency until the right zero crossing is found, confirmed by monitoring the beatnote on a spectrum analyzer.

## PDH error signal

the Pound-Drever-Hall (PDH) error signal starting from the real, quantum-normalized phase-modulated electric field expression. We aim to show how the demodulated signal is a linear combination of the real and imaginary parts of the cavity reflection coefficient, with the demodulation phase selecting the appropriate quadrature for locking.

### Input Phase-Modulated Field

The electric field at the input of the cavity is assumed to be a coherent state that has been phase-modulated at frequency  $\Omega$ , such that the classical (real) electric field takes the form:

$$E_{\text{cl}}^{(\text{PM})}(t) = i\sqrt{\frac{\hbar\omega_0}{2\varepsilon_0}} \alpha_0 \left[ e^{-i\omega_0 t} - e^{i\omega_0 t} + \frac{i\epsilon_\phi}{2} (e^{-i(\omega_0-\Omega)t} + e^{i(\omega_0-\Omega)t}) + \frac{i\epsilon_\phi}{2} (e^{-i(\omega_0+\Omega)t} + e^{i(\omega_0+\Omega)t}) \right] \quad (\text{V.14})$$

where  $\alpha_0$  is the coherent amplitude of the carrier,  $\epsilon_\phi \ll 1$  is a small modulation index (related to the phase modulation depth), and  $\omega_0$  is the optical carrier frequency. This field includes both the positive and negative frequency components, as expected for a physical (Hermitian) electric field operator.

### Reflection from the Cavity

Each frequency component of the field is reflected with a complex frequency-dependent amplitude reflection coefficient  $r(\omega)$ , such that the reflected field is:

$$\begin{aligned} E_{\text{refl}}(t) = i\sqrt{\frac{\hbar\omega_0}{2\varepsilon_0}} \alpha_0 & \left[ r(\omega_0)e^{-i\omega_0 t} - r^*(\omega_0)e^{i\omega_0 t} \right. \\ & + \frac{i\epsilon_\phi}{2} (r(\omega_0 - \Omega)e^{-i(\omega_0-\Omega)t} + r^*(\omega_0 - \Omega)e^{i(\omega_0-\Omega)t}) \\ & \left. + \frac{i\epsilon_\phi}{2} (r(\omega_0 + \Omega)e^{-i(\omega_0+\Omega)t} + r^*(\omega_0 + \Omega)e^{i(\omega_0+\Omega)t}) \right] \end{aligned} \quad (\text{V.15})$$

### Photodetected Intensity

The photodetector measures the intensity:

$$I(t) \propto |E_{\text{refl}}(t)|^2$$

We isolate the terms oscillating at  $\Omega$ , which arise from the interference between the carrier and sideband components. Keeping only the beat terms between the carrier and sidebands, we find:

$$I(t) \supset \epsilon_\phi \cdot \operatorname{Re}[A_+ - A_-] \cos(\Omega t) + \epsilon_\phi \cdot \operatorname{Im}[A_+ - A_-] \sin(\Omega t) \quad (\text{V.16})$$

where we define:

$$A_\pm = r(\omega_0)r^*(\omega_0 \pm \Omega)$$

### Demodulation with Arbitrary Phase

The signal is demodulated using a local oscillator  $\cos(\Omega t + \phi)$ , where  $\phi$  is the demodulation phase. Using trigonometric identities:

$$\cos(\Omega t + \phi) = \cos(\Omega t) \cos \phi - \sin(\Omega t) \sin \phi$$

we multiply Equation (V.16) and low-pass filter to obtain:

$$\epsilon_{\text{PDH}}(\phi) \propto \epsilon_\phi \{\operatorname{Re}[A_+ - A_-] \cos \phi + \operatorname{Im}[A_+ - A_-] \sin \phi\} \quad (\text{V.17})$$

### Sidebands Far Off-Resonance Approximation

In the standard PDH regime, the modulation frequency is much greater than the cavity linewidth:

$$\Omega \gg \kappa$$

so the sidebands are far off-resonance. This means:

$$r(\omega_0 \pm \Omega) \approx 1 \Rightarrow A_\pm \approx r(\omega_0)$$

and therefore:

$$A_+ - A_- \approx 0$$

However, if we retain the asymmetry between the sidebands (e.g., due to dispersion), or keep the finite detuning contribution, we approximate:

$$A_+ - A_- \approx r(\omega_0) [r^*(\omega_0 + \Omega) - r^*(\omega_0 - \Omega)] = r(\omega_0) \Delta r^*$$

### Final Result

Substituting into Equation (V.17), we obtain:

$$\epsilon_{\text{PDH}}(\phi) \propto \epsilon_\phi \{\operatorname{Re}[r(\omega_0) \Delta r^*] \cos \phi + \operatorname{Im}[r(\omega_0) \Delta r^*] \sin \phi\} \quad (\text{V.18})$$

In the limit where  $\Delta r^* \rightarrow 1$  (normalized, symmetric sidebands), this simplifies to:

$$\epsilon_{\text{PDH}}(\omega_0, \phi) \propto \cos \phi \cdot \text{Re}[r(\omega_0)] + \sin \phi \cdot \text{Im}[r(\omega_0)] \quad (\text{V.19})$$

## 7. Interpretation

Equation (V.19) shows that the demodulated error signal is a linear superposition of the real and imaginary parts of the complex reflection coefficient. The demodulation phase  $\phi$  selects the detected quadrature:

- $\phi = 0$ : error signal is proportional to  $\text{Re}[r]$  — symmetric around resonance, not suitable for locking.
- $\phi = \pi/2$ : error signal is proportional to  $\text{Im}[r]$  — antisymmetric, ideal dispersive error signal.
- $\phi \neq 0, \pi/2$ : mixes quadratures, possibly introducing offset or distortion.

This derivation makes explicit how the PDH method uses phase-sensitive detection to extract the component of the reflection coefficient that varies linearly with detuning, enabling precise feedback locking of the laser to the cavity resonance.



# Appendix C: Three Mirror cavities

In this appendix, we detail calculation details not mentionned in the main text regarding three-mirror cavities.

## Three-mirror cavity fields

We consider an input coupler mirror with amplitude reflectivity and transmissivity  $r_1$  and  $t_1$ , a second mirror with  $r_m$  and  $t_m$  (to be consistent with the main text) and a third mirror with  $r_2$  and  $t_2$ . We will consider the input and output mirrors to be HR mirrors i.e.  $R_i = |r_i|^2 \sim 1$  and  $T_i = |t_i|^2 \ll 1$  for  $i = 1, 2$ . This will allow us to neglect terms in  $t_1^2$  and  $t_2^2$  in the following calculations. The input-output relation at various coupler interfaces read

$$\begin{aligned}\hat{a}_R &= t_m \hat{a}_L + r_m \hat{a}'_R \\ \hat{a}'_L &= t_m \hat{a}'_R + r_m \hat{a}_L\end{aligned}$$

as well as the reflections on the input and output couplers

$$\begin{aligned}\hat{a}_L &= -r_1 \hat{a}_R e^{i\phi_L} + t_1 \hat{a}_{\text{in}} \sim -\hat{a}_R e^{i\phi_L} + t_1 \hat{a}_{\text{in}} \\ \hat{a}'_R &= -r_2 \hat{a}_R e^{i\phi_R} \sim \hat{a}_R e^{i\phi_R}\end{aligned}$$

where  $\phi_L = 2kL_1$  and  $\phi_R = 2kL_2$  are the lengths of the two sub-cavities. Here we will consider the reflection coefficient of the input/output couplers to be  $r_i \sim -1$  for  $i = 1, 2$ , and  $r_m = |r_m|$  and  $t_m = i|t_m|$  for the middle mirror / membrane. Injecting the second system in the first one yields

$$\begin{aligned}(1 - r_m e^{i\phi_R}) \hat{a}_R &= t_m e^{i\phi_L} \hat{a}'_L + t_m t_1 \hat{a}_{\text{in}} \\ (1 - r_m e^{i\phi_L}) \hat{a}'_L &= t_m e^{i\phi_R} \hat{a}_R + r_m t_1 \hat{a}_{\text{in}}\end{aligned}$$

such that isolating the  $\hat{a}_{\text{in}}$  and considering the mean fields yields

$$\frac{\alpha_R}{\alpha'_L} = \frac{|t_m|(2|r_m| \sin \phi_L + i)}{|r_m|^2 - e^{i\phi_R}}$$

and the power ration for a driven cavity yields

$$\frac{P_R}{P'_L} = \frac{|t_m|^2(4|r_m|^2 \sin^2 \phi_L + 1)}{|r_m|^4 - 2|r_m|^2 \cos \phi_R + 1}$$









# Bibliography

- [1] H. J. Kimble et al. “Conversion of conventional gravitational-wave interferometers into quantum nondemolition interferometers by modifying their input and/or output optics”. In: *Physical Review D* 65.2 (Dec. 2001), p. 022002. ISSN: 0556-2821. DOI: [10.1103/PhysRevD.65.022002](https://doi.org/10.1103/PhysRevD.65.022002). URL: <http://link.aps.org/doi/10.1103/PhysRevD.65.022002> (cit. on p. 19).
- [2] Jérôme Poirson et al. “Analytical and experimental study of ringing effects in a Fabry–Perot cavity. Application to the measurement of high finesse”. In: *J. Opt. Soc. Am. B* 14.11 (Nov. 1997), pp. 2811–2817. DOI: [10.1364/JOSAB.14.002811](https://doi.org/10.1364/JOSAB.14.002811). URL: <https://opg.optica.org/josab/abstract.cfm?URI=josab-14-11-2811> (cit. on p. 29).
- [3] A. A. Clerk et al. “Introduction to Quantum Noise, Measurement and Amplification”. In: *Reviews of Modern Physics* 82.2 (Apr. 15, 2010), pp. 1155–1208. ISSN: 0034-6861, 1539-0756. DOI: [10.1103/RevModPhys.82.1155](https://doi.org/10.1103/RevModPhys.82.1155). arXiv: [0810.4729](https://arxiv.org/abs/0810.4729) [cond-mat, physics:quant-ph]. URL: <http://arxiv.org/abs/0810.4729> (visited on 05/27/2024) (cit. on pp. 57, 59).
- [4] H. J. Kimble et al. “Conversion of conventional gravitational-wave interferometers into quantum nondemolition interferometers by modifying their input and/or output optics”. In: *Physical Review D* 65.2 (Dec. 26, 2001), p. 022002. ISSN: 0556-2821, 1089-4918. DOI: [10.1103/PhysRevD.65.022002](https://doi.org/10.1103/PhysRevD.65.022002). URL: <https://link.aps.org/doi/10.1103/PhysRevD.65.022002> (visited on 05/22/2023) (cit. on p. 64).
- [5] A. M. Jayich et al. “Dispersive optomechanics: a membrane inside a cavity”. In: *New Journal of Physics* 10.9 (Sept. 2008), p. 095008. ISSN: 1367-2630. DOI: [10.1088/1367-2630/10/9/095008](https://doi.org/10.1088/1367-2630/10/9/095008). URL: <https://dx.doi.org/10.1088/1367-2630/10/9/095008> (visited on 08/27/2024) (cit. on p. 66).
- [6] J. C. Sankey et al. “Strong and tunable nonlinear optomechanical coupling in a low-loss system”. In: *Nature Physics* 6.9 (Sept. 2010). Publisher: Nature Publishing Group, pp. 707–712. ISSN: 1745-2481. DOI: [10.1038/nphys1707](https://doi.org/10.1038/nphys1707). URL: <https://www.nature.com/articles/nphys1707> (visited on 08/27/2024) (cit. on pp. 66, 68).

- [7] C. A. Regal, J. D. Teufel, and K. W. Lehnert. “Measuring nanomechanical motion with a microwave cavity interferometer”. In: *Nature Physics* 4.7 (May 2008), pp. 555–560. ISSN: 1745-2473. DOI: [10.1038/nphys974](https://doi.org/10.1038/nphys974). URL: <http://www.nature.com/doifinder/10.1038/nphys974> (cit. on pp. 93, 114).
- [8] J. C. Sankey et al. “Strong and tunable nonlinear optomechanical coupling in a low-loss system”. In: *Nature Physics* 6.9 (June 2010), pp. 707–712. ISSN: 1745-2473. DOI: [10.1038/nphys1707](https://doi.org/10.1038/nphys1707). URL: <http://www.nature.com/doifinder/10.1038/nphys1707> (cit. on pp. 97, 109).
- [9] J. D. Thompson et al. “Strong dispersive coupling of a high-finesse cavity to a micromechanical membrane.” In: *Nature* 452.7183 (Mar. 2008), pp. 72–75. ISSN: 1476-4687. DOI: [10.1038/nature06715](https://doi.org/10.1038/nature06715). URL: <http://www.ncbi.nlm.nih.gov/pubmed/18322530> (cit. on p. 109).
- [10] D. J. Wilson et al. “Measurement-based control of a mechanical oscillator at its thermal decoherence rate”. In: *Nature* (2015), pp. 2–6. ISSN: 0028-0836. DOI: [10.1038/nature14672](https://doi.org/10.1038/nature14672). URL: <http://www.nature.com/doifinder/10.1038/nature14672> (cit. on p. 109).



---

## Sujet : Squeezed light optomechanics: Theory and Experiments

---

**Résumé :** Cette thèse de doctorat étudie les limites quantiques à l'oeuvre dans la détection interferométrique de petits déplacements mécaniques, et comment surmonter ces dernières en utilisant de la lumière comprimée. Dans un premier temps, le travail traite théoriquement la faisabilité d'une lumière comprimée dépendante en fréquence via l'utilisation d'une cavité de filtrage/rotation en sortie d'un amplificateur paramétrique optique. Dans un second temps, il se concentre sur la faisabilité d'une détection sous la limite quantique standard (SQL) en détaillant deux expériences réalisées. La première implémente un système « membrane at the edge » (MATE) basé sur une membrane en nitrure de silicium à haut facteur de qualité mécanique monté dans une cavité Fabry Perot de grande finesse. La deuxième expérience présente une source de lumière comprimée indépendante de la fréquence. Ces deux expériences sont pilotées à l'aide de locks optiques digitaux basé sur FPGA et développé au laboratoire, permettant un fonctionnement stable dans les conditions requises pour des mesures à la limite quantique.

**Mots clés :** Optomecanique, Lumière comprimée, Cavité de grande Finesse, Interferométrie, Bruit thermique, Bruit de grenaille quantique, Resonateur de grand facteur de Qualité, Interféromètres pour la detection d'ondes gravitationnelles, Bruit de pression de radiation quantique

---

## Subject : Optomechanics and squeezed light

---

### Abstract:

**Keywords :** Optomechanics, Squeezing, High-Finesse cavity, Interferometry, Thermal Noise, Quantum Shot Noise, High-Q Resonator, Gravitational wave Interferometer, Quantum Radiation Pressure Noise

